



VERÖFFENTLICHUNGEN
des Instituts für Geotechnik
der Technischen Universität Bergakademie Freiberg

Herausgeber: H. Konietzky

Heft 2018-2

47. Geomechanik-Kolloquium

Freiberg • 16. November 2018

Freiberg 2018

Veröffentlichungen des Instituts für Geotechnik der TU Bergakademie Freiberg

Herausgeber: Prof. Dr.-Ing. habil. Heinz Konietzky

Anschrift: TU Bergakademie Freiberg
Institut für Geotechnik
Gustav-Zeuner-Straße 1
09596 Freiberg
Telefon: 03731 39-2458
Fax: 03731 39-3638
E-Mail: ifgt@ifgt.tu-freiberg.de
Internet: <http://tu-freiberg.de/fakult3/gt/>

Herstellung: SDV Direct World GmbH
Printed in Germany

Ohne ausdrückliche Genehmigung der Hausausgeber ist es nicht gestattet, das Werk oder Teile daraus nachzudrucken oder auf fotomechanischem oder elektronischem Wege zu vervielfältigen.

Für den Inhalt ist der Autor allein verantwortlich.

© Institut für Geotechnik - TU Bergakademie Freiberg - 2018

ISSN 1611-1605

Table of contents

Geomechanische Charakterisierung von lithologischen Trennflächen und Anisotropieeffekten Salzgesteinen <i>Wolfgang Minkley, Sebastian Knöfel, Till Popp, (IfG GmbH); Thomas Frühwirt (TU Bergakademie Freiberg)</i>	1
Representing seismicity and caving in Sweden's deep mines <i>Jessa Vatcher, Jonny Sjöberg, Fredrik Perman (Itasca Consultants AB, Sweden)</i>	11
Numerical simulation of geomembranes as bottom sealing below salt heaps <i>Jan-Peter Schleinig, Christian Artschwager, Christian Dumperth (K + S Aktiengesellschaft); Fabian Weber, Heinz Konietzky (TU Bergakademie Freiberg)</i>	31
Damage detection of shield tunnel structure by CCD camera system <i>Wei Chen, Zheng Huang, Helin Fu, (Central South University, Changsha, China)</i>	41
Rock mechanics of the Spent Nuclear Fuel disposal programme in Finland <i>Topias Siren, Jouni Valli (Rock Mechanics Consulting Finland Oy); Johannes Suikkanen (Posiva Oy, Finland); Jussi Mattila (Geological Survey of Finland); Rodney S. Read (RSRead Consulting Inc., Finland)</i>	69
Developing a hydro-mechanical coupled numerical model for a long-term prognosis for the underground mine Teutschenthal <i>Fabian Weber, Heinz Konietzky (TU Bergakademie Freiberg); Vera Böttge (Landesamt für Geologie und Bergwesen Sachsen-Anhalt)</i>	103
Simulation of Gas migration in Canadian Potential Host Rocks for Radioactive Waste Disposal <i>M. Fall, Z. Li, G. Guo, X. Wei (University of Ottawa, Canada)</i>	117
Geology, geometry and kinematics of an active deep-seated rock slide (Ötztal valley, Austria) <i>Christina Rechberger, Christian Zangerl, Christian Fey (University of Natural Resources and Life Sciences Vienna, Austria)</i>	135
TRIPLE C - the host rock adaptable container concept for disposal of high radioactive waste <i>Albert Kerber (SiCeram GmbH); Jürgen Knorr (GWT-TUD GmbH) Heinz Konietzky, Ya-Nan Zhao (TU Bergakademie Freiberg)</i>	157
Neubau Albulatunnel II, Herausforderungen beim Bau des zweithöchsten Alpendurchstichs der Schweiz <i>Uwe Holstein (AF Toscano AG, Switzerland)</i>	169

Blasting experiences from different tunnel excavations <i>Alfred Zettler (zConsult ZT GmbH)...</i>	185
The Koralmtunnel underground emergency stop – geotechnical design and construction <i>Thomas Pilgerstorfer, Harald Hölzl (Geoconsult ZT GmbH, Austria); Bernd Moritz (ÖBB-Infrastruktur AG, Austria)</i>	191
Solutions for Geotechnical Challenges in the Design of the Boezbergtunnel <i>Karl Grossauer (Amberg Engineering AG, Switzerland); Thomas Zieger (Swiss Federal Railway Authorities, Switzerland); Werner Schmid (Implenia Schweiz AG, Switzerland)</i>	205
Stress Measurements using Hydraulic Fracturing for the Assessment of the State of Stress and the Softening Conditions in Potash and Salt Mining <i>Axel Stäubert, Alexander Lechner, (K-UTECH AG)</i>	215

Additional paper

Experimental study on Mode I and Mode II fracture of granite after thermal shock treatments <i>Xiang Li, Zhuoyao Zhang, Wei Chen; (Central South University, Changsha, China)</i>	229
--------------------------------------------------------------------------------------------------------------------------------------------------------------------------------------------	-----

Geomechanical characterisation of lithological discontinuities and anisotropy effects in salt rocks

Geomechanische Charakterisierung von lithologischen Trennflächen und Anisotropieeffekten in Salzgesteinen

Wolfgang Minkley¹, Sebastian Knöfel¹, Till Popp¹, Thomas Frühwirth²

¹ IfG Institut für Gebirgsmechanik GmbH, Leipzig

² TU Bergakademie Freiberg, Institut für Geotechnik

Abstract

As part of a joint research project conducted by the Department of Rock Mechanics of the Freiberg University of Mining and Technology (TUBAF) and the Institute of Geomechanics GmbH (IfG Leipzig), the properties of potential interfaces in the layered salinar were to be systematically investigated using the geomechanical laboratory methods and equipment which are available at both institutions. The objective was the characterization of three lithologically and texturally distinct types of salt rock (weakly and strong layered rocks and change of salt type), but without location reference. As a result, extensive rock mechanical data sets of the various rock varieties were determined. It showed that not every macroscopically recognizable anhydrite / clay layer within the salt host rock is also a weakening plane. It follows that for each site an individual case-specific examination (with in-situ and laboratory investigations and, if necessary, subsequent modeling / numerical calculations) must be carried out.

Zusammenfassung

Im Rahmen einer gemeinschaftlich vom Lehrstuhl Felsmechanik der TU Bergakademie Freiberg (TUBAF) und dem Institut für Gebirgsmechanik GmbH (IfG Leipzig) betreuten Diplomarbeit sollten die Eigenschaften von potentiellen Trennflächen im geschichteten Salzgebirge systematisch gesteinsmechanisch untersucht werden, unter Nutzung des an beiden Institutionen vorhandenen geomechanischen Laborspektrums. Zielstellung war die Charakterisierung von drei lithologisch und textuell deutlich unterschiedlichen Salzgesteinstypen (schwach – stark geschichtet sowie ein Materialwechsel), allerdings ohne Lokationsbezug. Im Ergebnis wurden umfangreiche gesteinsmechanische Datensätze der verschiedenen Gesteinsserien bestimmt. Dabei zeigte sich, dass nicht jede makroskopisch erkennbare Anhydrit-/Tonlinie im Salz gleichzeitig auch eine „Schwächefläche“ ist. Daraus folgt, dass für eine Bewertung der bergbaulichen Relevanz von Trennflächen für jeden Standort eine einzelfallspezifische Untersuchung (mit in-situ und Laboruntersuchungen sowie ggf. nachfolgenden Modellrechnungen) durchzuführen ist.

1 Einführung

Trennflächen in Geomaterialien sind von entscheidender Bedeutung für die resultierenden Eigenschaften des Gebirges, da sie die Gebirgsfestigkeit in hohem Maße limitieren können und auch die Permeabilität des Gebirges stark beeinflussen. Obwohl das Salzgebirge häufig als Kontinuum angesprochen wird, treten auch dort Diskontinuitäten auf, die z. B. für die Bewertung der Firstflächenstabilität bzw. das Pfeilertragvermögens wesentlich sind (z. B. Minkley et al., 2007). In der Literatur sind allerdings bisher sehr selten umfassende experimentelle Untersuchungen an Haft- und Trennflächen von Salzgesteinen dokumentiert.

Im Rahmen der Diplomarbeit sollten die Eigenschaften von potentiellen Trennflächen im geschichteten Salzgebirge systematisch geomechanisch untersucht werden. Das zum Einsatz gebrachte methodische Spektrum bildet die technischen Möglichkeiten beider gesteinsmechanischen Labors ab und umfasste u. a. direkte Zugversuche, Spaltzugversuche und direkte Scherversuche für ein weites Spektrum von Normalspannungen mit gleichzeitiger Variation der Verformungsgeschwindigkeiten sowie triaxiale Festigkeitsversuche mit Bestimmung der Bruchfestigkeit bis in den Restfestigkeitsbereich und der Dilatanz.

2 Untersuchungsmaterial

Als repräsentative Auswahl des möglichen Spektrums wurden drei Salz-Varietäten von unterschiedlichen Lokationen ausgewählt, die einerseits (1) starke textuelle Unterschiede (schwach – stark texturiert) und (2) einen Materialwechsel aufwiesen:

- (Typ1) Steinsalz mit deutlichen Tonlöserhorizonten bzw. Schichtflächen – scharfer Kontaktübergang – Teilblöcke und Kernmaterial Hangendes Steinsalz (Herkunft: Spanien),
- (Typ2) Steinsalz mit diffuser Schichtung bzw. dünne Anhydritschnüre im Steinsalz (Herkunft: Werrarevier),
- (Typ3) Salzgestein mit Materialwechsel Steinsalz/Carnallitit – deutlicher Schichtübergang (Herkunft: Kalirevier Werra).

Am intensivsten konnte die Salzvarietät (Typ1) mit Tonlöserhorizonten beprobt werden, da von diesem ausreichend Material sowohl als Großblock als auch als Kernmaterial vorlag. Diese Ergebnisse werden nachfolgend auszugsweise dargestellt.

Anzumerken ist, dass der Großblock schon vor Beginn der Bearbeitung bereits auf zwei Tonhorizonten abgeglitten war und somit in drei Teilen vorlag, was auf die geringe Festigkeit potentieller Trennflächen hinweist. Damit ist zwar keine quantitative Untersuchung der Mindestfestigkeit dieser Versagensflächen möglich, aber die exakt aufeinander passenden Scherflächen wurden wieder zusammengefügt, womit zumindest die Restfestigkeit aufgrund der vorhandenen Trennflächenrauigkeit untersucht werden konnte.



Abb. 1: Probenmaterial (v.l.n.r.): (Typ1) "Upper Salt" - Steinsalz mit Tonlöserhorizonten, (Typ2) Steinsalz mit diffuser Schichtung, (Typ3) Materialwechsel Carnallit auf Steinsalz

3 Ergebnisse Salzvarietät (Typ1)

3.1 Scherfestigkeit

3.1.1 Versuchstechnik

Systematische Untersuchungen der Scherfestigkeit potentieller Trennflächen bilden eine wesentliche Grundlage zur Durchführung von Standsicherheitsberechnungen im geklüfteten oder geschichteten Gebirge. Für die Durchführung der Schertests wurden sowohl das konventionelle MTS-Shear Test System (Modell 816) des IfG (für Details s. Naumann et al., 2008) als auch die Eigenentwicklung der TUBAF, das Großrahmen-Felsschergerät GS 1000 (Konietzky et al., 2012) eingesetzt. Beide Groß-Schergeräte besitzen einen zweiachsigen Versuchsaufbau mit horizontaler und vertikaler Krafteinleitung, der auf einen zentral angeordneten Scherkasten-/Probenaufbau wirkt. Neben den Prüfkräften (IfG: 500 kN Axialkraft, 250 kN Druck / 160 kN Zug Horizontalkraft; TUBAF: 1000 kN Axialkraft) unterscheiden sich beide Prüfsysteme im Aufbau des Probenkastens. Während beim IfG der Probenaufbau einfach wechselbar ist, womit größere Probenserien durchgeführt (Schergeschwindigkeit: < 1 mm/s) werden können, wird die Probe bei der TUBAF im Prüfrahmen zementiert, womit ein extrem steifer Probenaufbau realisiert wird. Über den angeflanschten horizontalen Hydraulizylinder sind Scherkräfte von -300 kN bis 800 kN (statisch und dynamisch) möglich und es können Schergeschwindigkeiten von 10^{-7} mm/s bis zu 70 mm/s realisiert werden. Mit den beiden servo-hydraulischen Scherprüfsystemen lassen sich die folgenden Versuchsabläufe realisieren:

- Scherversuch unter konstanter Normallast (CNL),
- Scherversuch unter konstanter Normalsteifigkeit (CNS),
- Dilatanzfreier Scherversuch (Normalverschiebung $u_{n,dil} = 0$).

3.1.2 Einfluss der Normalspannung

Mit dem MTS-Schergerät des IfG wurden insgesamt 12 Scherversuche mit einer Standard-Verschiebungsgeschwindigkeit von 0,002 mm/s bei Normalspannungen σ_n zwischen 0,16 MPa und 8,0 MPa an vergleichbaren Tonlöserhorizonten sowie zusätzlich ein dilatanzfreier Scherversuch durchgeführt.

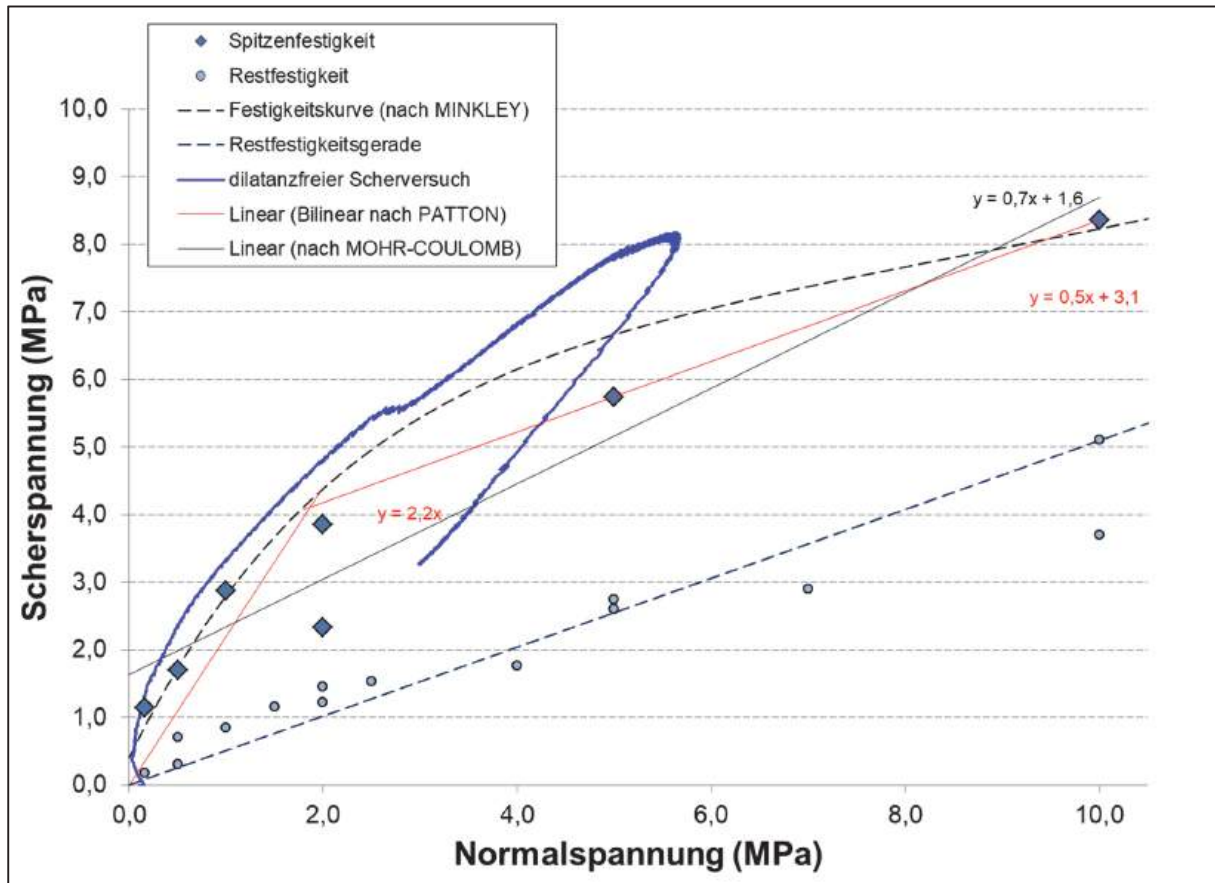


Abb. 2: $\tau - \sigma$ -Diagramm Steinsalz mit Tonlöserhorizonten – Salzvarietät (Typ1)

Die in Abbildung 2 im Scherspannungs-Normalspannungs-Diagramm dargestellten Ergebnisse zeigen eine gewisse Streuung der Peak-Festigkeiten, während die Restfestigkeit nahezu linear verläuft. Dabei ist es wichtig anzumerken, dass die Restfestigkeit intakter Proben noch eine geringe Kohäsion (ca. 0,2 MPa) aufweist, während sie für bereits offene Trennflächen erwartungsgemäß 0 ist. Die Festigkeitskurve des dilatanzfreien Scherversuchs ergibt eine vollständige Scherspannungs-Normalspannungs-Kurve, die eine obere Einhüllende bildet.

Zur Beschreibung der Festigkeitswerte wurden verschiedene lineare Ansätze (nach MOHR-COULOMB, bi-linear nach PATTON) sowie der nicht-lineare Ansatz nach MINKLEY angepasst, wobei letzterer die qualitativ beste Beschreibung ermöglichte.

3.2 Variation der Verschiebungsrate

Zur Untersuchung der Abhängigkeit der Scherfestigkeit von der Verformungsgeschwindigkeit wurden Scherversuche unter gleicher Normalspannung mit Variation der Verschiebungsgeschwindigkeit zwischen: *Langsam*: $2,0 \cdot 10^{-5}$ mm/s, *Standard*:

0,002 mm/s bzw. *Schnell*: 10 mm/s durchgeführt, woraus effektive Versuchszeiten von ca. 2 s, 3 h und ca. 5 d resultierten.

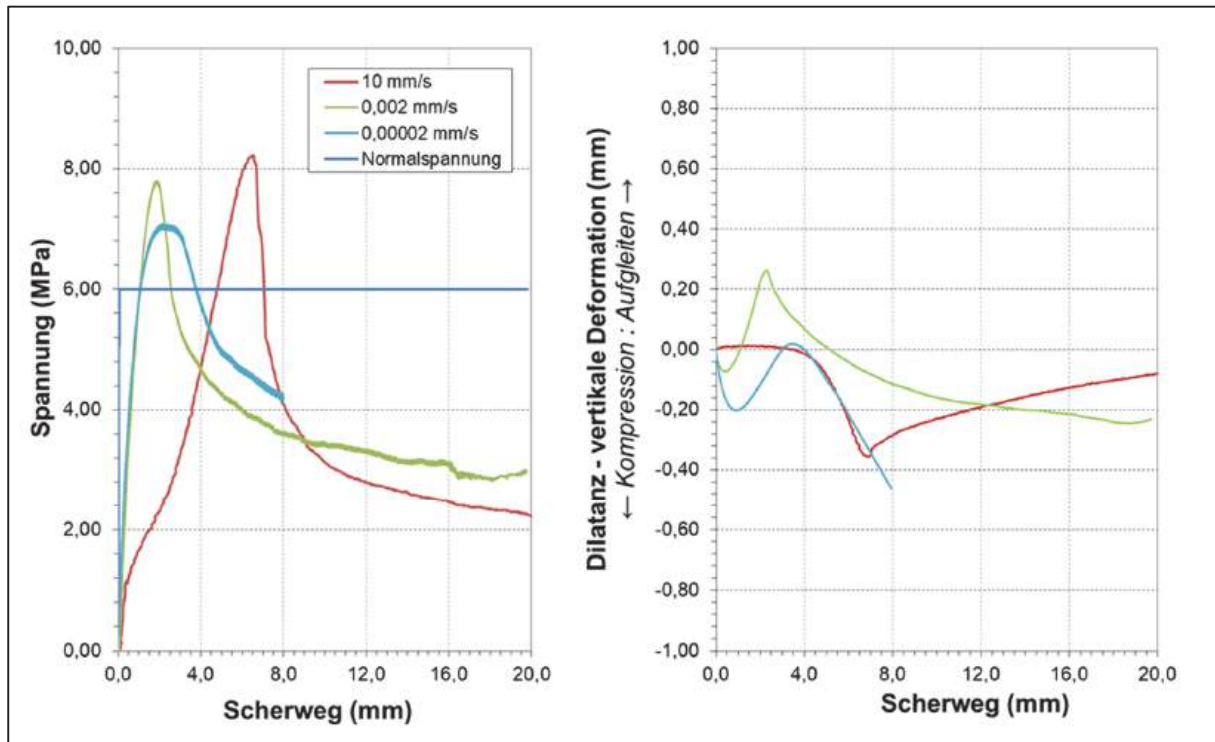


Abb. 3: Einfluss der Schergeschwindigkeit auf die Scherfestigkeitsentwicklung und Dilatanz ($\sigma_n = 6 \text{ MPa}$)

Die in Abbildung 3 dargestellten Scherspannungs-/Verformungskurven dokumentieren, dass bei sehr schnellen, dynamischen Scherprozessen (im Versuch: 10 mm/s Schergeschwindigkeit) kurzzeitig sehr hohe Spitzenscherfestigkeiten vorliegen, aber sich nach schlagartigem Versagen im Nachbruchbereich nur ein sehr geringes Restfestigkeitsniveau einstellt. Während sehr langsame Scherprozesse (im Versuch: $2,0 \cdot 10^{-5} \text{ mm/s}$) eine geringere Spitzenscherfestigkeit mit ausgeprägtem Plateau erreichten, stellte sich im Nachbruchbereich ein höheres Restfestigkeitsniveau ein.

Zur Dokumentation und genaueren Untersuchung der unterschiedlichen Versagensprozesse wurden am Lehrstuhl Felsmechanik Oberflächenscans der durchgeschernten Scherflächen durchgeführt (Abbildung 4). Auffällig war danach, dass mit zunehmender Schergeschwindigkeit der Scherbruch konzentriert in einem Tonhorizont verläuft. Hingegen konnte bei geringeren Scherraten die Bruchausbreitung durch Steinsalzzwischenmittel entlang mehrerer Tonschichten beobachtet werden.

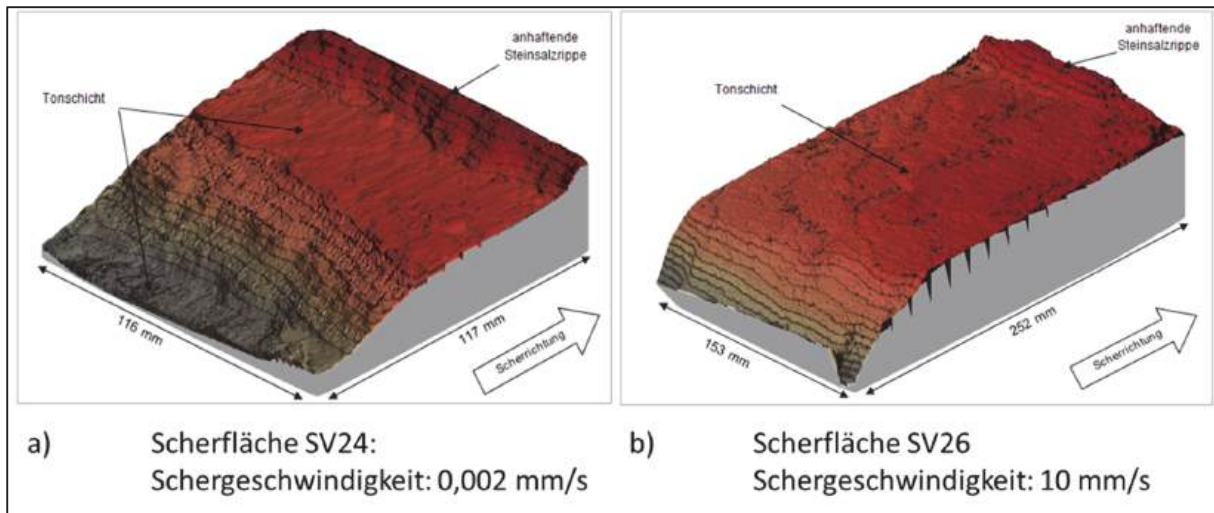


Abb. 4: Oberflächenscans der entstandenen Scherflächen von geschichteten Steinsalzproben (Typ1), die mit unterschiedlichen Verschiebungsraten geschert wurden.

3.3 Direkte Zugfestigkeit und Spaltzugfestigkeit

Die Bestimmung der direkten Zugfestigkeit möglicher Trennflächen erlaubt eine unmittelbare Bewertung eines Versagensrisikos. Hier wurde für potentielle Schichtflächen der Salzvarietät (Typ1) mit Tonlöserhorizonten eine mittlere Zugfestigkeit von $0,7 \pm 0,3$ MPa bestimmt (Abbildung 5). Dabei ist zu berücksichtigen, dass, weil der Probenblock bereits vorab an zwei Trennflächen zerfallen war, diese Werte sicherlich eher ein oberes Festigkeitsspektrum darstellen.



Abb. 5: Haftzugfestigkeit von Steinsalz mit Tonlöserhorizonten – Salzvarietät (Typ1) nach Versagen in einem Tonlöserhorizont

Aufgrund der schwierigeren Herstellung geeigneter Prüfkörper wurden zumeist Spaltzugversuche an Proben aus Kernsegmenten durchgeführt. Sie ermöglichen eine indirekte Bestimmung der Zugfestigkeit, wobei vor allem die Richtungsabhängig-

keit der Krafteinleitung und die Größe des Kernstücks die Versuchsergebnisse beeinflussen können.

Dieser Effekt wurde in einer umfangreichen Testserie untersucht, wobei die Spaltzugfestigkeiten richtungsabhängig zwischen 3,7 MPa und 0,2 MPa variieren und die kleinsten Werte bei schräggestellten Schichtflächen auftraten (Abbildung 6). In letzterer Versuchsanordnung war die Streuung der Kennwerte am höchsten. Somit ermöglicht die Ermittlung der Spaltzugfestigkeit von unterschiedlich ausgerichteten Proben eine Abschätzung der Anisotropie.

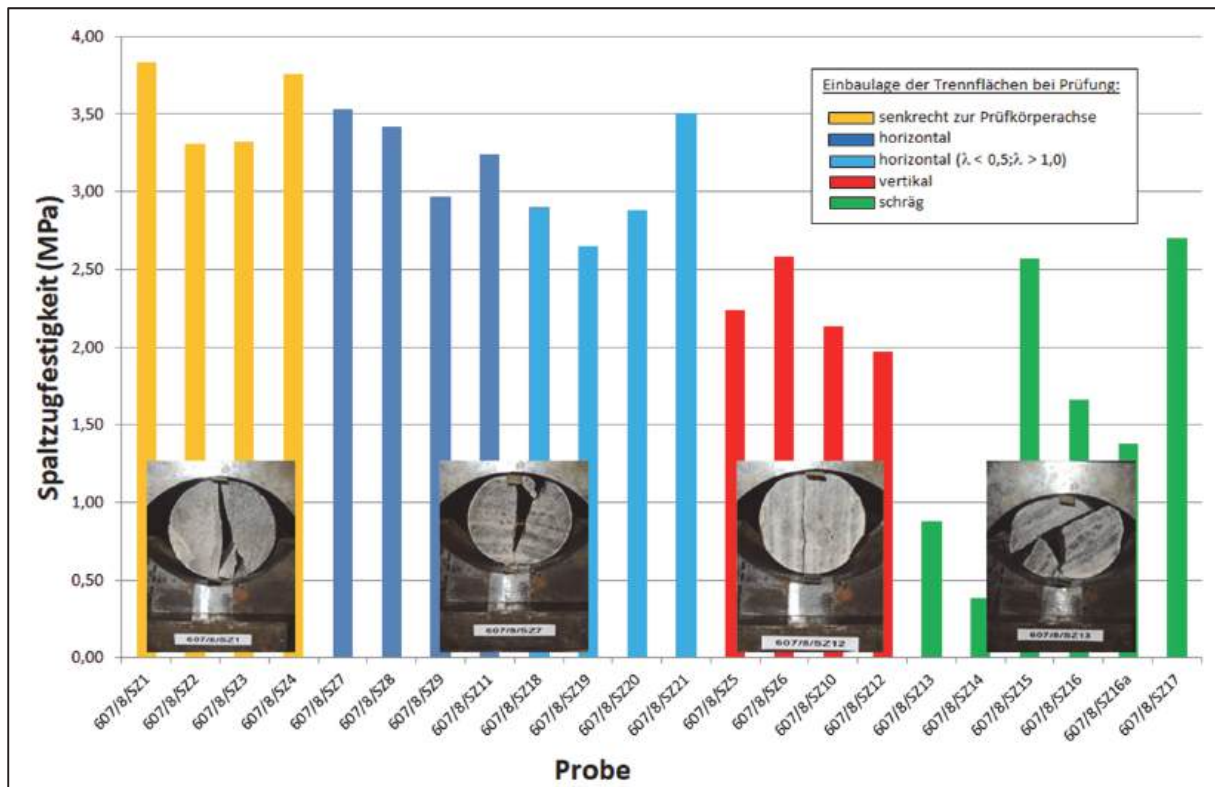


Abb. 6: Spaltzugfestigkeit von Steinsalz mit Tonlöserhorizonten – Salzvarietät (Typ1) bei Variation der Einbaulage zur Belastungsrichtung (vgl. Fotoinsets)

3.4 Triaxiale Druckfestigkeit

Am IfG Leipzig werden für triaxiale Festigkeitsuntersuchungen von großvolumigen sowie festen Salzproben routinemäßig servo-hydraulische Prüfmaschinen nach dem Kármán-Prinzip ($\sigma_1 \neq \sigma_2 = \sigma_3$) eingesetzt (Kármán, 1911), die zusätzlich auch eine Bestimmung der Dilatanz (Volumenänderung infolge Kompaktion oder Rissbildung) ermöglichen. Die Belastungsrichtung erfolgt standardmäßig senkrecht zur Schichtfläche, wobei Isotropie vorausgesetzt wird.

In der Realität sind die Festigkeiten im geschichteten Salzgebirge deutlich richtungsabhängig, wie Abbildung 7 zeigt. Abhängig von der Belastungsrichtung zeigen die Proben Festigkeitsunterschiede bis zum Faktor 2, wobei die höchsten Festigkeiten senkrecht zur Schichtung und die niedrigsten in einem Winkel von 60° dazu (Versagen auf Trennflächen) gemessen werden.

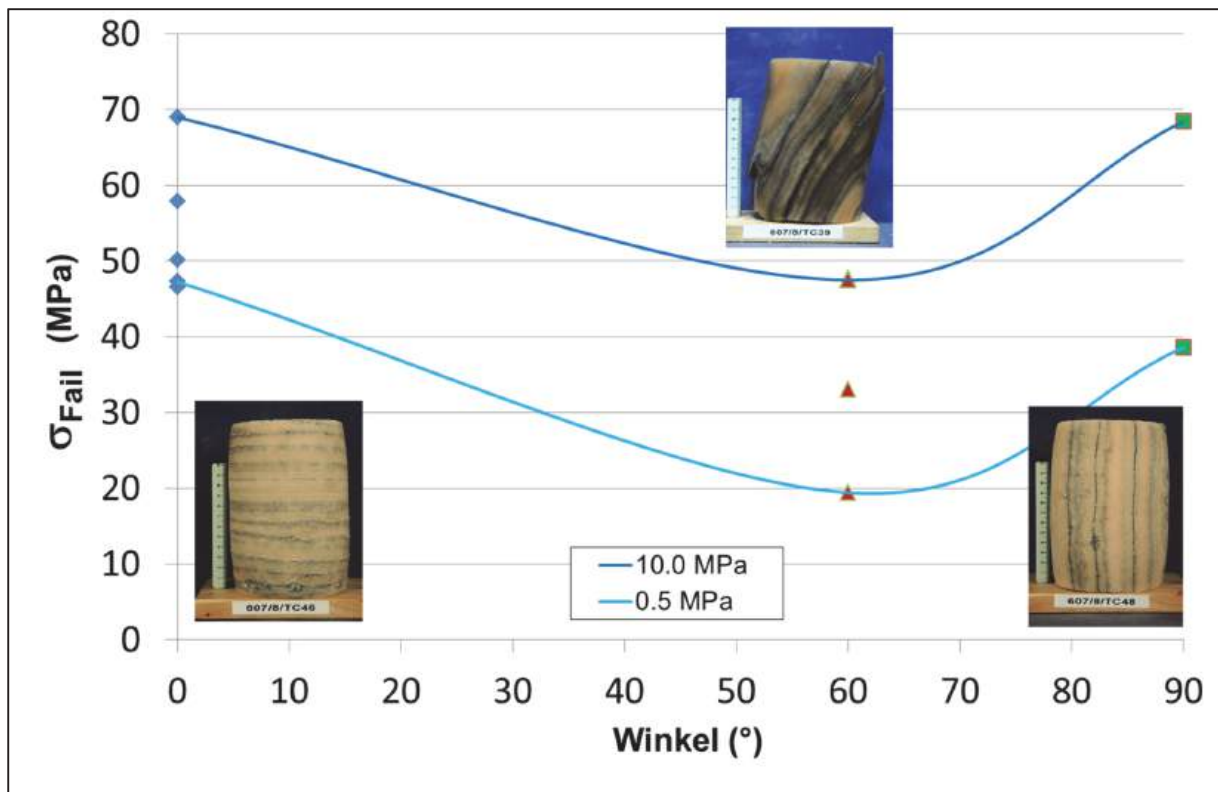


Abb. 7: Anisotropie der triaxialen Druckfestigkeit abhängig vom Einfallswinkel (bei radialen Einspannungen von $\sigma_3 = 0,5$ bzw. $10,0$ MPa)

4 Diskussion / Schlussfolgerungen

Die Untersuchungen dokumentieren das breite Spektrum von Festigkeitseigenschaften von Salzgesteinen, wenn zusätzlich Trennflächen auftreten. Es wird deutlich, dass Standardtests (z. B. uniaxiale oder triaxiale Drucktests sowie Spaltzugversuche) und zahlenmäßig begrenzte Versuchsserien nicht ausreichend sind, um repräsentative Eigenschaften bestimmen zu können, die als Basis einer numerischen Modellierung, z. B. zur Risikowertbewertung eines möglichen Firstfalls, dienen können. Die Gewinnung nicht vorgeschädigter Proben, z. B. mittels Großblocktechnik, ist dafür essentiell, wobei auch die „schwächsten“ Trennflächen erfasst werden müssen.

Im Unterschied zu Trennflächen im Fels müssen bei Schichtflächen im salinaren Gebirge neben Reibungsvorgängen zusätzlich Kohäsions- und Haftreibungseigenschaften berücksichtigt werden. Salzgesteine besitzen bereits unter normalen bergbaulichen Belastungsbedingungen die Fähigkeit zur Reaktivierung von Adhäsions- bzw. Kohäsionskräften an Trennflächen bzw. Schichtflächen. Eine Entfestigung der Trenn- bzw. Schichtflächen wird durch Haftreibungsverlust und das Abscheren von Unebenheiten bei zunehmender Scherverschiebung verursacht. Das bedeutet, dass bei qualifizierten Stoffmodellen der Einfluss der Verformungsgeschwindigkeit und der Verformungsbetrag berücksichtigt werden muss, wie z. B. bei Minkley et al., 2007.

Abschließend ist für die Bewertung der Stabilität von bergmännisch erstellten Hohlräumen unter Einbeziehung möglicher Trennflächen im Salzgestein festzuhalten, dass wegen der Heterogenität von Salzlagerstätten, die durch ihre Genese und tektonische Verformungen (Halokinese) strukturell geprägt wurden, nur eine lagerstätten-

spezifische, individuelle Begutachtung oder auch geomechanische Prüfung der Relevanz von Trennflächen und deren Eigenschaften möglich ist.

5 Literatur

Kármán von Th. (1911): *Festigkeitsversuche unter allseitigem Druck*. Z. Verhandl. Deut. Ingr. 55 (1911), 1749-1759.

Konietzky, H., Frühwirt, T., Luge, H. (2012): *A new large dynamic rock mechanical direct shear box device*. In: Rock Mechanics Rock Engineering, Jahrgang 45, Nr. 3, 427 - 432.

Minkley, W., Mühlbauer, J., Storch, G. (2007): *Dynamic processes in salt rocks - a general approach for softening processes within the rock matrix and along bedding planes*. In: Wallner, M., Lux, K.H., Minkley, W., Hardy, H.R.: The Mechanical Behavior of Salt – Understanding of THMC Processes in Salt: 6th Conference (SaltMech6), Hannover, Germany, 22 - 25 May 2007. Publ.: Taylor and Francis, ISBN: 9780415443982, 295-303.

Naumann, D., Popp, T., Minkley, W. (2008): *Labortechnische Ermittlung von Scherfestigkeitsparametern an Trennflächen mittels MTS-Schertestsystem des IfG Leipzig – Methodik und Beispiele*. In: Gattermann, J., Bruns, B. (Eds.): Fachseminar - Messen in der Geotechnik 2008. 23. - 24. Oktober 2008 Braunschweig. Mitteilung des Instituts für Grundbau und Bodenmechanik – Technische Universität Braunschweig. Heft Nr. 87, 127-144.

Representing seismicity and caving in Sweden's deep mines

Seismizität und Bruchbau in Schweden

Jessa Vatcher, Jonny Sjöberg, Fredrik Perman
Itasca Consultants AB
Luleå, Sweden

Abstract

As caving mines extend towards depth, the amount and severity of complex and challenging rock mass behaviours increases. Numerical representation of seismicity and the caving process is of great interest to caving mines. It is through numerical representation that we can understand the historic rock mass behaviour, and thereby forecast future outcomes. Caving mines in Sweden have three major dilemmas when it comes to rock mass behaviour: 1) surface subsidence associated with caving, 2) seismicity and damage underground, and 3) ground vibrations in nearby communities associated with mining induced seismicity. These dilemmas are explored in this paper for Luossavaara-Kiirunavaara AB's (LKAB) two caving mines, the Kiirunavaara Mine and the Malmberget Mine. For each dilemma, a description of the rock mass behaviours provided, followed by a summary of related important works, and discussion of ideas about the future of numerical representation. Clever algorithms to reduce computing time, coupled codes, and an exploration of damage processes point towards a bright future for numerical representation of seismicity in caving.

Zusammenfassung

Bruchbau breitet sich mit zunehmender Tiefe aus. Es nehmen auch Anzahl und Schwierigkeit komplexer Felsverhalten zu. Die numerische Darstellung der Seismizität und der Bruchprozesse sind von entsprechend großem Interesse. Durch die numerische Darstellung wird es möglich, historische Felsenmassenverhalten zu verstehen und dadurch zukünftige Ergebnisse voraussagen zu können. Im Bruchbau in Schweden gibt es drei Hauptprobleme, wenn das Massenverhalten von Fels betrachtet wird: 1) Oberflächensenkung durch die Einstürze, 2) Seismizität und Untergrundschädigungen und 3) Bodenvibrationen in nahe gelegenen Ortschaften, die gekoppelt sind an die vom Bergbau induzierte Seismizität. Diese Probleme werden hier für die Luossavaara-Kiirunavaara AB'S (LKAB) anhand von zwei Bruchbaubergwerken (Kiirunavaara Mine und die Malmberget Mine) erforscht. Für jedes Problem wird eine Beschreibung der Felsenmassen gegeben, gefolgt von einer Zusammenfassung von damit verbundenen wichtigen Arbeiten und einer Diskussion von Ideen über die Weiterführung der numerischen Berechnung. Effektive Algorithmen zur Einsparung von Rechenzeit, gekoppelte Codes und die Erforschung der Schadenprozesse führt zu einer Verbesserung für die numerische Darstellung von Seismizität im Bruchbau.

1 Introduction

As caving mines extend towards depth, the amount and severity of complex and challenging rock behaviour increases. It is precisely these challenging behaviours in Swedish mines that had led to a variety of studies and ideas about the future of numerical modelling for such environments. Active, deep, caving mines in brittle and high stress environments exhibit behaviours such as significant surface subsidence, mining induced seismicity, ground falls, strain bursting, and rock bursting, all of which pose a risk to personnel, infrastructure, and stakeholders, including communities near the mining operations. Developing an understanding of these phenomena is highly prioritised by stakeholders, so that risk mitigating design can be undertaken.

Specific challenges and rock mass behaviour in large, deep, caving mines include: 1) surface subsidence associated with caving, 2) underground damage often with associated mining induced seismicity, and 3) ground vibrations associated with mining induced seismicity. While there exist many agreed upon ways to describe and measure these behaviours, it is less agreed upon how one can gain an understanding for design purposes. It is widely accepted the numerical modelling is the leading tool in rock mechanics to evaluate complex rock mass behaviour. However, gaps in literature exist under all aspects of numerical representation, from selection of representative material properties, level of detail, scale, selection of critical geomechanical features, selection of appropriate constitutive model, and selection of analysis techniques and methodologies. Unanswered questions remain in the field of rock mechanics concerning understanding rock mass behaviour in deep caving mines, such as: How do we best represent caving? How do we best represent mining induced seismicity and associated damage?

It is exactly these rock mass challenges and questions that numerous works have focused upon for large, Swedish caving mines, such as the Luossavaara-Kiirunavaara AB's (LKAB) Kiirunavaara Mine and Malmberget Mine. This article provides a review of the rock mechanics related works which address these questions at these mines, with a focus on numerical modelling. The paper is organized around the three previously mentioned rock mass behaviour challenges, presenting existing works on the subject for LKAB's two caving mines, followed by a discussion of key observations concerning modelling techniques and opinions about promising future techniques.

2 Background: Kiirunavaara Mine and Malmberget Mine

Both the Kiirunavaara Mine and Malmberget Mine, located in northern Sweden in the cities of Kiruna (150 km north of the Arctic Circle) and Malmberget (70 km north of the Arctic Circle) respectively, use the sublevel caving mining method to extract iron ore. The Kiirunavaara Mine is one of the largest underground mines in the world, producing approximately 28 million tonnes of iron ore per annum (Fig. 2.1). The deposit is approximately 4.5 km in length along strike, with a dip of 50° to 70°, a thickness of a few metres to over 150 m, extended to surface, and is open at depth. The orebody is continuous and massive. The host rock is generally brittle with high strength and large variability, while the ore tends to be softer. (Vatcher *et al.*, 2016) Many joints exist throughout the mine, with large variability in orientation and relatively unclear definition between geomechanical domains (Vatcher *et al.*, 2016). Volumes

of clay alteration exist, occasionally associated with discontinuities, as well as in the form of voluminous lenses of up to tens of metres in diameter are present in some portions of the mine. Larger scale structures, such as faults, are sparse. (Berglund and Andersson, 2013) The major principal stress is oriented at approximately 83° North, perpendicular to the strike of the orebody. The active main haulage level (at mine Level 1365 m) is approximately 1100 m below ground surface.

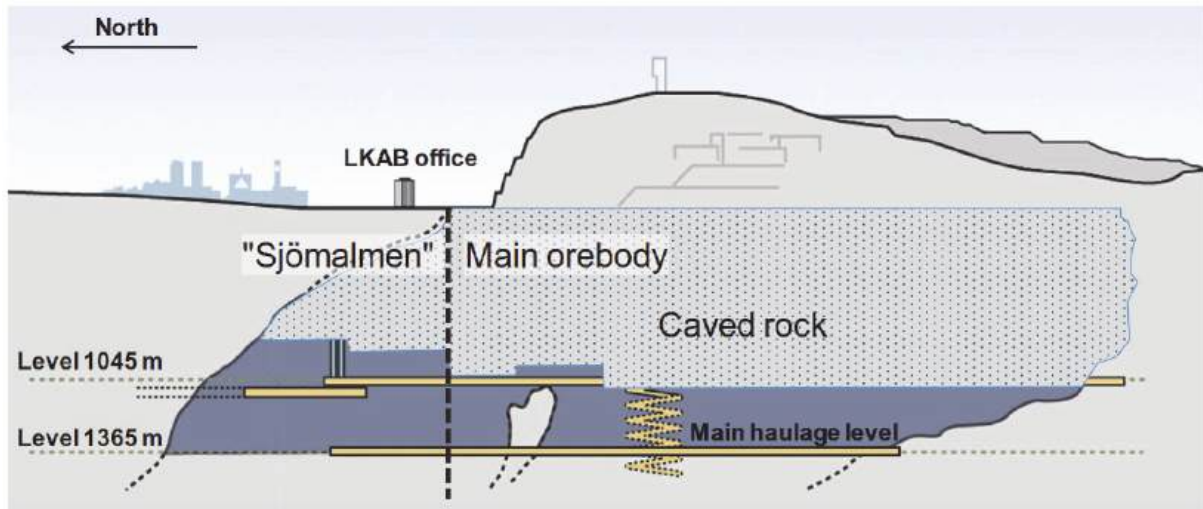


Fig. 2.1: Sketch of the Kiirunavaara Mine from the footwall towards the hangingwall and city of Kiruna, looking in the approximate direction of major principal stress (Sjöberg *et al.*, 2017).

The Malmberget Mine is comprised of 20 orebodies, with varying size, depth, shape, and orientation over an area of 8 km² (Fig. 2.2). The host rock is generally of moderate to high strength while the ore is softer. There also exists weak and soft biotite zones often following the footwall contacts. A number of large-scale deformation zones are identified in the mining area, but the characteristics of these, including exact location and orientation, are the subject of further studies. The active main haulage level (at mine Level 1250 m) is approximately 1000–1100 m below ground surface. The major horizontal stress is oriented at 132° North.

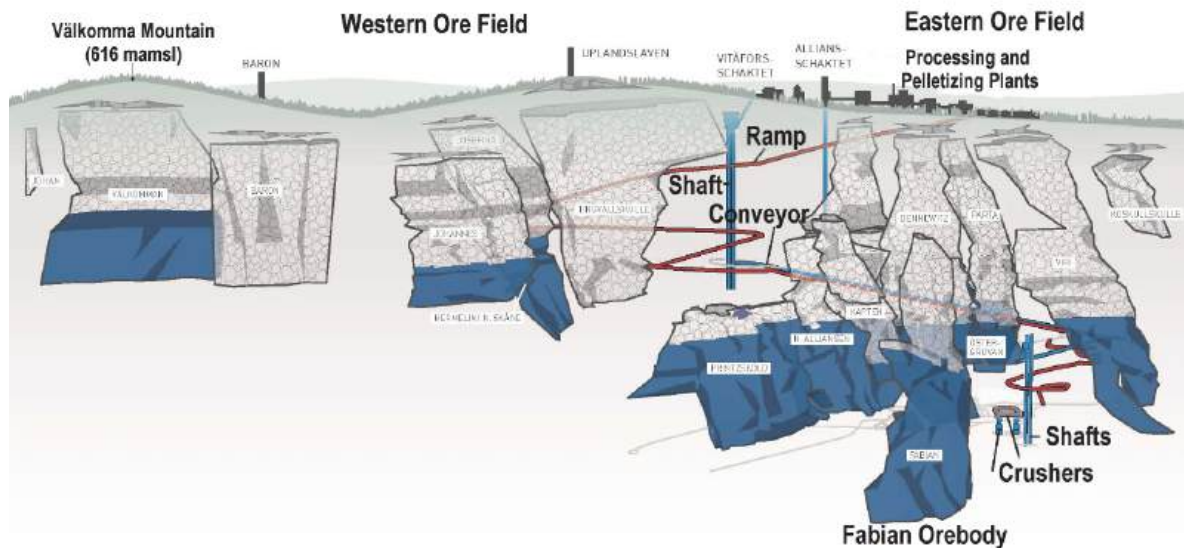


Fig. 2.2: Sketch of the Malmberget Mine. (courtesy of LKAB)

3 Dilemma 1: Surface subsidence associated with caving

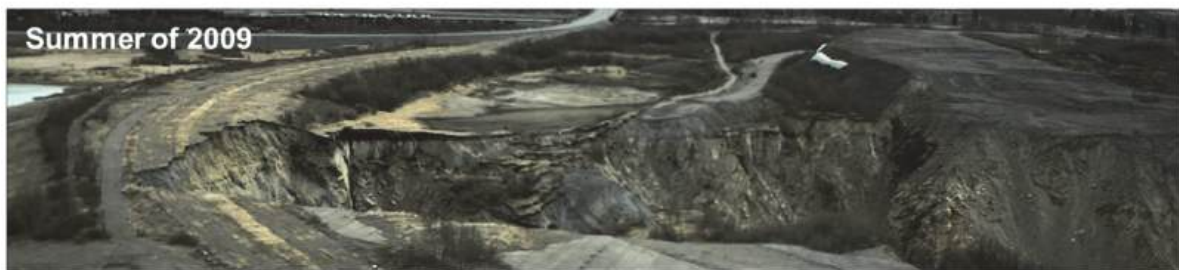
Surface subsidence is an expected outcome when employing caving mining methods. Mining activities at both the Kiirunavaara Mine and the Malmberget Mine have led to cavities that extend to the ground surface, leaving significant, measurable and easily visible subsidence and deformation (Fig. 3.1). These surface deformations are of importance to both mines since they are located within their respective city boundaries. Surface subsidence has resulted in the ongoing urban transformation process, where portions of the of the cities of Kiruna and Malmberget have already been relocated.

a. Existing works

Surface subsidence and caving at the two mines has been of much interest of recent studies. Sjöberg *et al.* (2017) describes the use of 1) 3-D modelling with Itasca’s caving algorithm, and 2) a 2-D simulation scheme to study the progression of caving in the northern portion of the Kiirunavaara Mine.

The 3-D models of Sjöberg *et al.* (2017) were at the mine scale, with back analysis focused on the northern portion of the mine, as this is the area that has the greatest influence on the urban transformation process. These 3D models used Itasca’s Caving Algorithm and CaveHoek constitutive model to simulate ore draw and the resulting caving of the rock mass. Twelve different cases were analysed where each case had a unique set of hangingwall rock mass properties. An image of the footwall and orebody in model is shown in Fig. 3.2, with the draw schedule sources labelled.

a)



b)



Fig. 3.1: Aerial images of surface subsidence at a) Kiirunavaara Mine (Sjöberg *et al.*, 2017) and b) Malmberget Mine.

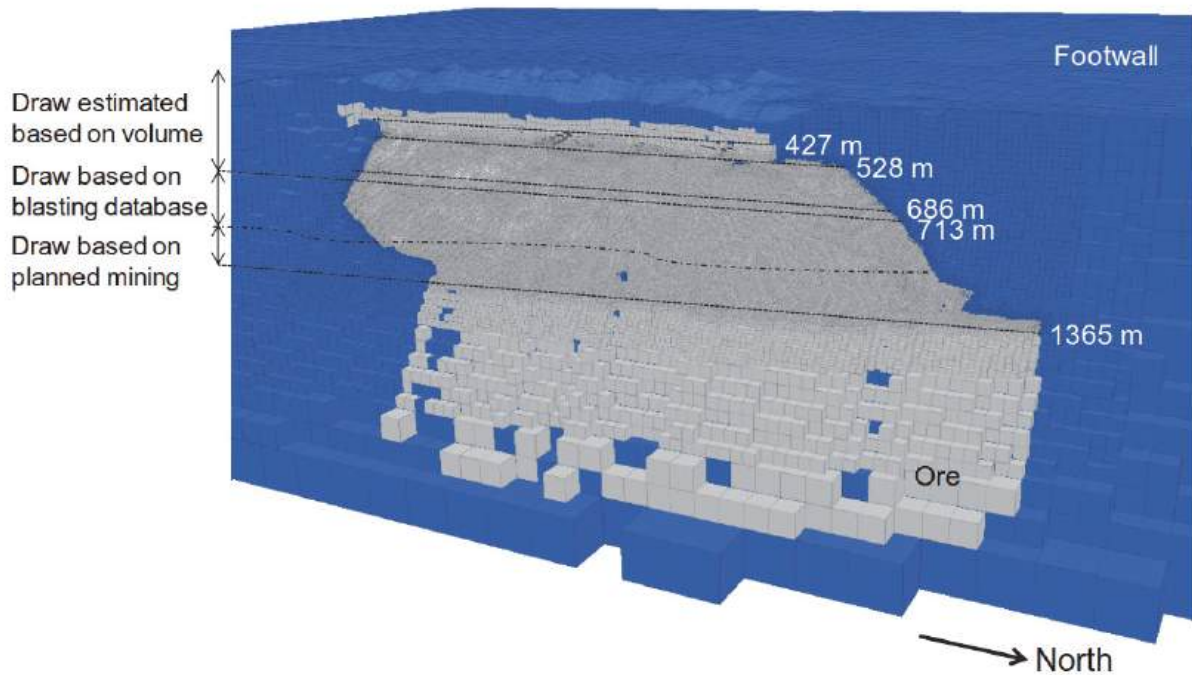


Fig. 3.2: Perspective view of the lack 3D model looking towards the footwall (blue). The ore-body is grey. Mining levels and draw schedule sources are labelled (Sjöberg *et al.*, 2017).

The caving algorithm is designed to numerically predict the geomechanical zones associated with the caving process described by Duplancic and Brady (1999). These include the elastic zone, the seismogenic zone, the yielded zone, the air gap, and the mobilised zone. This numerical technique has been applied to many caving operations. The algorithm avoids excessive computation times associated with representation of the exact physical, discontinuous phenomena of caving by using a continuum-based approach. Mass balance routine is implemented to represent the tonnage-based production schedule accurately in the model. Small strain mode is used to avoid issues caused by the large deformations associated with caving. Instead, zone density is adjusted to reflect the volumetric changes associated with bulking. Draw is simulated by the removal of a layer of zones at the draw points, followed by forces on the grid points that represent resistance provided by the extraction level on the floor and a downward velocity on the roof proportional to the draw rate. The density of the zones in the caved material is updated for mass balance purposes based on volumetric strain. Displacement and yielding can occur in the overlying zones allowing the caved progress upwards. A threshold of vertical displacement is used to identify if a zone has been excavated. The strain softening CaveHoek constitutive model developed by Itasca is used in combination with the caving algorithm. For more details about the algorithm and the CaveHoek constitutive model, refer to Sjöberg *et al.* (2017).

Model results from historic mining were evaluated by comparing the extent of the crater developed in the numerical model to the observed and measured crater on surface. An example comparison of these craters is shown in Fig. 3.3. These models were also run to predict the extent of caving caused by future mining. Results showed that the use of the Caving Algorithm in 3-D agreed well with actual meas-

ured data, but that the 2-D models, using a different simulation scheme, were less useful for this problem. (Sjöberg *et al.*, 2017)

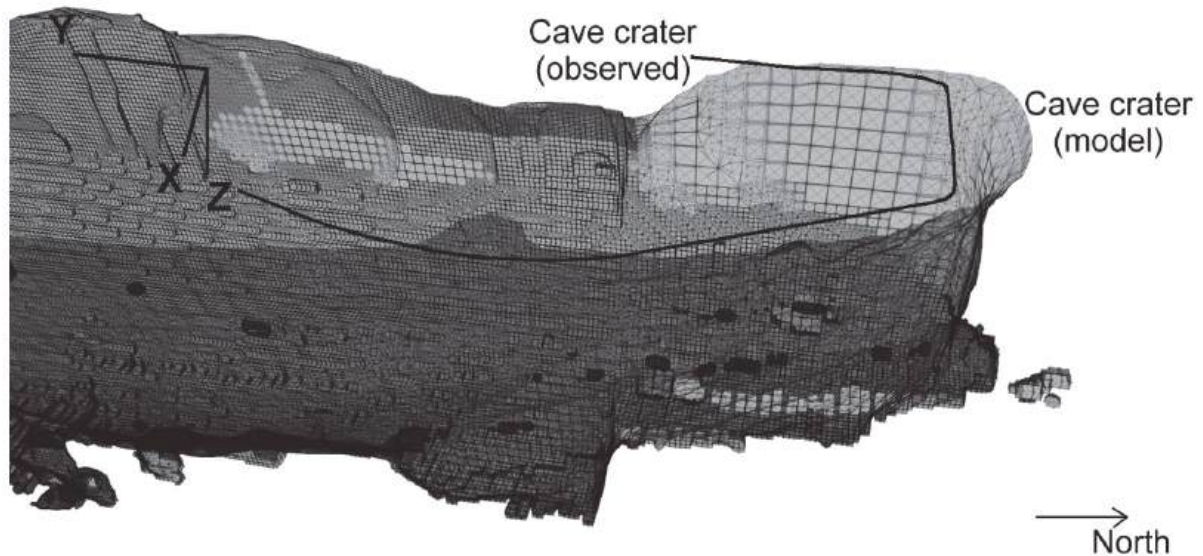


Fig. 3.3: Perspective view of the resultant crater developed in the model and the observed crater on surface for the year 2014 (Sjöberg *et al.*, 2017).

Caving and surface subsidence for specific orebodies of the MalMBERGET Mine have also been analysed. Banda (2017) presents extensive work in understanding the caving mechanisms for the Printzsköld orebody using different techniques than the Caving Algorithm. Techniques included 2-D and 3-D modelling, with a focus on discontinuum modelling. Of particular interest, Banda (2017) used the technique of Bonded Block Modelling (BBM) in the Itasca's *3DEC* code to evaluate cave development above this orebody.

BBM represents the rock mass as a volume of connected blocks, where connections are mechanical interfaces which have the ability to break and move. It is through these interface failures that one understands the damage process that the rock mass undergoes. An example of Banda's (2017) results is shown in Fig. 3.4, where one can see cave formation through failure of both the intact block as well as the contacts between blocks. The caving development through this modelling technique corresponded well with the seismogenic zone identified from locations of seismic events. (Banda, 2017)

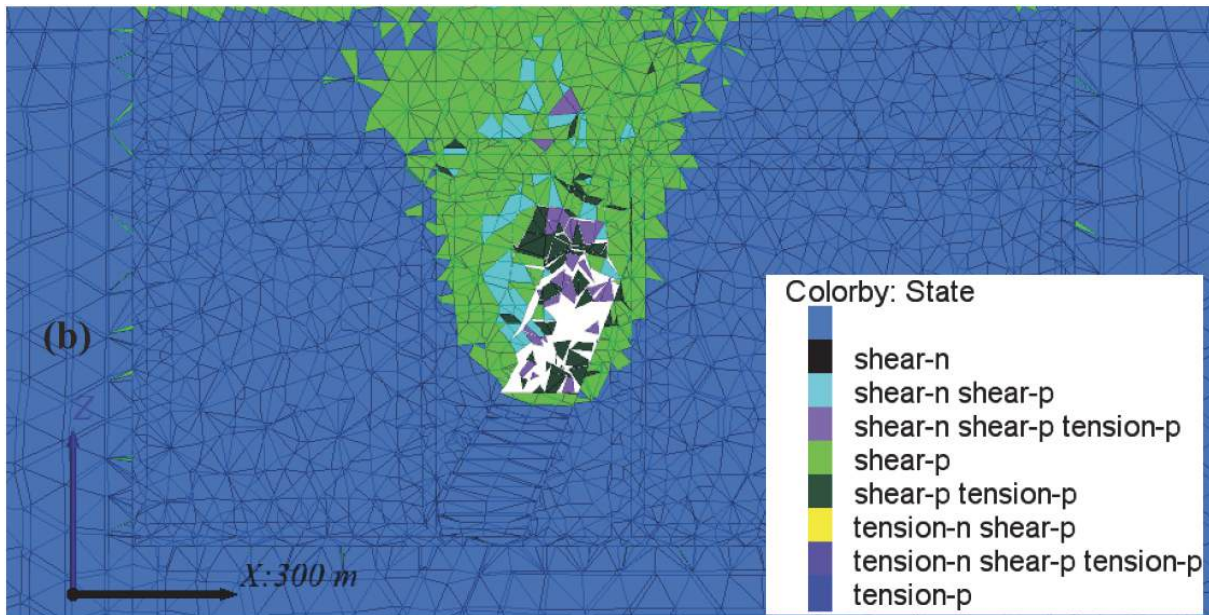


Fig. 3.4: 2-D slice of the 3-D BBM models, showing cave development caused by draw (Banda, 2017).

b. Discussion

Understanding the caving process and surface subsidence is clearly very important to caving mines. Relatively recent advances in modelling techniques and computing power are enabling a much deeper understanding of caving.

The primary advantage of Itasca’s Caving Algorithm with the CaveHoek constitutive model is that it has been tested on many cases. Unfortunately, these models are often computationally intensive, requiring weeks to run.

The BBM technique is a promising development in understanding rock mass failure. This is one of the cutting-edge damage modelling techniques, and as such we are only in the infancy of understanding its potential. The current major drawback of BBM is that these models are also computationally intensive (even more so than the Caving Algorithm). To analyse damage progression, one wants small blocks to enable enough resolution. However, when it comes to caving problems, the volume to analyse is large. This results in a need to compromise on block size. As computing power intensifies, and programs are potentially updated to better handle these types of analyses, BBM is a technique that offers much promise to understand damage processes, but improvements would need to be significant to be able to model large caving volumes.

A third cave development modelling technique exists that has not yet been applied in Sweden. Hebert and Sharrock (2018) present a coupled finite difference-cellular automata solution to evaluate cave initiation, propagation, ore flow, and surface subsidence. The cellular automata solution, *CAVESIM*, is bidirectionally coupled with a continuum model in Itasca’s *FLAC3D*. Cellular automata are well suited to studying large problems with limited physics. *FLAC3D* is used to evaluate cave propagation based on material failure. *CAVESIM* uses the cavity from *FLAC3D* and stimulates the gravity flow of caved rock, material bulking, and the accumulated airgap in cavities. It can

represent overhangs, hangups, sidewalls, and complex cavity geometry. This information about the flow, bulking, and airgap is returned to *FLAC3D* to be used in the next calculation of cave development. This cycling between *FLAC3D* and *CAVESIM* continues until production is finished. (Hebert and Sharrock, 2018)

Models that use *CAVESIM* coupled with *FLAC3D* to evaluate caving have much faster run times than the previously mentioned caving modelling techniques. Due to these fast run times, it is even possible to include many discontinuities in the *FLAC3D* model. Hebert and Sharrock (2018) provided an example of how important a discontinuity can be on cave propagation. This fast and powerful technique appears to be very promising for the future of numerical modelling of cave progression, cave material flow, and airgap development.

4 Dilemma 2: Seismicity and damage underground

Before underground damage can be discussed, the usage of a few key terms concerning damage mechanisms has to be clarified:

- **Rockburst:** a violent ejection of rock causing damage to infrastructure, equipment, and/or personnel, resulting from stress concentrations and/or slip along discontinuities in brittle rock;
- **Strainburst:** a violent ejection of rock resulting from high stress concentrations in brittle rock;
- **Spalling:** onion-like flaking of the rock in layers that are a few centimetres thick, resulting from brittle failure, tensile damage, and confinement reduction.
- **Shakedown:** the ejection of previously separated blocks or pieces of rock due to vibrations often caused by blasting or mining induced seismicity. These pieces of rock may exist due to other damage mechanisms, such as those previously mentioned.

The Kiirunavaara Mine experiences difficult ground conditions, typical for deep, hard rock environments. This includes mining induced seismicity and ground falls. Seismicity at this mine tends to focus in the footwall, relatively close to production with some events further away. Seismic events also occur in the hangingwall, however the seismic system provides less coverage in this area, making the localization and magnitude determination of these events less reliable. Ground falls have mixed mechanisms including rock bursting, strainbursting, spalling, shakedown, and failure associated with pre-existing discontinuities. An example of a ground fall associated with a single seismic event is shown in Fig. 4.1. Ground falls and damage occur in most types of mine infrastructure, including the footwall drifts, crosscuts, and ore passes. In general, there are more falls of ground with increasing depth and in the central portion of the Kiirunavaara Mine. (Vatcher *et al.*, 2017)

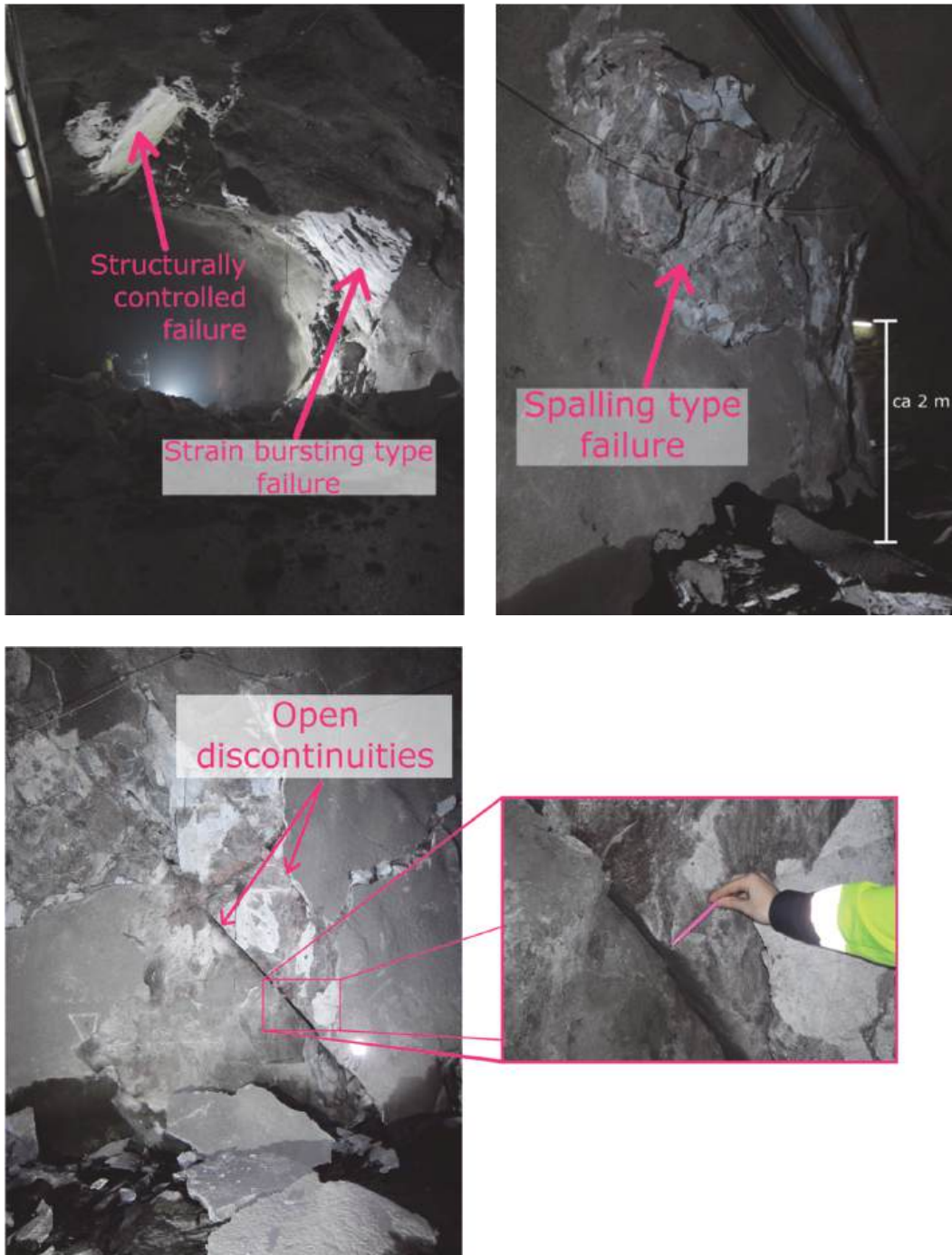


Fig. 4.1: Ground falls on Level 1198 m over approximately a 10 m stretch of drift associated with a single seismic event (local magnitude 0.8), displaying mixed mechanisms (Vatcher, 2017).

The Malmberget Mine also experiences underground damage, however it has been less extensively studied at the mine-scale to date. Unlike the Kiirunavaara Mine, seismicity here tends to be concentrated in the hangingwall and cap rock, where the caving process is underway. The host rock is of moderate to high strength while the ore is softer, ground falls do occur underground, and often involve mechanisms such as spalling, strainbursting, shakedown, and failure associated with pre-existing discontinuities. The biotite tends to be problematic underground from a ground control perspective.

tive, as it is much softer than the surrounding rock and is under intensive loading due to the high stress environment.

a. Existing works

At the Kiirunavaara Mine, significant effort has been placed into developing a better understanding of the geomechanical environment. Numerous numerical modelling techniques have been used to evaluate rock mass behaviour underground, with a focus on the problems associated with mining induced seismicity.

One study of interest, Vatcher (2017), focused on developing an understanding of the geomechanical environment and rock mass behaviour to better understand induced seismicity at the mine-scale. A 3-D geomechanical model was developed by Vatcher *et al.* (2016) that statistically evaluated rock quality designation (RQD), evaluated 3-D domains based on mapped structures, and created a 3-D model of volumes of clay alteration. The 3-D clay alteration model extends over a specific portion of the mine and represents volumes that are more likely to contain clay alteration (Fig. 4.2). In addition, behaviour at the mine was spatially and temporally analysed for statistical patterns that may provide information about the rock mass, and how the behaviour changes with the progression of mining. (Vatcher *et al.*, 2017)

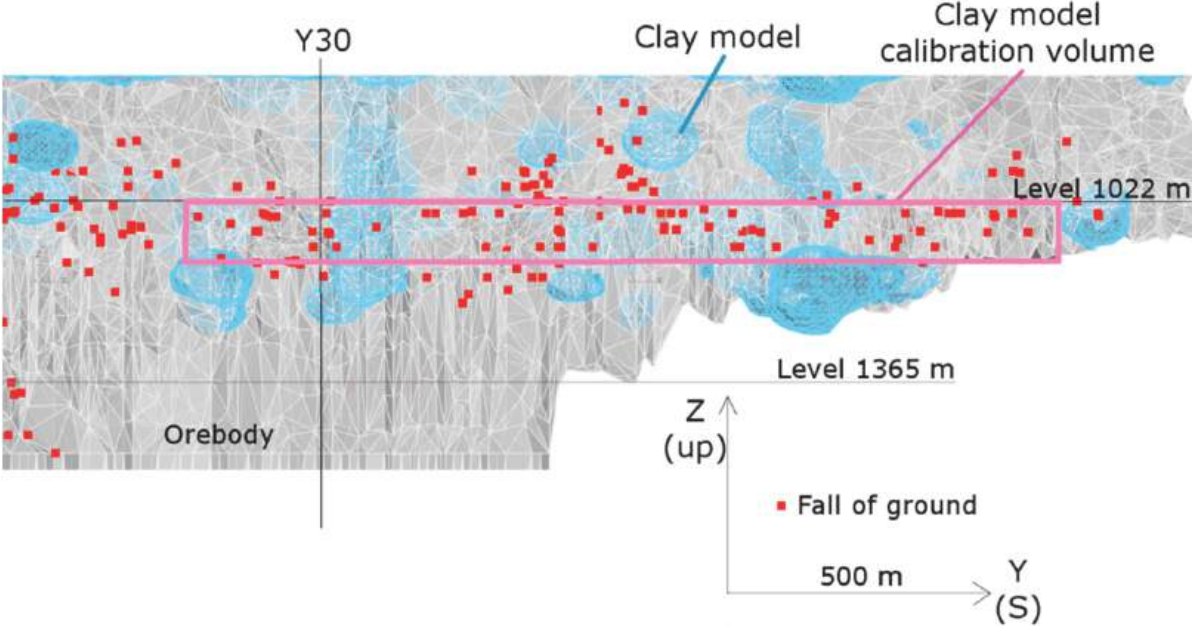
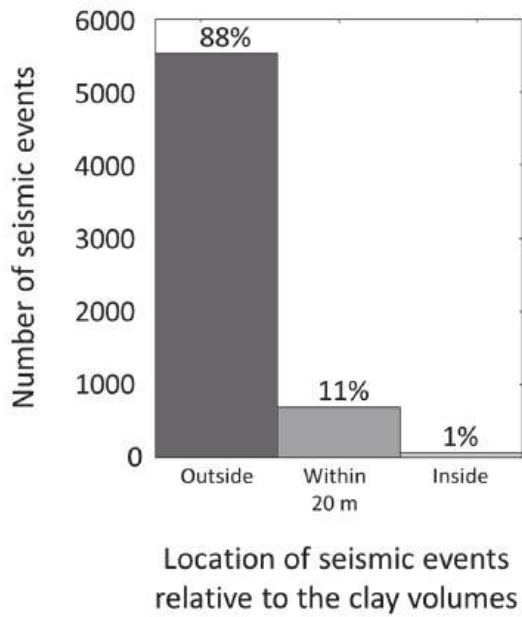


Fig. 4.2: 3D clay alteration model in cyan, orebody in grey (Vatcher *et al.*, 2016).

When combining these analyses, an interesting result emerged. As one would expect with soft material, very few seismic events were located inside of the model of clay alteration. Induced seismic events concentrated in the intact rock mass in between the clay rich volumes (Fig. 4.3). This led to the hypothesis that the clay volumes are significantly influencing the stress field, and therefore seismicity. (Vatcher, 2017)

a)



b)

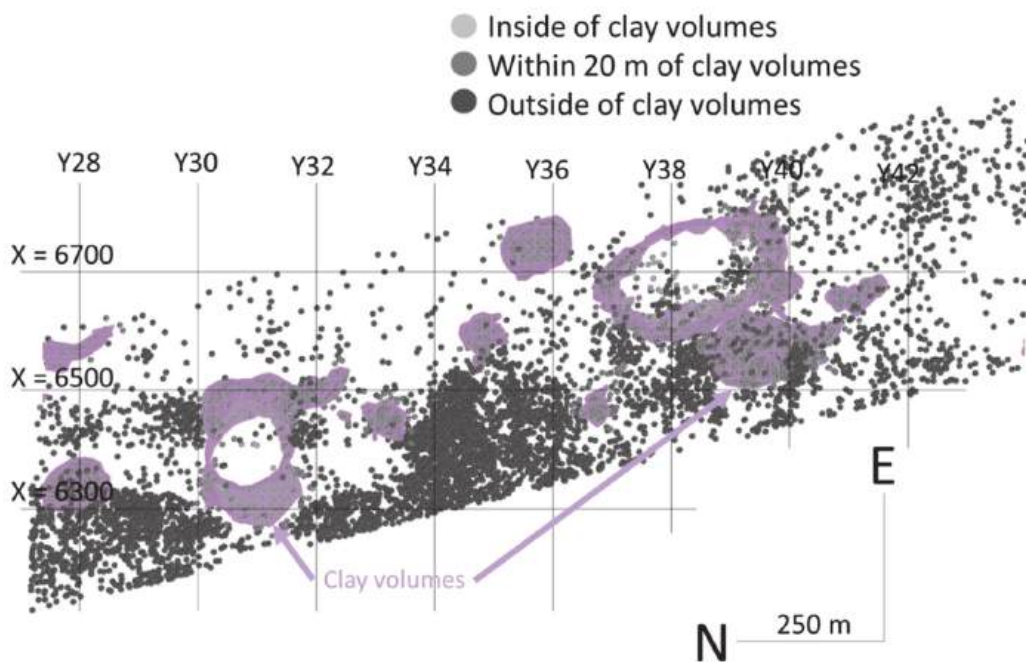


Fig. 4.3: a) Histogram of all seismic events located within the model of clay rich volumes, within 20 m of the boundaries of the clay rich volumes, and outside of the clay rich volumes. b) View from above of the model of clay rich volumes and seismic events (Vatcher, 2017).

Numerical modelling was used as a tool to explore if and how the clay volumes may influence the stress field and seismic behaviour. Large, mine-scale, 3-D numerical models were built in the Itasca code *FLAC3D* (Itasca Consulting Group, Inc., 2017). Despite that the Kiirunavaara has is often considered a 2D problem due to the length of the orebody, early in this work, Vatcher (2017) demonstrated that mining induced stress in the middle portion of the orebody is overestimated by a 2D approach. A

methodology to evaluate if geological features that exhibit significantly different stiffness properties than the surrounding rock mass contribute to rock mass behaviour was developed. A base model, without representation of volumes of clay alteration, was compared to a test model, with representation of volumes of clay alteration. In the test model, clay was numerically represented as voids that were present before excavations associated with mining. (Vatcher, 2017)

The comparison of the test and base model showed that the clay volumes result in significant induced stresses near production areas. Indicators of seismic activity were evaluated in both models. Two underlying mechanisms of seismicity were considered: 1) development of new fractures, and 2) slip along discontinuities.

To evaluate potential development of new fractures, plasticity and differential stress was used. Volumes of plastic failure represent rock that is yielded and may have experienced seismicity. It should be noted that crack initiation in laboratory tests begins before the material is yielded, the actual volume of the rock mass that experiences crack initiation may be larger than what is predicted by the volume of plastic failure. Diederichs (2000) illustrated that a threshold value of differential stress, calculated by the unconfined compressive strength multiplied by a constant, can represent shear failure, and therefore development of new fractures. Results at the Kiirunavaara Mine showed that the clay volumes did not significantly influence plastic failure (Fig 4.4), however they did affect the extent of the volume with high differential stresses. The clay alteration therefore has the potential to influence seismicity caused by crack initiation. (Vatcher, 2017)

The potential for slip along discontinuities was evaluated by the technique developed by Ryder (1988). Excess Shear Stress (ESS) evaluates if slip along a single discontinuity is possible based on the Mohr-Coulomb slip condition for dynamic slip. It should be noted that this is the potential for slip and does not necessarily indicate seismic slip. Perman *et al.* (2013) calculated ESS for mapped discontinuities based on numerical results for the Malmberget Mine. Vatcher (2017) calculated ESS at various locations and stages in production for all possible orientations of discontinuities (Fig. 4.5). Results showed that the onset of the potential for slip of discontinuities occurs earlier due to the clay alteration. (Vatcher, 2017)

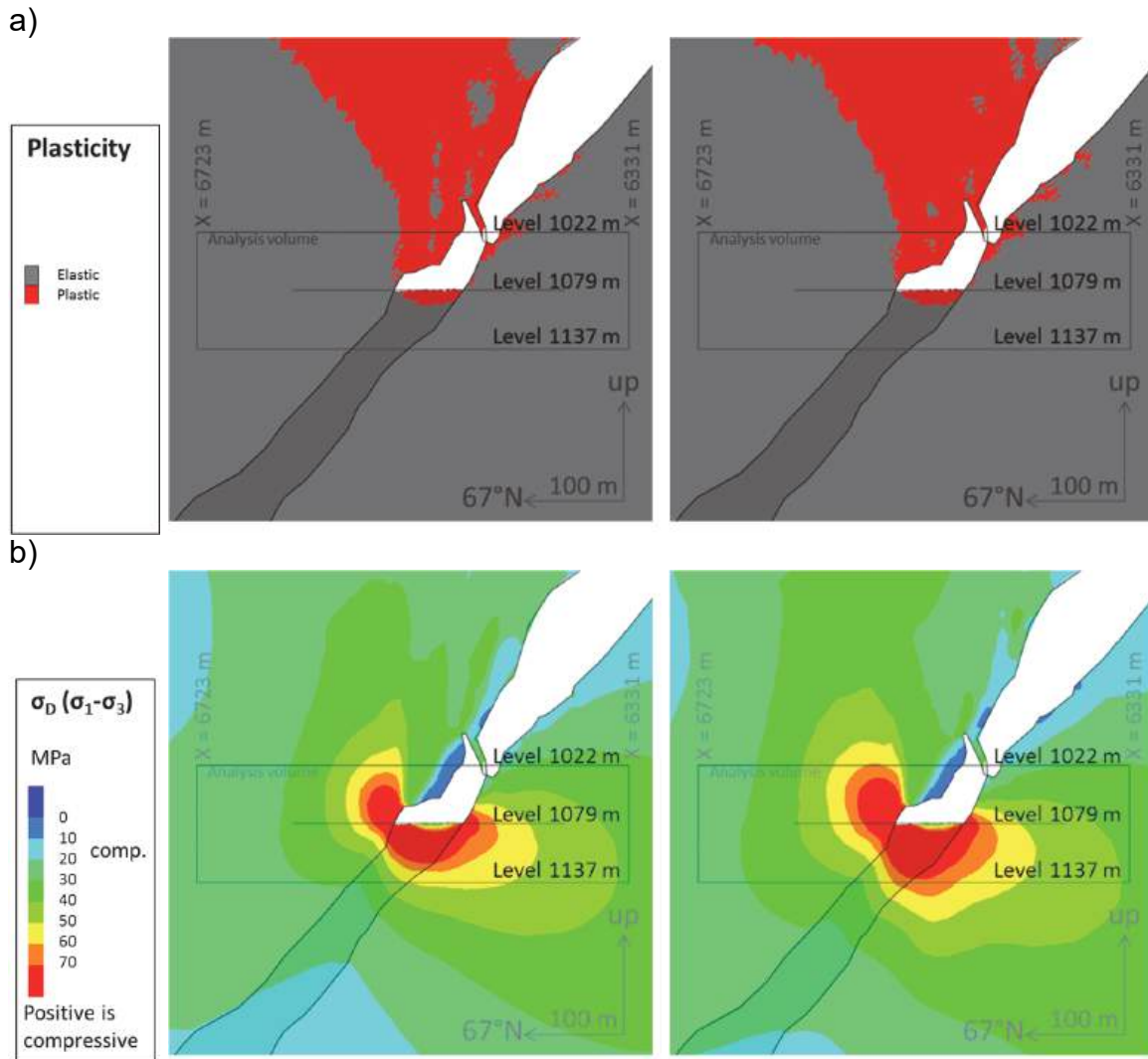


Fig. 4.4: Results of a) plasticity and b) differential stress. Without (left) and with clay alteration (right) (Vatcher, 2017).

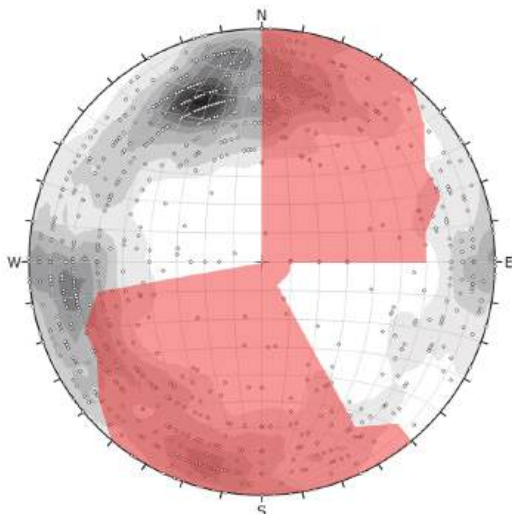


Fig. 4.5: Example of orientations of discontinuities that can slip (red shaded) located at the footwall drift when production is two levels below the analysis point. Mapped discontinuities from the area are plotted in the lower-hemisphere stereonet in grey with poles (Vatcher, 2017).

In another study of interest, Svartsjaern *et al.* (2017), examined large-scale damage and failure in the footwall of the Kiirunavaara Mine using Itasca's Particle Flow Code (PFC) in 2-D (Itasca Consulting Group, Inc., 2015). Failure in the footwall is a likely contributor to seismic activity in the footwall, which is of concern to the mining company as the vast majority of infrastructure and personnel are located in the footwall. Breakage between the contacts was used to represent rock mass failure (Fig. 4.6). (Svartsjaern *et al.*, 2017)

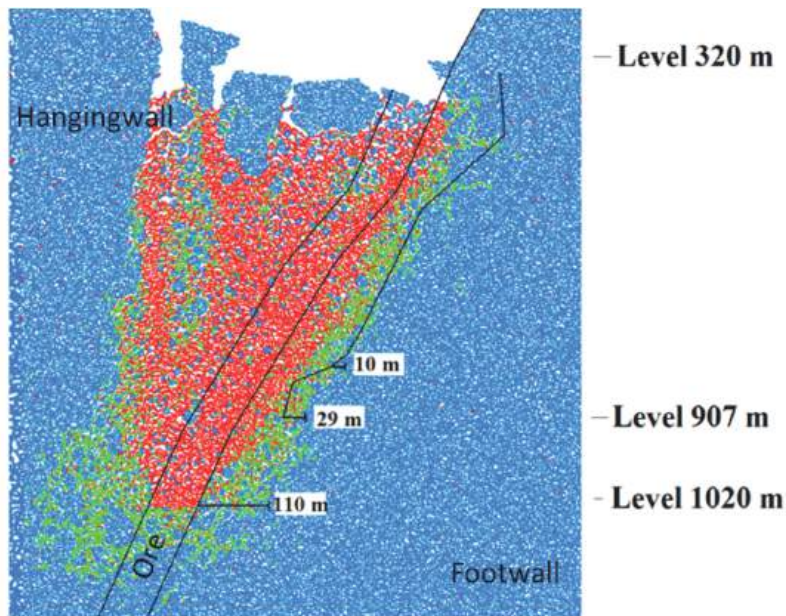


Fig. 4.6: Parallel bonds state, where blue is unyielded and red and green show broken bonds. The blackline shows the extent of damage mapped underground. Modified from Svartsjaern *et al.* (2017).

The location of damage in the model agreed well with underground damage mapping data. Through the use of numerical modelling as a laboratory, Svartsjaern *et al.* (2017) were able to demonstrate that the strength of the hangingwall rock mass significantly influences the extent and magnitude of damage in the footwall, which likely corresponds to at least the extent of the seismically active volume in the footwall. This highlights the importance of understanding the rock mass properties of the hangingwall, despite the lack of infrastructure located within it.

Sjöberg *et al.* (2011) presented an interesting study of a specific, fatal rockburst event that occurred in 2008. The seismic event that resulted in this rockburst had a local magnitude of 3.0. Their analysis attempted to identify the most likely cause of the event through damage mapping, structural mapping, seismological analysis, and 3-D numerical modelling. During this work, two larger scale discontinuities were identified near the rockburst event. A local model in the Itasca code *3DEC* was created of the area with the two large-scale structures, two joint sets, and accurate production geometry (Fig. 4.7). The analyses showed that slip along pre-existing discontinuities was the likely cause of the seismic event and thereby the rockburst. (Sjöberg *et al.*, 2011)

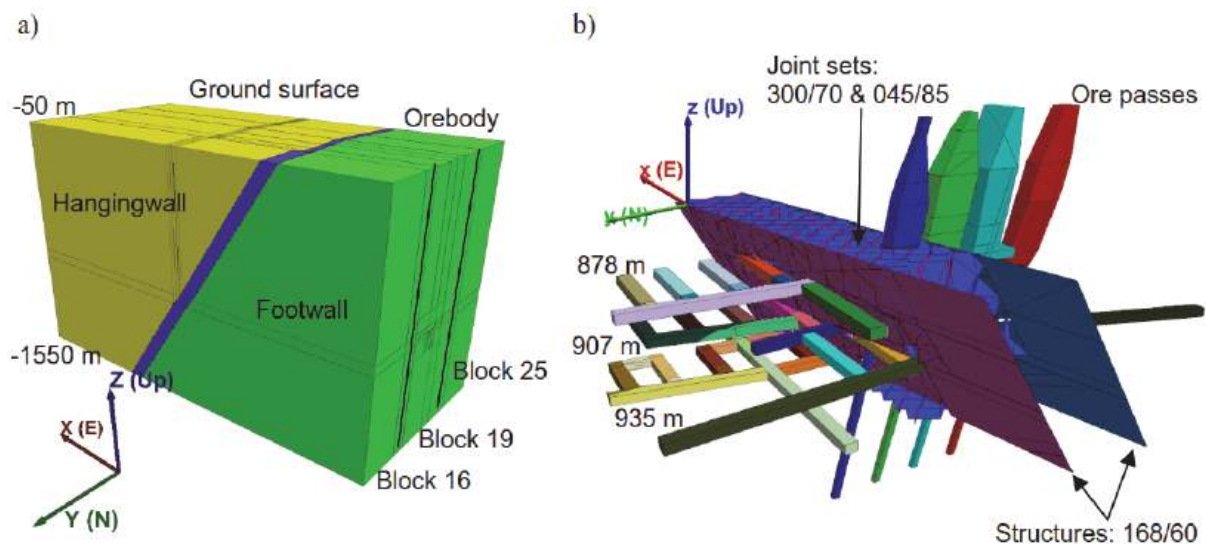


Fig. 4.7: a) Geometry of the 3DEC local model, and b) view of the two discontinuities, joint sets, and infrastructure modelled (Sjöberg *et al.*, 2011).

b. Discussion

While it is widely accepted that mining induced seismicity is a result of crack initiation and slip along discontinuities, it is less clear how one should use numerical modelling to explore mining induced seismicity. A variety of continuum techniques have been presented to attempt to identify volumes that are more likely to experience seismicity related to crack initiation. These techniques, however, use proxies for rock damage such as differential stress thresholds, or plastic failure. It is expected in the future the more effort will be placed upon physical modelling of damage processes, such as to the use of BBM. While constitutive model development is likely to continue, issues with parameter selection, laboratory testing, and scaling of parameters are likely to persist.

In Sweden, we have used both continuum and discontinuum methods to numerically represent slip along pre-existing discontinuities. A discontinuum technique is appropriate when sufficient data exists to be able to model individual structures. This situation often occurs when you have a particularly damaging event resulting in the opportunity to do extra damage mapping. It works well for back analysis. However, explicit inclusion of discontinuities can prove to be more challenging for forward analysis due to lack of data. The application of an old analysis technique (ESS) in a new way was very useful to develop the initial understanding of which orientations of discontinuities should be mapped and further studied. While potential for slip can be calculated, seismic potential is more challenging. Research in this area is of great interest to mining engineers.

When one does have good seismic data, exactly what parameters to compare to what modelling results remains unanswered in the literature. Research efforts are being made around the world to address this question. Part of the difficulty is that advanced seismological parameters are based on earthquake seismology, where faults are well defined, and the majority of seismicity is a result of fault slip. Such is not the case with mining induced seismicity.

The majority of the models run in Sweden evaluating seismicity around production are at a relatively large scale. A local model is currently being evaluated exploring how production sequencing, transverse versus longitudinal sublevel caving, and unplanned pillars may influence seismic behaviour. This model uses a detailed production sequence that includes all drill fans in the region.

5 Dilemma 3: Ground vibrations in nearby community associated with mining induced seismicity

The Kiirunavaara and Malmberget Mines have towns on surface quite close to the mining operations. In the case the Kiirunavaara Mine, the town sits on the hangingwall and is currently being relocated due to the extension of the surface subsidence. Vibrations caused by mining activities are not significant problems here. However, the town of Malmberget is located above and surrounding the multiple orebodies of the Malmberget Mine. The town experiences vibration because of mining induced seismicity. Vibration thresholds are government regulated.

a. Existing works

Few studies to date examine the ground vibrations on surface for the Kiirunavaara and Malmberget Mines. Those that exist are unpublished.

b. Discussion

A major reason why there are so few studies on this topic is due to the complexity of the issue. Wave travel paths are rarely simple in reality; the interplay between geological features, and complex and varying waves sources (such as mining induced seismicity) is not well understood. A gap in the literature exists concerning our understanding of how to model waves within complex rock masses and over long distances. The influence of source magnitude and distance to source upon vibrations felt on ground is not clear.

Due to these uncertainties, the authors see research potential in this area. Ground vibrations are clearly an issue the need to be understood, and modelling techniques need to be developed.

6 Concluding remarks

Numerical modelling has proved to be a useful tool when it comes representing seismicity and caving in Sweden's deep mines. There are multiple techniques available to represent these behaviours, each with their own drawbacks and assets. Models of caving tend to be moving towards trying to develop an understanding of the processes. However, as always, we are limited by computing power. Due to this, algorithms are developed to numerically represent these processes in a more compact fashion, for example *CAVESIM* coupled with *FLAC3D*.

Numerical representation of seismicity at depth should see immense improvements in the future. Our understanding of the damage process will be improved by modelling techniques such as BBM. The use and application of coupled codes is promising.

We look forward to helping to develop the use of seismological data and parameters to interpret rock mass behaviour, and even rock mass characteristics.

Vibrations that result from caving mines are in some cases problematic. Much research is required to understand the processes involved, and how we can numerically represent them.

The future of numerical representation of caving and seismicity is bright. We have a lot of interesting work ahead of us that will lead to safer, more productive mines.

7 References

Banda, S. U. (2017) *Caving mechanisms for a non-daylighting orebody*. PhD. Luleå University of Technology.

Berglund, J. and Andersson, U. B. (2013) *Kinematic analysis of geological structures in Block 34, Kiirunavaara*. Internal report (13.746) 13–746. Kiruna, Sweden: LKAB, p. 48.

Diederichs, M. S. (2000) *Instability of Hard Rockmasses: The Role of Tensile Damage and Relaxation*. PhD. University of Waterloo.

Duplancic, P. and Brady, B. H. (1999) 'Characterisation of Caving Mechanisms By Analysis of Seismicity And Rock Stress', in. *9th ISRM Congress*, International Society for Rock Mechanics and Rock Engineering.

Hebert, Y. and Sharrock, G. (2018) 'Three-Dimensional Simulation of Cave Initiation, Propagation and Surface Subsidence using a Coupled Finite Difference - Cellular Automata Solution', in. *Caving 2018*, Vancouver.

Itasca Consulting Group, Inc. (2015) *Particle Flow Code (PFC)*.

Itasca Consulting Group, Inc. (2017) *Fast Lagrangian Analysis of Continua in 3 Dimensions (FLAC3D)*. Itasca Consulting Group.

Perman, F., Sjöberg, J. and Wettainen, T. (2013) 'Numerical Modeling of Mining-Induced Seismicity--Review and Case Study Example from the Malmberget Mine', in *6th International Symposium on In-Situ Rock Stress. In-Situ Rock Stress 2013*, Sendai, Japan (South African Institute of Mining and Metallurgy Monograph Series Geostatistics), pp. 17–32.

Ryder, J. A. (1988) 'Excess shear stress in the assessment of geologically hazardous situations', *Journal of the South African institute of Mining and Metallurgy*, 88(1), pp. 27–39.

Sjöberg, J., Dahnér, C. and Malmgren, L. (2011) 'Forensic analysis of a rock burst event at the Kiirunavaara Mine – results and implications for the future', in Sainsbury, D., Hart, R., Detournay, C., and Nelson, M. (eds) *Proceedings of the 2nd International FLAC/DEM Symposium. Continuum and Distinct Element Numerical Modeling in Geomechanics--2011*, Melbourne, Australia: Itasca International Inc., pp. 67–74.

Sjöberg, J., Perman, F., Lope Álvarez, D., Stöckel, B.-M., Mäkitaavola, K., Storvall, E. and Lavoie, T. (2017) 'Deep sublevel cave mining and surface influence', in Weseloo, J. (ed.) *Proceedings of the Eighth International Conference on Deep and High*

Stress Mining. Deep Mining 2017, Perth, Western Australia, Australia: Australian Centre for Geomechanics, pp. 357–372.

Svartsjaern, M., Saiang, D., Svartsjaern, M. and Saiang, D. (2017) 'Discrete Element Modelling of Footwall Rock Mass Damage Induced by Sub-Level Caving at the Kii-runavaara Mine', *Minerals*, 7(7), p. 109. doi: 10.3390/min7070109.

Vatcher, J. (2017) *Listening to the story of the rock mass : The integration of conventional and unconventional data to understand rock mass behaviour at the Kii-runavaara Mine*. PhD. Luleå University of Technology.

Vatcher, J., McKinnon, S. D. and Sjöberg, J. (2016) 'Developing 3-D mine-scale geomechanical models in complex geological environments, as applied to the Kii-runavaara Mine', *Engineering Geology*. (Special Issue on Probabilistic and Soft Computing Methods for Engineering Geology), 203, pp. 140–150. doi: 10.1016/j.enggeo.2015.07.020.

Vatcher, J., McKinnon, S. D. and Sjöberg, J. (2017) 'Geomechanical characteristics inferred from mine-scale rock mass behaviour', in *Proceedings of the Eighth International Conference on Deep and High Stress Mining. Eighth International Conference on Deep and High Stress Mining (Deep Mining 2017)*, Perth, Australia: Australian Centre for Geomechanics, pp. 555–568.

Numerical simulation of geomembranes as bottom sealing below salt heaps

Numerische Simulation von Kunststoffdichtungsbahnen als Basisabdichtung unter Salzhalden

Jan-Peter Schleinig, Christian Artschwager, Christian Dumperth

K + S Aktiengesellschaft

Bertha-von-Suttner-Straße 7, 34131 Kassel

Fabian Weber, Heinz Konietzky

TU Bergakademie Freiberg, Institut für Geotechnik

Gustav-Zeuner-Str. 1, 09599 Freiberg

Zusammenfassung

Das Aufhalden von Salzrückständen an der Erdoberfläche geht immer mit Fragen zum Grundwasserschutz einher. Diesbezüglich untersucht K+S neben den in der Praxis bereits erprobten Anwendungen neue Lösungsansätze. Im Rahmen einer Machbarkeitsstudie wurde im ersten Schritt der Einsatz einer Kunststoffdichtungsbahn (KDB) als Untergrundabdichtung unter Rückstandshalden, unter Berücksichtigung des Einflusses typischer Setzungen sowie des viskosen Bewegungsverhaltens von Salzhalden, zweidimensional modelliert. Ziel der Studie ist die Untersuchung der Modellierbarkeit einer KDB unter einer Salzhalde zur Ermittlung der daraus resultierenden Beanspruchungen und möglicher Versagensszenarien mittels numerischer Modellierung. Dieser Artikel gibt einen Überblick über die hierzu durchgeführten Studien, die verwendete Modellierungssoftware, die angewandten Methoden und Materialeigenschaften und betrachtet verschiedene Extremfälle, welche mögliche Versagensszenarien beschreiben.

Abstract

Heaping up salt residuals at the surface always comes along with questions about groundwater protection. The K+S company investigates, besides the already proven types of applications, new methods, respectively. Within the frame of a feasibility study, the basic usage of a geomembrane (GMB) as basal seal of salt residual piles was modelled two-dimensional, considering the influence of typical settlement, as well as the viscous movement of salt heaps. The aim of the study is the investigation of the modellability of a GMB under a salt residual pile, to determine resulting stresses and possible failure scenarios of a GMB with the method of numerical modelling. This paper gives an overview of the conducted studies, the used modelling software, the applied methods and material properties, and considers different extreme cases describing possible failure scenarios.

1 Introduction

The K+S company is operating underground mines, as well as the production and processing of potassium raw salts in Thuringia and Hessa. The mined potassium salts are delivered to the surface, where they are processed to potassium and magnesium products that are used as fertilizer and base material for the chemical and pharmaceutical industry. Salt residuals which are not further used are heaped up at the surface. K+S is continuously investigating and improving this process. Nonetheless the ongoing mining process is more and more demanding for heap space. Thus, heap expansions associated with onward changes in the overall environmental protection standards are an inevitable part of the future investigations.

The usage of a geomembrane (GMB) as an element of a basal seal for salt residual piles was examined. Besides technical restrictions by the specific establishment of a GMB as a basal seal, the potential of its applicability, as well as its influence on the system "heap - basal seal - underground", have to be evaluated in advance. The numerical modelling of salt residual heaps has to consider several aspects: the large scale relations of salt heaps, the basal seal and the underground, including their complex interaction with the GMB and especially the settlement induced deformations, as well as the viscous movement, which is important for long-term predictions. Special attention has to be paid to the simulation of the GMB and its two respective interfaces: one to the subsoil and one to the salt heap. So far, no comparable experience exists.

2 Methods and materials

2.1 Simulation software and model setup

The 2D numerical simulations are conducted by using FLACTM (ITASCA, 2011). The code is based on the Finite Difference Method and the theory of continuum mechanics. Each material is represented by zones whereas the material behavior is prescribed by build-in constitutive models. Materials can behave elastic, plastic or even visco-elasto-plastic. The grid is able to deform and move accordingly. The implementation of distinct planes on which separation or sliding can occur is possible. These interfaces simulating the border between heap and GMB as well as GMB and underground are prescribed by individual built-in stress-strain laws. Additionally FLACTM offers the opportunity of simulating structural elements. So called beam elements are used for modelling the GMB. Beam elements are two-dimensional elements behaving linearly elastic including axial tensile strength limits. The continuum based approach of FLACTM in combination with interfaces and beam elements is well suited for modelling a system consisting of a large scale residual salt heap coupled to a millimeter thin GMB laying on a particular underground.

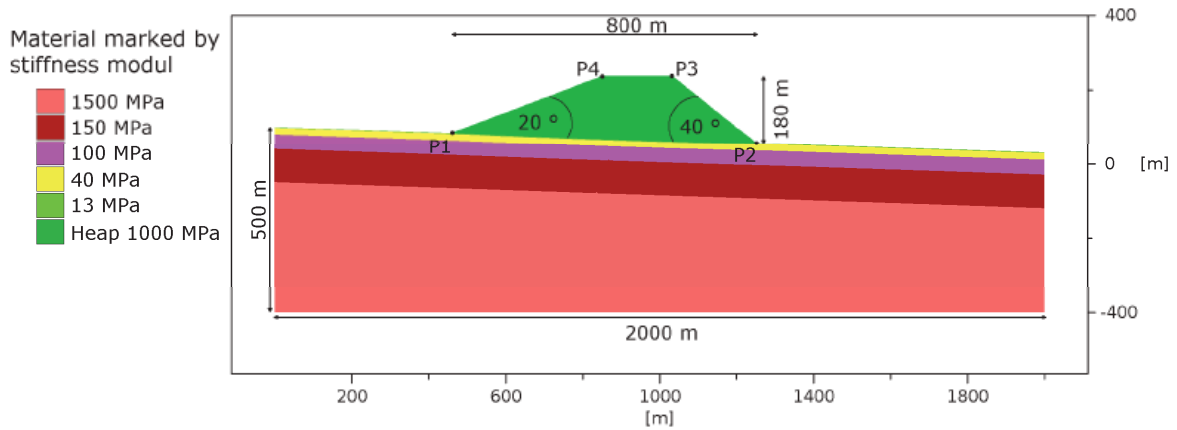


Fig. 2.1: Conceptual model with geometrical data and layered underground indicated by stiffness values.

The 2D numerical model is based on a conceptual model emphasizing typical in-situ conditions in terms of dimensions and underground situations (Fig. 2.1). The underground within the numerical model consists of individual homogenous layers. Its inclination, including the geological layers, is about two degrees. Two other additional underground models with different layering were also investigated, but they are not presented in this paper. Additionally, a groundwater level, situated one meter below the surface, is considered. Roller boundaries are applied at the left and right model side, while the lower boundary is fixed. Land surface as well as the heap are able to move freely.

The GMB is implemented via a beam element with two interfaces. One interface is located between the heap and the GMB (Int_{H-G}) and another one between the GMB and the underground (Int_{G-U}). A coupled multi-layer system of heap - interface - GMB - interface - underground originates (Fig. 2.2).

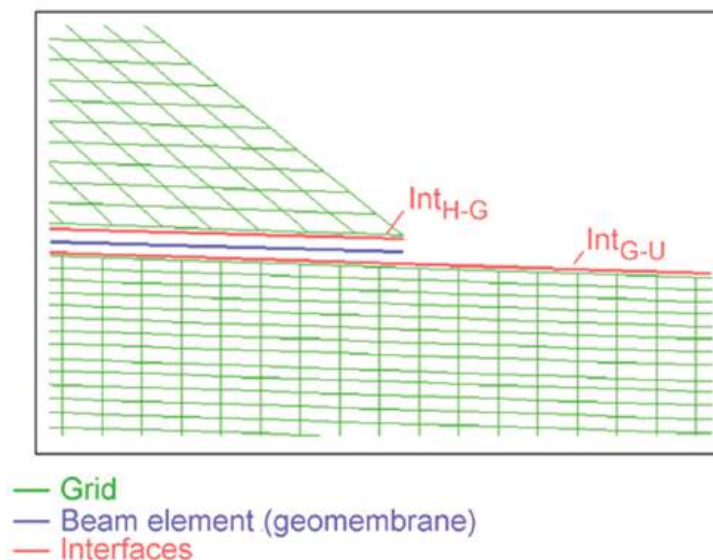


Fig. 2.2: Scheme of the “three layer system”.

After grid generation and parameter initialization the numerical simulation is divided into the following steps:

- 1) Elastic calculations until initial equilibrium incl. heap up of dump and considering ongoing density increase in salt heap,
- 2) Elasto-plastic calculation for operation phase,
- 3) Elasto-visco-plastic calculation for post-operation phase until lifetime of 30 years.

The complete heap is set-up suddenly. Subsequently a FISH-routine is implemented to model the density increase from the top of the heap to its core. After a simulated lifetime of 30 years results of the model and especially the GMB can be examined in terms of creep behavior of the heap, settlements and horizontal displacements on the surface, strain on the surface, forces and strain inside the GMB as well as its failure.

2.2 Material laws and parameters

The underground below the salt heap is modelled by the Mohr-Coulomb (M-C) constitutive model with non-associated flow rule and tension cut-off. The underground is represented by three homogenous layers according to Chapter 2.1.

Elasto-plastic and viscous deformations of the heap material are considered separately. Elasto-plastic behavior is simulated by M-C constitutive model with non-associated flow rule and tension cut-off. Creep behavior is simulated by the crushed salt model (ITASCA, 2011).

The GMB is modelled by beam elements with linear elastic behavior including an axial tensile strength limit. Since GMB below salt heaps are a new kind of usage, thickness and tensile strength of the GMB are assumed according to governmental regulations (regulatory limits) for repositories (BAM, 2014). Especially the tension limit is a critical parameter for failure of the GMB. BAM (2014) also gives a critical axial tensile strain limit of 6 % (for a temperature of 20 °C) which should not be exceeded in order to guarantee the integrity of the GMB.

Tab. 2.1: Mechanical parameters for the GMB including limiting values of BAM, 2014.

Parameter	Value
Thickness [mm]	2.5
Width [m]	1
Density [kg/m ³]	950
Young's modulus [MPa]	200
Tensile strength [MPa]	15

Tab. 2.2: Mechanical parameters for the interfaces.

Parameter	Value
Normal stiffness [MPa/m]	15.6
Shear stiffness [MPa/m]	7.8
Cohesion [MPa]	0
Friction angle [°]	35, 20
Tensile strength [MPa]	0

The mechanical parameters of the simulated GMB are highlighted in Tab. 2.1. Other aspects like temperature or deformation depending stiffness of the GMB as well as aggressive fluid impact are not considered within this feasibility study. Tab. 2.2 summarizes the mechanical parameters for the interfaces.

2.3 Case studies

The aim of the present simulations is to get a general feeling about the opportunities for modelling the GMB behavior below residual salt heaps and to reveal the influence of the contact (interface) parameters. Therefore it is necessary to not only investigate intact GMB behavior (H1, H2), but also activated failure scenario case studies (H3 and H4). The simulations H3 and H4 were performed in order to generate failure of the GMB by reducing its tensile strength σ_{t-G} (H3) or by sliding of the heap and GMB on the ground surface due to a strongly reduced friction angle $\phi_{Int-G-U}$ of the lower interface (H4). The documented simulation cases with the characteristic interface and GMB properties are summarized in Tab. 2.3.

Tab. 2.3: Conducted case studies (other parameters are according to Tab. 2.1 and 2.2).

Simulation case	Variation
H1	$\phi_{Int-H-G} = \phi_{Int-G-U} = 35^\circ$
H2	$\phi_{Int-H-G} = \phi_{Int-G-U} = 20^\circ$
H3	$\sigma_{t-G} = 3 \text{ MPa}, \phi_{Int-H-G} = \phi_{Int-G-U} = 20^\circ$
H4	$\phi_{Int-H-G} = 20^\circ, \phi_{Int-G-U} = 5^\circ$

3 Results and discussion

The presented results focus on the mechanical behavior and failure state of the GMB and its attached interfaces. Fig. 3.1 shows the failed sections of the GMB and the occurring slip at the interfaces. For case H1 (Fig. 3.1a) the GMB is intact since no failure occurs during the simulated life time of 30 years. Due to the friction angle of 35° for the interfaces no sliding is noticed and the interfaces show elastic behavior.

The results for GMB and interface failure state of model H4 are illustrated in Fig. 3.1d. Due to the reduction of the friction angle in interface Int_{G-U} , large displacements are noticed on the right side of the salt heap. Those are represented by a deformed heap contour. Various slip events at Int_{G-U} are leading to a sliding of the heap and the GMB on the underground. The deformations on the right end are also leading to slip events in Int_{H-G} . Additionally, large sections of the GMB fail. The axial stresses inside the GMB overcome the tensile strength (15 MPa). However, the inclination of the underground results in smaller deformations and stresses at the left end of the model. Therefore no GMB failure occurs in this area.

In case H2 (Fig. 3.1b) a friction angle of 20° leads to some slip in the interface at the left and right end below the heap. The normal stress on the interfaces in this areas is not high enough to prevent slip. These slip events have negligible influence on the creep behavior of the residual salt heap. Therefore, no failure of the GMB occurs.

When reducing the tensile strength of the GMB to 3 MPa (Fig. 3.1c) several sections fail. According to model H2 the load and creep behavior of the heap generates similar stresses inside the GMB. Differing from model H2, these stresses now exceed the tension limit of the GMB, leading to the failure pattern shown in Fig. 3.1c. The shape of the heap contour indicates that the failure of the GMB has no negative influence on the overall creep behavior of the residual salt heap. Interface states show similar pattern as in case H2.

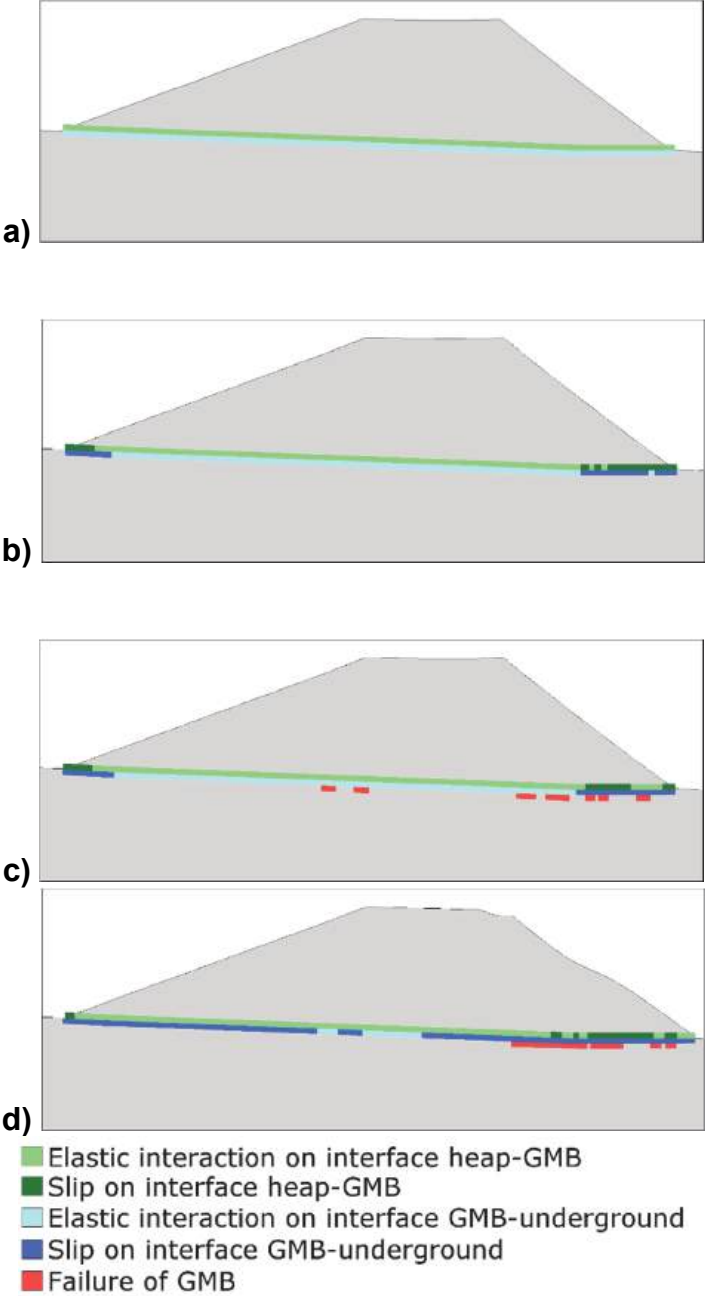


Fig. 3.1: State of interface interaction and failure sections of the GMB for a) H1, b) H2 c) H3 and d) H4.

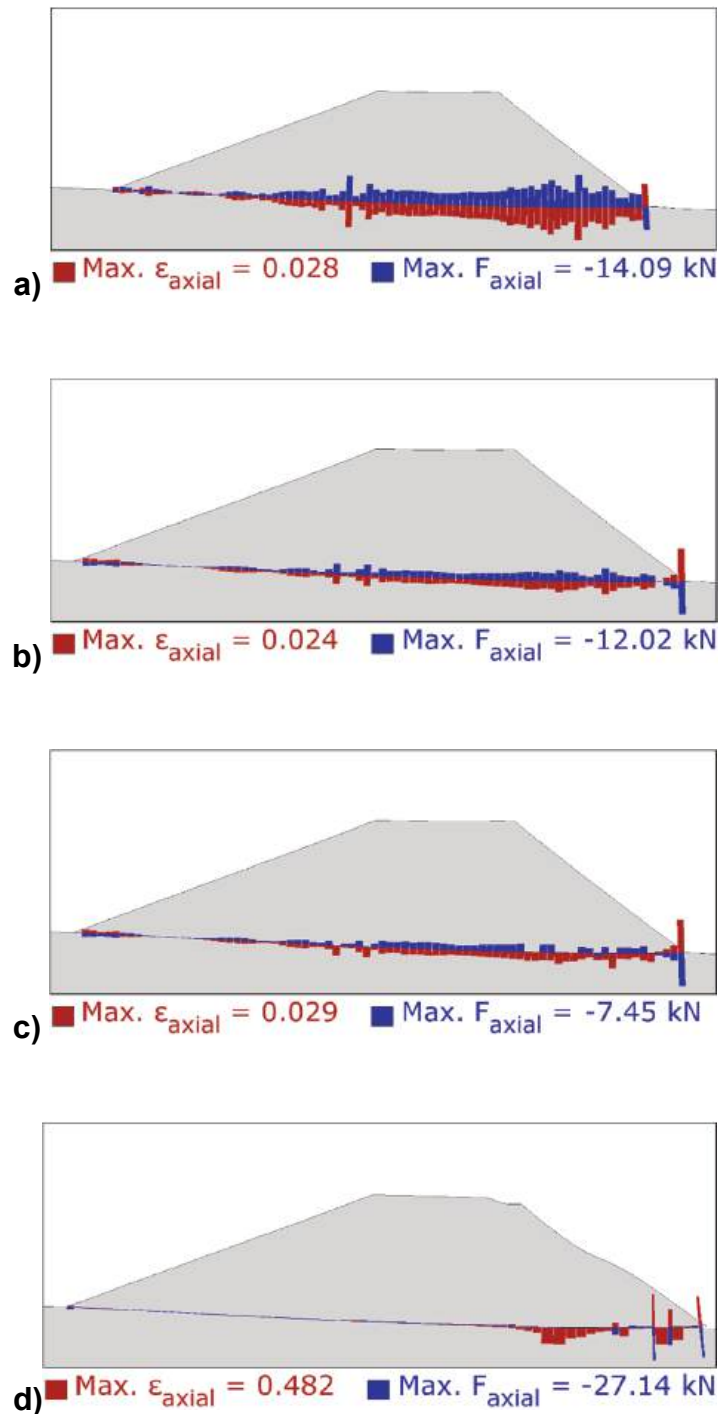


Fig. 3.2: Distribution of axial strain and force inside the GMB for a) H1, b) H2 c) H3 and d) H4 with maximum values for tensile axial strain and force.

The resulting axial forces and axial strains inside the GMB, due to the loading and creep deformation of the residual salt heap, are shown in Fig. 3.2. Tensile forces and deformations are represented by blue bars showing in upwards direction and red bars pointing downwards, respectively. Fig. 3.2 shows the maximum values for tensile strain and force.

For model H1 (Fig. 3.2a) a maximum tensile force F_{axial} of about -14.09 kN is developed after a lifetime of 30 years. This equals an axial tensile stress of about 5.64 MPa. The axial deformation ϵ_{axial} develops similar to the axial force with a maximum strain of about 2.8 %. In the areas at the left and right end of the heap a slight uplift (arching) of the underground is observed which results in some local compressional forces and deformations. This is visualized by the upwards pointing red bars representing compressive strains and by blue bars with downwards direction for compressive stresses. Due to the slope inclination of underground the deformations and forces are the highest beneath the right end of the heap. Axial tensile stresses and deformations in the GMB are lower than the limit values according to BAM (2014).

In general model H2 (Fig. 3.2b) shows a similar behavior compared to H1 in terms of axial forces and deformations. Values are slightly lower due to the localized slip of the interfaces at the two ends of the GMB. A maximum tensile force F_{axial} of about -12.02 kN develops resulting in an axial stress of 4.81 MPa. Maximum strain is about 2.4 %. Analog to model H1 some local compressional forces develop at the left and right end of the salt heap. Again the axial tensile stress and deformation in the GMB are lower than the limit values given by BAM (2014).

The distribution of axial force F_{axial} and axial strain ϵ_{axial} for model H3 is given in Fig. 3.2c. Nearly the same characteristics as for model H1 and H2 are noticed. However, there are some sections where the GMB is not able to carry the axial tensile load. The bars of F_{axial} are vanishing at the failed sections (see Fig. 3.1c). Axial tensile deformation is the highest within these sections. The beam-segment is torn in the failed areas showing plastic material behavior without influencing the intact beam-segments. The remaining maximum tensile force F_{axial} inside the intact GMB segments is about -7.45 kN which equals an axial stress of about 2.98 MPa. This value correlates with the tensile strength of the GMB (3 MPa) and indicates that the next segment is going to fail in the near future. Maximum tensile strain ϵ_{axial} is about 2.9 %.

Fig. 3.2d shows the pattern of F_{axial} and ϵ_{axial} for model H4. In the central and left part of the heap forces and deformations inside the GMB are not vanishing as implied by the figure. Due to the linear scaling in reference to the large forces and deformations at the right end of the heap force and strain are poorly visible in the other parts. Nonetheless, the GMB is again not able to carry the axial load in the teared areas beneath the right end of the heap (see Fig. 3.1d). Due to the large deformations of the residual salt heap high tensile forces of about -27.1 kN are generated in the remaining intact GMB segments. This tensile force corresponds to about 10.8 MPa axial tensile stress. Tensile deformations in the failed sections increases up to 48.2 %. The correlation between deformation increase and GMB failure is well visible. Again, local compressional forces develop at the left and right end of the salt heap. Failure and deformation limits according to BAM (2014) are strongly exceeded.

4 Summary

This feasibility study documents that the deformation and potential failure behavior of a GMB beneath a large residual salt heap can be investigated in a suitable manner with 2D models. Different constellations in respect to GMB and interface properties can either show an intact GMB (see H1, H2) or cause local failure (see H3, H4) under assumption of extreme parameter constellations. The simulations are able to detect

individual sections of GMB failure and allow to evaluate each individual part of the system $Int_{H-G} - GMB - Int_{G-U}$.

This preliminary study indicates in principle, that a relatively tight connection of the GMB with the underground and a relatively low friction between salt heap and GMB are favorable for long-term integrity of the GMB.

5 References

BAM, 2014. Richtlinien für die Zulassung von Kunststoffdichtungsbahnen für Depo-
nieabdichtungen, s.l.: Bundesamt für Materialforschung und -prüfung.

ITASCA, 2011. FLAC Manual, Itasca Consulting Group, Inc. Minneapolis, Minnesota,
USA

Damage detection of shield tunnel structure by CCD camera system

Schadensdetektierung im Tunnelausbau mittels CCD-Kamera-System

Wei Chen^{1,2}, Zheng Huang^{1,2}, Helin Fu^{1,2}

¹School of Civil Engineering, Central South University

²National Engineering Laboratory for Construction Technology of
High Speed Railway

No.22 Shaoshan South Road, 410075 Changsha, China

Abstract

The damage of lining, such as excessive deformation, cracking, concrete spalling and water leakage, widely existing in metro shield tunnels, may affect the durability of the structure and even cause accidents. Investigation and evaluation of the lining damage is an essential work for maintenance during the service life of the structure. A rapid damage detection system has been applied in the shield tunnel of Metro Line 2 in Changsha, China. The system can obtain high resolution image information of tunnel surface through multiple array CCD cameras at high speed, and use intelligent analysis method to identify and quantify the damage. The type, geometrical morphology and distribution characteristics of structural damages are analyzed based on the automatic detection results. Some causes and factors which are related to the structural damages are discussed.

Zusammenfassung

Schäden im Tunnelausbau wie extreme Deformationen, Risse, Abschalungen und Wasserzutritte treten häufig bei Metro-Schild-Tunneln auf. Sie können die Lebensdauer des Bauwerks beeinflussen und auch Unfälle hervorrufen. Die Untersuchung und Bewertung von Schädigungen im Ausbau ist daher eine Kernaufgabe in der Unterhaltung des Bauwerks während seiner Nutzungsdauer. Ein schnelles Schadensdetektionssystem wurde beim Schild-Tunnel der Metro-Linie 2 in Changsha, China, eingesetzt. Mit dem System können hochaufgelöste Informationen von der Tunneloberfläche mittels eines multiplen CCD Kamera Arrays mit hoher Geschwindigkeit erhalten werden. Es nutzt eine intelligente Analysemethode, um die Schäden zu detektieren und zu quantifizieren. Typ, geometrische Morphologie und Verteilungscharakteristik der strukturellen Schädigungen werden basierend auf den automatischen Detektionsergebnissen analysiert. Ursachen und Faktoren werden in Bezug auf die strukturellen Schädigungen diskutiert.

1 Introduction

In order to solve the problem of traffic congestion, great efforts have been made to build more metro tunnels in China. By the end of 2017, the total mileage of 31 urban rail transit lines in China has reached 4400 km, and the total mileage in 2020 will reach 7700 km (Huang et al., 2018). In the urban metros, the shield tunnel is the main type of structure. It is usually influenced by construction conditions, surrounding environment and human activities. A slight carelessness may cause tunnel structure accident (Tonon et al., 2002). For example, since the operation of Shanghai Metro Line 1, tunnel lining cracking and water leakage occurred frequently (Chen and Zhan, 2000). Guangzhou Metro Line 1 was disturbed by the construction of the foundation pit, which seriously damaged the tunnel structure (An and Song, 2005). In 2017, the lining structure of Shenzhen Metro Line 11 was broken by a pile driving on the ground, which interrupted the train operation.

The frequent occurrence of damage problems in metro tunnel structures has made the researchers pay more attention during investigation of the tunnel structures. For the artificial investigation, Dong et al. (2017) analyzed the influence of structural form, steel bar configuration and operation time on the damage state in Beijing metro tunnel. Lai et al. (2015) analyzed the structural damage due to water inrush accident in Xi'an metro tunnel. Lin et al. (2015) investigated the damage types of metro shield tunnel structure in soft soil area. However, the artificial visual investigation method has some limitations, which is low degree of quantification and lack of consistency for the results. Sensing technology has been widely used in tunnel damage detection because of its dynamic recognition function. For example, Zhang et al. (2014) fused and investigated the damage data of tunnel structure from different types of sensors. Based on Zigbee and wireless sensor technology, some researchers (Huang and Zhang, 2015; Zhang et al., 2016) have built the Wireless Sensing Network (WSN) for monitoring the deformation, joint opening and water leakage of tunnel structures. Wang et al. (2013) formed a sensing neural network in shield tunnel with long-distance optical fiber and developed a realized long-distance and high-precision monitoring system for the deformation. Li et al. (2008) developed a metal groove encapsulating technique for bare Fiber Bragg Grating (FBG) to measure the surface strain of structure. However, these sensors are generally limited to measure the strain (or deformation). In addition, the sensitivity and the service life of sensors are affected by the external environment, such as train vibration, air temperature and humidity. In recent years, artificial intelligence and machine vision have been used for tunnel damage detection, which has improved the efficiency and accuracy of tunnel structure safety assessment (Montero et al., 2015). Menendez et al. (2018) developed a semi-supervised computer vision system to detect tunnel defects, and used an ultrasonic sensor robotic tool to measure width and depth of the detected cracks. Maximum error of the vision system and the ultrasonic sensor is 16 mm and 2 mm, respectively. Erkal and Hajjar (2017) used high-resolution three-dimensional surface laser scanning technology and image capture method to detect and quantify the surface cracking of concrete structures. The mobile robot system which was proposed by Yu et al. (2007) can get images with resolution of 0.3 mm/pixel. The measurement error for cracks was less than or equal to 10 %. Yao et al. (2003) used a machine mobile robot for tunnel deformation detection. Huang et al. (2017) designed an image capture system based on CCD camera, which can be well applied for tunnel structure, when the crack width is larger than 0.3 mm. Attard et al. (2018) proposed a computer vision system which is able to detect deformation as small as

10 cm in any dimension. However, the aforementioned intelligent detection devices are limited to a specific damage detection, and the efficiency of detection, high accuracy and intelligent analysis need further development.

In this paper, a high precision and efficient surface damage detection and intelligent analysis system for shield tunnel structures is introduced. The system is equipped with high-speed CCD camera, multi-layer auxiliary lighting system, and multi-sensor compensation technology, which can get high resolution images of damage on the surface of tunnel lining. A large number of image data information is stored by the vehicle acquisition platform. The tunnel lining damage is quantified using artificial intelligence analysis system. The detection speed of this system can reach 30 – 40 km/h. The system was applied for detection and quantification of damages in Changsha metro line 2. Then, some causes and influencing factors of structural damages are concluded.

2 The background of metro line 2 in Changsha

The 22.26 km long Changsha metro line 2 (the blue line in Fig. 1) was built using the shield construction method and it includes 19 stations. It was opened in 2013 and now it is the largest east-west traffic flow corridor in Changsha (the largest daily passenger volume is more than 350 thousands). Currently, the operation is frequently plagued by construction defects, material damage, external forces, groundwater, and subsidence. Since metro line 2 has been opened, the tunnel structure has experienced varying amounts of degradation. The periodic damage assessment of the tunnel structure is the necessary work to ensure the safety of metro operation. Therefore, the priority task is to detect, summarize and analyze the structural damages.

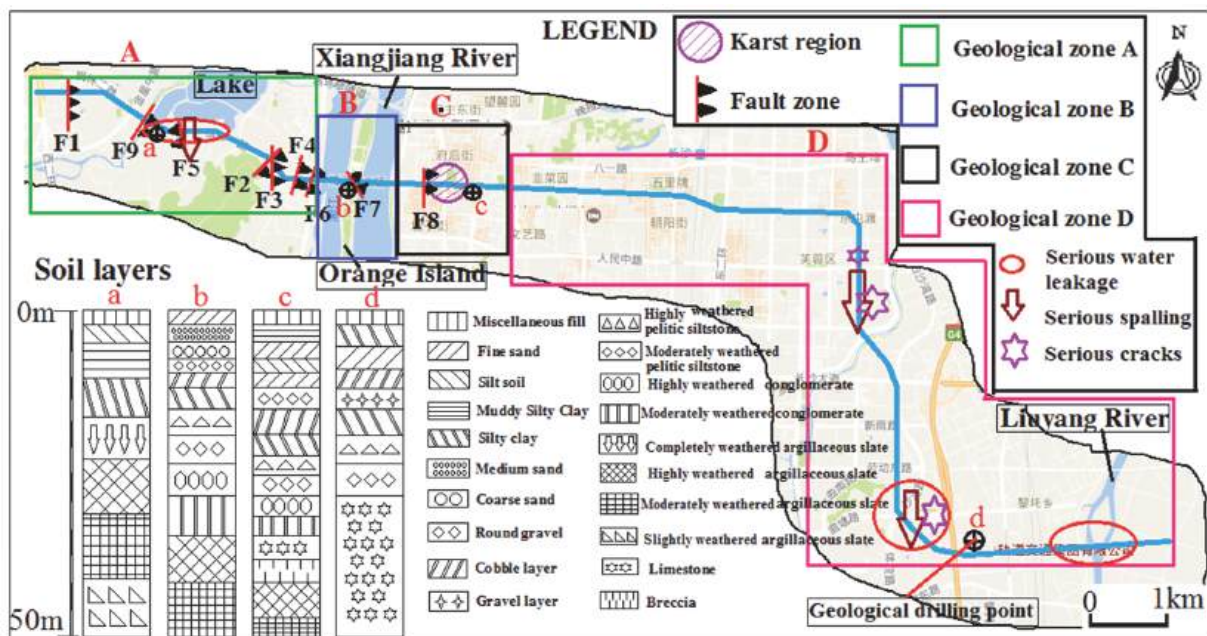


Fig. 1: An overview of the Changsha metro line 2

Fig. 1 also shows the hydrological and geological characteristics along metro line 2. The geomorphic features along the metro line are classified into A, B, C and D. Area A is the erosion hilly valley, area B is Xiangjiang high terrace, area C is Xiangjiang

two terrace, and area D is the one or two eroded alluvial terrace of the Liuyang river. Area A, B, C and D have their own typical geological strata. We have chosen the corresponding geological profiles (a, b, c and d, see Fig. 1) to describe the stratigraphic structure. The position of the corresponding exploration points is shown in Fig.1.

A single layer reinforced concrete lining was used for the shield tunnel. There are a total of six lining blocks for one cross-section, including one cap block, two adjacent blocks, and three standard blocks. The external diameter of the lining is 6 m, the internal diameter is 5.4 m, the thickness is 0.3 m, and the ring width is 1.5 m. The lining structure is made of C50 waterproof concrete and the impermeability grade is P12. HPB235 and HRB335 grade steel are mainly used for the steel frame structure inside the segments. The thickness of the protective layer for the outer and inner reinforcement lining is 50 and 40 mm, respectively. The design of lining section is shown in Fig. 2. The lining blocks were assembled with the staggered joints which were connected by M27 bolts. The waterproofing measures were adopted along the longitudinal and circumferential joint surfaces and bolts (Fig. 2).

3 Detection system

The evaluation of tunnel structure damage requires a large amount of detection data. In order to collect these data, artificial eye inspection and photo collection are generally adopted. However, these methods cannot meet the needs of metro operation management considering the work efficiency and detection precision. Therefore, for detecting the damage in the tunnel structure of the metro line 2, a rapid detection and analysis system developed by the Nanjing HuoYang Hou Mdt InfoTech Ltd (Fig.3), was applied in the metro line 2. This system has the following functions and features:

- 1) Multi-channel array high-speed CCD (Charged Couple Device) camera for synchronous acquisition of image information of the whole tunnel. The central angle of tunnel section scanning is 260° , and the laser scanning space points are indicated in Fig.3;
- 2) Multi-sensor compensation technology under complex environment eliminates effects of vibration and unstable speed of vehicle platform during running in the tunnel;
- 3) Multi-layer auxiliary lighting system (two rows of directional LED lamps (Fig.3));
- 4) Accurate multiple positioning technology (reference object positioning technology + image positioning technology + mileage positioning technology + infrared laser positioning technology (Fig.3)). The real-time locating accuracy of the locomotives on a smooth track surface is 2 mm;
- 5) The system has the capability of high-speed distributed storage and distributed computing for big data. Taking 50 km tunnel as an example, the whole data is about 15 TB, which can be in-time stored and processed;
- 6) Machine vision and artificial intelligence have been applied for tunnel detection and analysis of structural damage. After collecting and analyzing the characteristics of the tunnel surface, the system automatically sorts all kinds of damages in the tunnel, establishes the damage characteristic database, and gradually makes the computer understand all kinds of targets of detection in the tunnel;
- 7) The detection speed in the tunnel can reach 30 - 40 km/h.

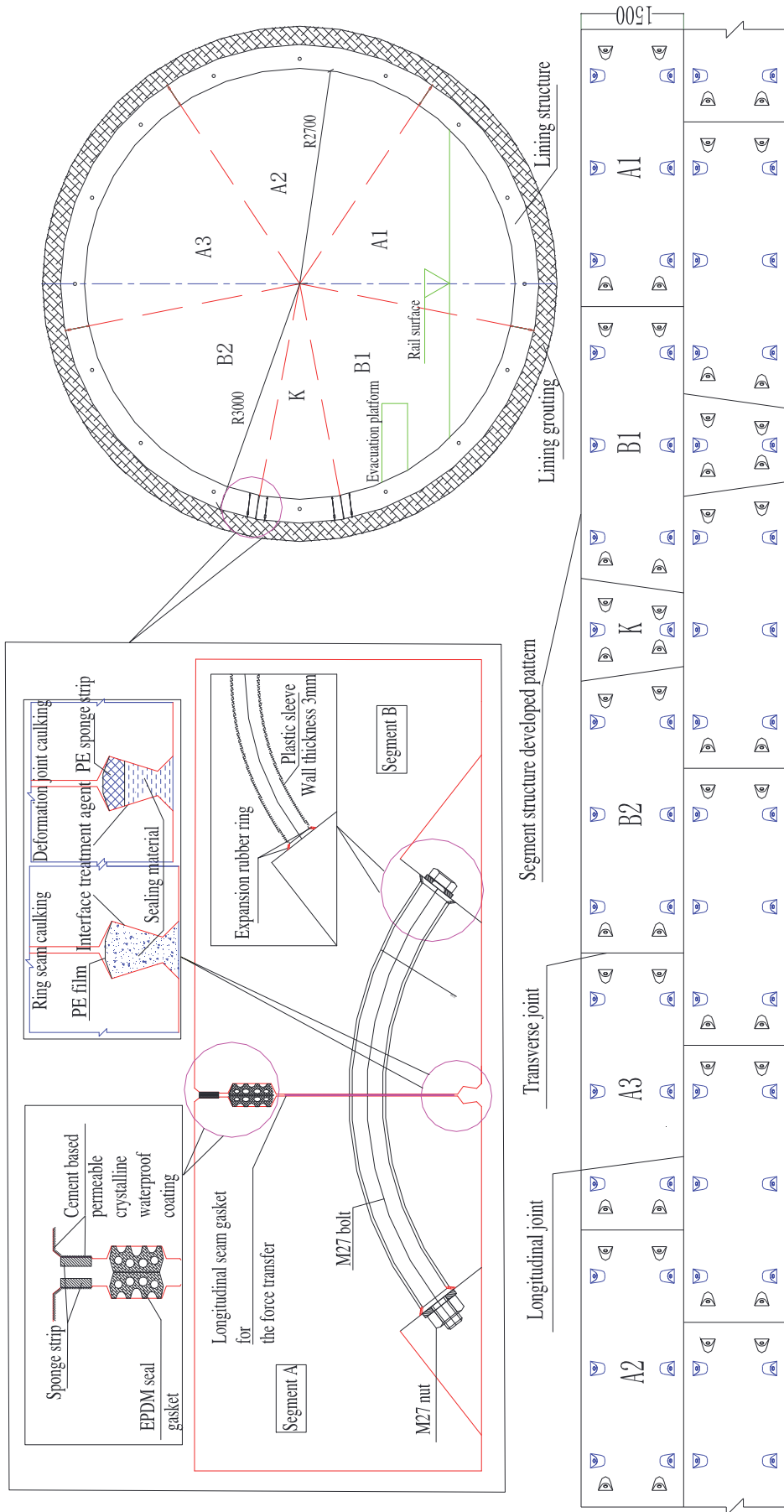


Fig. 2: Design of lining section and the unfolded form of the lining

The main detectable items and the accuracy of the system are listed as follows:

- i) Cracks:
 - The width of the cracks that can be detected: ≥ 0.15 mm;
 - The crack length that can be detected: ≥ 0.4 mm;
 - The calculation error of the actual length and width: ≤ 0.3 mm;
- ii) Deformation along cross section:
 - The coordinate error of the whole space points: < 3 mm;
 - Number of space points (Fig. 3) : 12000 points;
 - Section space interval: ≤ 2 mm;
 - Section width: 680 mm;
 - The number of cross sections per kilometer: 1470;
- iii) Spalling and leakage:
 - The spalling or seepage area that can be detected: ≥ 100 mm²;
 - Missing rate: 2 %;
 - False detection rate: 16 %.

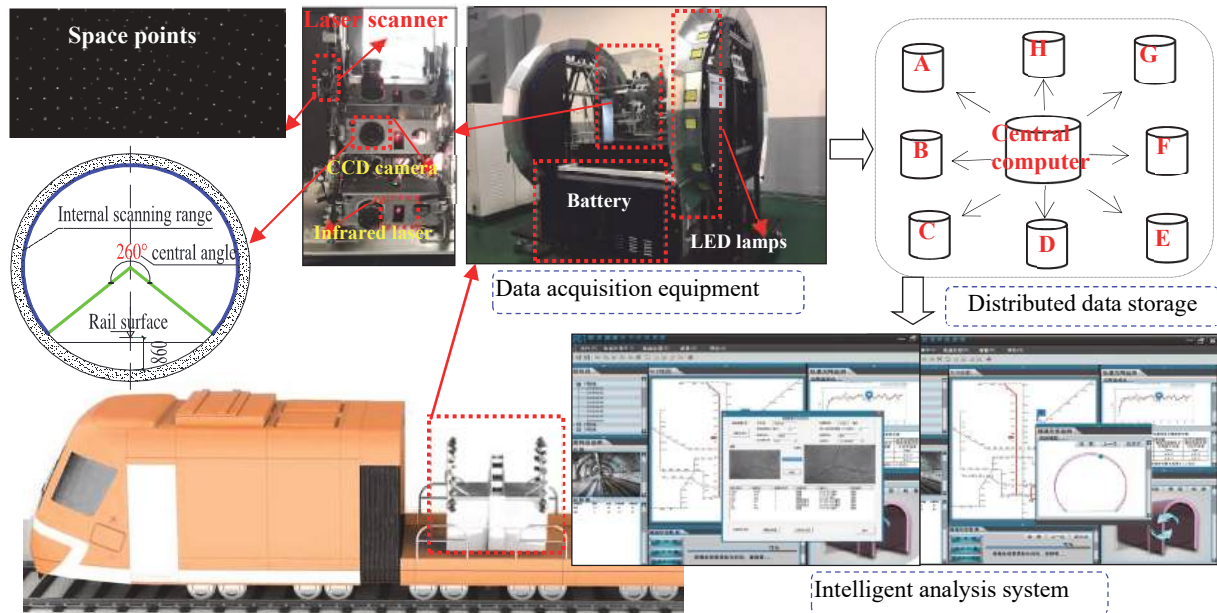


Fig. 3: Rapid detection and analysis system

The implementation steps of the rapid detection and analysis system for the structural damage detection of the shield tunnel are shown in Fig. 4.

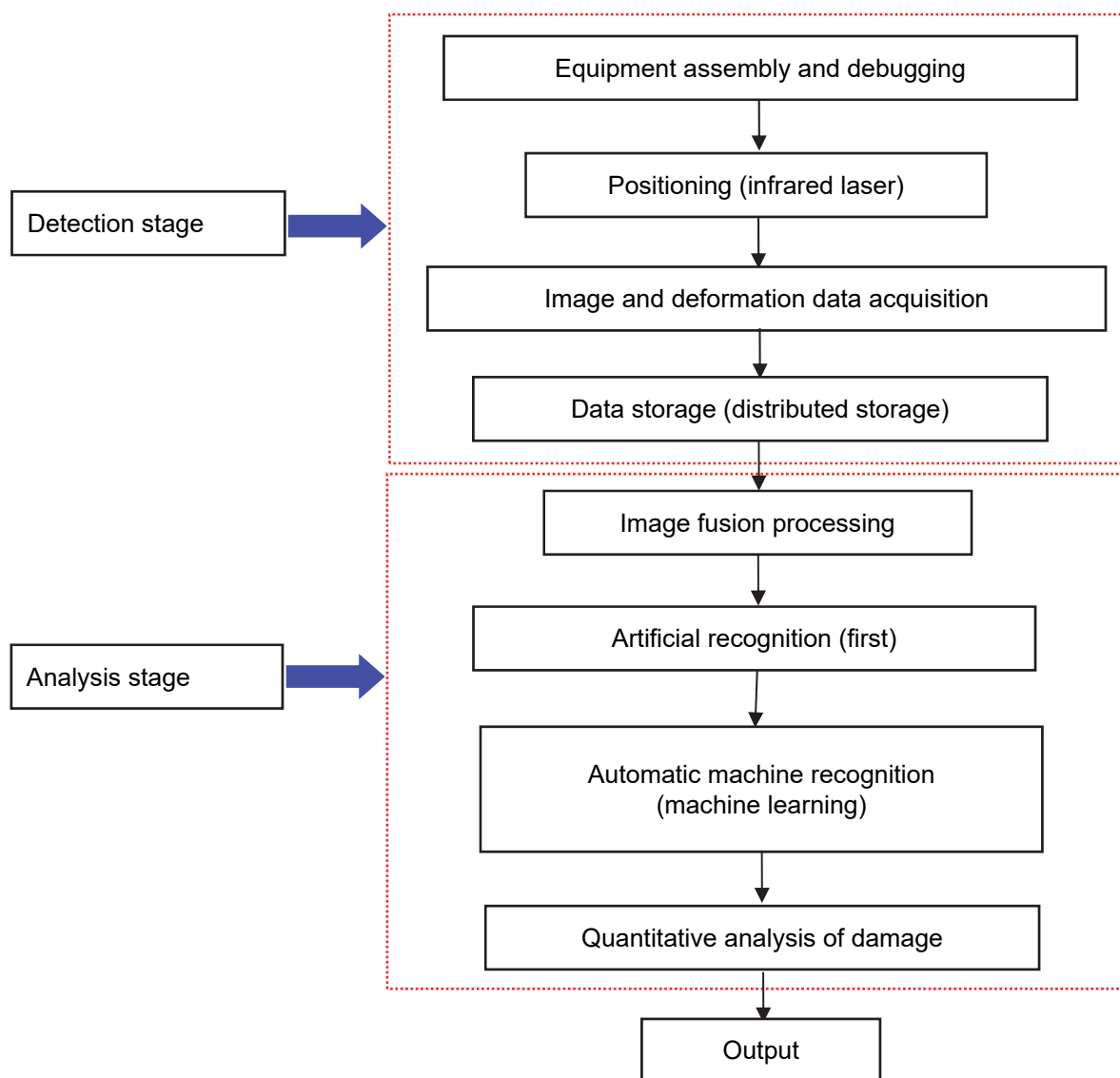
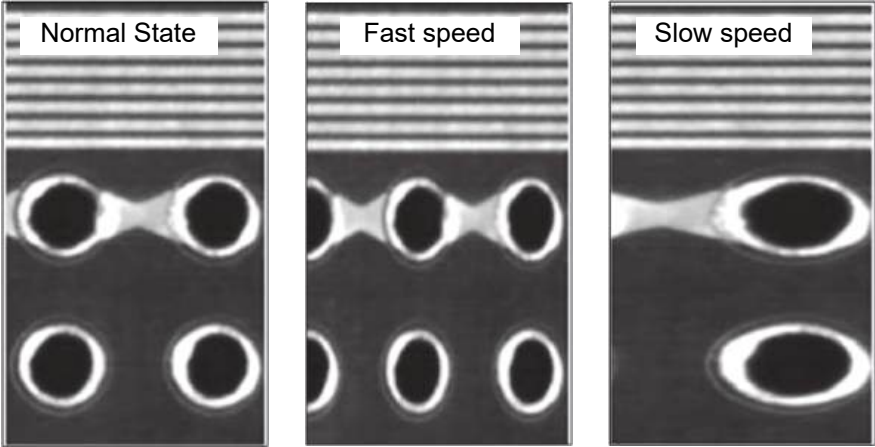


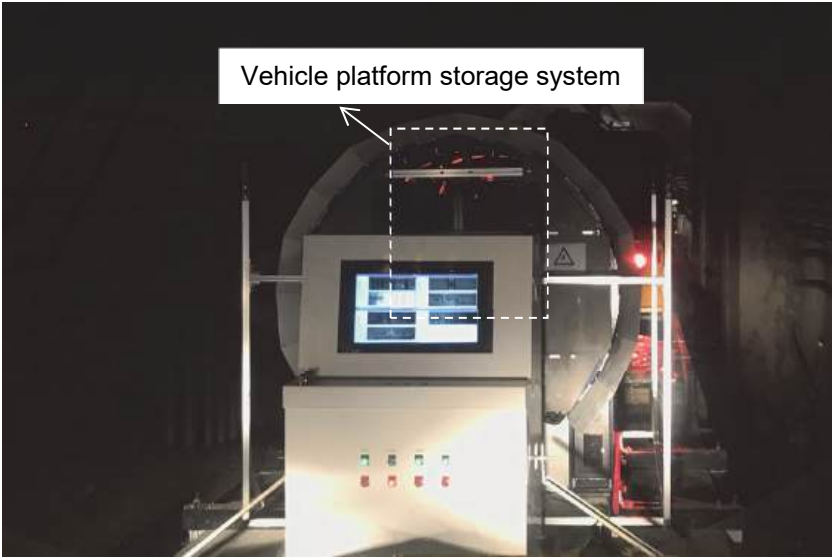
Fig. 4: Steps of tunnel damage detection and analysis

The working process of the system is divided into detection stage and analysis stage. During the detection stage, the equipment is assembled and debugged to ensure the normal work of each component before testing. The accurate position and detection starting position of the equipment in the tunnel are determined by location technology, which is mainly composed of several infrared laser rangefinders. The resolution of the image of the tunnel structure directly affects the detection precision. In the light of two rows of directional LED lamps, the surface array CCD camera with high frequency has the capability to obtain high resolution image of tunnel structure (each ring of the lining includes 6 pictures and the resolution of each picture is 5000×4000 pixels). In the machine vision inspection equipment, there are linear array cameras and surface array cameras. The linear array camera requires that the detection process is under uniform motion. However, the quality of image and the accuracy of the results are affected by the vibration due to equipment movement, speed variation during start and stop the process and the track irregularity (Fig. 5 (a)). The surface array camera used in this system can obtain the whole image information, which can make up the shortage of the linear array camera, but it has a strict requirement for image fusion processing. The machine vision inspection equipment can photograph at a

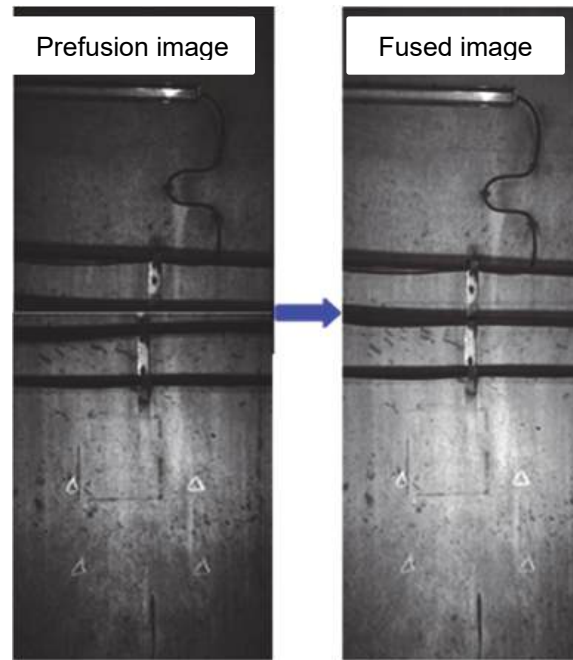
speed of 15 frames per second. A single camera can generate data about 300 MB per second. Therefore, the system is equipped with a vehicle acquisition platform (Fig.5 (b)) which has an efficient distributed storage system. The maximum storage volume of each task can satisfy the requirement for detecting 60 km long tunnel. During the analysis stage, to quantify the surface damage of tunnel structure, the system uses image algorithm to fuse the associated images into a super large image (Fig. 5 (c)). Artificial identification of damage types is necessary, which is carried out by experienced engineers (a tunnel only needs one-time artificial identification). On the basis of artificial identification of damages, the system uses machine learning algorithm to analyze the damage intelligently and provides more rapid damage identification for the next detection in the same tunnel (Fig. 5 (d)). Finally, the structural damages which are identified by the machine are statistically analyzed, and the quantitative results of the structural damages (including damage location, damage size, damage distribution characteristics) are obtained.



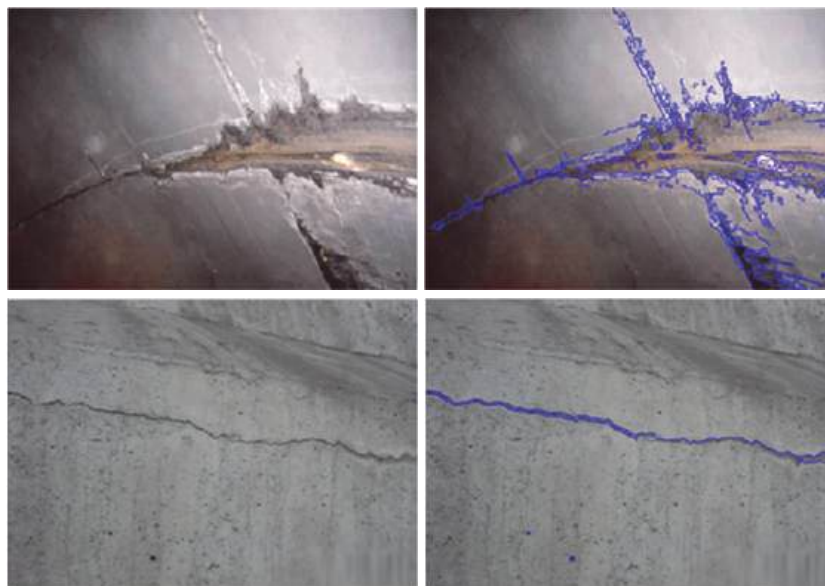
(a) Influence of moving speed on the image acquisition by a linear array camera



(b) Vehicle platform storage system



(c) Image fusion



(d) Intelligent identification of damage

Fig. 5: Properties and functions of the rapid detection and analysis system

4 Analysis of lining damages based on detection results

In 2016 and 2017, we have used the system to investigate the structural damage in the tunnel of the metro line 2. It was found out that there were significant structural damages in some sections of the tunnel. Water leakage, lining cracks and concrete spalling were quite common (Fig. 6). As shown in Fig. 6, the proportion of the water leakage is the largest, up to 53.61 %. The water leakage mainly occurs around lining joints. The proportion of lining cracks is 28.97 %, and the types of cracks mainly include longitudinal cracks and cracks on the edges of the joints. The proportion of concrete spalling is 15.01 % and the spalling is mainly located at the vault of the lin-

ing structure. In addition, the proportion of ballastless bed leakage is 2.41 % (manual investigation and statistics).

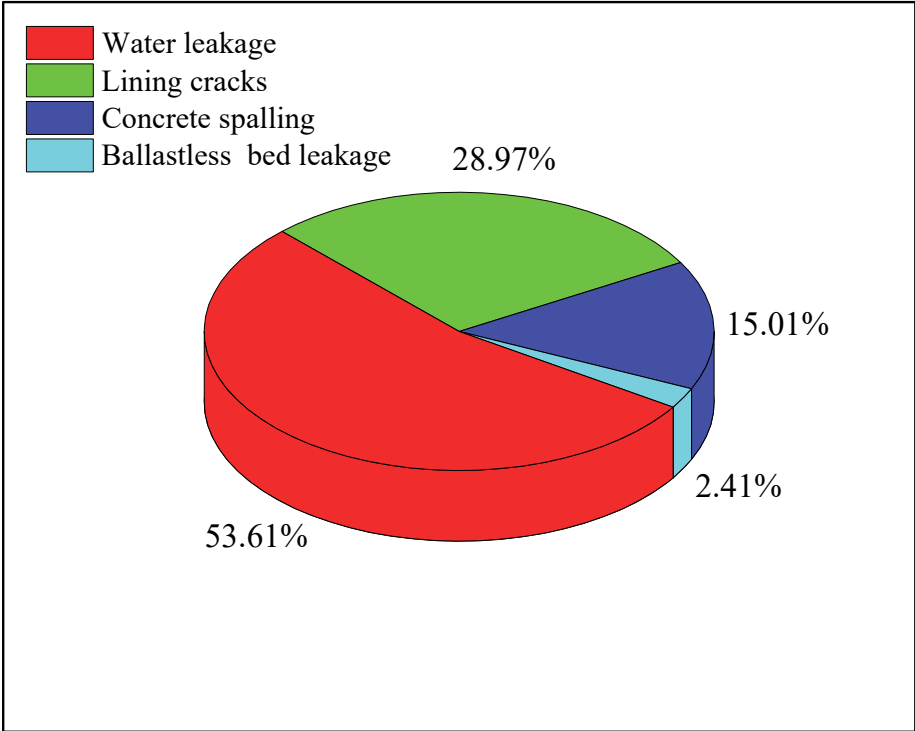


Fig. 6: Statistical results of structural damage in the tunnel of metro line 2

Combined with the engineering geological conditions, the damage distribution area of the shield tunnel is shown in Fig. 1. The densely damaged sections are mainly concentrated in the areas A and D. In area D, shield tunnel are mainly passes through completely-, strongly-, and moderately-weathered silty sandstone and silt layer. It belongs to No. 1 and No. 2 terrace of Liuyang River, and the underground water is rich. In area A, there are many fault zones and the tunnels pass through a big lake and a river. It can be concluded that engineering geological conditions have a certain impact on the damages of the tunnel structure. In fact, the damages are also closely related to construction quality and operation environment (Yang et al., 2017; Zhou et al., 2016; Li and Wang, 2009).

4.1 Section deformation

The lining of the shield tunnel is assembled from prefabricated segments which are connected by bolts. Therefore, there are many joints. When the stress state surrounding the tunnel changes, deformation in the structure occurs (especially in case the deformation resistance ability of the joints is weak). The elliptical deformation of the tunnel section forms due to the dislocation and extrusion between the segments. The excessive elliptical deformation of tunnel section leads to the invasion of the tunnel structure and endangers the safety of train operation. Meanwhile, it causes the variation of the structural stresses, which may induce structural cracking. In addition, the excessive deformation of joints also causes the failure of the waterproof material and may result in water leakage.

Ellipticity is the index of measuring the deformation of tunnel section, which is defined by the length of the long axis of the actual section shape of the shield tunnel minus that of short axis.

In this paper, the detection data of section deformation of the downlink at a particular location (the newly-built metro line 4 beneath passing the metro line 2) has been analyzed. The minimum vertical net distance between metro line 4 and metro line 2 is about 2.86 m and the horizontal distance between metro line 2 and the foundation pit of metro line 4 ranges from 5.1 to 6.0 m (as shown in Fig. 7). 14 sections at an interval of 5 m were monitored. After the completion of metro line 4, the ellipticity of the monitoring sections of the metro line 2 is shown in Fig. 8. It can be concluded that the 14 monitoring sections have different degrees of ellipticity deformations. The closer to the construction location of the metro line 4, the greater the degree of ellipticity is. According to the specifications of the China metro, the ellipticity limitations are $\pm 6\%$ of the outer diameter of the shield tunnel (the outer diameter of metro line 2 is 6 m and the corresponding ellipticity limitations are ± 36 mm). Therefore, 5 sections have exceeded the limited values and are located in a small area above the metro line 4.

The ellipticity of the tenth section is the largest (42.3 mm), the average ellipticity value is 25.4 mm, and the over-limit rate is 35.7%. The results show that the construction of metro line 4 has a serious influence on the ellipticity deformation of metro line 2. In addition, the causes (were not directly found in the metro line 2, but according to some literatures) for the deformation of tunnel section may also include the ground overload (Huang et al., 2017), the lateral unloading (Shi et al., 2016), etc.

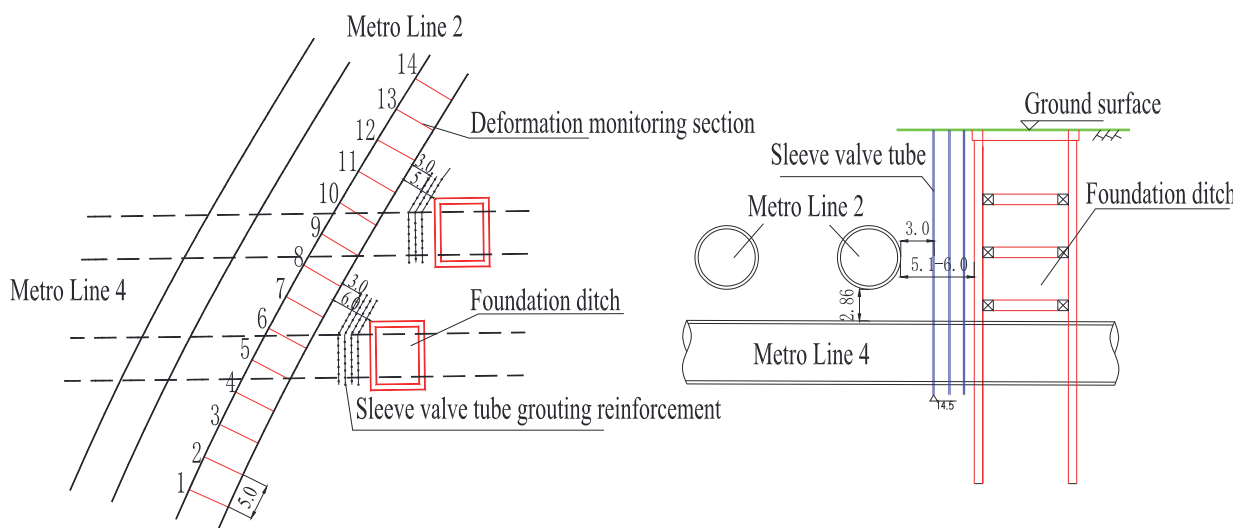


Fig. 7: Section deformation monitoring at the cross location between metro line 2 and newly-built metro line 4

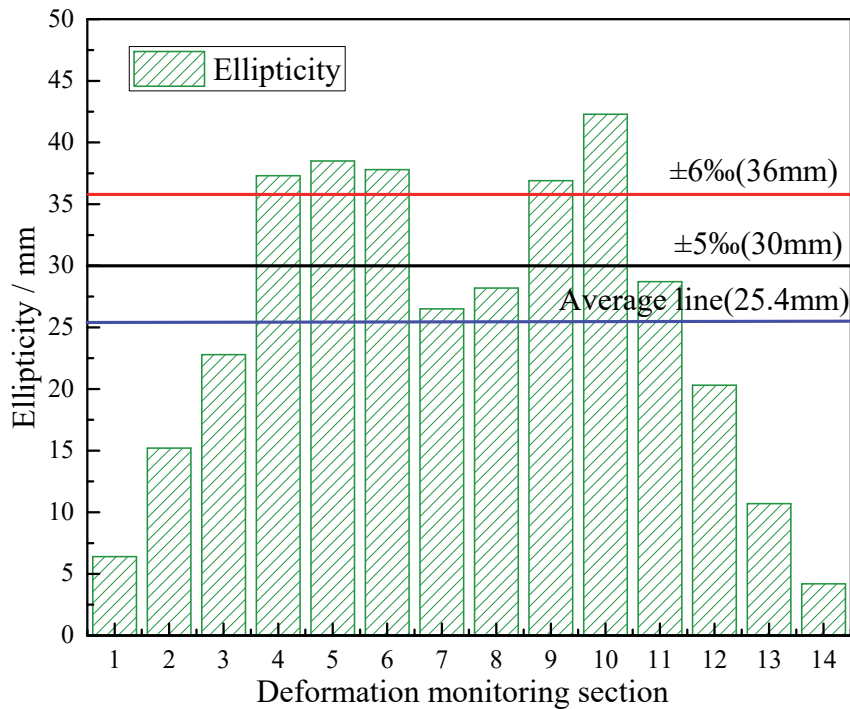
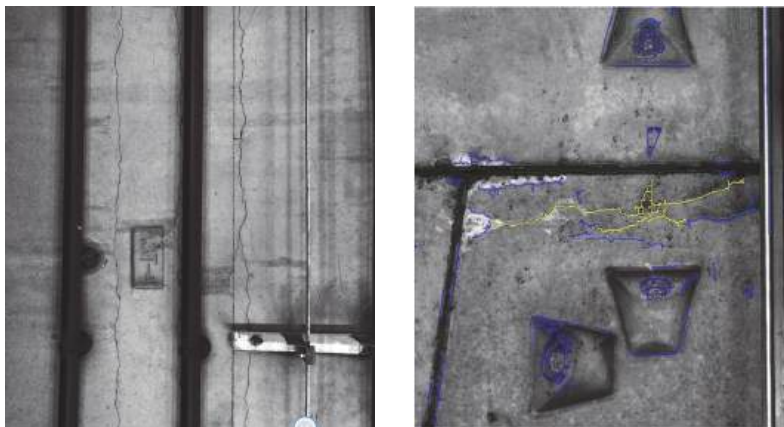


Fig. 8: Detection results of ellipticity of tunnel section

4.2 Cracks

The cracks in the lining are the common forms of damage. The detection and analysis results of the metro line 2 show that typical cracks are longitudinal cracks and the cracks on the joint edges (Fig.9). The proportion of the cracks at the edges of the joints is 65.4 %, and the proportion of longitudinal cracks is 34.6 %.



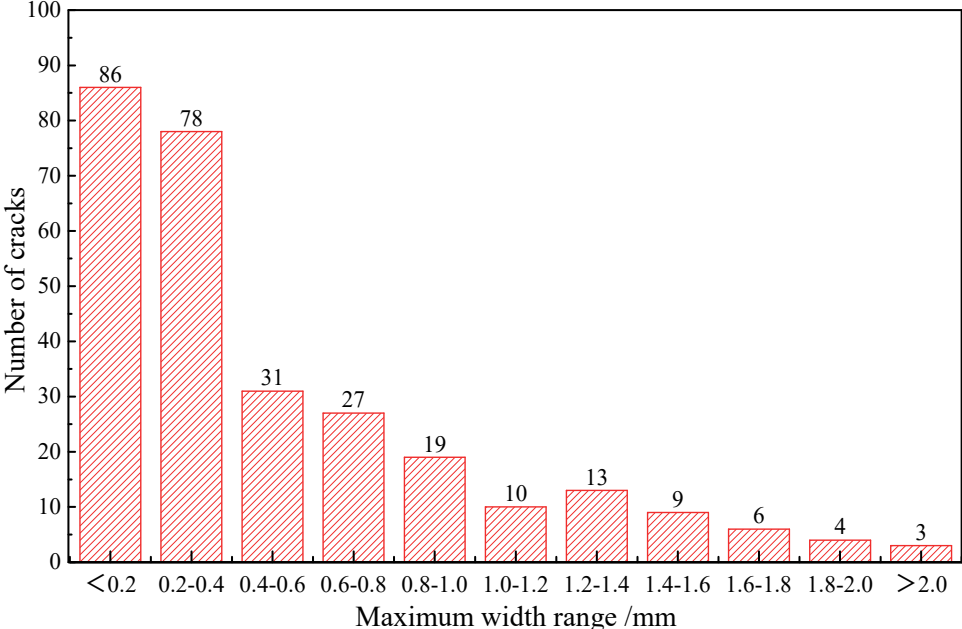
(a)longitudinal cracks

(b)cracks at the edge of the joint

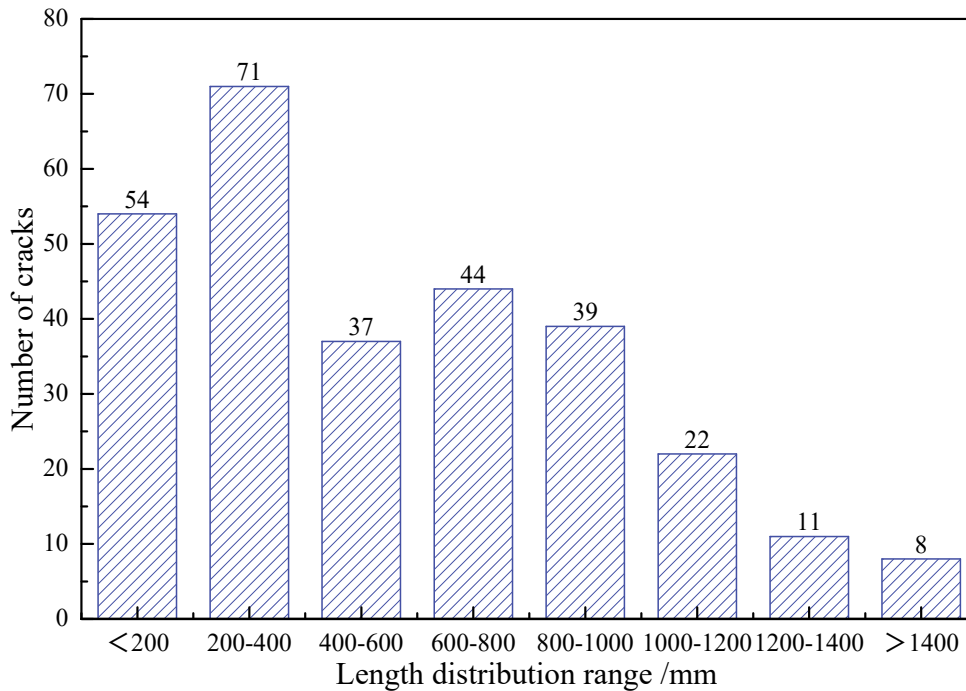
Fig. 9: Crack types of metro line 2

The longitudinal cracks have the greatest impact on the stability and safety of tunnel structures (Han et al., 2018). Longitudinal cracks usually appear on the vault of the lining, which reduces the ability of the structure to resist external forces. Therefore, it is necessary to further analyze the depth and width of the longitudinal cracks of the metro line 2. We extracted the length and the maximum width distribution of 286 longitudinal cracks from the collected data and obtained maximum depth distri-

bution of the cracks using ultrasonic crack depth tester. As shown in Fig. 10 (a), the maximum width of the cracks mainly lies in the range of < 0.4 mm, but the number of cracks with the maximum width of more than 0.4 mm is 122, accounting for 42.66 % of the total number of the cracks. Fig.10 (b) exhibits the length distribution of the longitudinal cracks. The number of cracks having 200 - 400 mm length is the largest (71 cracks) and the number of cracks with the length ≥ 600 mm is 124, accounting for 43.36 % of the total number of cracks. It is well known that width, length, and depth of cracks all have an influence on the mechanical performance of the structure. Therefore, the stress state of the structure in these positions should be theoretically and numerically analyzed to determine whether repair measures need to be taken for the corresponding cracks (find the limit values of width, length, and depth for considering repair). Generally, if the concrete crack does not penetrate through the tunnel structure and has no development trend, it is regarded as no large safety risk for the tunnel structure. However, the existence of cracks will affect the service durability of the structure. Some standards have indicated that the crack with width ≥ 0.3 mm should be filled with the epoxy resin slurry and the crack with width > 1.0 mm should be repaired by micro expansion cement slurry.



(a) Maximum width distribution of longitudinal cracks

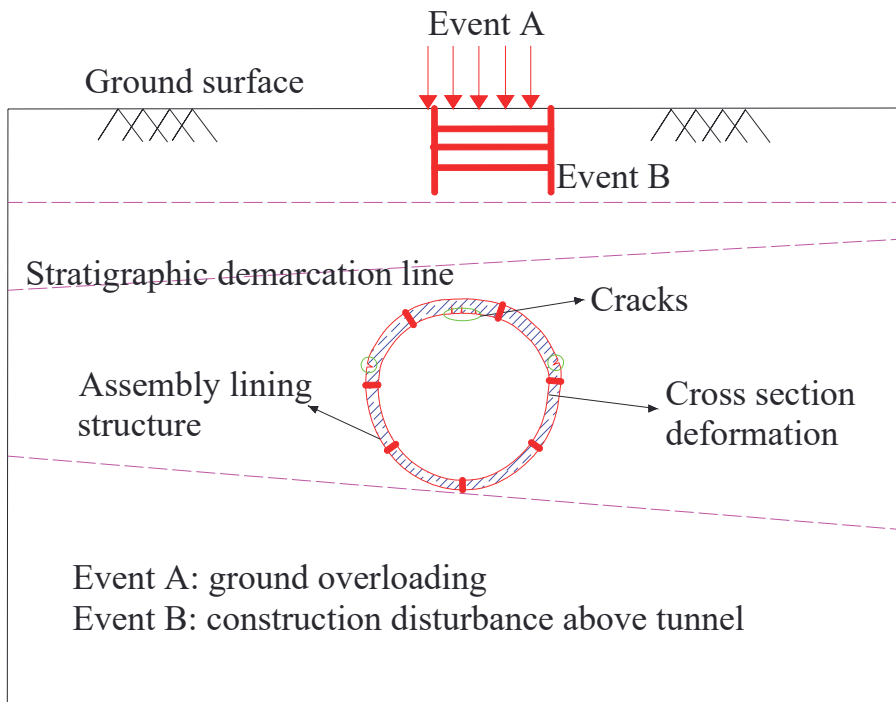


(b) Length distribution of longitudinal cracks

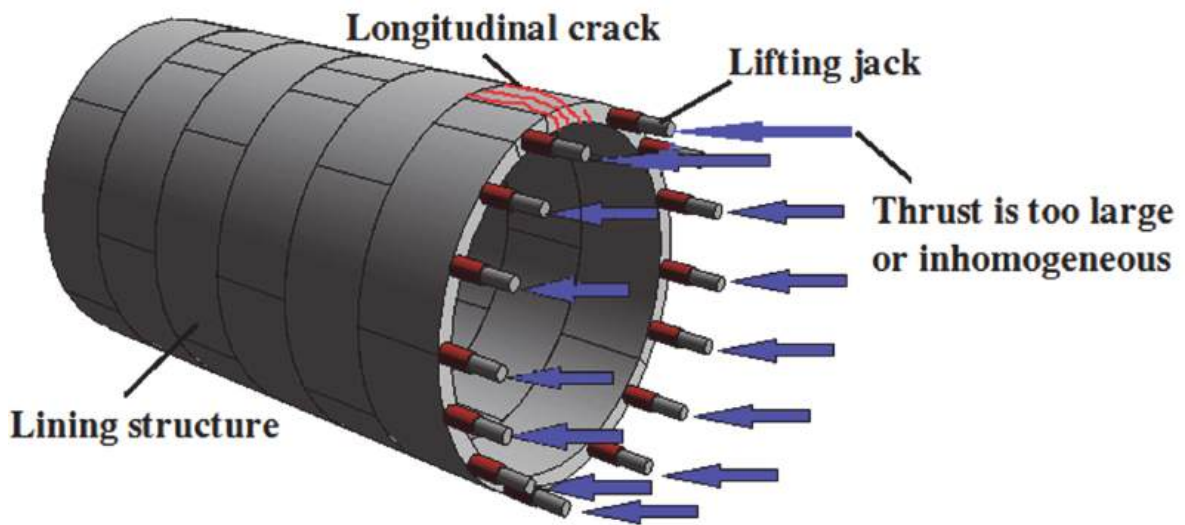
Fig. 10: Statistical results of the 286 longitudinal cracks

The formation and expansion of concrete cracks are accompanied by the accumulation and release of energy (Zhang et al., 2018). The deformation of tunnel lining structure will cause the energy accumulation. When it exceeds the ultimate capacity of the structure, cracks occur and the energy releases. When new energy accumulates in the lining, the existing cracks further expand or new cracks form. The shield tunnel lining belongs to the assembly structure, and the shape of the crack varies depending on the different influencing factors. For example, the longitudinal cracks of shield tunnels are mostly located on the vault due to the excessive load at the top of the structure (Huang et al., 2017), construction load near the ground surface (Shi et al., 2016; Chen et al., 2016), grouting pressure around the lining during construction and uneven thrust from the jack (Chen and Mo, 2009) (as shown in Fig. 11).

The cracks at the joint are usually distributed at the edge of the joint, which obliquely propagate from the bolt hole towards the concrete surface (Fig. 12 (b)). This type of cracks is closely related to the structural form of the shield tunnel. The shield tunnel structure of the metro line 2 is made up of a single layer of precast segments which are connected by bolts. The segment is the bearing body of the tunnel, and the bolt and the joint are the boundary conditions (Fig. 12 (a)). When the segment is subjected to external force, the lining joint opens or squeezes, which may cause segment dislocation and concrete collapse at the joint. When the joint deformation is restricted, the connecting bolt continues to resist the external force, and the stress concentration develops near the bolt hole. That is why the concrete near the joint and the bolt hole is easy to crack. The cracks extend outward along the concrete surface, which eventually result in concrete spalling (Fig. 12 (b)).



(a) Load actions at the top of the structure



(b) Uneven thrust from jack

Fig. 11: Main causes of longitudinal cracks

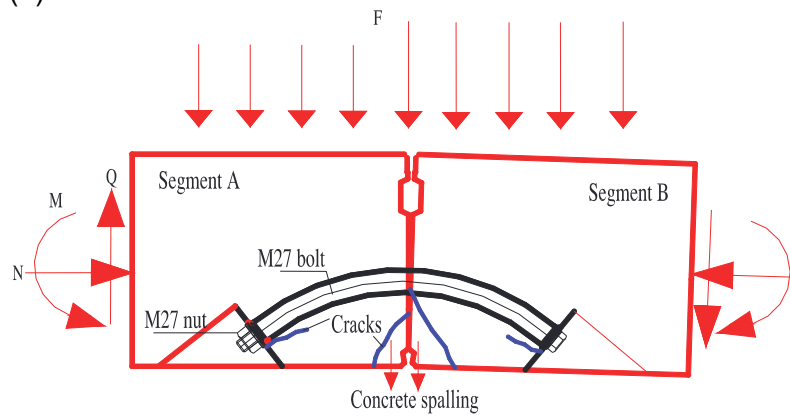
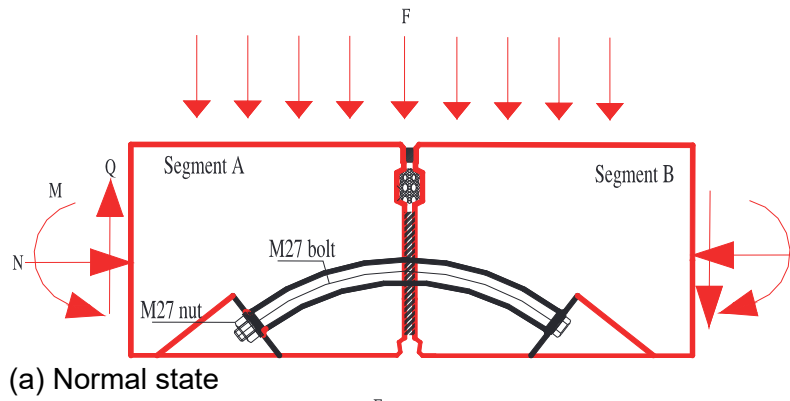


Fig. 12: The cracking process at the edge of the joint

4.3 Concrete spalling

As shown in Fig. 12 (b), when the edge cracks around the joint continuously develop, the concrete spalling emerges. According to the survey results (Fig. 13), concrete spalling at the vault, shoulder and waist of the structure, account for 74 %, 20.67 %, and 5.33 %, respectively. Overall, spalling usually occurs at the edges of the joints (Fig. 14).

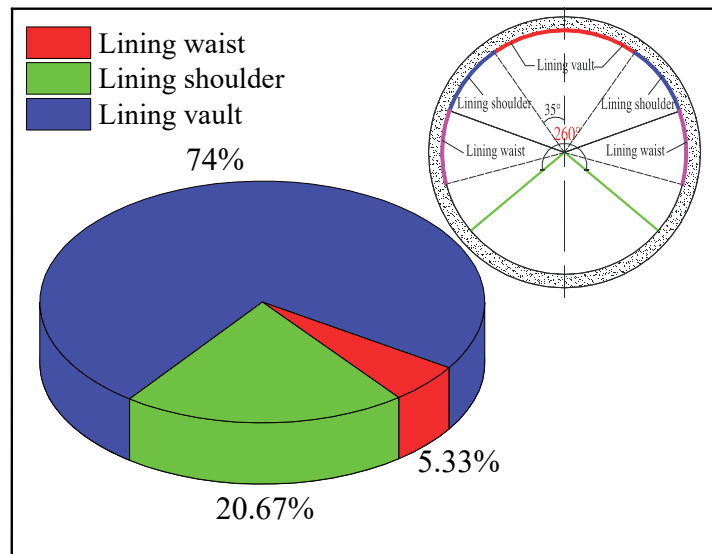


Fig. 13: Statistics of concrete spalling in different positions

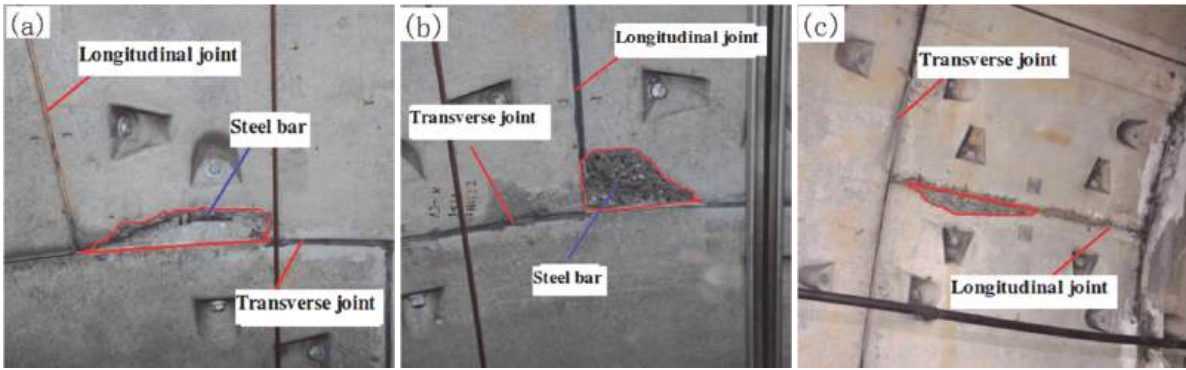


Fig. 14: Positions of concrete spalling, (a) transverse joint edge; (b) joint corner; (c) longitudinal joint edge

60.38 % of the steel reinforcement and 10.06 % of bolts are exposed to the environment in these spalling positions. The area of spalling in different positions are measured by the system (Fig. 15). We found that the area of concrete spalling is concentrated within 0.05 m^2 . Small scale concrete spalling will not cause a great safety risk to tunnel structure. However, concrete spalling may pose a safety threat to running trains. Therefore, the potential spalling concretes need to be cleared away and repaired with cement to reduce the risk of train operation.

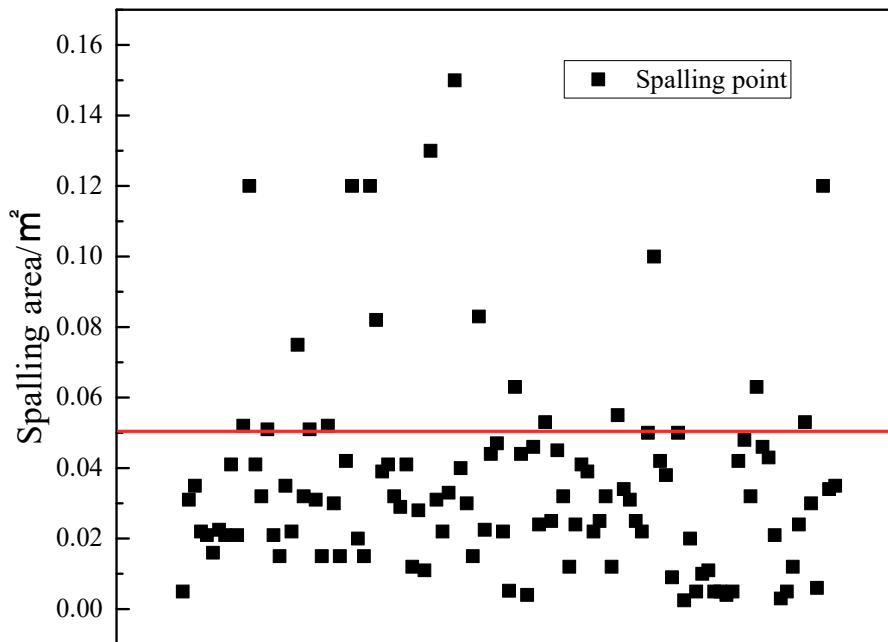


Fig. 15: Area distribution of spalling

The reasons for the cracking and the spalling of shield tunnels are complex. Due to manufacturing errors, undetectable cracks are commonly present in the tunnel segments. Transportation and installation of tunnel segments may cause damage (Chen and Mo, 2009). During construction, the tail brush may also lead to damage (Han et al., 2017). The existence of these micro-cracks might be the potential source of the damage during operation. Uneven settlement of the surrounding rock can lead to local stress concentrations around these micro-cracks (within the lining structure), which further results in cracking of the lining. According to our investigation, settle-

ment of the strata may have an impact on concrete spalling. Fig. 16 shows the relationship between the position of lining spalling and the settlement of strata in a station of metro line 2. It can be observed from the figure that the spalling phenomena occur more frequently at locations where dramatic variation in settlement occurs. Therefore, we can confirm that some damages in metro line 2 are directly related to the uneven settlement. However, the cracking and the spalling may also occur in some stable places, which may be controlled by other factors. For example, metro line tunnels exist in a complex urban environment and experience both, internal and external forces. The internal forces include structural vibration and the aerodynamic forces from the passing trains. Previous studies have shown that the vibration effect and the aerodynamic effect can alter the stress state of the tunnel lining to some extent (Zhang and Cui, 2017; Niu et al., 2016). Even a train crash (Yan et al., 2018) may lead to serious damage of the lining. In addition, external forces including construction of surrounding structures and ground overload may also be causes of damage. There is a large-scale irregular spalling at the vault and shoulder of segments between lining rings 1167 and 1182 (Fig. 17). We investigated the ground situation and found that lining rings 1167-1182 are near the excavation construction of a foundation pit. Therefore, the causes of damage in shield tunnel of metro line 2 should be synthetically concluded based on further continuous monitoring. At present, we can only identify some cracking and spalling directly related to aforementioned uneven settlement and adjacent constructions (Figs. 16 and 17).

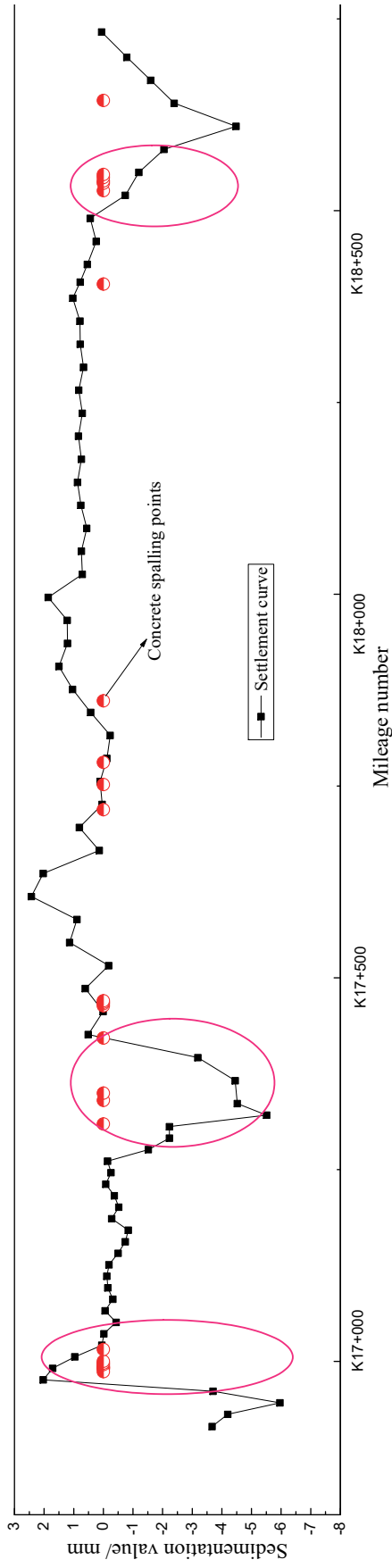


Fig. 16: Relationship between the position of lining spalling and settlement of strata in a section of metro line 2



Fig. 17: Large-scale irregular spalling caused by the construction of a foundation pit

4.4 Water leakage

Water leakage mainly occurs at the joints, bolt holes, grouting holes, ballastless beds, and connections between stations and the shield tunnel (Fig. 18 (a - e)). Water leakage is commonly accompanied by white calcification that gradually forms a relatively hard calcareous layer at the leakage location. The proportion of water leakage in transverse joint, longitudinal joint and bolt hole is 58.35 %, 20.33 %, and 16.20 %, respectively (Fig. 18 (f)).

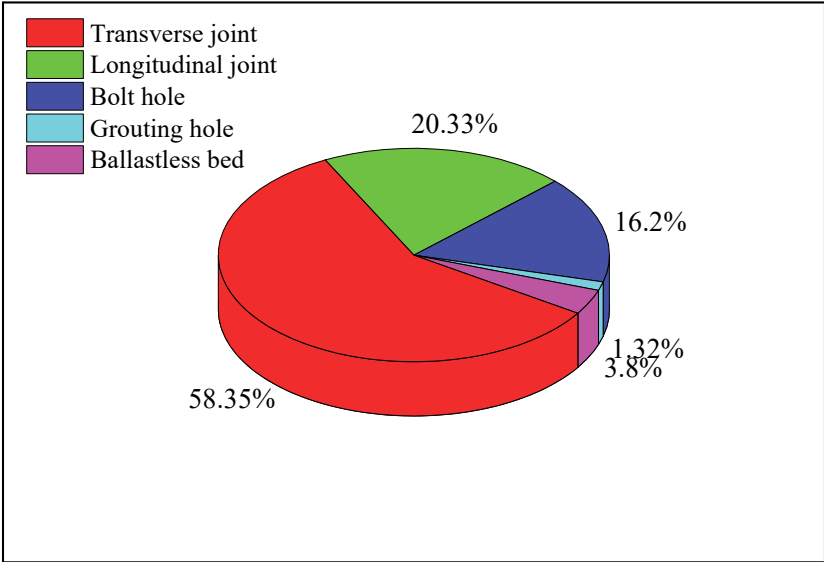
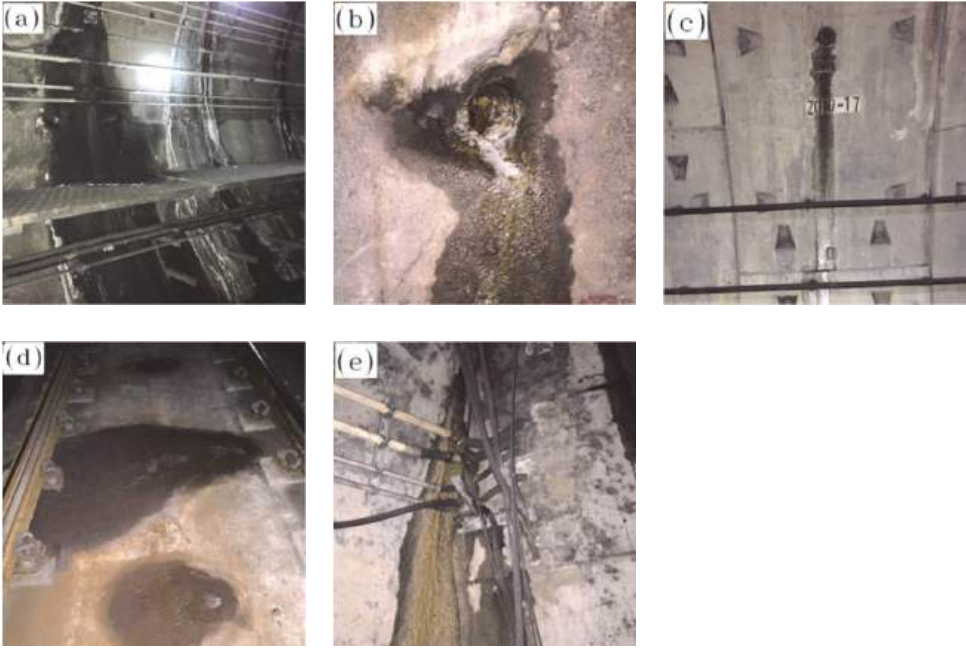


Fig. 18: Water leakage location of shield tunnel, (a) segment joint, (b) bolt hole, (c) grouting hole, (d) ballastless bed, (e) connection between station and tunnel, and (f) statistics of the water leakage location

Seasonal rainfall is obvious in Changsha, and the summer rain is quite common. We have summarized the total water leakage area of the linings in two sections of metro line 2 during 6 times of investigations (indicated by imaginary lines in Fig. 19). The variations of the rainfall and the total water leakage area of the linings are shown in

Fig. 19. It can be recognized that the variation trend of the total water leakage area follows the change of rainfall (the total water leakage area increases with increase in rainfall and decreases with decrease in rainfall). The peak value of the total water leakage area is delayed in respect to the rainfall, which may be related to the time requirement of the rain infiltrating into the surrounding rocks.

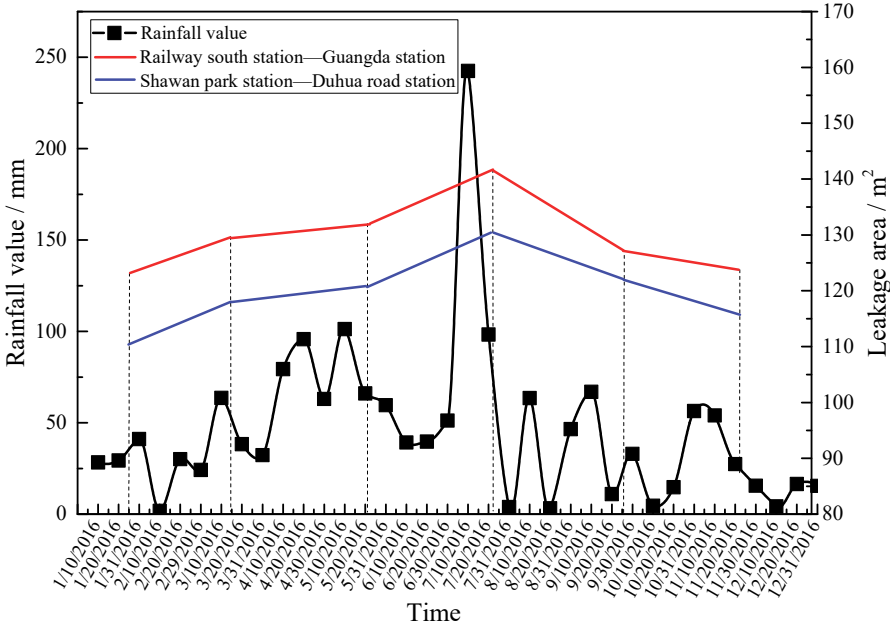


Fig. 19: Variations of rainfall and the total water leakage area of the linings

The hydrostatic pressure surrounding the tunnel increases with the rise of the groundwater level. Previous studies have shown that the influence of groundwater level on permeability variation is significant (Fernandez and Moon, 2010; Mohamed, 2003; Kolymbas and Wagner, 2007; Huang and Han, 2009; Wu et al., 2014). Fig. 20 shows the number of leakage points per 30 lining rings versus the depth below groundwater level in a section of metro line 2. The red lines in Fig. 20 represent the upper and lower boundary of the leakage points. It can be concluded that the number of leakage points increases with increasing depth below groundwater level.

The different types of rocks surrounding the tunnel have various permeabilities; the higher the weathering of the rocks, the greater the permeability (Worthington et al., 2016). Fig. 21 shows the average number of leakage points per 500 m in the tunnel within moderately weathered argillaceous slate, fully, strongly and moderately weathered argillaceous sandstone, and silty clay. The number of leakage points obviously increases where the tunnel is surrounded by fully and strongly weathered argillaceous sandstone.

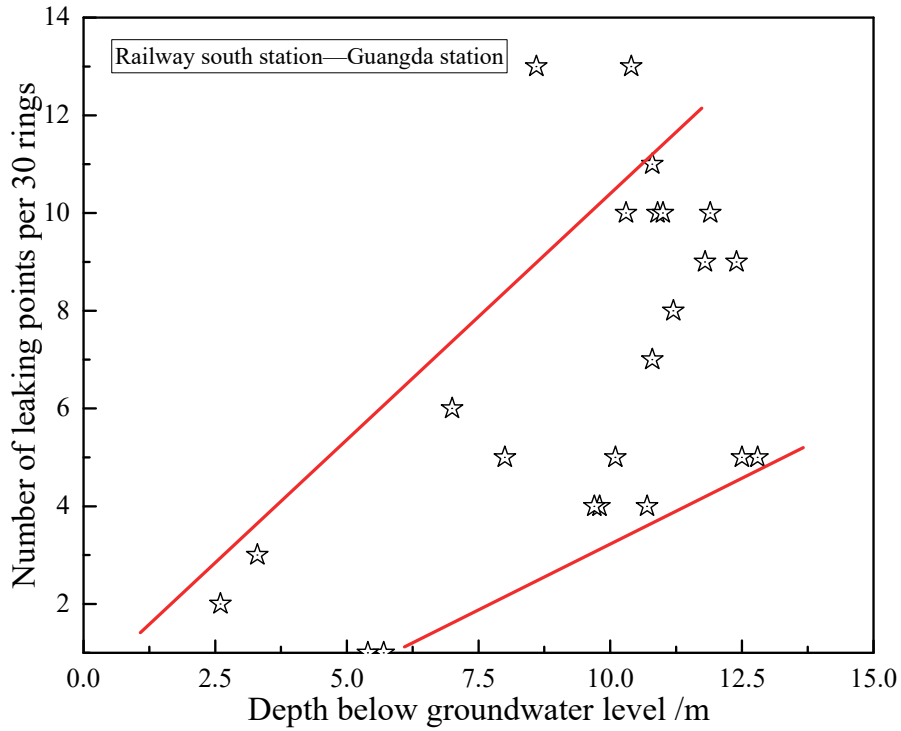


Fig. 20: Relationship between the number of leakage points and the depth below groundwater level in a section

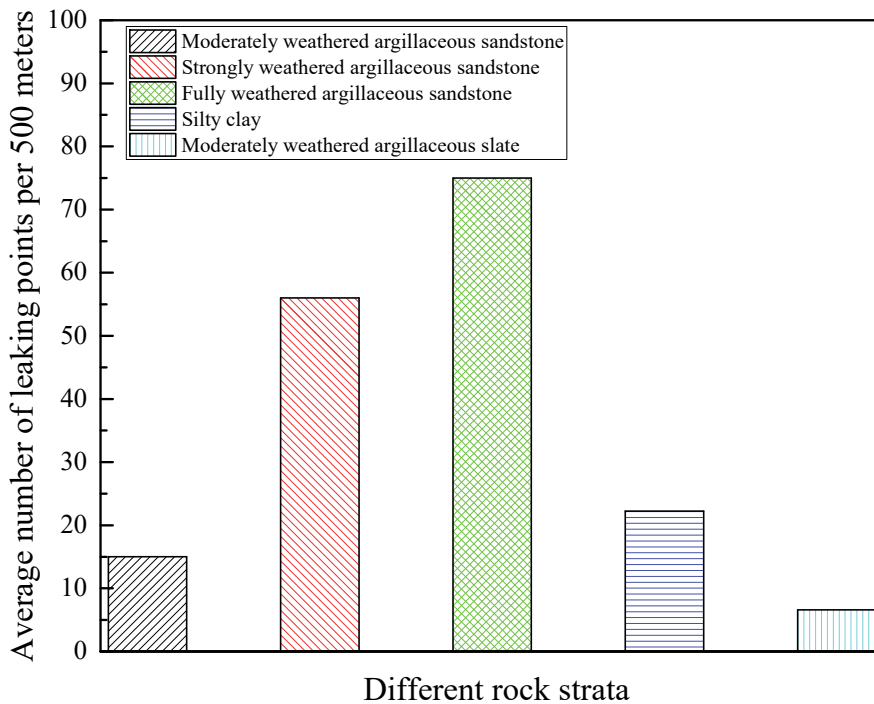


Fig. 21: Relationship between the number of leakage points and rock types

Great attention should be paid to the waterproof of the single layer of shell lining which has a large number of joints. Generally, the watertight performance of the lining relies on the following: (1) impermeability of the concrete; (2) effectiveness of the joint sealing material; (3) watertight bolt joints; and (4) impermeability of the connec-

tion between the tunnel and the station. However, human and natural factors may lead to the failure of watertightness. These factors include the following: (1) uneven settlement causing slip between the lining rings and causing failure of the watertightness of lining (as shown in Fig. 22, many leakage points are concentrated in the locations with dramatic uneven settlement. Some pink circles indicate that the uneven settlement is big. Also, the distribution of leakage points indicated by the small red squares in these pink circles is more than that of other places); (2) improper installation of sealing material and premature installation; (3) cracks in the lining structure; and (4) abscission or deterioration of sealing material.

In addition, the groundwater in Changsha is weakly corrosive to the iron. It was found that the bolt corrosion rate is up to 73 % for the bolts near water leakage in the metro line 2. Corrosion of metallic anchor materials significantly shortens the tunnel's service life (Xia, 2005). Therefore, it is necessary to pay attention to the effect of bolt corrosion on the long-term deterioration of the structure performance.

5 Conclusions

The damage investigation by a rapid detection and analysis system in Changsha metro line 2 is taken as a case study in this paper. Not only the types and distribution characteristics of structural damages are statistically summarized, but some causes and influencing factors of the damages are also analyzed. The main conclusions are as follows:

- (1) The system can effectively detect the main types of damages, such as cross-section deformation, lining cracks, concrete spalling and water leakage. The database of damages is quite useful for further safety analysis, maintenance and management.
- (2) The new construction in close distance greatly affects the existing tunnel structure (leads to uneven deformation, changes the stress state and even causes damages). Lining cracks and concrete spalling are generally related to additional forces (from construction disturbance, ground load, grouting pressure of the new construction, jack thrust, train vibration etc.) and uneven settlement of the strata. The water leakage in the tunnel structure is closely related to the rainfall in the region, the variation of the groundwater level, the characteristics of the strata and the effectiveness of the waterproof material. The quality control and the construction technology in the construction process have an important influence on the development of early damage of the tunnel structure.
- (3) High efficiency and precision, intelligent and automatic detection technologies should be applied to maintain and manage metro structures.

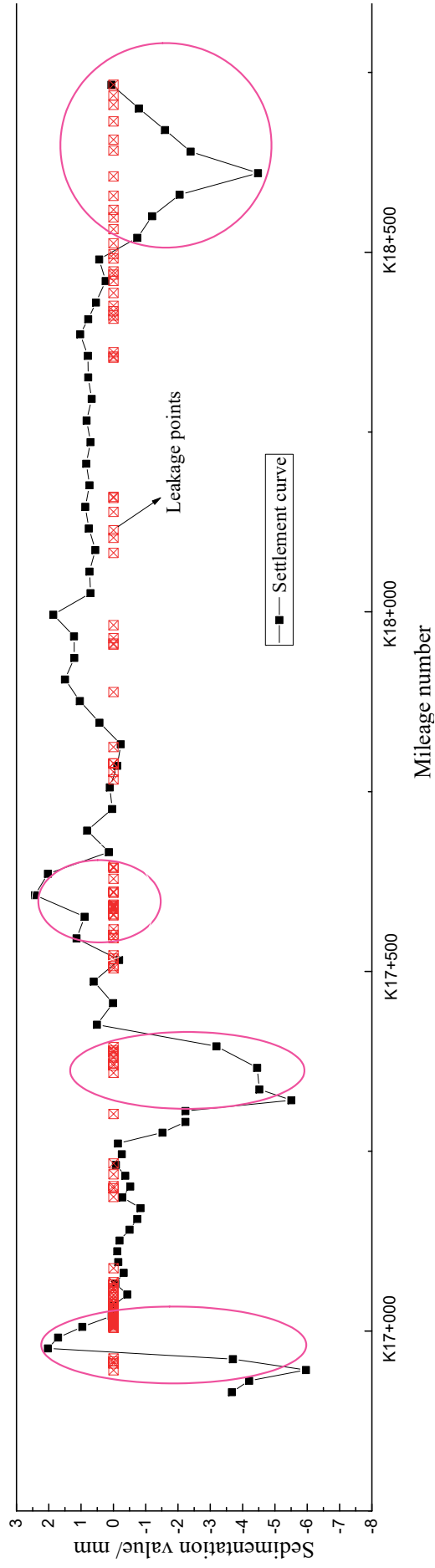


Fig. 22: Relationship between water leakage and settlement in a section

References

- Attard, L., Debono, C.J., Valentino, G. and Castro, M.D. (2018). *Vision-based change detection for inspection of tunnel liners*. Automation in Construction, 91, 142 - 154.
- Chen, J.S. and Mo, H.H. (2009). *Numerical study on crack problems in segments of shield tunnel using finite element method*. Tunnelling and Underground Space Technology, 24, 91 - 102.
- Chen, J.W. and ZHAN, L.X. (2000). *Deformation measuring of the metro tunnel and deformation data analysis of Shanghai Metro Line No.1*. Shanghai Geology, 2, 51 - 56.
- An, G.F. and Song, E.X. (2005). *The analysis of excavation monitoring for the Pazhouta subway station in Guangzhou*. Chinese Journal of Geotechnical Engineering, 26 (3), 333 - 337.
- Chen, R.P., Meng, F.Y., Li, Z.C., Ye, Y.H. and Ye, J.N. (2016). *Investigation of response of metro tunnels due to adjacent large excavation and protective measures in soft soils*. Tunnelling and Underground Space Technology, 58, 224 - 235.
- Dong, F., Fang, Q., Zhang, D.L., Xu, H.J., Li, Y.J. and Niu, X.K. (2017). *Analysis on defects of operational metro tunnels in Beijing*. China Civil Engineering Journal, 50 (6), 104-113.
- Erkal, B.G. and Hajjar, J.F. (2017). *Laser-based surface damage detection and quantification using predicted surface properties*. Automation in Construction, 83, 285 - 302.
- Fernandez, G. and Moon, J. (2010). *Excavation-induced hydraulic conductivity reduction around a tunnel - Part 1: Guideline for estimate of ground water inflow rate*. Tunnelling and Underground Space Technology, 25 (5), 560 - 566.
- Han, J.Y., Zhao, W., Jia, P.J., Guan, Y.P., Chen, Y. and Jiang, B.F. (2018). *Risk analysis of the opening of shield-tunnel circumferential joints induced by adjacent deep excavation*. Journal of Performance of Constructed Facilities, 32 (1), 04017123-1-12.
- Han, L., Ye, G.L., Chen, J.J., Xia, X.H. and Wang, J.H. (2017). *Pressures on the lining of a large shield tunnel with a small overburden: A case study*. Tunnelling and Underground Space Technology, 64, 1 - 9.
- Huang, H.W. and Zhang, D.M. (2015). *Quantitative Geotechnical Risk Management for Tunneling Projects in China*. 5th International Symposium on Geotechnical Safety and Risk, Rotterdam, Netherlands, 61 - 75.
- Huang, H.W., Shao, H., Zhang, D.M. and Wang, F. (2017). *Deformational responses of operated shield tunnel to extreme surcharge: a case study*. Structure and Infrastructure Engineering, 13 (3), 345 - 360.
- Huang, H.W., Sun, Y., Xue, Y.D. and Wang, F. (2017). *Inspection equipment study for subway tunnel defects by grey-scale image processing*. Advanced Engineering Informatics, 32, 188 - 201.

- Huang, J. and Han, J. (2009). *3D coupled mechanical and hydraulic modeling of a geosynthetic-reinforced deep mixed column-supported embankment*. *Geotextiles and Geomembranes*, 27 (4), 272 - 280.
- Huang, Z., Fu, H.L., Wang, H. and Zhang, J.B. (2018). *Accident analysis and smart management model of metro safety*. *Electronic Journal of Geotechnical Engineering*, 23 (01), 79 - 96.
- Kolymbas, D. and Wagner, P. (2007). *Groundwater ingress to tunnels-the exact analytical solution*. *Tunnelling and Underground Space Technology*, 22 (1), 23 - 27.
- Lai, J.X., Qiu, J.L., Pan, Y.P., Cao, X.J., Liu, C. and Fan, H.B. (2015). *Comprehensive monitoring and analysis of segment cracking in shield tunnels*. *Modern Tunnelling Technology*, 52 (2), 186 - 191.
- Li, C., Zhao, Y.G., Liu, H., Wan, Z., Zhang, C. and Rong, N. (2008). *Monitoring second lining of tunnel with mounted fiber Bragg grating strain sensors*. *Automation in Construction*, 17 (5), 641 - 644.
- Lin, N., Li, P. and Xie, X.Y. (2015). *Research on evolution mechanism of shield tunnel disease based on segment performance analysis*. *Chinese Journal of Underground Space and Engineering*, 11 (S2), 802 - 809.
- Li, Y.P. and Wang, Z.Y. (2009). *Study of Influence of Subway Station Excavation on Existing Metro Deformation*. 9th International Conference of Chinese Transportation Professionals, Harbin, China, 3339 - 3345.
- Menendez, E., Victores, J.G., Montero, R., Martínez, S. and Balaguer, C. (2018). *Tunnel structural inspection and assessment using an autonomous robotic system*. *Automation in Construction*, 87, 117 - 126.
- Mohamed, E.T. (2003). *Circular tunnel in a semi-infinite aquifer*. *Tunnelling and Underground Space Technology*, 18 (1), 49 - 55.
- Montero, R., Victores, J.G., Martínez, S., Jardón, A. and Balaguer, C. (2015). *Past, present and future of robotic tunnel inspection*. *Automation in Construction*, 59, 99 - 112.
- Niu, J.Q., Zhou, D., Liu, T.H. and Liang, X.F. (2016). *Numerical simulation of aerodynamic performance of a couple multiple units high-speed train*. *Vehicle System Dynamics*, 55(5), 681 - 703.
- Shi, C.H., Cao, C.Y., Lei, M.F., Peng, L.M. and Ai, H.J. (2016). *Effects of lateral unloading on the mechanical and deformation performance of shield tunnel segment joints*. *Tunnelling and Underground Space Technology*, 51, 175 - 188.
- Tanon, F., Mammion, A. and Bernardini, A. (2002). *Multiobjective optimization under uncertainty in tunneling application to the design of tunnel support reinforcement with case histories*. *Tunneling and Underground Space Technology*, 17 (1), 33 - 54.
- Wang, F., Huang, H.W. and Zhang, D.M. (2013). *Deformation sensing method of shield tunnel based on optical fiber sensing technology of BOTDA*. *Chinese Journal of Rock Mechanics and Engineering*, 32 (9), 1901 - 1908.
- Worthington, S.R.H., Davies, G.J. and Alexander, E.C. (2016). *Enhancement of bed-rock permeability by weathering*. *Earth-Science Reviews*, 160, 188 - 202.

- Wu, H.N., Huang, R.Q., Sun, W.J., Shen, S.L., Xu, Y.S., Liu, Y.B. and Du, S.J. (2014). *Leaking behavior of shield tunnels under the Huangpu River of Shanghai with induced hazards*. *Natural Hazards*, 70 (2), 1115 - 1132.
- Xia, N. (2005). *Study on the mechanical Property of corroded anchor age structure and its durability evaluation*. Doctoral Dissertation of Hohai University, 2005.
- Yang, Y.B., Zhou, B., Xie, X.Y. and Liu, C. (2017). *Characteristics and causes of cracking and damage of shield tunnel segmented lining in construction stage-a case study in Shanghai soft soil*. *European Journal of Environmental and Civil Engineering*, 1 - 15.
- Yan, Q.X., Xu, Y.J., Zhang, W.L., Geng, P. and Yang, W.B. (2018). *Numerical analysis of the cracking and failure behaviors of segmental lining structure of an underwater shield tunnel subjected to a derailed high-speed train impact*. *Tunnelling and Underground Space Technology*, 72, 41- 54.
- Yao, F.H., Shao, G.F., Takaeue, R. and Tamaki, A. (2003). *Automatic concrete tunnel inspection robot system*. *Advanced Robotics*, 17 (4), 319 - 37.
- Yu, S.N., Jang, J.H. and Han, C.S. (2007). *Auto inspection system using a mobile robot for detecting concrete cracks in a tunnel*. *Automation in Construction*, 16 (3), 255-261, <https://doi.org/10.1016/j.autcon.2006.05.003>.
- Zhang, C.L. and Cui, Z.D. (2017). *Numerical simulation of dynamic response around shield tunnel in the soft soil area*. *Marine Georesources & Gotechnolgy*, 7, 1018 - 1027.
- Zhang, D.M., Huang, H.W., Wang, F. and Wu, Y. (2016). *Wireless Sensing Network based Monitoring System for Safety of Shield Tunnel Structures*. The 2016 Academic Annual Conference of the China Civil Engineering Society, Beijing, China, 78 - 91.
- Zhang, W., Sun, K., Lei, C.Z., Zhang, Y.C., Li, H.X. and Spencer, B.F. (2014). *Fuzzy Analytic Hierarchy Process Synthetic Evaluation Models for the Health Monitoring of Shield Tunnels*. *Computer-aided Civil and Infrastructure Engineering*, 29 (9), 676 - 688.
- Zhang, X.P., Jiang, Y.J. and Sugimoto, S. (2018). *Seismic damage assessment of mountain tunnel: A case study on the Tawarayama tunnel due to the 2016 Kumamoto Earthquake*. *Tunnelling and Underground Space Technology*, 71, 138 - 148.
- Zhou, S.H., Di, H.G., Xiao, J.H. and Wang, P.X. (2016). *Differential settlement and induced structural damage in a cut-and-cover subway tunnel in a soft deposit*. *Journal of Performance of Constructed Facilities*, 30 (5), 04016028.

Rock mechanics of the Spent Nuclear Fuel disposal programme in Finland

Felsmechanik im finnischen nuklearen Endlagerprogramm

Topias Siren

Rock Mechanics Consulting Finland Oy

Jouni Valli

Rock Mechanics Consulting Finland Oy

Johannes Suikkanen

Posiva Oy

Jussi Mattila

Geological Survey of Finland

Rodney S. Read

RSRead Consulting Inc.

Abstract

Finland is the first country in the world actively constructing a deep geological repository for the final disposal of spent nuclear fuel. The repository is being constructed at Olkiluoto Island, located in Western Finland. The geology at Olkiluoto Island consists of highly heterogeneous and anisotropic crystalline bedrock characterised mainly by migmatitic and foliated gneisses, intersected by major low angle brittle fault zones and subordinate subvertical fault zones. An underground rock characterization facility, known as ONKALO, was constructed in the central part of Olkiluoto Island for the purposes of detailed site characterization and testing of the disposal concept. The ONKALO underground facility consists of an access tunnel and three shafts that have been excavated to the anticipated repository level at a depth of 420 m below ground surface. The rock mass quality encountered during the construction of ONKALO has in general been good or very good below a depth of about 130 m. The *in situ* rock stress state has been thoroughly characterised at Olkiluoto and especially in the ONKALO facility. The stress measurement results indicate that the maximum principal stress at Olkiluoto is oriented NW-SE, but the direction is affected in the vicinity of major fault zones. The magnitudes of the major and intermediate principal stress components are fairly isotropic, which together with a competent but heterogeneous rock mass, result in a unique rock mass response not observed in other international repository locations. During the execution of various *in situ* tests at the ONKALO facility, the rock mass has been observed to exhibit a geologically-controlled failure mechanism.

Zusammenfassung

Finnland ist das erste Land in der Welt, das aktiv ein tiefes Endlager für verbrauchten Kernbrennstoff baut. Das Endlager wird auf der Insel Olkiluoto gebaut, die im Westlichen Finnland gelegen ist. Der geologische Untergrund der Insel besteht aus stark heterogenen und anisotropen Kristallingesteinen, die hauptsächlich von migmatitischen geschieferten Gneisen gebildet werden, welche von flach

einfallenden Störungszonen und untergeordnet von fast vertikalen Störungen durchsetzt werden. Im Hauptteil der Insel Olkiluoto wurde eine Einrichtung gebaut, um den Untergrundfels charakterisieren zu können, bekannt als ONKALO. Damit wurden ausführlich die Gegebenheiten untersucht und das Endlagerkonzept geprüft. Die ONKALO besteht aus einem Zugangstunnel und drei Schächte, die zum vorgesehenen Endlagerniveau in 420 m Tiefe aufgeföhren wurden. Die während des Aufföhrens von ONKALO vorgefundene Felsqualität ist im Allgemeinen gut bis sehr gut ab Teufen von etwa 130 m. Der Situ-Spannungszustand ist unter Olkiluoto und besonders in der ONKALO gründlich charakterisiert worden. Die Spannungen zeigen an, dass die maximale Hauptspannung an Olkiluoto NW-SE orientiert ist. Sie ist an Hauptfalten an deren Ausrichtung gekoppelt. Die Magnituden der großen und mittleren Hauptnormalspannungen sind nahezu isotrop. Zusammen mit den guten, aber heterogenen Felsenqualitäten auf eine einzigartige und in anderen internationalen Endlagern nicht beobachtete Felsenqualität hinausläuft. Während verschiedener InSitu-Tests an der ONKALO hat man beobachtet, dass die Felsenmasse hier einem geologisch kontrollierten Versagensmechanismus folgt.

1 Introduction

In the early 2020's, Finland will be the first nation in the world to start the geological disposal of spent nuclear fuel (SNF). The road toward construction of a SNF repository in Finland has been systematic and straightforward since 1978 when studies for different options of safe final disposal concepts began, just after the first nuclear power reactors were built in Loviisa (Fig. 1 and Fig. 2). The general strategy and timeline for Finnish nuclear waste management was set at that time, and it has been followed faithfully since (Fig. 1).

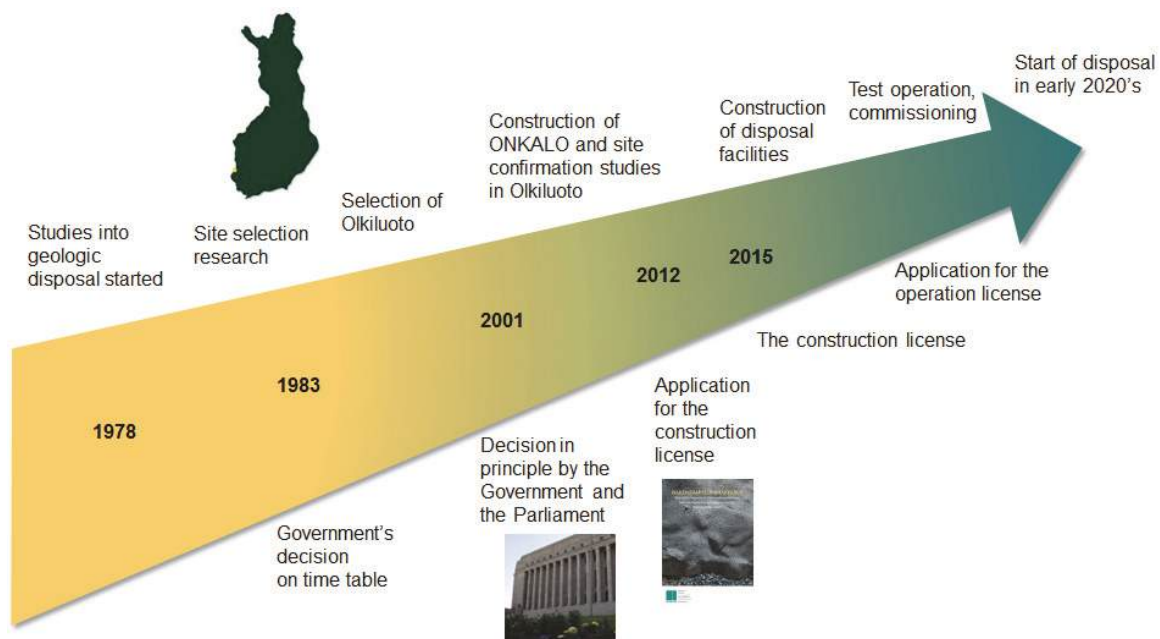


Fig. 1: Timeline for the Finnish nuclear waste management program (Courtesy of Posiva Oy).

Finland currently has four operating nuclear reactors, and two others are being built. Two pressurized water reactors (VVER) are located at Loviisa in Southern Finland, each producing 510 MW of electricity, with the first reactor beginning its operation in 1977. Two Boiling Water Reactors (BWRs) currently in operation at Olkiluoto in

Western Finland, each producing 880 MW of electricity, began operation in 1979 and 1982, respectively. Construction of the fifth reactor in Finland at Olkiluoto, a 1600 MW European Pressurized Reactor (EPR), began in 2005 and operation will soon begin. Additionally, a sixth reactor is being built at Pyhäjoki in Northern Finland (latest VVER type) and will produce 1200 MW of electricity when ready (Fig. 2).

Finnish nuclear waste management is handled Posiva Oy, which was established in 1995 by the two power companies currently operating nuclear power plants in Finland, Teollisuuden Voima Oyj (TVO) and Fortum Power and Heat Oy. The mission of Posiva Oy is the safe final disposal of spent nuclear fuel produced by its owner companies (see Fig. 3). Spent nuclear fuel will be deposited in a final repository being built by Posiva at Olkiluoto Island (Fig. 2). The repository is designed to hold 3,250 canisters that contain 6,500 tons of highly active spent nuclear fuel. In addition, the two aforementioned power companies operate their own low- and intermediate level waste repositories for waste generated by the operation and maintenance of the power plants (Fig. 3).



Fig. 2: The location of the Olkiluoto site on the western Finland.

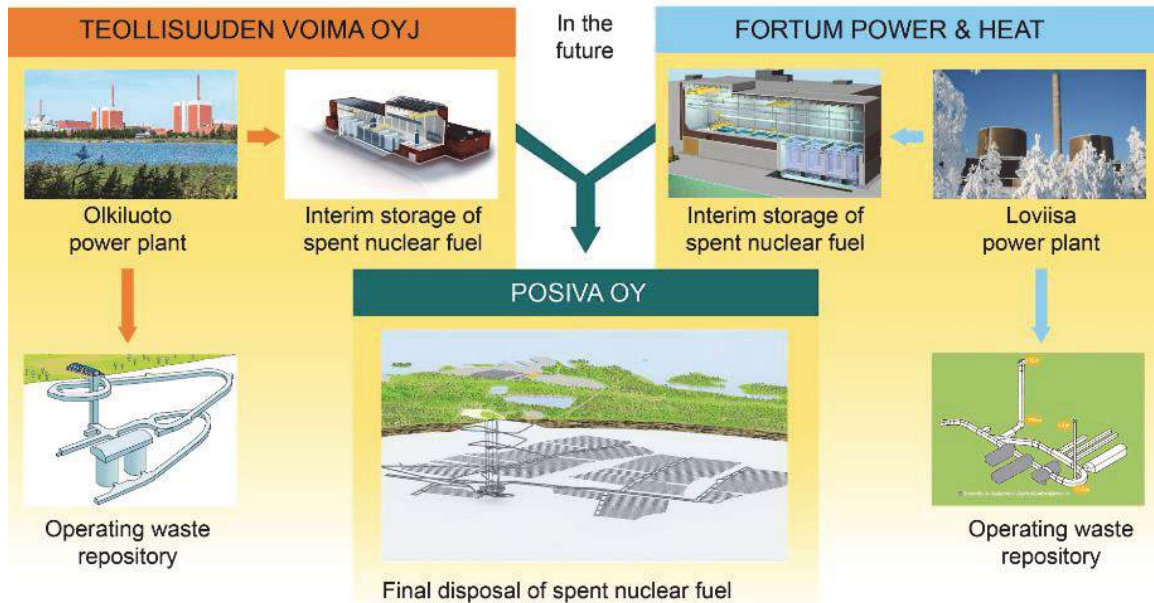


Fig. 3: Organization of Finnish nuclear waste management program (Courtesy of Posiva Oy).

Development of the spent nuclear fuel management program in Finland has been conducted in close collaboration with the Swedish Nuclear Fuel and Waste Management Co. (SKB). Both Posiva Oy and SKB have benefited not only from knowledge exchange, but also from the Finnish program having access to the Äspö Hard Rock Laboratory in Sweden and vice versa. The Swedish spent nuclear fuel disposal program is heading for the implementation and construction phase in the next decade.

One of the key success factors in the progression for disposal of spent nuclear fuel in Finland has been the political commitment and the two-phase-approach, where a second generation underground research laboratory called ONKALO has been built at Olkiluoto Island, located in Western Finland (Fig. 2). ONKALO has been used to conduct multidisciplinary studies to confirm favourable conditions and suitability of the repository site before applying for the construction license for the actual final disposal facility. Consequently, corroborative bedrock characterization programs conducted in ONKALO have provided detailed data and increased confidence in the long term safety analyses to a point that it was possible for the Finnish government to grant the construction licence for the spent nuclear disposal facility to be constructed at Olkiluoto Island (TEM, 2015).

Following the selection of Olkiluoto Island as the site for the final repository facility, Posiva Oy began construction of the ONKALO rock characterization facility at Olkiluoto Island in 2004. The construction of ONKALO served multiple purposes, but primarily it was used to develop repository construction methods and to study the construction effects on bedrock stability and processes related to geochemistry and hydrology. In 2012, after years of conducting multidisciplinary research in ONKALO, Posiva Oy submitted a licence application for the construction of a final disposal facility to the Finnish Government. After thorough review of the supporting Safety Case, the Finnish Radiation and Nuclear Safety Authority stated in February 2015 that a final disposal facility can be safely built at Olkiluoto (Posiva, 2012; STUK, 2015). In November 2015, the Finnish Government granted a licence to Posiva for

the construction of the world's first final disposal facility for spent nuclear fuel (TEM, 2015). The decision made Finland an international pioneer in nuclear waste management and provides commercial opportunities in developing nuclear waste management in other countries.

Within the current schedule, Posiva will start operating the repository for the final disposal of SNF in 2024, after the disposal facilities have been constructed and operation license application has been approved by the Finnish Government. During the period since 1978, the spent nuclear fuel rods have been cooled down for about 30 to 40 years in interim storage (Fig. 3). As this interim storage period is required before final disposal in order to limit the amount of excess heat, the repository facility will be operating 30 to 40 years after the closure of the last nuclear reactors in Finland. Hence, the current estimate is that the repository facility will operate for 120 years before closure.

2 Disposal concept

The Finnish and Swedish plan for spent fuel management is based on construction of a deep geological disposal facility applying the multi-barrier KBS-3 concept. According to the KBS-3 concept, the spent fuel rods will be deposited in a cast iron insert surrounded by a copper canister with a copper lid that is friction stir welded in place (Posiva, 2014). The iron insert provides mechanical strength while the copper canister protects the spent fuel rods from corrosion of the canister. The copper canisters will then be deposited at approximately 400 to 500 m depth in crystalline rock conditions in a selected geological domain. The copper canisters will be emplaced in specifically cored deposition holes and surrounded by compacted bentonite clay, then all deposition tunnels will be backfilled using a bentonite and rock mixture, and the tunnels finally sealed using a concrete plug (Fig. 4).

Currently, two design alternatives of the KBS-3 disposal concept exist according to the alignment of the emplaced canisters as illustrated in Fig. 5. The reference concept for Finnish nuclear waste management is the vertical KBS-3V concept (Fig. 5, left), while the horizontal KBS-3H concept (Fig. 5, right) is kept as an alternative. In both design alternatives the principle of multiple protective barrier systems is followed from engineered barrier systems consisting of the canister and backfill, to the natural barrier consisting of the host rock at a depth of 400 to 500 m.

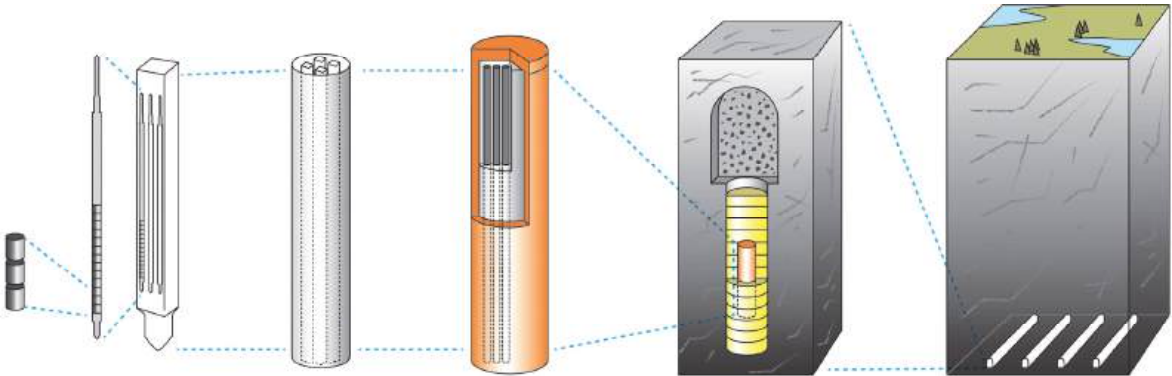


Fig. 4: Schematic illustration of the different barriers associated with KBS-3 deposition concept. (Courtesy of Posiva Oy)

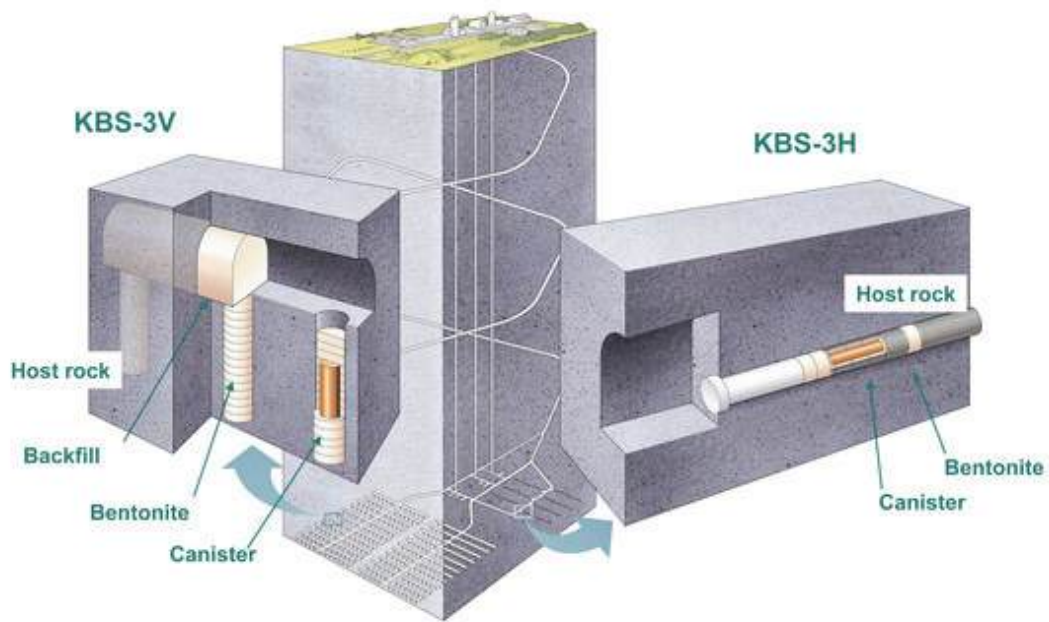


Fig. 5: Comparison between vertical (KBS-3V) and horizontal (KBS-3H) variants of the KBS-3 deposition concept, figure courtesy of SKB, illustrator: Jan Rojmar.

3 Geology of Olkiluoto Island

Olkiluoto Island is situated within the Paleoproterozoic crystalline basement of the southern Fennoscandian shield. The bedrock at Olkiluoto is composed of metasedimentary and igneous rocks, which have been affected by multiple stages of deformation, both within ductile and brittle regimes. Different ductile deformation events that took place between about 1.88 and 1.79 Ga ago resulted in a penetrative regional NE-SW-trending and southeast-dipping large-scale foliation and mechanical anisotropy. The anisotropy was further enhanced by partial melting of the host rock and formation of granitic-tonalitic veins, which intruded mostly into the planes defined by the large-scale foliation. Later metamorphic events resulted also in the formation of massive, coarse-grained pegmatitic granites, which occur both parallel to the plane of the anisotropy and in orientations discordant to this (see Figure 6). A total of four separate deformation phases have been identified in the Olkiluoto area and each of these phases is characterised by unique deformation structures and intensity of the deformation phases, which are strongly controlled both by the rheological properties and composition of different bedrock units and the past tectonic stress regimes. Due to this long-lasting and complex multiphase evolution, the bedrock in Olkiluoto is both heterogeneous and anisotropic from the microscale to the mesoscale, and the mechanical properties of the bedrock therefore exhibit significant variability at different scales (Aaltonen *et al.*, 2016).

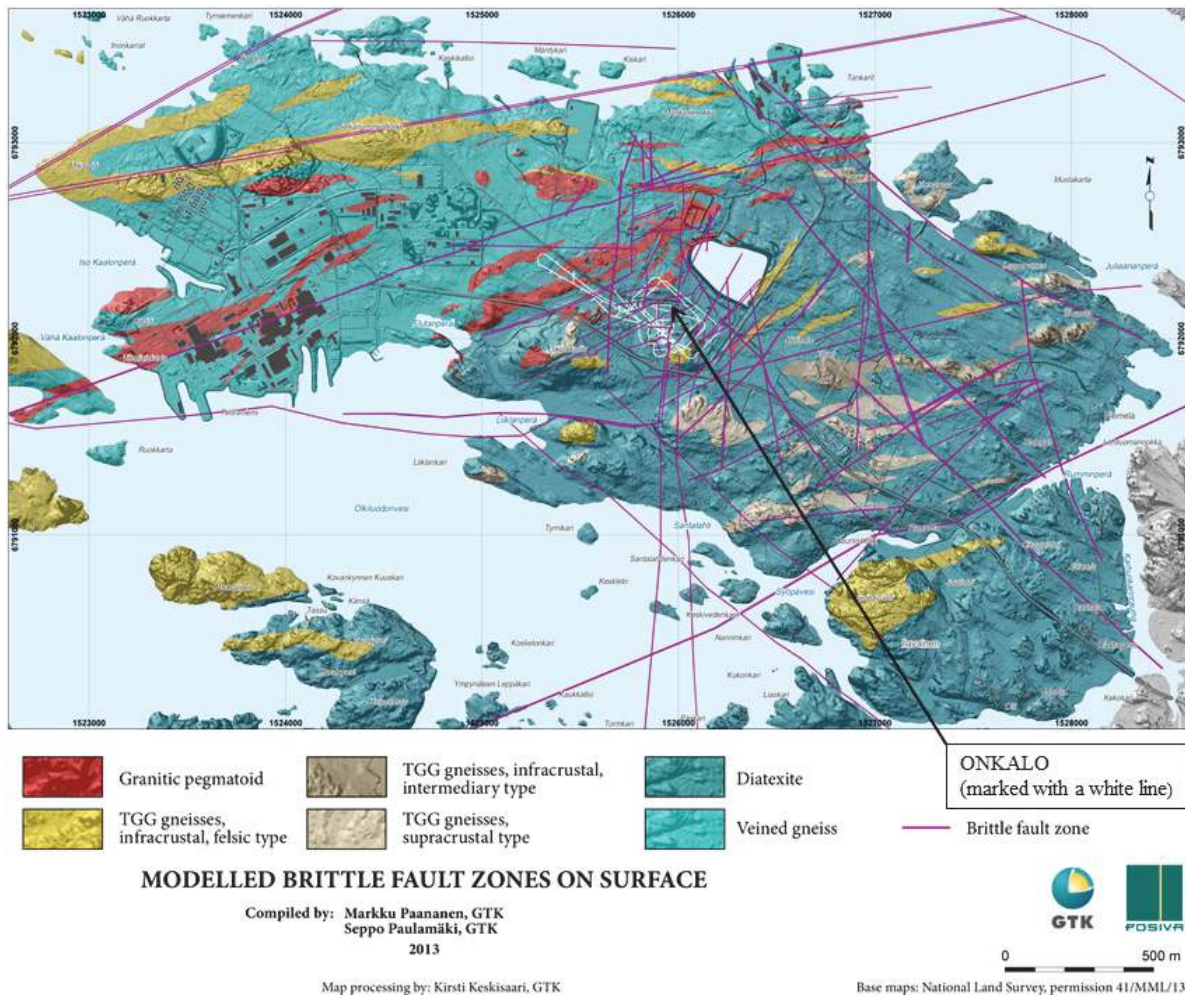


Fig. 6: Bedrock map of Olkiluoto with ONKALO facility included. (Modified from Aaltonen *et al.*, 2016)

Olkiluoto Island is also intersected by fault zones of different scales. The main brittle fault zones at Olkiluoto can be broadly subdivided into three different geometric populations: low-angle thrust faults dipping generally to the SE, subvertical strike-slip faults that strike N-S to NE-SW, and subvertical strike-slip faults that strike in the E-W direction. Out of these groups of fault zones, the low angle fault zones are the most prominent ones and typically follow the main anisotropy planes formed during the main ductile deformation event. These faults typically have surface areas from several square kilometres to tens of square kilometres and reach depths of several kilometres. The subvertical faults, on the other hand, can be described as subordinate, having smaller surface areas and being mostly discordant with the general anisotropy of the bedrock. Occasionally the N-S to NE-SW striking subvertical faults do however overprint narrow mylonitic shear zones, formed at later stages of ductile deformation and crosscutting the main anisotropy. The low angle faults at the island are also the main conduits for groundwater flow which may be explained by their more continuous nature, well-developed architecture with breccia- and clay-bearing fault cores and damage zones forming prominent flow paths, and optimal orientation with respect to the present day stress regime. These zones are also potential hosts for earthquakes. Consequently, the main low angle zones are classified as critical structures and their locations guide the planning of the repository layout (Fig. 7). The main critical structures of the island are the low-angle fault zones labelled as BFZ20a and BFZ20b (both combined in Fig. 7 as Zone 20CV2 including

also their hydrological effect area and respect distance to tunnels), which intersect the access tunnel of the ONKALO facility and the shafts at a depth of approximately 300 m (see Fig. 11 and Fig. 12).

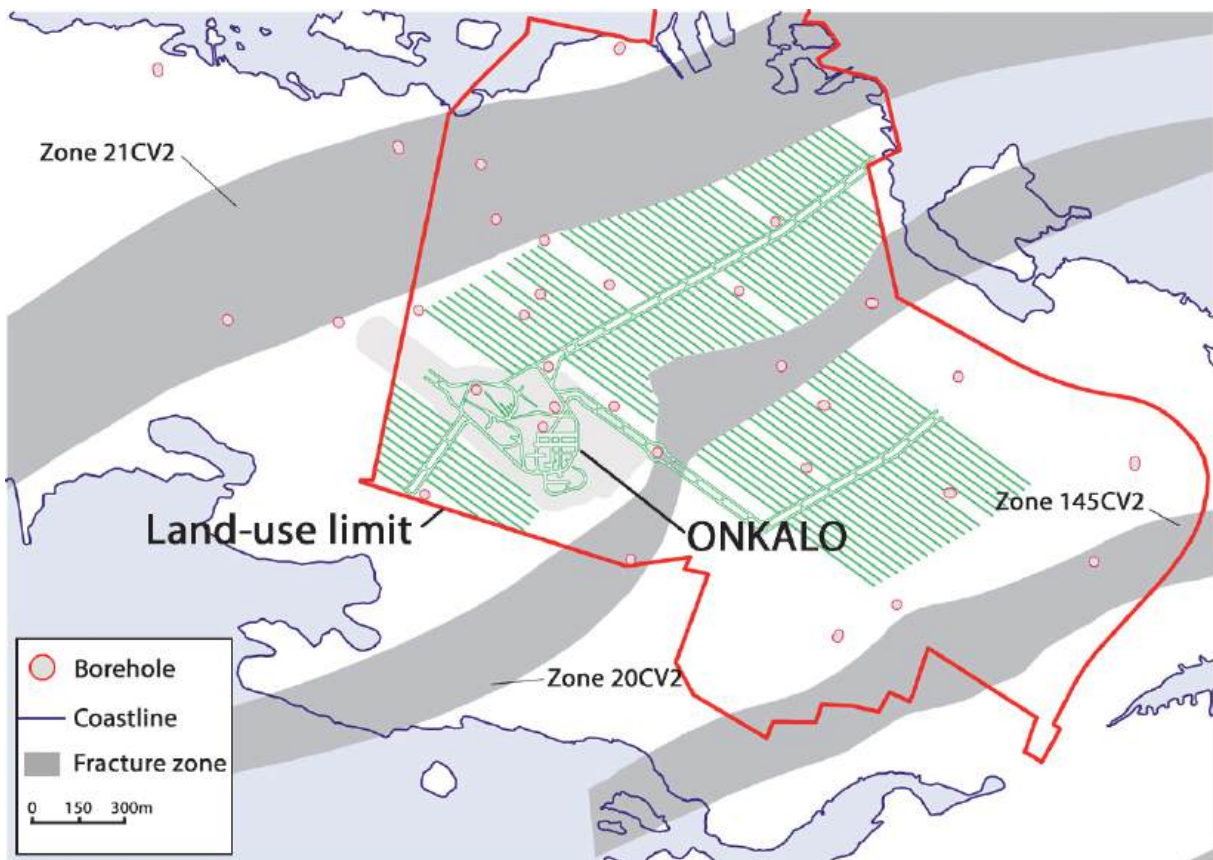


Fig. 7: Main critical structures and the volumes they cover (grey areas) of Olkiluoto Island which steer the planning of the repository layout. Surface boreholes, to be avoided during the construction of the repository facility in order not to form additional connections to ground surface, marked with red/grey circles.

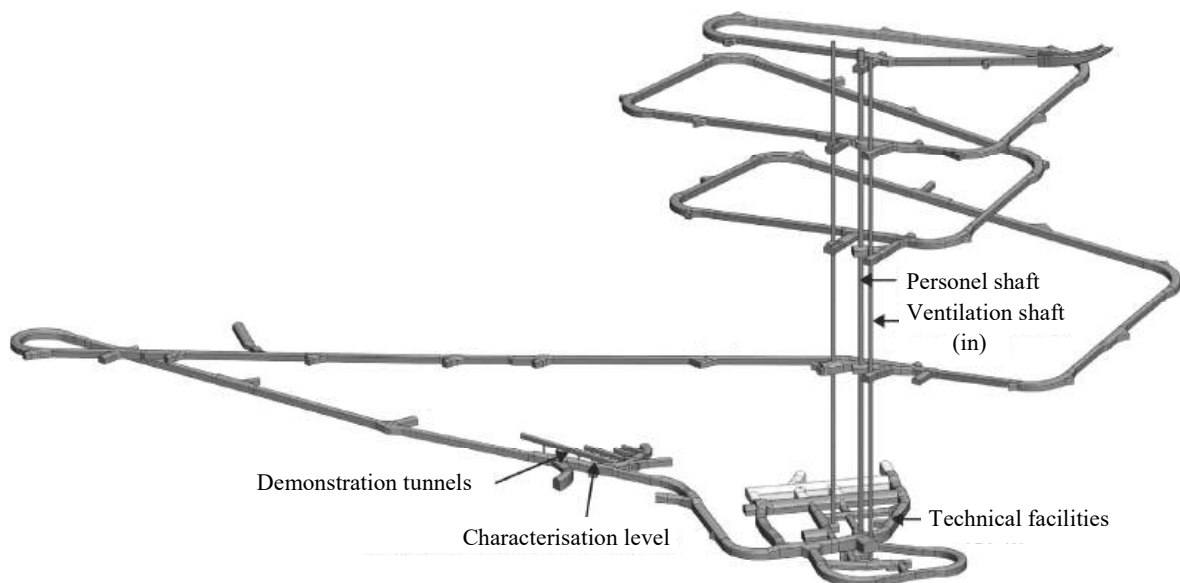


Fig. 8: ONKALO underground research facility from SW direction with notable locations within the facility marked.

The ONKALO facility, constructed in the central part of Olkiluoto Island, consists of an access tunnel excavated to a depth of 457 m using the drill-and-blast method (Fig. 8). The facility also includes three raise-bored shafts (one personnel shaft Ø 4.5 m and two ventilation shafts Ø 3.5 m) which each extends down to a depth of 450 m. Technical components of the repository facility have been excavated at a depth of 437 m, while demonstration tunnels have been excavated at a depth of 420 m (Fig. 8). The demonstration tunnels are the current focus of research and development, as these include an actual size replica of the deposition tunnel and hole design. The demonstration tunnels are utilized in installation, testing and verification of the engineering barrier systems such as the canister and backfill. The demonstration tunnels also serve as a unique opportunity to develop methodologies for the process of locating suitable rock volumes for actual disposal tunnels and holes.

The ONKALO facility is surrounded by 58 diamond-cored drillholes utilized in the characterization of the surrounding rock volume (Fig. 7). During the construction of the ONKALO facility and upcoming repository, the projected locations of the surface drillholes are to be avoided in order not to form additional pathways to the ground surface. Due to avoidance of the large deformation zones during construction and strict grouting procedures, the total groundwater inflow to the whole ONKALO facility was only 32 l/min in 2016 (Posiva, 2017).

During construction of the underground facilities, geological mapping is conducted in three stages. The pilot core from each round is mapped before excavation in order to decide whether the layout should be modified. After the excavation of a specific tunnel section, a coarse "*round mapping*" is conducted as an initial means of obtaining tunnel scale data. After the installation of reinforcement to the tunnel roof, detailed geological and geotechnical mapping is conducted during which systematic fracture information is collected for further modelling purposes (Norokallio, 2015). The detailed mapping has resulted in collection of an extremely comprehensive fracture database, consisting of more than 100,000 mapped fractures both hydrologically active and inactive. Each mapped fracture is associated with tens of different attributes related to geological, geotechnical and hydrological properties such as transmissivity, roughness, etc. In addition, the trace of each fracture encountered during detailed mapping has been accurately mapped in 3D by using total stations and stored in a fracture database (see Fig. 12). In general and with respect to rock quality estimations, the average rock mass quality in general has been Good or Very Good below a depth of about 130 m (Johansson *et al.*, 2015). Poor rock quality is almost exclusively observed at locations where the ONKALO access tunnel is intersected by large scale brittle fault zones.

4 Rock stress regime in Olkiluoto

During the disposal site selection and the early phases of the ONKALO investigation facility excavation, rock stress in Olkiluoto was measured in multiple boreholes using various techniques, mainly Hydraulic fracturing and Overcoring (Fig. 9). Significant scatter, however, has been apparent in the measurement results and the interpreted stress states from both methodologies have been inconsistent (Posiva, 2013). Semi-integration which combined the most reliable hydraulic fracturing and overcoring measurement data resulted in mean values for horizontal stress magnitudes and their orientations, but did not reduce the significant uncertainty of either (Ask, 2011;

Posiva, 2013). This may have resulted from oversimplified data grouping and the assumption of linearity.

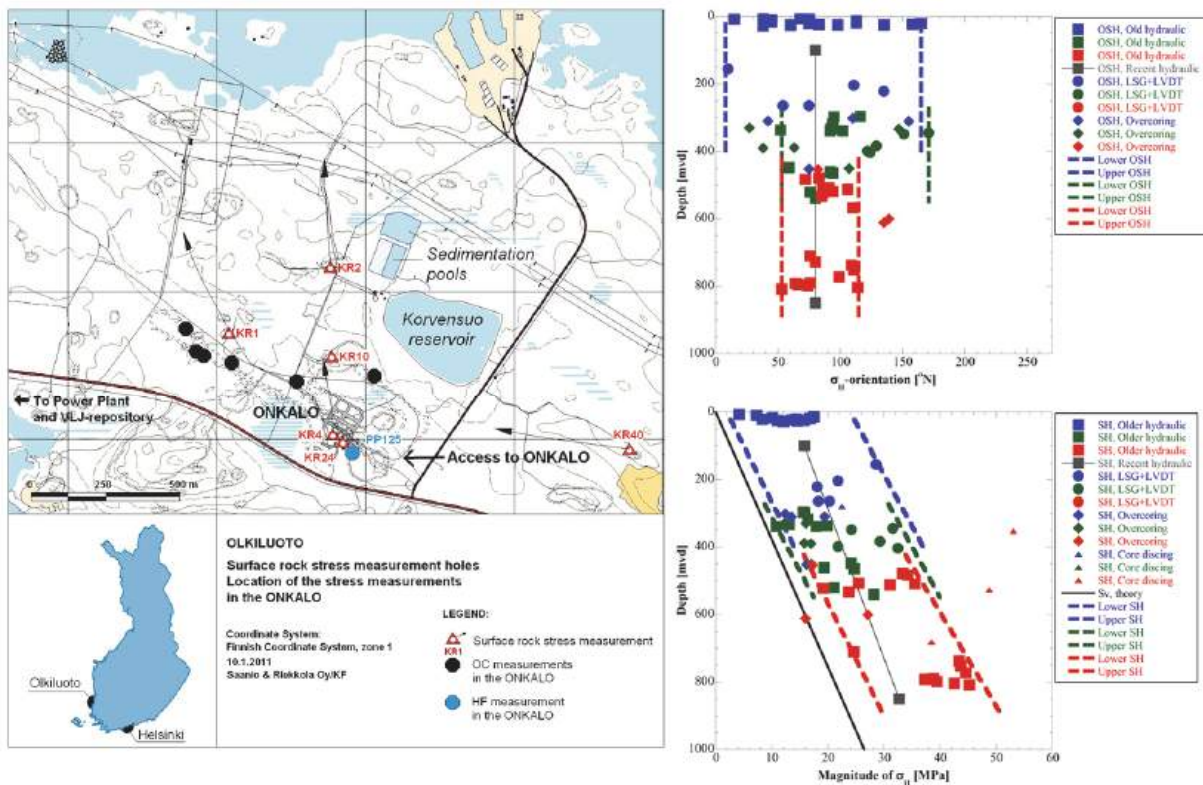


Fig. 9: Measurements and understanding of rock stress state at Olkiluoto from 2011. On left: Map of the Olkiluoto site, showing the location of ONKALO where the stress measurements were carried out in 2011. Upper right: Measured major principal stress directions vs. depth. Lower right: Measured major principal stress magnitudes vs. depth. (Posiva, 2013)

This led to the development of the LVDT cell, which is able to overcome the issues encountered with traditional borehole based stress measurement techniques, such as formation of en échelon fractures during hydraulic fracturing or debonding of strain gauges during overcoring, in addition to chemical constraints issued on foreign materials allowed to be used within the repository spaces. The measurement method does, however, require a pre-existing underground space as measurements are executed from the surface of an existing tunnel. As a result, LVDT measurements could only be performed as ONKALO excavations progressed. The LVDT cell is a two-dimensional overcoring device that measures four diametrical convergences caused by full or partial stress release (Fig. 10). The LVDT cell is designed to measure the secondary stress state. The solution of the *in situ* stress state is achieved by performing a numerical inversion of the LVDT results, in which the stress perturbation caused by the tunnel geometry is taken into account assuming a continuous, homogeneous, isotropic and linearly elastic (CHILE) material. Transverse anisotropy or orthotropy can also be applied in the inversion.

A typical LVDT measurement hole is generally short at about 1 m in length, provided the excavation damage zone or ring disking is not encountered i.e. rock conditions do not require a greater hole depth. Experience suggests a measured hole length of greater than 500 mm from the excavation surface is generally sufficient (Hakala *et al.*, 2012). One of the main advantages of the LVDT method is that drilling can be

performed with a compact drill rig enabling measurements in limited spaces such as shafts. The main improvements of the new method are the large measurement hole diameter which minimizes the vulnerability to small scale rock heterogeneity and a mechanical mounting system which eliminated glue related problems such as debonding, drifting and long curing times. In high stress states, partial stress release can be achieved reliably by means of sidecoring, for instance when ring dinking is encountered during overcoring. Since the development of the LVDT method, stress measurements with the LVDT cell have been continuously conducted in ONKALO, coupled with the progression of tunnel excavation to new areas such as deposition panels (see Fig. 11 and Fig. 12).

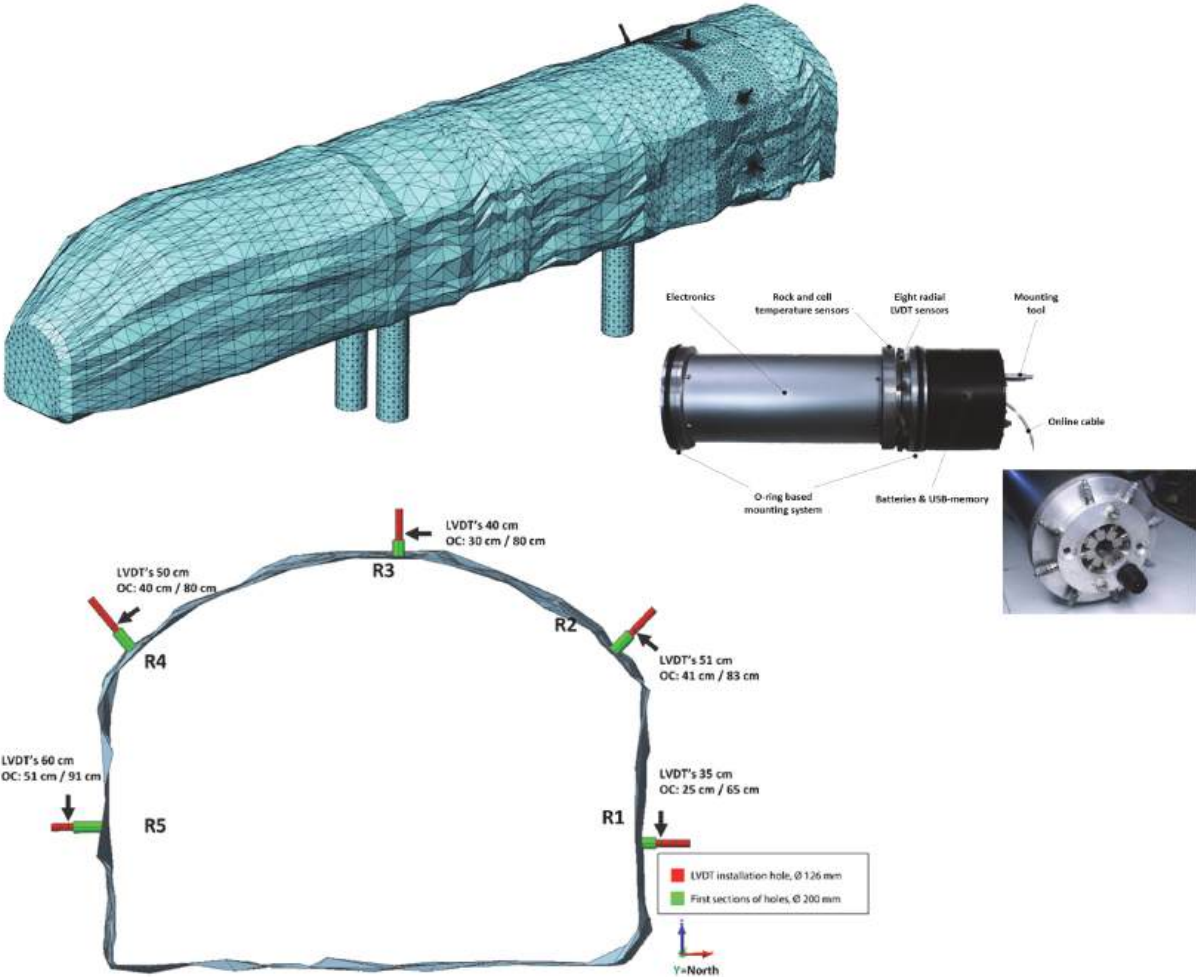


Fig. 10: Rock stress measurement using LVDT method at the rock mechanics investigation niche chainage 61 m and photographs of the LVDT cell.

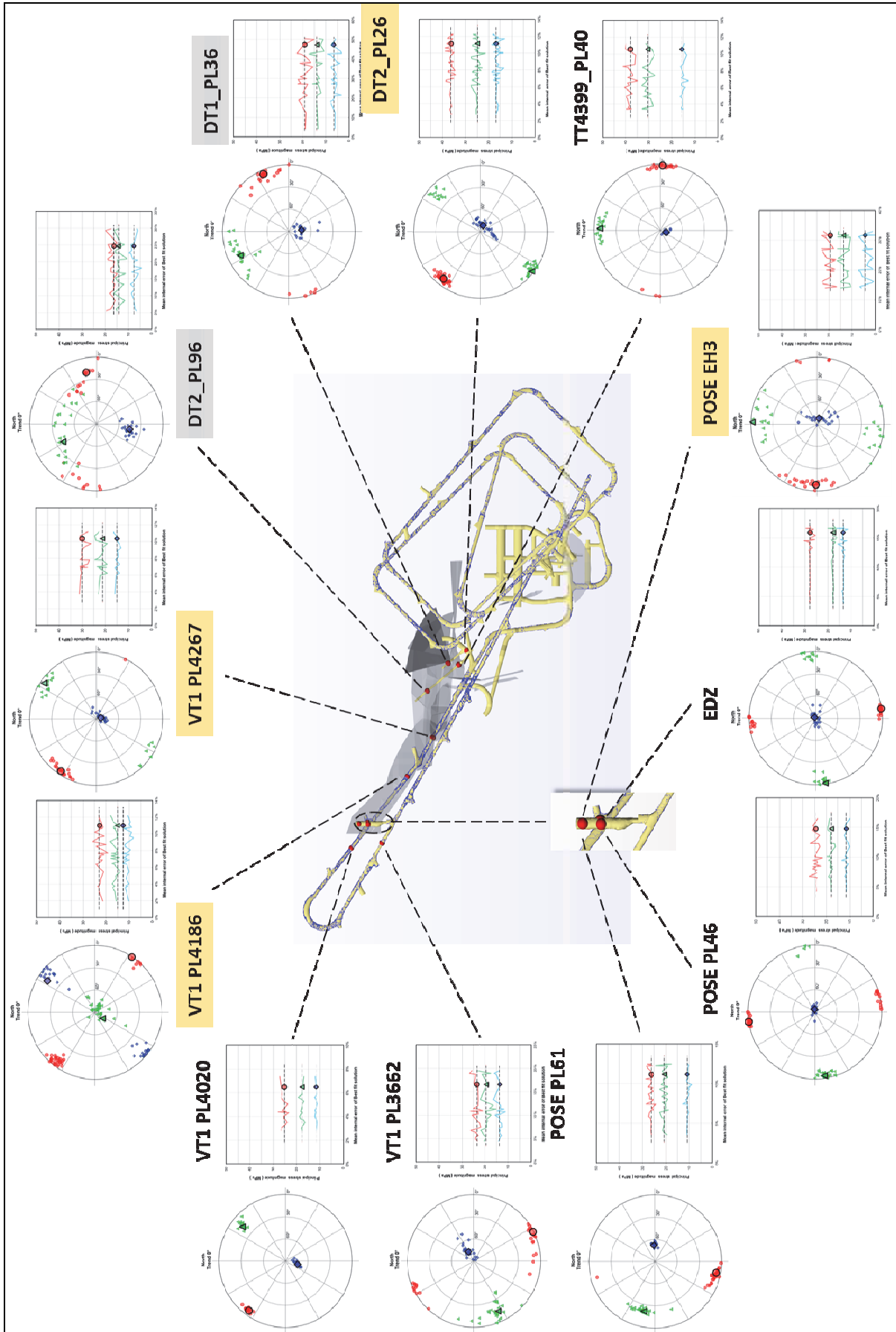


Fig. 11: LVDT measurement results along ONKALO access tunnel with known BFZ's intersecting the tunnel. Unreliable measurements in grey and measurements close to BFZ's in orange. (Hakala *et al.*, 2017)

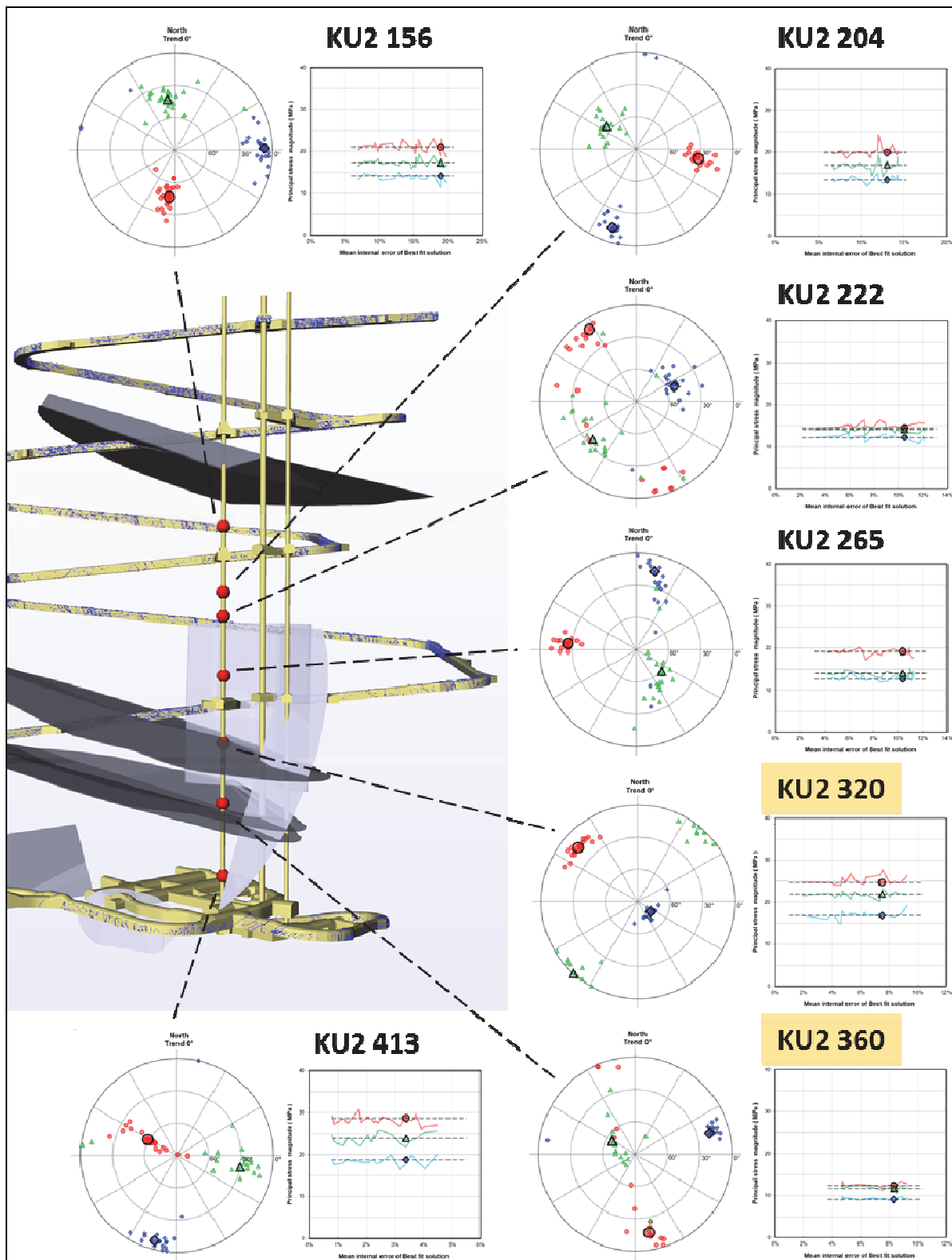


Fig. 12: LVDT-cell measurement results at different locations along ONKALO shaft. Major BFZ intersection marked with light blue, mapped fracture traces in tunnel walls as dark blue (Hakala *et al.*, 2017).

The combined results of the LVDT cell measurements (see Fig. 13) indicate that the principal component of the rock stress tensor at Olkiluoto is oriented NW-SE, which agrees with the ridge push force orientation of northern Europe (see Heidbach *et al.*, 2008). The stress state within the ONKALO facility is highly variable, in terms of both stress magnitude and orientation, as the stress state is affected by intersections of

large brittle fault zones (BFZ's) (see also Valli *et al.*, 2016). The principal stress magnitudes and orientations according to the current interpretation of the LVDT measurements at the deposition depth (400 to 425 m) are: $\sigma_1 = 30.7$ MPa ($300^\circ / 8^\circ$), $\sigma_2 = 23$ MPa ($031^\circ / 12^\circ$) and $\sigma_3 = 17.8$ MPa ($177^\circ / 75^\circ$) (Hakala *et al.*, 2017). An important observation is that the principal stress components deviate from the vertical and horizontal axes.

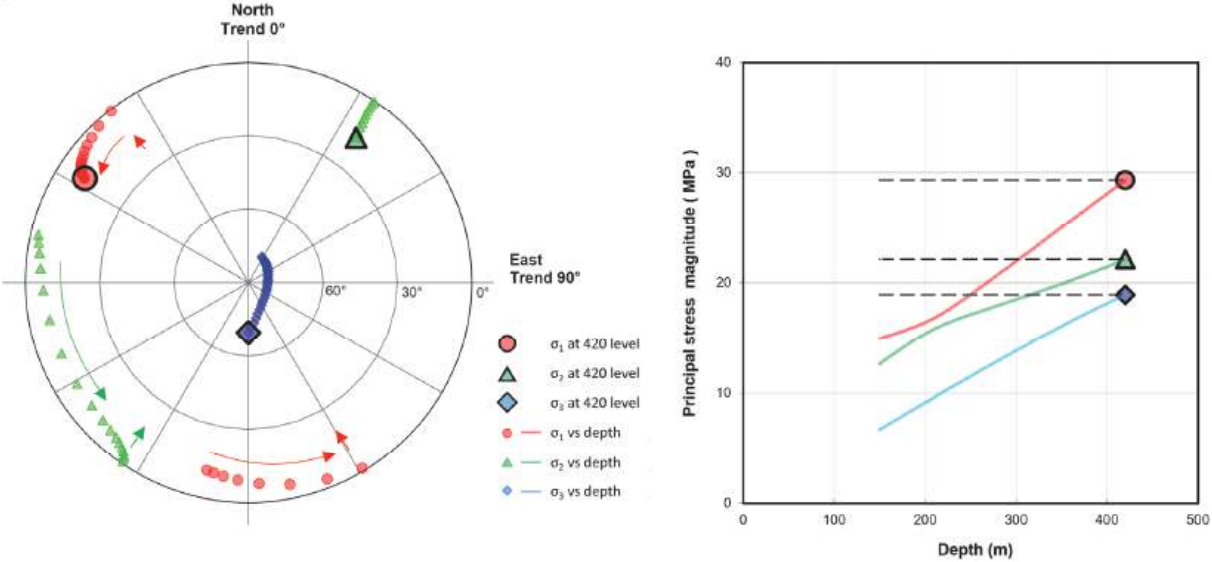


Fig. 13: The ONKALO area *in situ* principal stress component orientations and magnitudes as a function of depth from the 150 m level to the 420 m level (Hakala *et al.*, 2017).

The recent LVDT based results have provided a stress model that indicates a stress state that varies with depth that is most likely influenced by brittle fault zones and as such better explains the scatter previously observed in the semi-integration stress interpretation (Tab. 1). The LVDT cell has been proven to reliably measure the local rock stresses even in very complex and heterogeneous geology such as encountered at Olkiluoto, where measurement success with other existing methods has been poor (Hakala *et al.*, 2017).

Tab. 1: A comparison of LVDT-measurement based stress interpretation with semi-integration results (Ask, 2011) at deposition depth level, 420 m below the ground surface (Hakala *et al.*, 2017). Note that the presented stress state is transformed to horizontal - vertical planes e.g. (σ_H , σ_h , σ_v) for comparison.

LVDT Stress interpretation	σ_H (MPa)	σ_H trend ($^\circ$)	σ_h (MPa)	σ_h trend ($^\circ$)	σ_v (MPa)
LVDT: deposition depth	30.5	118	22.7	208	18.3
Min	27	102	19	192	12
Max	35	143	26	233	24
Semi-integration (Ask, 2011)					
Mean	23.4	112	15.6	202	10.1
Min	13.5	53-171	9.6	143-261	10.1
Max	35.6	53-171	23.6	143-261	12.2

5 Rock strength in Olkiluoto

In the geological concept of nuclear waste disposal, the *in situ* stress state along with rock mass strength are key factors when estimating the extent and severity of potential stress-induced damage at the disposal facility. *In situ* rock mass strength can be estimated from conventional rock mechanics laboratory test results such as Unconfined Compressive Strength (UCS) tests when combined with estimated maximum near-field tangential stresses around underground openings. Previous investigations and research in Canada and Sweden of the rock mass response given a particular geometry, rock strength and *in situ* stress state were studied for applicability at Olkiluoto.

A significant amount of research and experiments were completed at Atomic Energy of Canada Limited's (AECL's) Underground Research Laboratory (URL), located approximately 120 km NE of Winnipeg, Manitoba, Canada within the Lac du Bonnet granite batholith near the western edge of the Canadian Shield (Read, 2004). During approximately 20 years of research, several large-scale *in situ* rock mass response experiments were conducted including the Mine-by Experiment, borehole breakout studies, the Heated Failure Tests (HFT), the Excavation Stability Study and the Tunnel Sealing Experiment (Read, 2004). By matching observations and measurements with back-analysis results, the *in situ* progressive failure mechanism and rock mass strength were determined. The *in situ* strength was, however, determined to be linked to lithology to a degree as coarser-grained granitic rock with heterogeneous grain structure was more prone to spalling than finer-grained granodioritic rock with more equigranular grain structure. Additionally, compared to the Olkiluoto site, the *in situ* stress magnitudes at the URL in Canada were much higher at 60 / 45 / 11 MPa for σ_1 , σ_2 and σ_3 , respectively (compare to Tab. 1). Finally, a multitude of other factors were found to influence the probability of breakout or spalling, with the stress path experienced by the rock mass and local tangential stress gradients being critical factors. The minimum spalling threshold was found to be about $0.59\sigma_c$ for granite (i.e., about 125 MPa) based on the HFT results, which involved a thermomechanical effect similar to that expected during the lifespan of the final deposition of spent nuclear fuel.

The HFT also served as a template for the Äspö Pillar Stability Experiment (APSE), conducted at the Äspö Hard Rock Laboratory (HRL) located north of Oskarshamn in Sweden. This experiment was conducted in a heterogeneous and slightly fractured rock mass, somewhat similar to the rock mass at the Canadian site. The rock type was largely diorite, with some local pegmatite and mylonite. The experiment involved the excavation of two adjacent 1.75 m diameter vertical boreholes, oriented nearly orthogonal to the orientation of the maximum principal stress (Andersson, 2007). In comparison to the AECL site, the stress magnitudes at the experiment depth of 450 m were much lower (50 %) than those observed at the URL. Consequently heating was used to induce failure, with spalling occurring at about $0.59 \pm 0.03\sigma_c$ for the Äspö diorite (Andersson, 2007; Martin & Christiansson, 2009).

As a result, Posiva's Olkiluoto Spalling Experiment (POSE) was designed and planned using the previous experiments as a template. The experiment was also planned to replicate the thermal stresses imposed by the excess heat from a spent nuclear fuel canister while also functioning as a Prediction-Outcome (P-O) exercise. Additionally, the experiment was planned to define the *in situ* stress state and spalling strength of the migmatitic gneiss at the Olkiluoto site (Hakala *et al.*, 2015).

Particularly the latter two objectives were of importance, as the applicability of the assumptions regarding rock failure mechanism or spalling strength from comparative sites was uncertain without verification *in situ* for the geological conditions of Olkiluoto.

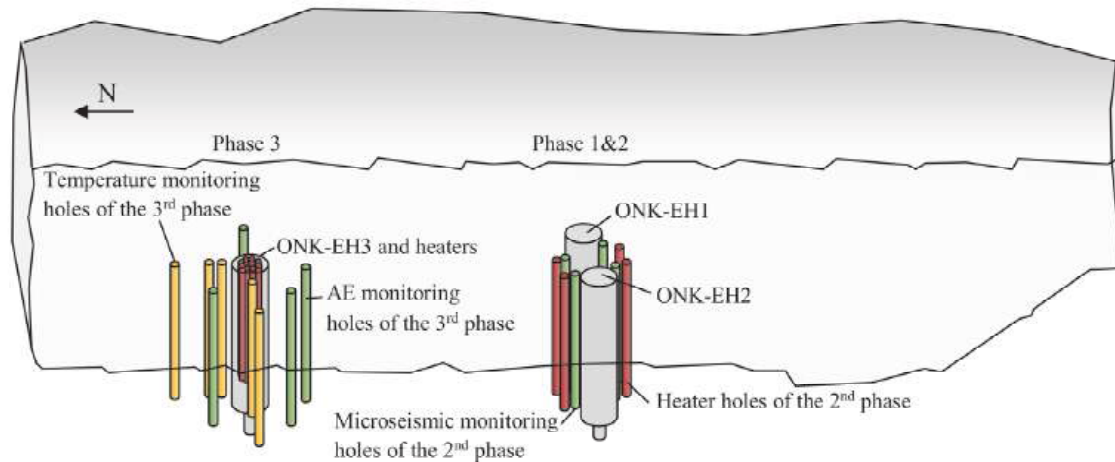


Fig. 14: Schematic representation of POSE in the ONKALO underground facility.

POSE was executed in the POSE niche at a depth of 345 m in the ONKALO facility and consisted of three separate phases (Fig. 14 and Fig. 15). The niche was selected partly because it is located in a volume with rock conditions representative of the deposition level, and exhibits a moderately high *in situ* stress state. The stress state at the time for the niche was interpreted as $\sigma_1 = 25.1$ MPa ($166^\circ / 1^\circ$), $\sigma_2 = 17.1$ MPa ($256^\circ / 10^\circ$) and $\sigma_3 = 12.3$ MPa ($068^\circ / 80^\circ$).

Phase 1 of POSE involved boring of two adjacent 1.524 m diameter experimental holes, thereby creating a thin ~ 0.87 m pillar between them (Fig. 14). The horizontal cross-sectional axis of the pillar was rotated counterclockwise 15° to North, based on stress measurements at the time. Phase 1 was designed to induce spalling in the pillar by concentrating the maximum principal stress in the pillar.

Phase 2 of POSE was executed in the same experimental holes, and was designed to increase the tangential stresses focused in the pillar by heating the pillar externally (Johansson *et al.*, 2014). This was achieved using heater elements installed symmetrically in drillholes close to the two large experimental holes.

Phase 3 of the POSE was executed in a single 1.524 m diameter experimental hole bored at the end of the POSE niche where more isotropic geological conditions prevailed (Valli *et al.*, 2014). Phase 3 involved heating the hole internally, thereby removing any ambiguity regarding the stress state orientation by increasing the tangential stresses near symmetrically in more homogeneous geological conditions than the previous phases.

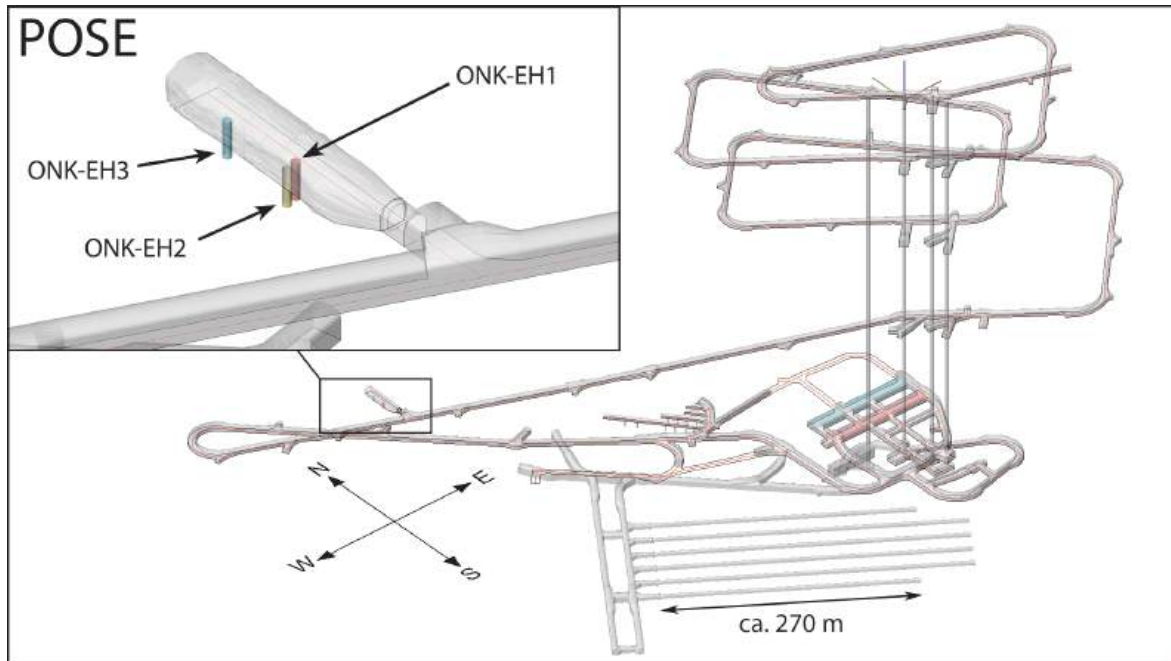


Fig. 15: The POSE niche and the experiment location in the ONKALO research facility.

The results from POSE Phase 1 were inconclusive with only three shear type fractures observed after completion of the pillar, primarily related to biotite-rich bands of foliation being sheared within the veined gneiss. The fractures did not form in the expected locations in the pillar where highest tangential stresses were expected to occur. Strain gauge monitoring results did, however, match predictions well. Phase 2 stress amplification by heating caused further damage (Fig. 16 and

Fig. 17), although it was also localized at lithologic contacts between veined gneiss and granitic pegmatoid (Johansson *et al.*, 2014). Spalling type failure, where extensile fracturing parallel to the excavation surface progresses in a localized zone, was not observed in Phase 1 or 2 of POSE. By applying forced scaling, flakes of rock to a maximum radial depth of 9 cm could be dislodged, with the scaled surface controlled largely by lithology. Finally, Phase 3 observations indicated minimal damage with 17 heating-induced fractures identified. Damage was primarily linked to shear or tensile failure of mica rich bands of foliation in the gneiss. Forced scaling performed in the third experimental hole ONK-EH3 resulted in a maximum radial depth of 7 cm.

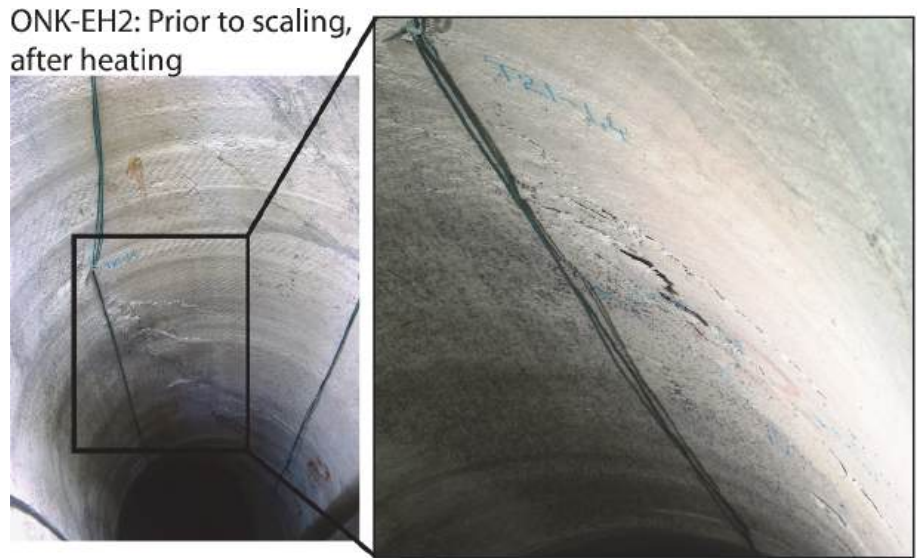


Fig. 16: Damage in ONK-EH2 experimental hole after heating, prior to scaling.

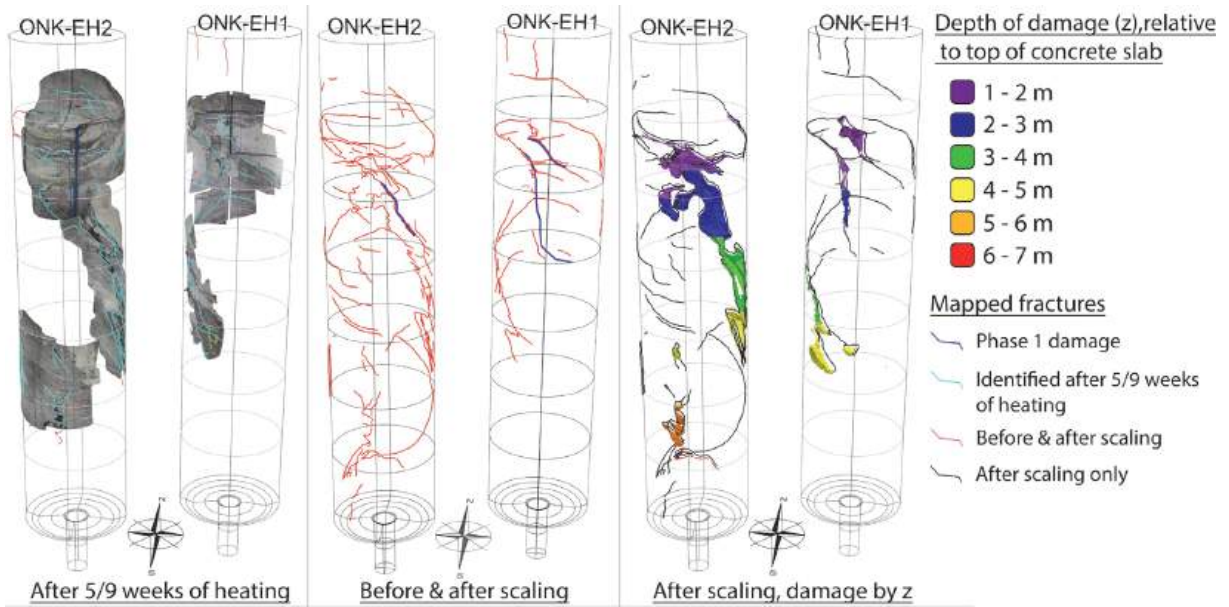


Fig. 17: Left: Partial photogrammetry constructed using photographs prior to scaling (Hakala *et al.*, 2018).

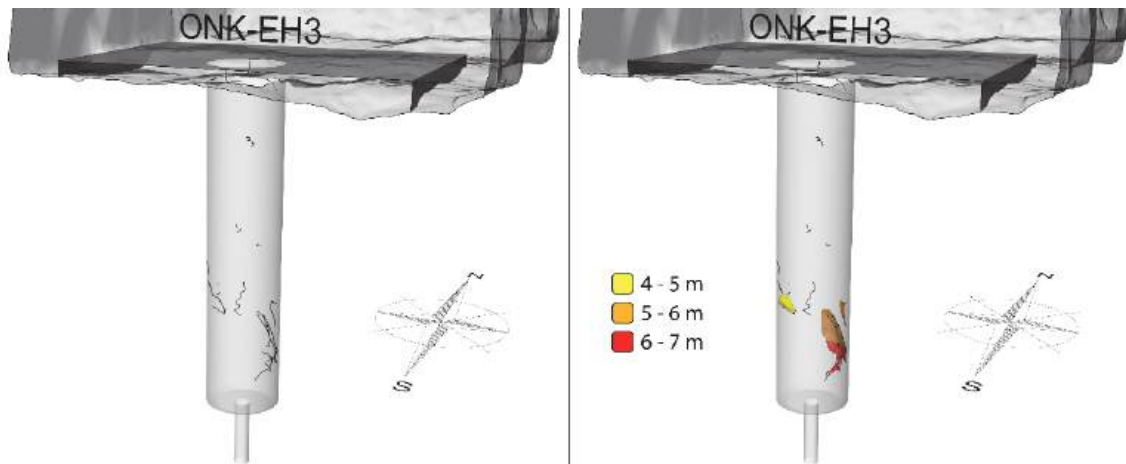


Fig.18: Observed fracturing of the POSE Phase 3 in ONK-EH3 experimental hole, viewed roughly from the south. Left: damage prior to forced scaling. Right: damage after forced scaling. Damage after scaling is coloured according to depth, measured from the top of the concrete slab. Crack damage is illustrated as black lines (Hakala *et al.*, 2018).

Back-analyses of all three phases of POSE were performed in order to understand the driving mechanisms of the observed response, as the rock response differed from the observations encountered at similar experiments conducted in Canada and Sweden. The back-analysis results were also compared to the predictions completed for all of the experiments beforehand, so as to define the key differences between predictions and experiment outcomes. Back-analyses of POSE were performed with multiple different approaches and simulation codes, although the depth of damage could be matched fairly well even with 3-dimensional discontinuum codes such as 3DEC (Fig. 19) (Itasca, 2018a). However, only a code that can simulate the formation of discrete discontinuities was able to simulate the type of damage observed during POSE. The best match between the observed experiment outcomes and back analysis was achieved with the Particle Flow Code, although due to geological complexity the model was limited to 2D (Itasca, 2018b).

Based on the POSE observations and back-analyses of the experiment, the current understanding is that a lithologically-controlled failure mechanism prevails in the ONKALO facility (Valli & Read, 2018). Given the heterogeneous geology, the *in situ* strength of granitic pegmatoid was determined to be much stronger than previously expected by means of true triaxial tests in comparison to veined gneiss (Behrestaghi *et al.*, 2016). The strength difference between the veined gneiss and pegmatoid granite causes stress concentrations to develop in the gneiss, which yields at locations where the orientation of the local maximum shear stress exceeds the shear strength of a specific foliation plane which acts as a plane of weakness (Valli & Read, 2018). This type of failure mechanism causes discrete damage in the form of individual fractures to develop, thereby limiting the likelihood of systematic rock mass failure, as the local stress state is relaxed by the shearing of the foliation surfaces. Probability of systematic rock failure is further reduced as the majority of the deposition volume has so far been determined to be gneiss where the aforementioned rock behaviour is expected to prevail.

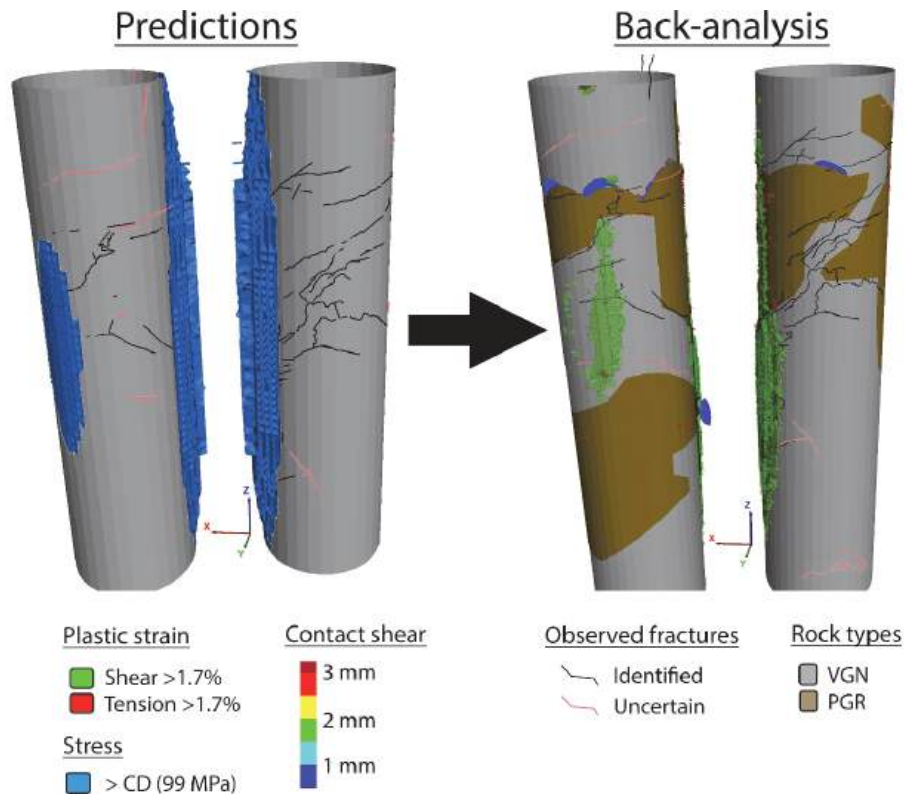


Fig. 19: POSE phase 1 & 2 prediction results vs back-analysis results viewed from the north. The damage estimate from predictions is based on the stresses that exceed the crack damage (CD) stress estimate at the time.

6 Excavation damage zone studies in ONKALO

Stress-driven rock damage and formation of an excavation damage zone (EDZ) have been identified to have a potential impact in relation to long-term safety. The damaged rock mass may change the hydraulic properties of the near-field rock mass and thereby affect compliance with the target properties of rock mass concerning limited groundwater flow and high transport resistance in the vicinity of the deposited canister locations.

Diverse methods of *in situ* EDZ studies have been carried out in ONKALO for the purposes of characterizing the properties of the EDZ occurring in geological conditions at Olkiluoto. The purpose of the EDZ studies is to validate the ability of relevant measurement techniques to establish general extent and hydraulic properties of EDZ occurring in the floor of the deposition tunnels after construction. The conducted *in situ* studies have mainly been concentrated in the POSE niche located at a depth of 345 m close to the actual deposition depth (Fig. 15). Various geophysical methods, hydraulic conductivity testing, and drill core logging in a specifically controlled study area with a size of 2 m x 9 m were conducted, during which unexpected large horizontally oriented fractures 50 to 70 cm below the tunnel floor were detected. These large fractures were observed without the typical characteristics of natural fractures found generally in Olkiluoto such as infill or shear movement in the fracture surfaces. In addition, anomalously large transmissivities $T > 10^{-5} \text{m}^2/\text{s}$ were measured in the EDZ study area in locations coinciding with the large horizontal fractures (Fig. 20).

The detailed characteristics of the fractures within the rock volume associated with EDZ studies were confirmed when part of the study area was cut out by wire sawing (Olsson *et al.*, 2015). Four blocks with a size of 1 m³ were sawed and removed from the study area (see Fig. 20) for further sectioning to 10 cm thick slabs and detailed mapping of the fracture network. The west wall of the resulting wire sawed area is presented in Fig. 21 where a large horizontal fracture (red) can be observed, located deeper than typically estimated EDZ fractures at the tunnel surface (yellow). During the detailed mapping of the wire sawed blocks, it was confirmed that the horizontal fractures do not contain any mineral infilling and do not possess other characteristics of a natural fracture, such as not following any geological features as natural fractures in ONKALO typically do (Olsson *et al.*, 2015).

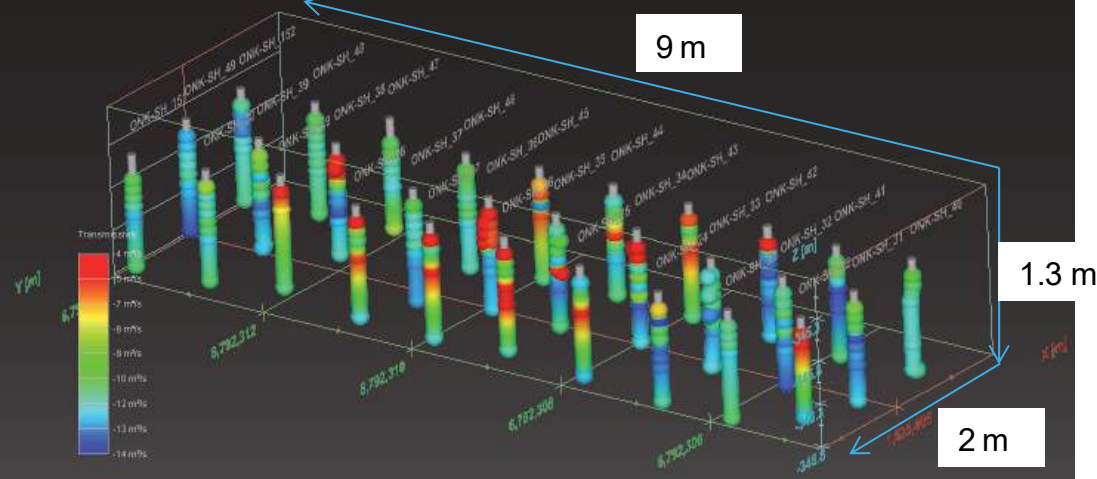


Fig. 20: 3D-visualization of measured transmissivities for each drill hole in the EDZ study field (Suikkanen *et al.*, 2016a).

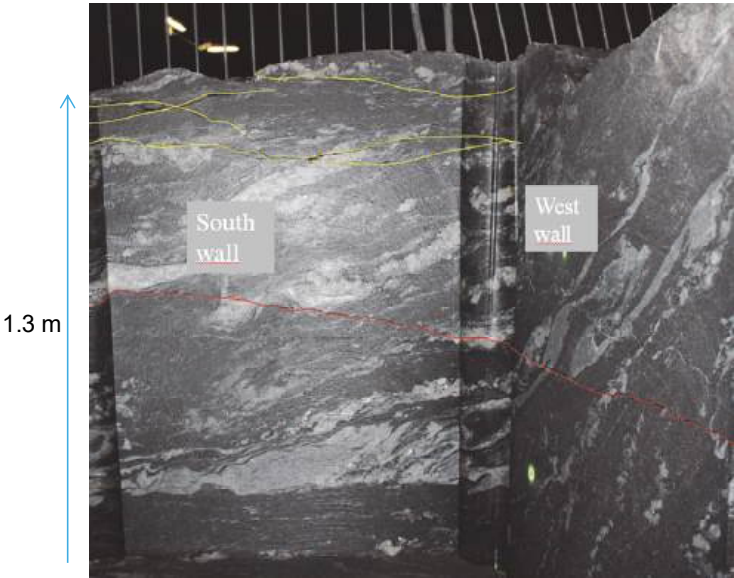


Fig. 21: A horizontal fracture characterized as EDZ_{S1} (red) and typical construction induced EDZ_{C1} fractures (yellow) below the POSE niche floor (Suikkanen *et al.*, 2016a).

A fracture network model of the EDZ study area was created based on all available information (Fig. 22), such as detailed mapping of the wire blocks, drill core observations, associated geophysical measurements, and existing lithological model

of the tunnel (Suikkanen *et al.*, 2016a). Measured flow properties from the EDZ study area could be assigned to each fracture within the fracture network model for further flow and transport models. Large horizontal fractures, estimated to develop due to re-distribution of the stress state after tunnel excavation, are presented in pink and cyan in Fig. 22.

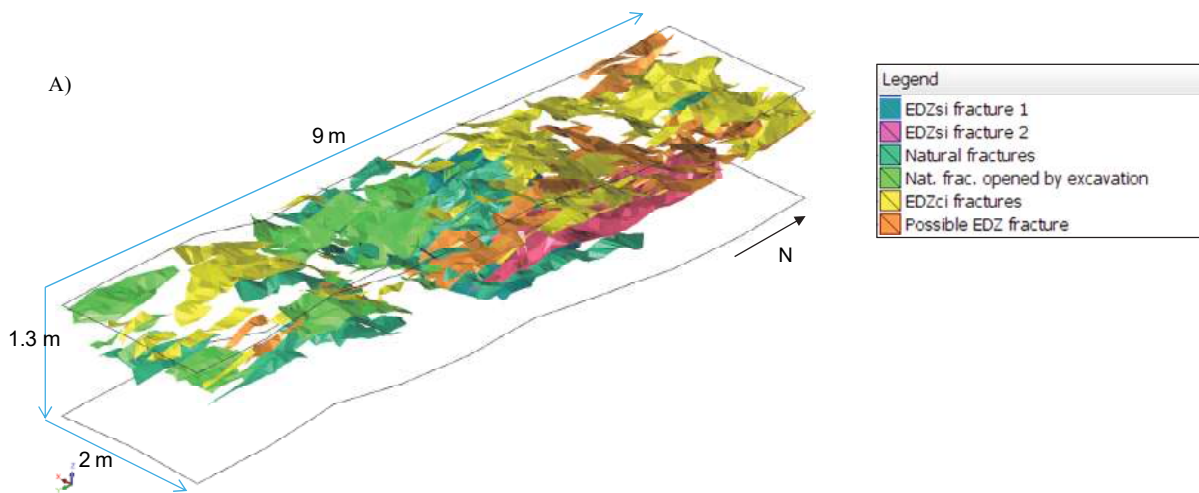


Fig. 22: Modelled fracture planes of the wire sawed area with the horizontal fracture in bluish green color (Olsson *et al.*, 2015).

The characteristics of the highly conductive horizontal fractures were studied by numerical modelling of the tunnel excavation sequence, and its effect on yielding of the nearby rock mass. The geology of the EDZ study area is mainly composed of veined gneiss (see Tab. 2 for properties). The numerical modelling was used to explore the impact of tunnel excavation on the disturbance of the EDZ study area, and whether it is possible to form large fractures at a depth of 50 to 70 cm below the tunnel floor due to re-distribution of *in situ* stress state.

Tab. 2: Material properties for the rock mechanics modelling (Suikkanen *et al.*, 2016a).

Parameter Value	Initial	Residual
<i>Young's modulus E</i>	60 GPa	
<i>Poisson's ratio, ν</i>	0.25	
<i>Uniaxial Compressive Strength, σ_{UCS}</i>	108 MPa	
<i>Crack Initiation Stress, σ_{CI}</i>	52 MPa	
<i>Indirect Tensile Strength, σ_T</i>	12.1 ± 2.9 MPa	0 MPa
<i>Initial friction angle, ϕ_i</i>	18°	63°
<i>Initial cohesion, c_i (MPa) 14.5</i>	14.5 MPa	0.1 MPa
<i>Dilatation angle, ψ</i>	7.5°	

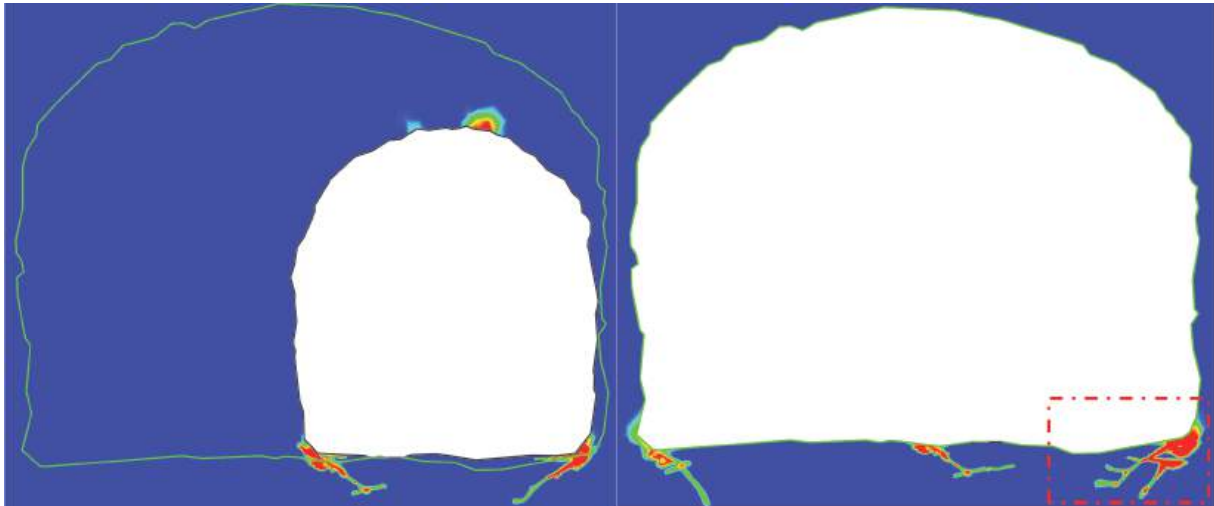


Fig. 23: Effect of ONK-TKU3620 tunnel excavation and further expansion to POSE niche geometry on yielding below the floor level (experiment location illustrated in Fig. 15). Yielded areas ranging from green to red according to severity and yielding of elements nearby. Intact rock mass presented in blue. Location of the EDZ study area marked as red box (Suikkanen *et al.*, 2016a).

The results indicate that the rock mass surrounding the deposition tunnel, and especially below the tunnel floor, is affected by yielding due to stress concentration at the tunnel corners. Yielding can occur up to depth of 70 cm at the edges of the tunnel perimeter where the large horizontal fractures were observed. Based on the multidisciplinary studies, it can be interpreted that these large horizontal features originate from the re-distribution of stress exceeding the rock mass strength, e.g. stress induced (EDZ_{SI}) Excavation Damage Zones, while the surface fracturing on the tunnel floor is more induced by the construction induced (EDZ_{CI}) Excavation Damage Zone. Backed up by the GPR (ground penetrating radar) tunnel measurements and fracture mechanics modelling from ÄSPÖ and ONKALO (Siren *et al.*, 2014) and old hydraulic conductivity measurements conducted in ZEDEX project the EDZ has led to meaningful separation of excavation damage in to two different components (Fig. 24).

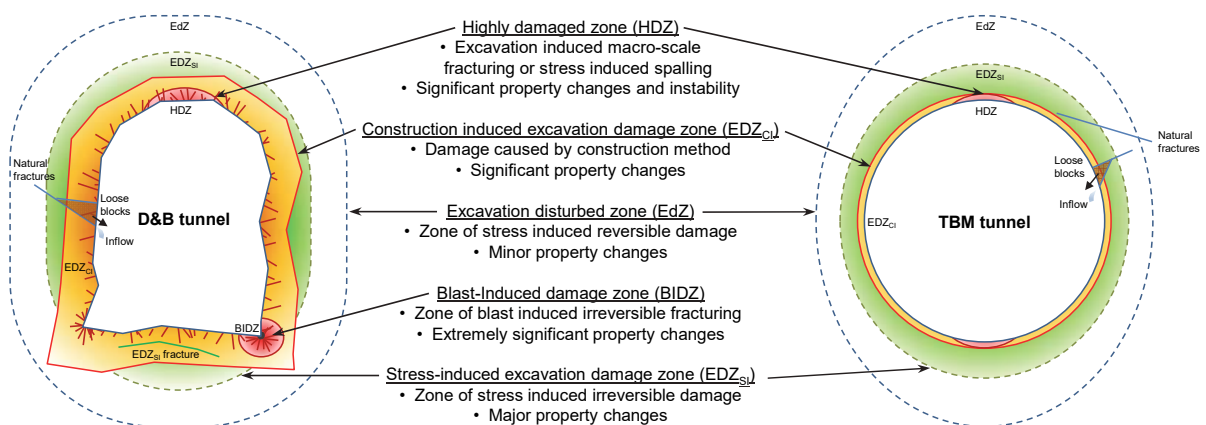


Fig. 24: Overview of the different types of Excavation Damage Zones (Siren *et al.*, 2015a).

The resulting conceptual model for the EDZ in Olkiluoto is that EDZ occurs as discrete features mainly from two separate origins with distinct properties. Small construction induced EDZ_{CI} fractures do occur in the tunnel surface to a depth of 30 cm. These EDZ_{CI} fractures can individually possess a high transmissivity but they

do not compose a hydraulically connected layer. However, large and highly conductive stress induced EDZ_{SI} fractures can be encountered up to depths of 70 cm from the tunnel floor. The EDZ_{SI} fractures are more likely candidates for forming additional pathways to natural fracture network, due to their larger dimensions and higher transmissivity if connected unfavourably.

The development of large continuous stress-induced fractures below the tunnel floor is primarily a function of the *in situ* stress state, rock strength, tunnel geometry and excavation method. Excavations with flat roof or floor geometries and sharp corners are more prone to this damage process than openings with an arched geometry (Read, 2004; Read & Martino, 2002). Besides optimization of the tunnel geometry bulkheads keyed into the rock mass can provide a cutoff in transmissivity. Several key shapes were investigated at the URL and tested at full scale as part of the Tunnel Sealing Experiment (Read, 2004), also currently in investigation by Posiva.

7 Impact of thermal stresses and glaciation on the integrity of deposition facilities

The rock mechanics research program of Olkiluoto aims to describe the initial state and properties of the host rock barrier of the repository volume to a detailed degree. The initial state of the host rock forms a basis for any forward evolution modeling of the repository system, as it represents the state of the host rock volume in which the canisters containing the spent nuclear fuel are deposited and sealed into after repository closure. Understanding the initial state of the repository system is required for constraining the uncertainty in models used to assess future evolution of the repository system. Such models of future evolution, and assessment of their uncertainties, are necessary to demonstrate the operational- and long term safety of the KBS-3 repository design during submission of the operational license application to Finnish Radiation and Nuclear Safety Authority. While the vertical KBS-3V deposition concept is selected as reference concept, lately especially the evolution of the alternative horizontal KBS-3H concept has been under further investigation.

Generally the lifespan of a final disposal facility can be divided into three distinct phases, which results in varying boundary conditions over the time period associated with long term safety analyses. In order to establish quantitative estimates of the repository rock mass stability evolution, and its impact on long term safety factors, the following phases of the repository lifespan have been studied and boundary conditions for a KBS-3H deposition drift from each phase have been derived (Suikkanen *et al.*, 2016b).

- The *construction phase*; as the rock transitions from an undisturbed state to the state after excavation of the horizontal deposition drifts there are stress re-distribution effects around the openings and drawdown of groundwater pressures. Considered as the *initial state* of the deposition drift.
- The *thermal phase*; as the radioactive decay of the fuel spent will continue throughout the entire operational time of the repository, excess heat flow into the surrounding barriers will occur (Saanio *et al.*, 2012). The heat generated by the deposited canisters will increase the temperature of the bedrock and induce thermal stresses (Fig. 25). Natural groundwater pressure levels will gradually be restored after construction, and the bentonite buffer will develop swelling pressure around the deposition drift perimeter.

- The *glacial phase*; before the radioactivity of the spent nuclear fuel decays to a safe level, multiple glaciations are anticipated in Fennoscandia. During the glacial phase, the state of stress will change as a result of the loading and unloading caused by a future ice sheet advancing and retreating over the Olkiluoto site (e.g. Fälth & Hökmark, 2014). In addition to the changes in stress, there will also be changes in groundwater pressure.

For estimating the resulting loads to a repository facility from the aforementioned phases, the three-dimensional distinct element code *3DEC*, v. 5.00 has been applied (Suikkanen *et al.*, 2016b). The consequences of the fracture growth around a KBS-3H deposition drift, and evolution of fracture network resulting from the loading, has been addressed with a two-dimensional boundary element code *Fracod*^{2D} based on displacement discontinuity method (DDM) (Shen *et al.*, 2014). The *Fracod*^{2D}, sometimes used by Posiva in back-calculating *in situ* experiments (Rinne *et al.*, 2013; Suikkanen *et al.*, 2016a; Siren, 2011; Siren, 2015b), is particularly useful when modelling fracture propagation taking in account rock anisotropy, however not very efficient for material heterogeneity and nonlinearity (Ma, 2012).

During the *thermal phase*, it is estimated that at least of 5 MPa of swelling pressure is induced by the bentonite barrier within the deposition drift perimeter providing support against the external loading. Modeling results, presenting the fracture growth in the nearfield rock of a horizontal KBS-3H deposition drift after construction, followed by the *thermal phase* and the onset of subsequent *glacial phase*, are presented in Fig. 26.

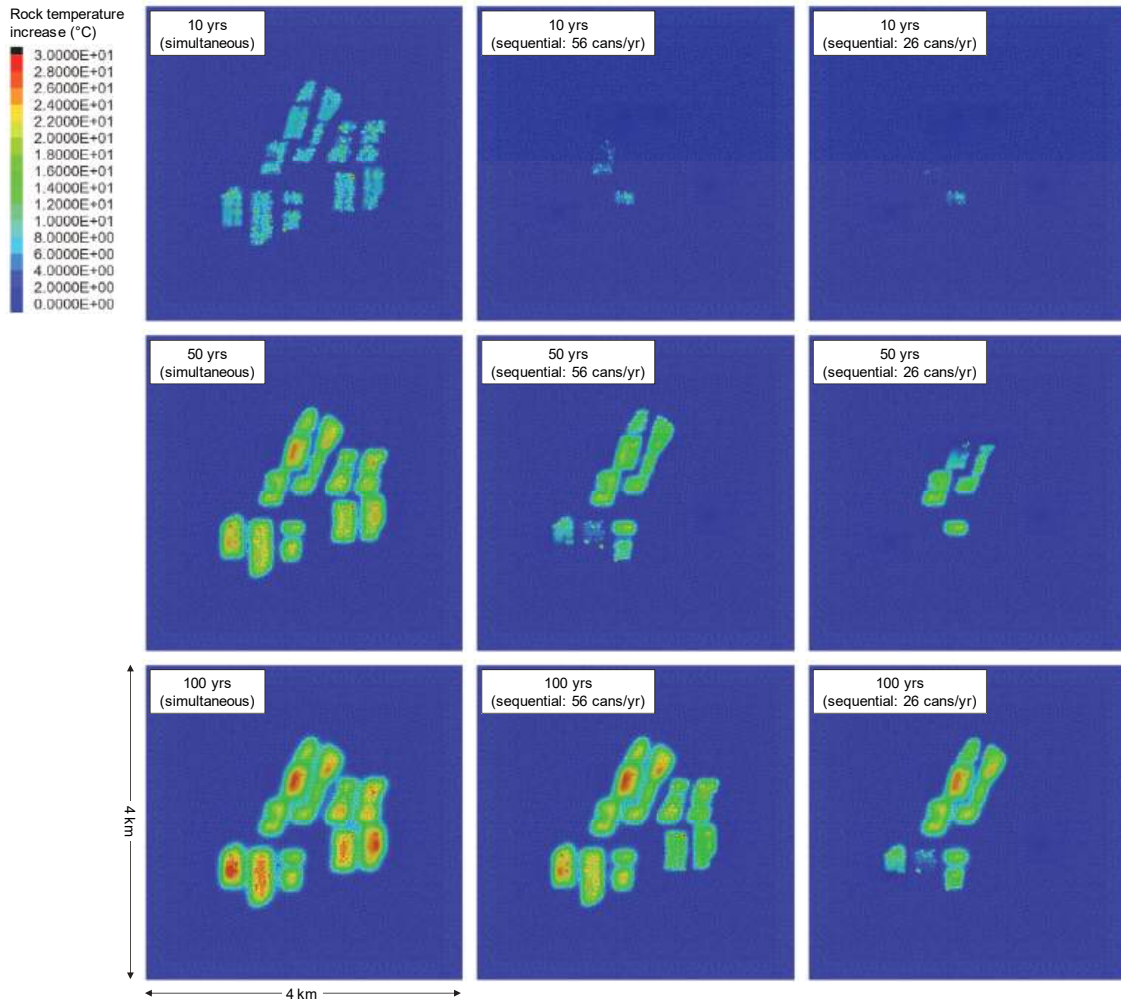


Fig. 25: Contour plots of the temperature increase of a KBS-3H repository at 25 m above deposition level (-395 m) in thermal phase. Left: Simultaneous deposition. Middle: Sequential deposition according to at a rate of 56 canisters per year. Right: Sequential deposition at a rate of 26 canisters per year (Suikkanen *et al.*, 2016b).

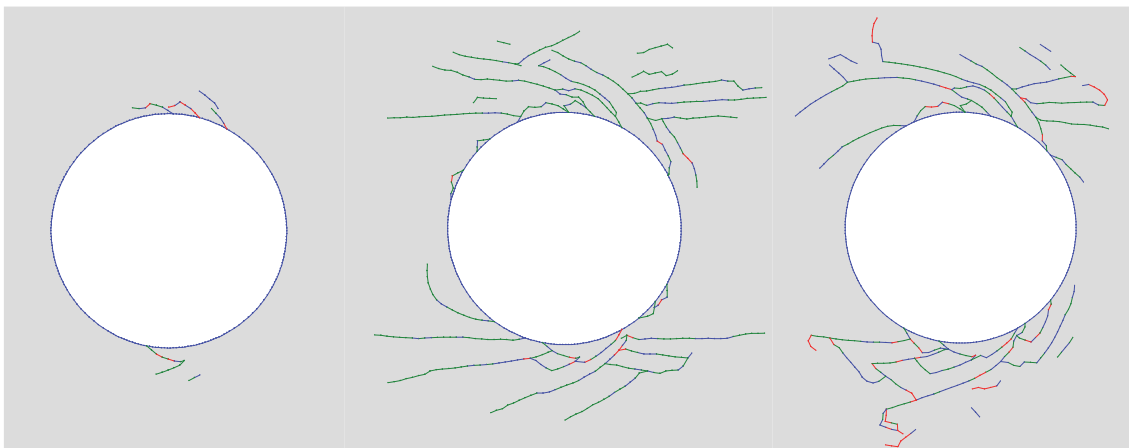


Fig. 26: Rock damage zone evolution for a horizontal KBS-3H deposition drift around the canister mid-point location during the construction phase (left), thermal phase (centre) and glacial forebulge (right). 5 MPa of bentonite swelling pressure within the drift is implemented starting from the thermal phase (centre). Fractures under tensile conditions are presented in red, fractures that have undergone slipping in green, and fractures that have not exceeded their stability (i.e., elastic fractures) in blue.

The modeling described above is meant to illustrate the general sequence of boundary conditions and possible effects on a relatively simplified rock mass in a KBS-3H configuration. As identified in POSE, the modeling codes used above have limitations in predicting fracture development in a complex geologic material. Nonetheless the identification of critical boundary conditions and relative effects of excavation, thermal loading, and glacial loading is useful for more detailed modeling using PFC. The POSE results provide a direct measure of rock mass response around vertical emplacement holes (equivalent to the KBS-3V configuration) under mechanical and thermal loading.

The rock mass in ONKALO has been observed to respond to increasing stresses by formation of new fractures in the previously intact rock mass, controlled by local geological conditions. It is mainly the properties that are a direct consequence of fracture aperture and fracture network connectivity, formed during the damage process, that have the most profound impact on long term safety targets such as increase in hydraulic conductivity and consequent decrease in transport resistance, rather than the extent of the damaged rock mass around the deposition drift. Additionally, with respect to the boundary conditions associated with different *phases* of the repository lifespan, the predicted fracture network associated with the damaged rock mass around a KBS-3H deposition drift has different aperture properties at various points in time (Fig. 27). The initiation and deformation of the fracture network around a deposition drift are a direct consequence of the varying stress states imposed on the rock barrier by the thermal stress field or loading by an ice sheet. The induced near-field stress states would be different for a vertical hole configuration.

According to the modelling conducted, the near-field stress state around the deposition drifts of a KBS-3H repository reaches a maximum tangential stress magnitude during the early period of the *thermal phase* due to the rapid stress increase caused by the differential thermal expansion of the rock mass from the canister heat flow. Rock strength in various locations is likely to be exceeded during this period, causing a fracture network to grow around the deposition drifts (Fig. 26). The swelling pressure induced by the clay barrier is not able to negate the formation of a fracture network around the deposition drift during the *thermal phase*. However, individual fractures of the damaged rock mass are closed, and their aperture is reduced, due to compressive stress state induced by the thermal expansion of the rock mass and swelling pressure of the clay barrier combined (Fig. 27). Ultimately, the fracture network initiated during the *thermal phase* is reactivated during the *glacial phase*, when effective normal stress (σ'_n) of individual fractures is decreased resulting in increased apertures (Fig. 27). The models presented by Suikkanen *et al.* (2016b) do not take into account the lateral connectivity of the damaged rock mass over large drift lengths due to the 2D nature of fracture mechanics approach, thus the model results can only be used to interpret the general behavior of the deposition facilities.

Observations from the *in situ* experiments conducted in ONKALO have indicated that the rock mass damage at the deposition scale occurs as discrete and discontinuous features, constrained by local geological conditions, even under high magnitudes of thermal stresses (Fig. 16 & Fig. 17). These observations suggest that the modeling results described above are not representative of observed conditions. This points to the importance of incorporating sufficient geological realism in models, and incorporating codes that are

able to bridge the transition from continuum to discontinuum behavior. The use of *in situ* experiments such as POSE conducted near the actual repository depth is invaluable in validating the results of predictive models, and in confirming if observations from other settings in Canada and Sweden regarding spalling and progressive failure of the rock mass are realistic outcomes at ONKALO.

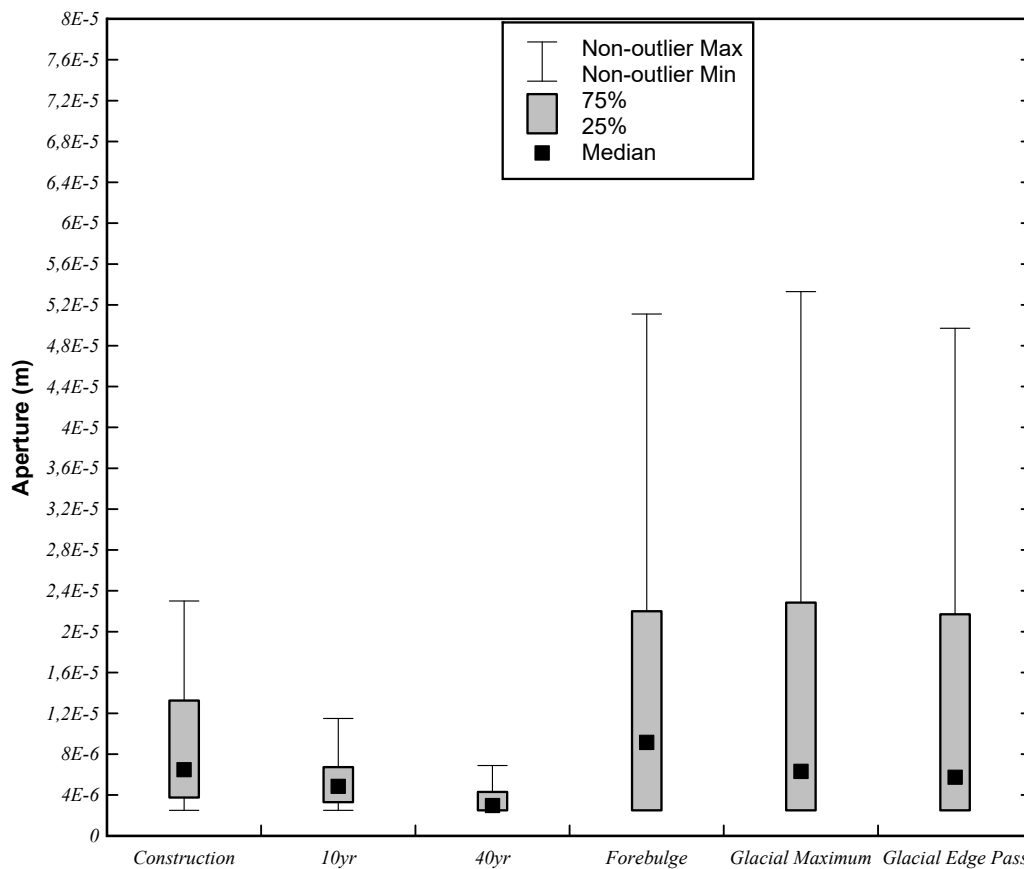


Fig. 27: Evolution of fracture aperture associated with damaged rock mass around KBS-3H deposition drift, based on the modelling results presented in Fig. 26. 5MPa of bentonite swelling pressure is assumed to develop within the deposition drift starting from 10 years (10yr) after the construction (Suikkanen *et al.*, 2016b).

8 Conclusions

Posiva Oy has developed its expertise for decades aiming for the objective of safe management of spent nuclear fuel of its owner companies. The construction of the onsite rock characterization facility ONKALO has enabled execution of direct *in situ* experiments, and development of different investigation tools for repository site characterization. All observations made during the development and execution of various *in situ* experiments at ONKALO have provided valuable information for the Olkiluoto repository site characterisation, thus increasing confidence in the ongoing site descriptive modelling. The ongoing test within the demonstration facilities will be used to confirm the design, construction and installation of various components associated with the final disposal process of spent nuclear fuel.

Based on semi-integration results of mostly surface stress measurements and the development of the new LVDT cell technique, results suggest that the principal component of the rock stress tensor in Olkiluoto is oriented NW-SE, which agrees with ridge push force orientation of northern Europe. The stress measurement results

show that important geological features have significant influence on the magnitudes and orientation of principal stresses – the brittle failure zone BFZ20 crossing the ONKALO domain alters the regional stress state and affects to some extent the near-field stress conditions around currently excavated tunnels at the disposal depth (Fig. 11 & Fig. 12). However, a clear thrust fault regime is present at the disposal depth of 420 m. The maximum far-field *in situ* stress ratio of 2:1 between the major- and minor principal stress magnitudes prevails at Olkiluoto Island. Consequently, the ambient stress conditions result in more uniform near-field stress conditions around underground openings compared to other analogous sites (e.g. AECL's URL with a 6:1 stress ratio). In addition, the stress magnitudes are lower compared to analogous sites in Canada and Sweden.

During the execution of *in situ* rock mass strength tests in Olkiluoto, the gneissic rock mass was observed to develop macroscopic damage through the generation of structurally-controlled failure planes instead of systematic progressive spalling type failure observed elsewhere. The low *in situ* stress ratio and associated peak tangential stress around underground openings is not sufficiently high to systematically exceed the prevailing rock strength. In locations of geologically constrained weaknesses, the difference in strength and deformation properties between the veined gneiss and pegmatoid granite causes strain localization in the gneiss. Damage occurs only at locations where the orientation of the local maximum principal stress results in a shear stress that exceeds the shear strength of a specific foliation plane which acts as a plane of weakness. Shearing of the foliation surfaces also relaxes the stress state and limits the extent of damage.

As a consequence of the failure mechanism focusing on structurally weak locations, the expected failure, the observed damage depth and extent in the underground openings in Olkiluoto repository conditions are relatively limited compared to observations from analogous sites. As seen in Fig. 28, the potential for strain burst and spalling at Olkiluoto is very low owing largely to the relatively low ratio of compressive to tensile strength of Olkiluoto rocks. Thus, failure processes are different compared to Äspö HRL's low potential for spalling, occurring only in heating experiments where the stress state was amplified beyond the point of failure, and to AECL's URL's very high spalling potential, with spalling occurring after excavation on tunnel surfaces under ambient temperature conditions, and amplified by heating.

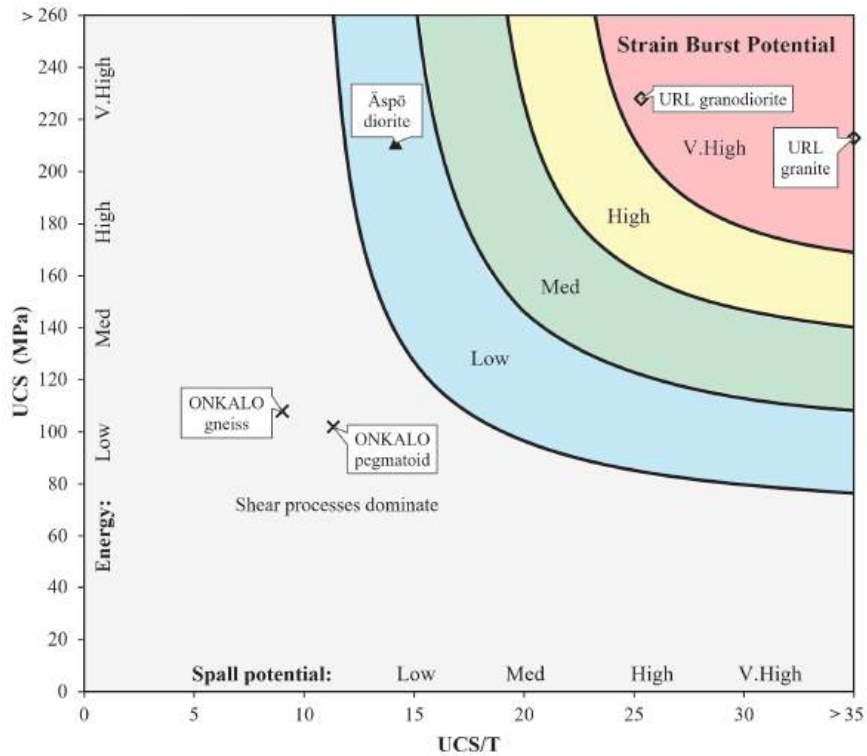


Fig. 28: Potential for spalling failure processes in intact rock based on compressive strength and tensile strength after Diederichs (2007).

The formation of an excavation damage zone (EDZ) identified to have a potential impact in relation to long-term safety has been studied comprehensively. The identified EDZ_{SI} fractures are more likely candidates for forming additional pathways to natural fracture network, due to their larger dimensions and higher transmissivity if connected unfavourably. Tunnel geometry and tunnel bulkheads keyed into the rock mass can provide a cutoff in transmissivity.

Besides the initial state of the repository system, the future evolution of the repository is considered in long term safety assessments. Considering the aperture of fractures as one critical parameter, the *thermal phase* has very minor total effects, but in the following *glacial phase* the apertures of individual fractures are increased due to decreasing effective normal stresses.

Models relevant to the Safety Case of a spent nuclear fuel repository, used in proving the safety of critical structures such as SNF repositories, should be validated against measurements and observations of *in situ* experiments conducted on site. In the absence of *in situ* data, confidence in the model uncertainties and results within regulatory processes cannot be established in the case of critical facilities such as SNF repositories. Consequently, research programs of critical facilities should be used to produce data and as a standard validation case against which critical modelling results can be assessed.

During the 10 years of detailed site characterization conducted in the ONKALO research facility, major steps toward a detailed understanding of the rock mechanics response of the Olkiluoto geological conditions have been achieved. Based on POSE and other observations from ONKALO, the expected severity and impact of rock damage processes on the final repository are estimated to be modest at worst, and the Olkiluoto site can be perceived to preserve its favorable properties for long term

safety over its lifespan. From a rock mechanics perspective, the Olkiluoto Island is well suited for the construction and operation of a spent nuclear fuel repository.

9 References

- Aaltonen, I., Engström, J., Front, K., Gehör, S., Kosunen, P., Kärki, A., Paananen, M., Paulamäki, S., Mattila, J., 2016. *Geology of Olkiluoto*, POSIVA Report 2016-16, Posiva Oy, Eurajoki, Finland, 398p.
- Andersson, J.C., 2007. *Äspö Pillar Stability Experiment, Final Report – Rock mass re-sponse to coupled mechanical thermal loading*. Technical Report TR-07-01, Svensk Kärnbränslehantering AB.
- Ask, D., 2011. *Semi-integration analysis of overcoring stress data and review of rock stress data at the Olkiluoto Site*. Working report 2011-16. Posiva Oy, Eurajoki, Finland.
- Behrestaghi, M., H., N., Young, R., P., Suikkanen, J., 2016. *ONKALO POSE Experiment - Strength, Deformation and Seismic Response of Olkiluoto Isotropic Pegmatitic Granite and Anisotropic Migmatitic Gneiss under a State of True-Triaxial Stress*. Working report 2016-41. Posiva Oy, Eurajoki, Finland, 68p.
- Diederichs, M., 2007 *The 2003 Canadian geotechnical colloquium: mechanistic interpretation and practical application of damage and spalling prediction criteria for deep tunnelling*. Canadian Geotech J 44, pp. 1082 - 1116.
- Fälth B., Hökmark H., 2014. *Approach to Assessing the Stability of Olkiluoto Deformation Zones During a Glacial Cycle*. Working Report 2013-37. Posiva Oy, Eurajoki, Finland.
- Hakala, M., Valli, J., 2015. *ONKALO POSE Experiment - Phase 1 & 2: 3D Thermo-Mechanics Prediction*. Working report 2012-68. Posiva Oy, Eurajoki, Finland, 84p.
- Hakala, M., Valli, J., Juvani, J., 2018. *ONKALO POSE Experiment – 3DEC Back-Analyses*. Working report 2018-15. Posiva Oy, Eurajoki, Finland, 104p.
- Hakala, M., Kemppainen, K., Siren, T., Heine, J., Christiansson, R., Martin, C.D., Koskinen, T., 2012. *Experience with a new LVDT-Cell to measure in-situ stress from an existing tunnel*. Proc. of the EUROCK 2012 - Rock Engineering and Technology for Sustainable Underground Construction, ISRM, Stockholm, Sweden, 14p.
- Hakala, M., Siren, T., Ström, J., Valli, J., Hakala, V., Heine, J., Sireni, S., Kemppainen, K., Savunen, J., 2017. *In Situ Stress Measurements in ONKALO with LVDT – Cell*. POSIVA report 2016-20. Posiva Oy.
- Heidbach, O., Tingay, M., Barth, A., Reinecker, J., Kurfess, D., Müller, B., 2008. *The 2008 release of the World Stress Map* (available online at www.world-stress-map.org)
- Itasca, 2018a. *Software: 3DEC overview*. Accessed 3 September 2018. <https://www.itascacg.com/software/3dec>
- Itasca, 2018b. *Software: PFC overview*. Accessed 3 September 2018. <https://www.itascacg.com/software/pfc>

- Johansson, E., Siren, T., Hakala, M., Kantia, P., 2014. *ONKALO POSE Experiment – Phase 1 & 2: Execution and Monitoring*. Working report 2012-60. Posiva Oy, Eurajoki, Finland, 130p.
- Johansson, E., Siren, T., and Kemppainen, K., 2015. *ONKALO – Underground Rock Characterization Facility for In-Situ Testing for Nuclear Waste Disposal*. Proc. of the 13th ISRM International Congress of Rock Mechanics, ISRM, Montreal, Canada, 17p.
- Juvankoski, M., 2013. *Buffer Design 2012*, Posiva report 2012-14, Posiva Oy, Eurajoki, Finland, 247p.
- Ma, G.W., 2012. *Discontinuous deformation analysis: Advances and challenges*. In: Qian & Zhou (eds) *Harmonising Rock Engineering and the Environment*, Taylor & Francis Group, London, pp 99-108. ISBN: 978-0-415-80444-8 eISBN: 978-0-203-13525
- Martin, C. D., Christiansson, R., 2009. *Estimating the potential for spalling around a deep nuclear waste repository in crystalline rock*. International Journal of Rock Mechanics and Mining Sciences, 46(2), 219 - 228.
- Norokallio, J., 2015. *Geological and Geotechnical Mapping Procedures in use in the ONKALO*. Posiva report 2015-1. Posiva Oy, Eurajoki, Finland, 54p.
- Olsson, M., Koittola, N., Mustonen, S., 2015. *Block Sawing Experiment in EDZ Study Area in ONK-TKU-3620*. Working report 2015-31. Posiva Oy, Eurajoki, Finland.
- Posiva, 2012. *Safety Case for the Disposal of Spent Nuclear Fuel at Olkiluoto - Synthesis 2012*. Posiva report 2012-12, Posiva Oy, Eurajoki, Finland, 277p.
- Posiva, 2013. *Olkiluoto Site Description 2011*, Posiva report 2011-02, Posiva Oy, Eurajoki, Finland, 1029 p.
- Posiva, 2014. *Posiva chose friction stir welding for the encapsulation of spent nuclear fuel*. Press release, http://www.posiva.fi/en/media/press_releases/posiva_chose_friction_stir_welding_for_the_encapsulation_of_spent_nuclear_fuel.2277.news
- Posiva, 2017. *Nuclear waste management of the Olkiluoto and Loviisa power plants - Summary 2016*. Yearly summary, http://www.posiva.fi/files/4658/Olkiluodon_ja_Loviisan_voimalaitosten_ydinja_tehuollon_toimintakertomus_2016_ENGLANTI._netti.pdf
- Read, R.S., 2004. *20 years of excavation response studies at AECL's Underground Research Laboratory*. International Journal of Rock Mechanics and Mining Sciences, 41(8):1251-75.
- Read, R.S., J.B. Martino., 2002. *To arch or not to arch – the role of tunnel design in controlling excavation damage development*. In Proc. of the EDZ Workshop, NARMS-TAC 2002, July 6, 2002, Toronto, Ontario, Canada.
- Rinne, M., Shen, B. & Backers, T., 2013. *Modelling fracture propagation and failure in a rock pillar under mechanical and thermal loadings*. Journal of Rock Mechanics and Geotechnical Engineering, 5(1), 73-83, ISSN 1674-7755.
- Saario, T., Ikonen, A., Keto, P., Kirkkomäki, T., Kukkola, T., Nieminen, J., Raiko, H., 2012. *Design of the Disposal Facility 2012*. Working report 2013-17. Posiva Oy, Eurajoki, Finland, 190p.

- Shen, B., Stephansson, O., Rinne, M., 2014. *Modelling Rock Fracturing Processes: A Fracture Mechanics Approach Using FRACOD*. Springer Science & Business Media.
- Siren, T., 2011. *Fracture Mechanics Prediction for Posiva's Olkiluoto Spalling Experiment (POSE)*. Working report 2011-23. Posiva.
- Siren, T., 2015a, *Excavation damage zones, fracture mechanics simulation and in situ strength of migmatitic gneiss and pegmatitic granite at the nuclear waste disposal site in Olkiluoto, Western Finland*, D.Sc.(Tech.) Thesis, Aalto University, Finland, 55p.
- Siren, T., 2015b. *ONKALO POSE Experiment – Phase 3: FRACOD2D Prediction*. Working Report 2012-59. Posiva Oy.
- Siren, T., Hakala, M., Valli, J., Kantia, P., Hudson, J.A., and Johansson, E., 2015a. In situ strength and failure mechanisms of migmatitic gneiss and pegmatitic granite at the nuclear waste disposal site in Olkiluoto, Western Finland. *International Journal of Rock Mechanics and Mining Sciences*, 79, 135 - 148.
- Siren, T., Kantia, P., Rinne, M., 2014. *Considerations and observations of stress-induced and construction-induced excavation damage zone in crystalline rock*. Elsevier Ltd. *International Journal of Rock Mechanics and Mining Sciences*. Volume 73, Pages 165-174. ISSN 1365-1609. DOI: 10.1016/j.ijrmms.2014.11.011.
- STUK, 2015. *Nuclear waste facility can be built to be safe*. Press release, <http://www.stuk.fi/web/en/-/stuk-nuclear-waste-facility-can-be-built-to-be-safe>
- Suikkanen, J., Koittola, N., Siren, T., 2016a. *Methods To Study, Model And Confirm The Existence Of Stress-Induced Excavation Damage Zone*. 7th International Symposium on In-Situ Rock Stress May 10-12, 2016 Tampere, Finland.
- Suikkanen, J., Lönnqvist, M., Hökmark, H., 2016b. *Analyses of the Stability of a KBS-3H Deposition Drift at the Olkiluoto Site during Excavation, Thermal Loading and Glacial Loading*, Posiva Report 2016-15, Posiva Oy, Eurajoki, Finland, 118p.
- TEM, 2015. *Posiva receives a construction licence for a spent nuclear fuel disposal facility*. Press release, http://valtioneuvosto.fi/en/article/-/asset_publisher/1410877/posivalle-kaytetyn-ydinpolttoaineen-loppusijoituslaitoksen-rakentamislupa
- Valli, J. & Read. R.S., expected 2018. *ONKALO POSE Experiment – POSE Final Report*, POSIVA report 2018-xx, Posiva Oy, Eurajoki.
- Valli, J., Hakala, M., Siren, T., 2016. *Stress-Geology Interaction Modelling at Olkiluoto*, Proc. of 7th International Symposium on In-Situ Rock Stress, ISRM, Tampere, Finland, 252-361.
- Valli, J., Hakala, M., Wanne, T., Kantia, P., Siren, T., 2014. *ONKALO POSE experiment – Phase 3: Execution and monitoring*, Working report 2013-41, Posiva Oy, Eurajoki, 172p.

Developing a hydro-mechanical coupled numerical model for a long-term prognosis for the underground mine Teutschenthal

**Entwicklung eines hydro-mechanisch gekoppelten numerischen Modells zur
Langzeitprognose für die Grube Teutschenthal**

Fabian Weber, Heinz Konietzky

TU Bergakademie Freiberg, Institut für Geotechnik
Gustav-Zeuner-Str. 1, 09599 Freiberg

Vera Böttge

Landesamt für Geologie und Bergwesen Sachsen-Anhalt
Köthener Str. 38, 06118 Halle (Saale)

Abstract

A longterm safety assessment for the mine complex Teutschenthal, Angersdorf and Salzmünde demands a hydro-mechanical coupled consideration of the three interconnected mines. A large scale 3-dimensional hydro-mechanical coupled numerical model was developed to simulate the longterm fluid migration inside the mine and the impact of the barrier system. The model considers a lot of aspects like creep-driven deformations of excavations and caverns, compaction of solid and past backfill and the flow barriers and sealing constructions. The migration of brine and potential hydraulic pressure built-up are predicted. The main intention of this kind of modelling is to proof the longterm safety of the barrier system and to optimize backfill process, flow barriers and sealing measures.

Zusammenfassung

Der Nachweise der Langzeitsicherheit für den Bergwerkskomplex Teutschenthal, Angersdorf und Salzmünde erfordert eine hydro-mechanisch gekoppelte Betrachtung der drei miteinander verbundenen Gruben. Ein großes 3-dimensionales hydro-mechanisch gekoppeltes numerisches Modell wurde entwickelt, mit dem die langzeitliche Fluidmigration innerhalb des Grubenkomplexes und dessen Auswirkungen auf das Barriersystem simuliert werden. Das Modell betrachtet eine Reihe von Aspekten, wie die durch Kriechen hervorgerufenen Deformationen der Abbauhohlräume und Kavernen, die Kompaktion des Feststoff- und Dickstoffversatzes oder die Dichtelemente. Die Migration der Sole sowie potentieller Druckaufbau werden prognostiziert. Die wichtigste Intention dieser Art der Modellierung ist der Langzeitsicherheitsnachweis für die Barrieren und die Optimierung des Versatzprozesses, der Strömungsbarrieren sowie der Verschlussbauwerke.

1 Introduction

The abandoned potash mine Teutschenthal (closed 1982) is connected with the mine panels Salzmünde and Angersdorf. The mine Teutschenthal is located 2 km west of the city Halle/Saale (Saxony-Anhalt). The mine is directly located below the small town Teutschenthal and close to other underground storage facilities. The mine Teutschenthal is about 9 km long with a maximum width of 1,75 km (Fig. 1.1). The mine is located between 600 m and 900 m below surface. Active mining lasted 75 years.

The shafts Teutschenthal, Salzmünde, Halle and Saale were sunk between 1905 and 1912. Huge rockbursts happened 1916 in the mine panel Angersdorf and 1940 in the mine Teutschenthal with significant earthquake-like vibrations at the surface (see Fig. 1.1). High extraction rate, wrong dimensioning of slender pillars between chambers and inadequate backfilling are reasons for these disastrous events. The rockburst dated 1940 is so far the most serious in the potash mining history: 42 miners were killed. 600.000 m² of excavation collapsed and significant surface subsidence followed.

The third and strongest rockburst happens 14 years after finishing the potash mining activities on September, 9, 1996, in the eastern panel of the mine Teutschenthal. According to MSK scale the epicentral intensity was 9 and the vibrations were registered even several 1000 km away and were felt by people within a radius of about 100 km. Within 2,5 seconds the whole eastern mining panel with an area of 2,5 km² and 700 long pillars collapsed without any precursor (see Fig. 1.1).

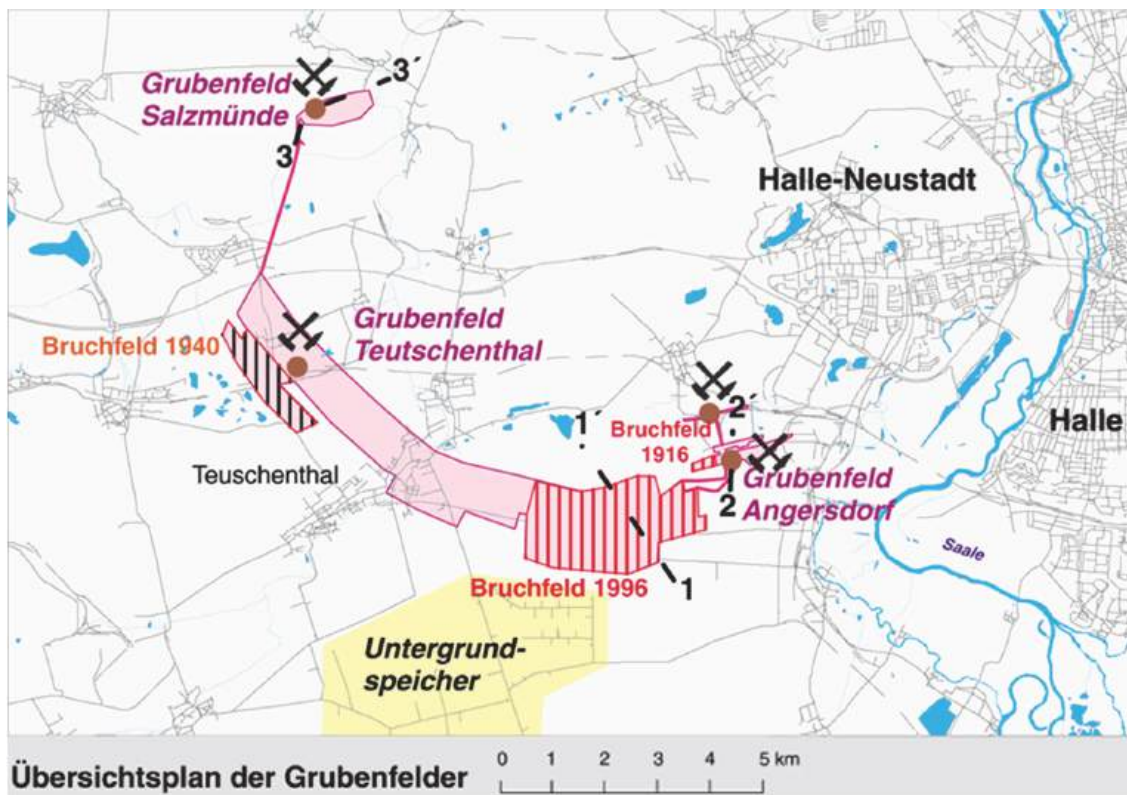


Fig. 1.1: Overview map of mine Teutschenthal with indication of rockburst areas (1916, 1940 and 1996)

The mine panels are located at the north flank of the Teutschenthal salt anticline. This anticline is bordered by the Hellische fault in the NE, the parallel orientated Teutschenthal or Lauchstädter fault in the SW and the Hornburger deep fault in the NW. According to latest geophysical interpretations the Merseburger fault is a tangent to the eastern boundary of the mine panel Angersdorf. The mine panels are close to the subsrosion boundary of the Zechstein salts. In the SE region of the east panel of the mine Teutschenthal they are tangent to or crossing the leaching area. The geological standard profile in the area of the excavations is characterized by the 200 m thick Staßfurt saliniferous formation as documented by the exaggerated SE-NW profil through the east panel of the mine Teutschenthal (see Fig. 1.2). In the upper part there is the app. 40 m thick potash layer, a tachydritic carnallitit seam. This seam was mined. The overlying strata are: gray salt clay, about 50 m thick anhydrite, about 50 m thick halite and about 15 m thick red salt clay. Further above are the rocks of the Aller sequence, which are partly or fully vanished due to subsrosion. The Bröckel shale and 300 to 400 m thick rocks of the lower and middle Buntsandstein follow below a shallow soil cover.

Mined to some extent were also the Staßfurt halite and the Leine halite below and above the potash layer, respectively. The overlying barrier for all mining panels is the Leine halit layer, which is reduced to about 38 m thickness due to subsrosion in the SE corner of the of the east panel.

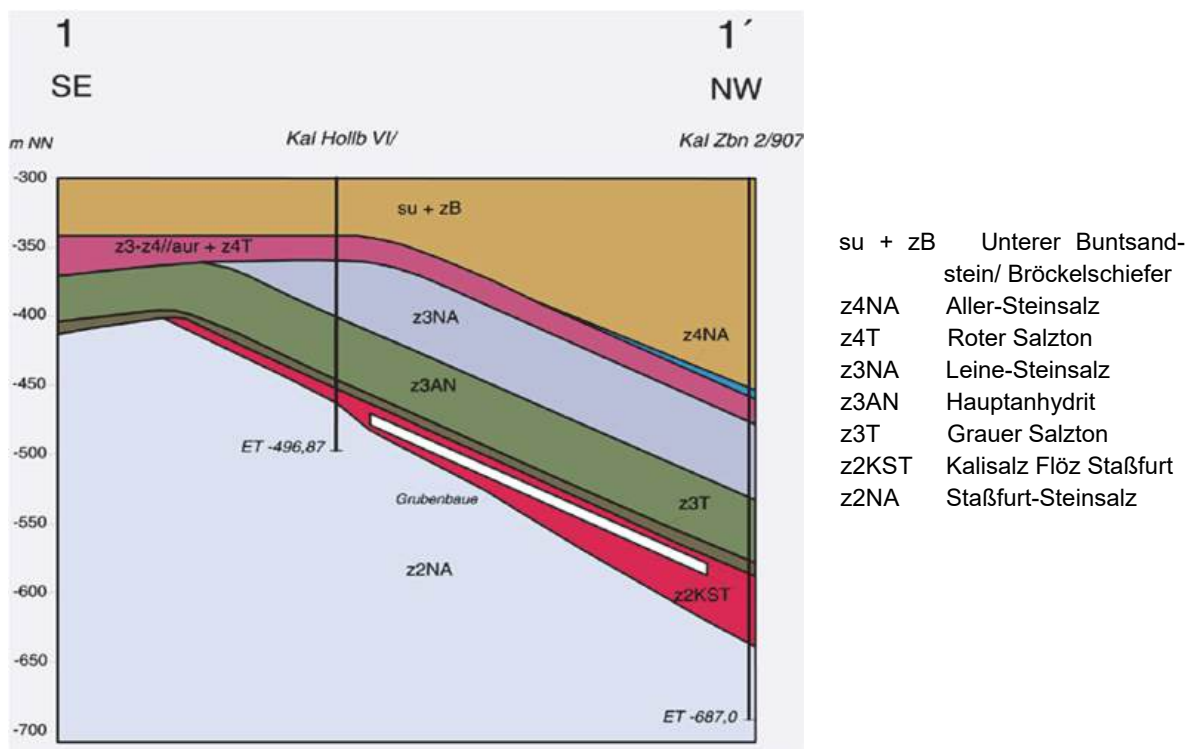


Fig. 1.2: Schematic geological profile through the east panel of the mine Teutschenthal

The backfilling process needs the consideration not only of the mine Teutschenthal, but has also to include the mine panels Salzmünde and Angersdorf (see Fig. 1.3). Besides the still existing rockburst risk within the mine Teutschenthal, the public safety hazard caused by the mine panel Angersdorf has to be considered.

Due to convergency, NaCl brine will be squeezed out of the caverns and will flood the potash excavations connected with uncontrolled solution processes, which will weaken the pillars until rockbursts occur. In this case failure of the already thickness reduced barrier layers above the Leine halit excavations cannot be excluded and water inflow into the mine workings has to be considered.

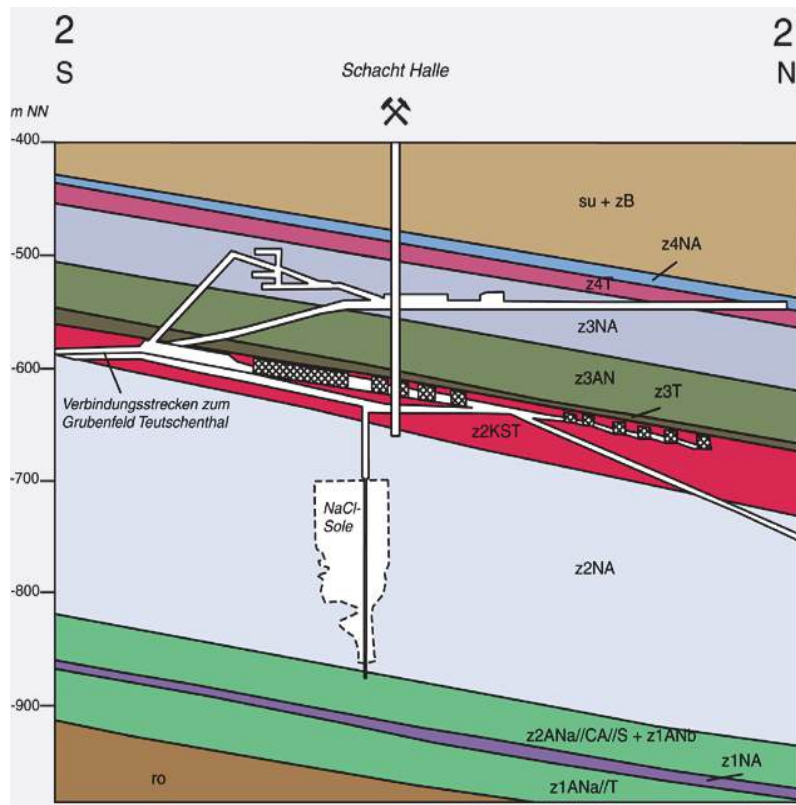


Fig. 1.3: Schematic geological cross section of mine panel Angersdorf

Due to these reasons and to minimize the risks in the future for the public safety, since 1993 backfilling is performed in the mine Teutschenthal.

A longterm safety evidence was performed for backfilling the underground excavations with waste-containing backfill material. Besides solid backfill also hydrated paste backfill is used and its behavior and handling is becoming a focal point. The use of paste fill (DSV) to protect the underground excavations, the existence of three brine-filled caverns and the other brine deposits inside the mine workings demand an adjustment of the safety concept for all three connected mine panels.

These complex investigations and evaluations are performed within the framework of the continuation of the longterm safety evidence by the Geological Survey of Saxony-Anhalt (Landesamt für Geologie und Bergwesen Sachsen-Anhalt) and the Geotechnical Institute of TU Bergakademie Freiberg. The focus is on a hydro-mechanical coupled model for the interconnected mine panels to proof the longterm safety. This model was developed from 11/2015 until 05/2017. Model set-up, calibration and validation was finished in May 2017 and first test simulations were successfully finished in June 2017. The aim of the backfilling process is, that a balance between the exist-

ing brine volume and the available pore and joint space is reached. Although a bigger amount of brine is existing in the mine, it has to be avoided that a critical fluid pressure develops, which can endanger the integrity of the geological and engineering barriers. That means the integrity of the barriers Leine halit (Na3), red salt clay (T4) and Aller halite (Na4) has to be guaranteed at any time even under conservative assumptions. Besides the backfilling of the old excavations also measures to reconstruct technogenic weak points (e.g. penetration of T4 and Na4, see Fig. 1.3), the construction of sealing structures in the anhydrite layer and the emplacement of suitable backfill to keep open fluid migration paths have to be taken.

With the help of the developed hydro-mechanical model significance and reliability of the conceptual planning were improved. The performed investigations have lead to an improvement of the conceptual planning for the sealing measures. Issues which could have negative impact on the integrity of the barriers were identified. Ongoing investigation concentrate on the optimization of the planned sealing measures.

2 General procedure and data

2.1 Modelling strategy

The challenge to predict the long-term behaviour for the carnallite and rock salt mine Teutschenthal is to combine several complex mechanisms together with the huge dimensions of the underground excavations. The time depending fluid calculation has to be coupled with the time depending viscous behaviour of the salt layers by taking compaction of different backfill materials into account. Also implemented flow barriers and sealing constructions have to be considered. In this framework the dimensions and arrangement of several millions of cubic meters of underground excavations which are partly or totally filled with fluid have to be simplified and modelled in a suitable manner. The used code for numerical simulation is FLAC3D™.

The workflow for model set-up is given in Fig. 2.1 showing the complex interactions between each working step. At first the large scale geological model with the implemented underground excavations is generated. The distribution of backfill material is than used for estimating the excavation void volume balance and the fluid volume balance in order to implement the fluid model with proper parameters. From this large scale model several sub models for calibration and verification are developed to obtain a calibrated numerical model. The results of the numerical simulation are used to determine the fluid pressure conditions inside the excavations and to evaluate the integrity of the barrier in the overlying strata.

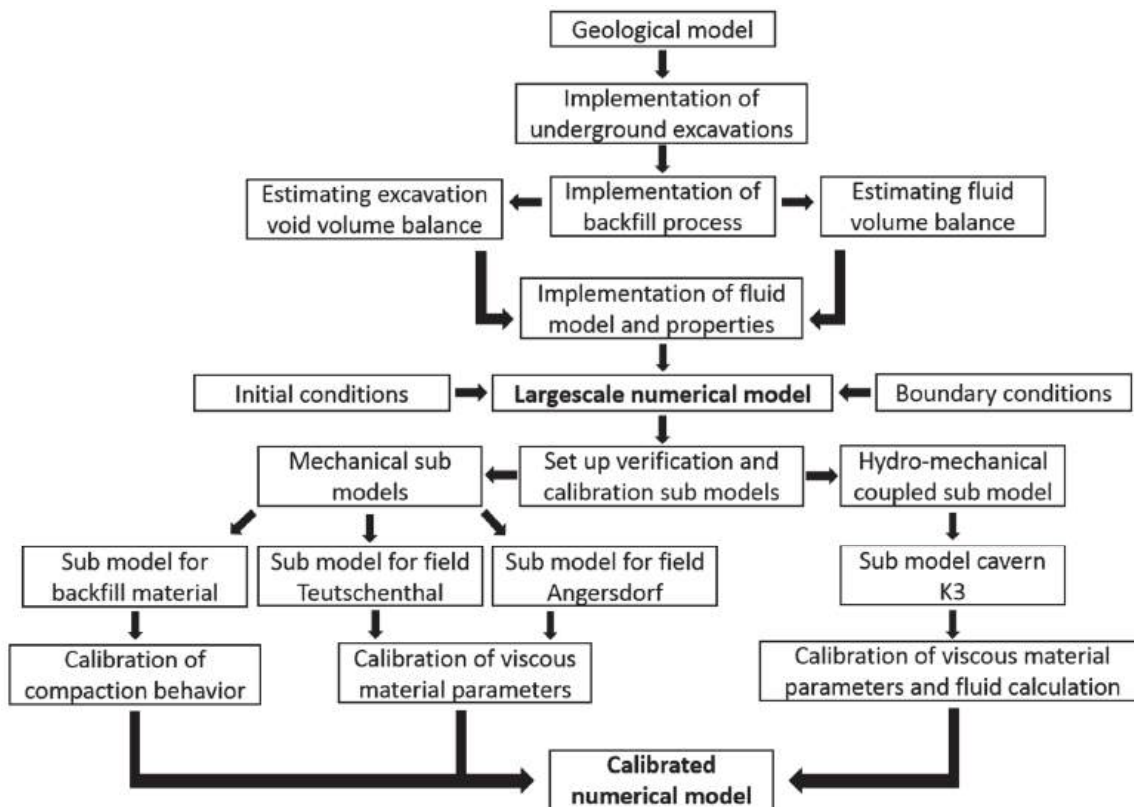


Fig. 2.1: Workflow for model generation of the large scale numerical model.

2.2 Numerical model setup

FLAC3D™ is a numerical continuum mechanical code based on the Finite Difference Method. The materials are represented by three dimensional zones with prescribed build-in constitutive models. Materials can behave elastic, plastic and even visco-elasto-plastic. Implementation of material compaction by means of mechanical deformation is also possible in order to describe e.g. backfill materials. The mechanical calculation can be coupled to hydraulic calculations which are described by Biot's Theory (1941) of porous media. The build-in fluid models allows prediction of fluid flow and pressure changes in the numerical model. Own developed complex routines based on the programming language FISH are used. Sealing constructions and flow barriers are simulated by elements with reduced permeability.

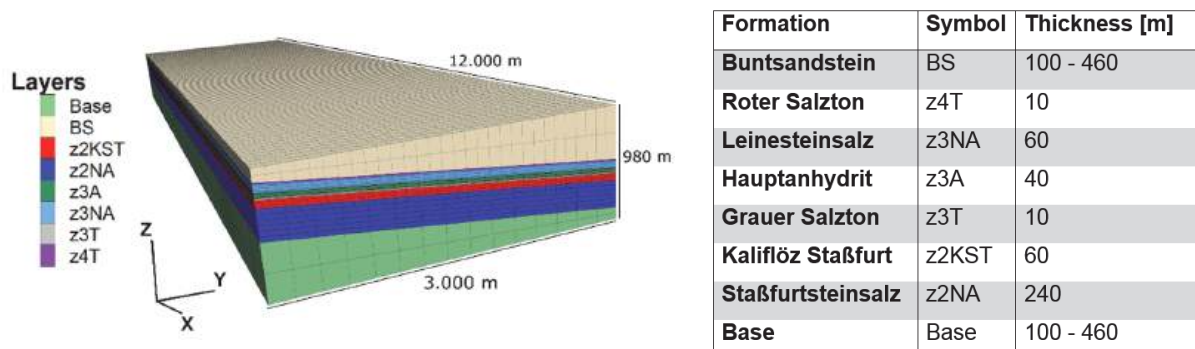


Fig. 2.2: Numerical model with geological layers.

As mentioned in chapter 2.1 a particular large scale model has to be set-up first. Therefore, the regional geology of the area under investigation is transformed into a numerical model (Fig. 2.2) of 12 km length in x- and 3 km width in y-direction. It represents a depth from -200 m to -1180 m b.s.l. Each geological layer dips with a constant angle of about 7°. The according layer thicknesses are given in Fig. 2.2. The Leinsteinsalz (z3NA) acts as a natural barrier above the underground mine.



Fig. 2.3: Mining excavations as they are implemented in the numerical model.

Mining excavations are arranged in the dipping layers of ‘Kaliflöz Staßfurt’ (z2KST), ‘Staßfurtsteinsalz’ (z2NA) and z3NA. The modelled excavations of the three mining fields Salzünde (SAL), Teutschenthal (TEU) and Angersdorf (ANG) are shown in Fig. 2.3. Due to limited zone size and the complex structure of the underground mine the layout is simplified. Therefore, not every chamber and pillar is modelled exactly. But the ratio between total chamber area and total mining area as well as chamber heights is approximated in a suitable manner. Fig. 2.4 shows some excavations and where they are situated in the context of geology.

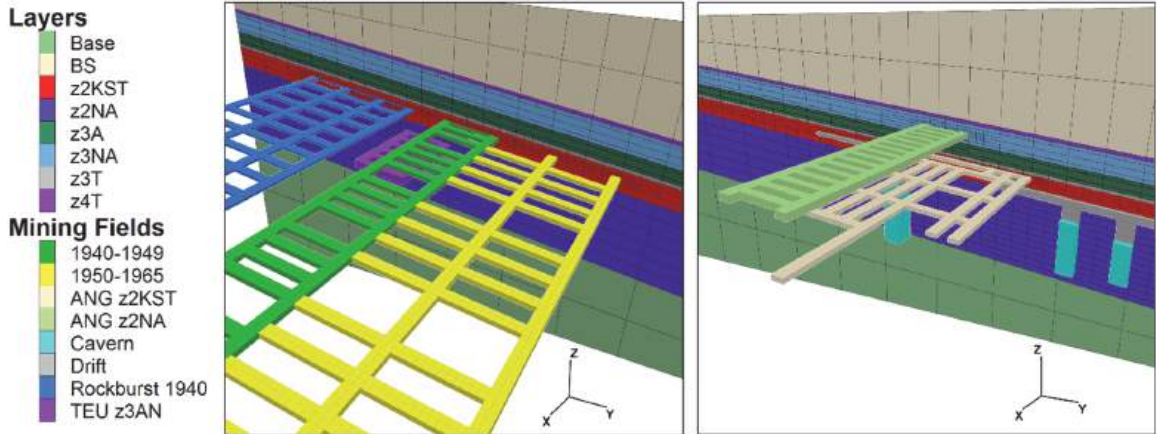


Fig. 2.4: Selected parts of the implemented excavations in context to geology.

After geometrical model set-up proper boundary conditions have to be applied to the outer model faces. Roller boundary conditions are assigned to the side walls of the model and the bottom is fixed. On the upper face a stress boundary condition is applied according to the mean weight density of the overlaying rockmass (0.0245 MPa/m). For stress initialization within the model a lateral earth pressure coefficient $\lambda = 1$ is used for the salt formations and $\lambda = 0.6$ in the ‘Buntsandstein’ (BS) formation.

The final simulation sequence is divided into the following three parts.

- 1) Elastic calculations for initial equilibrium of the geological model.
- 2) Hydro-mechanical coupled elastic calculation with implemented excavations.
- 3) Hydro-mechanical coupled visco-elasto-plastic calculations with filled underground excavations.

For step two a FISH-routine is implemented which assigns a fluid pressure in the excavations of ANG and SAL below a depth of -650 m b.s.l. This pressure represents the already fluid filled parts of the underground mine, especially the three large caverns before the backfilling process starts. The used fluid density is 1.400 kg/m^3 . Step two is necessary to calculate the specific stress redistribution around the underground excavations.

Step three represents the backfilled state of the mine. The time depending deformation of the salt layers and the compaction behavior of the backfill material inside the excavations are taken into account. All excavations are assumed to be completely filled with proper backfill materials (except the caverns). Remaining void volumes in the filled excavations are represented by specific porosity values based on excavation void volume balance. The amount of fluid for each mining area is assigned by particular saturation values. Saturation is implemented via a highly sensitive and complex fluid volume balance elaborated for the underground mine.

The BS, 'Hauptanhydrit' (z3A), 'Grauer Salzton' (z3T) and the base rock of the model are represented by linear-elastic material behavior (ITASCA, 2013). For all other formations (z2KST, z2NA, z3NA, 'Roter Salzton' - z4T) the Norton power law (Norton, 1929) is used.

The backfill material is modelled by the double-yield constitutive law (ITASCA, 2013) taking volumetric compaction into account. Three different backfill materials are in operation at the mine Teutschenthal. The difference in compaction is represented by different stress-strain curves for the materials (see Chapter 3.2).

For fluid flow simulation the isotropic build-in fluid model (ITASCA, 2013) is used. Fluid flow is enabled only within the excavations and the hanging wall up to the lower boundary of z3NA since the salt formations are nearly impermeable. This assumption leads to conservative results. The hydraulic parameters porosity and saturation are assigned based on complex volume balances for each individual mining field. The permeability of the backfill is in the order of $1\text{E-}16 \text{ m}^2$. Permeability for the hanging wall ranges between $1\text{E-}18$ and $1\text{E-}24 \text{ m}^2$.

3 Model calibration

3.1 Calibration of cavern submodel K3

As shown in Chapter 2.1 an extensive calibration phase was necessary to perform reliable long-term predictions for the mine Teutschenthal. At first the two time depending processes of visco-elastic material behaviour and fluid flow are calibrated in order to obtain reliable results and to ensure that the modelled time scales are accurate. First calibration considers the squeezing-out of fluid from the caverns. Since

there is a large data base for K3 it offers the opportunity for calibration. Therefore, a calibration simulation was set up with a submodel representing only the area in which cavern K3 is situated. Observations and other simulations show that the fluid outflow from K3 is about $1.000 \text{ m}^3/\text{a}$ under the assumption that fluid outflow volume is equal to the convergence volume of K3. These topic has to be considered for long-term prognosis. Initial and boundary conditions remain the same compared to the large scale model. The initial volume of the cavern is about 433.000 m^3 . A specific fixed pore pressure condition is applied on top of the cavern in order to enable fluid outflow. Due to the assumption that fluid outflow volume should equal convergence volume of K3 nearly no pressure increase in the cavern is expected since the fluid can easily be squeezed-out. The calibration is performed for 1.000 years and show good agreement with other simulations.

Fig. 3.1 shows the pore pressure distribution in the simplified cavern at the begin of the simulation and after 1.000 years. The initial pore pressure inside the cavern due to hydrostatic pressure is about 2.95 MPa. After 1.000 Years the pressure decreases slightly but no large pressure change occurs. In order to estimate fluid outflow volume and convergence volume of K3 a FISH-routine is implemented monitoring these volumes during simulation. Fig. 3.2 shows the outflow volume and convergence volume in respect to the convergence volume estimated by IfG (Institut für Gebirgsmechanik Leipzig).

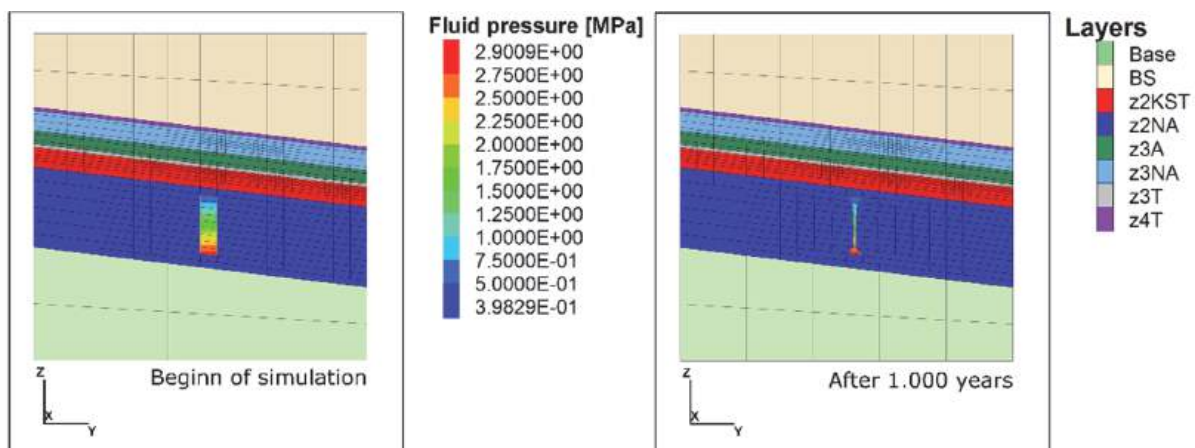


Fig. 3.1: Pressure distribution inside the cavern for the calibration submodel.

It can be noticed that fluid outflow and convergence volume are nearly equal with only slight differences. After 1.000 years a volume of about 400.000 m^3 is pressed out which means that the cavern is nearly closed. The amount of fluid squeezed-out in the first 100 years is in well coincidence with the measured amount of fluid outflow. The numerical results are in good agreement with the prognosis from IfG. Only the last 200 years differ from the prognosis since structure of the cavern is highly simplified, the model approach is different between the simulations and different constitutive laws have been used. But the difference is only about 12 % and fluid outflow is larger in the present model which lead to conservative results. The cavern is nearly closed at this time and the most of the fluid is already squeezed-out.

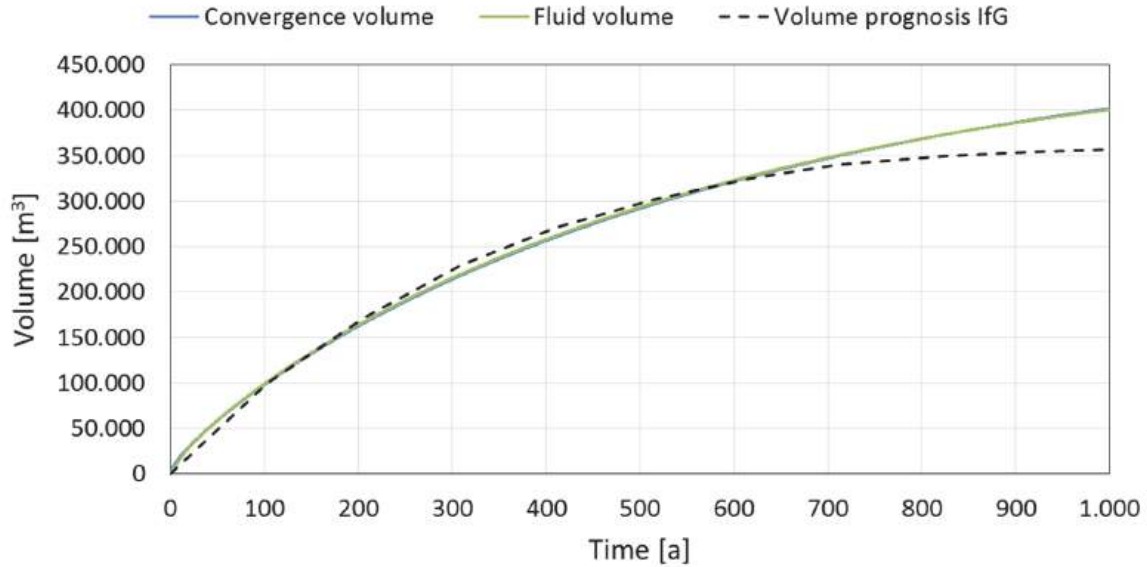


Fig. 3.2: Comparison of convergence and pressed out fluid volume from cavern K3 in respect to volume prognosis.

3.2 Calibration of backfill material

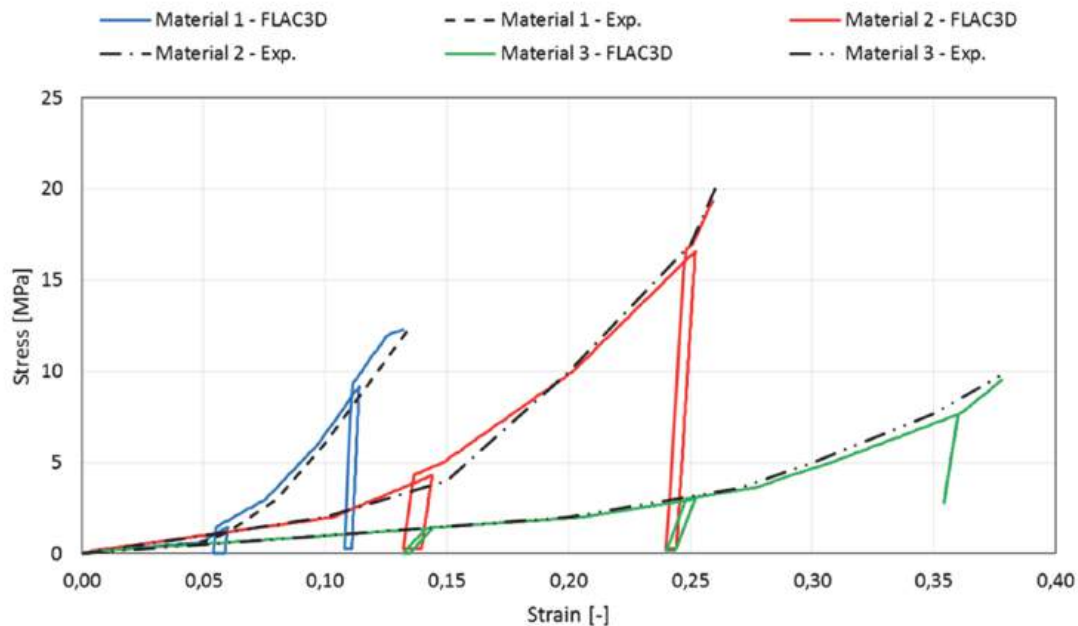


Fig. 3.3: Stress-strain curves describing the particular compaction behavior of the three backfill materials.

The difference in compaction for the three particular backfill materials is represented by different stress-strain curves for the materials (Fig. 3.3). Each curve was calibrated in FLAC3D with a simulated oedometer test. Measured and simulated results are in good coincidence. Due to the fact that the excavation model has to be simplified

the stress-strain curves are then corrected based on the excavation volume in the model with respect to original excavated volume in the real mining areas.

3.3 Calibration on submodel Teutschenthal and Angersdorf

In order to verify the general geomechanical behaviour of the numerical model two additional submodels are generated. One contains the excavations in ANG, the other one the excavations of the central part of TEU. These models are used to calibrate the geomechanical behaviour based on measured and simulated settlements, deformations and stresses. The initial and boundary conditions for both models are the same compared to the large scale model. Only hydraulic coupling is neglected since only the mechanical part is verified.

For ANG the roof settlement of the chambers in the z3NA layer as well as the stress distribution around the mining field ANG are compared to another prognosis calculated by IfG. In this case cavern K3 is filled with backfill material. The chambers which are used for verifying the roof settlement are shown in Fig. 3.4 together with calculated settlement over 1.000 years at these points. A roof settlement of about 1.3 m develops during the calculation which is again in good agreement to the prognosis from IfG.

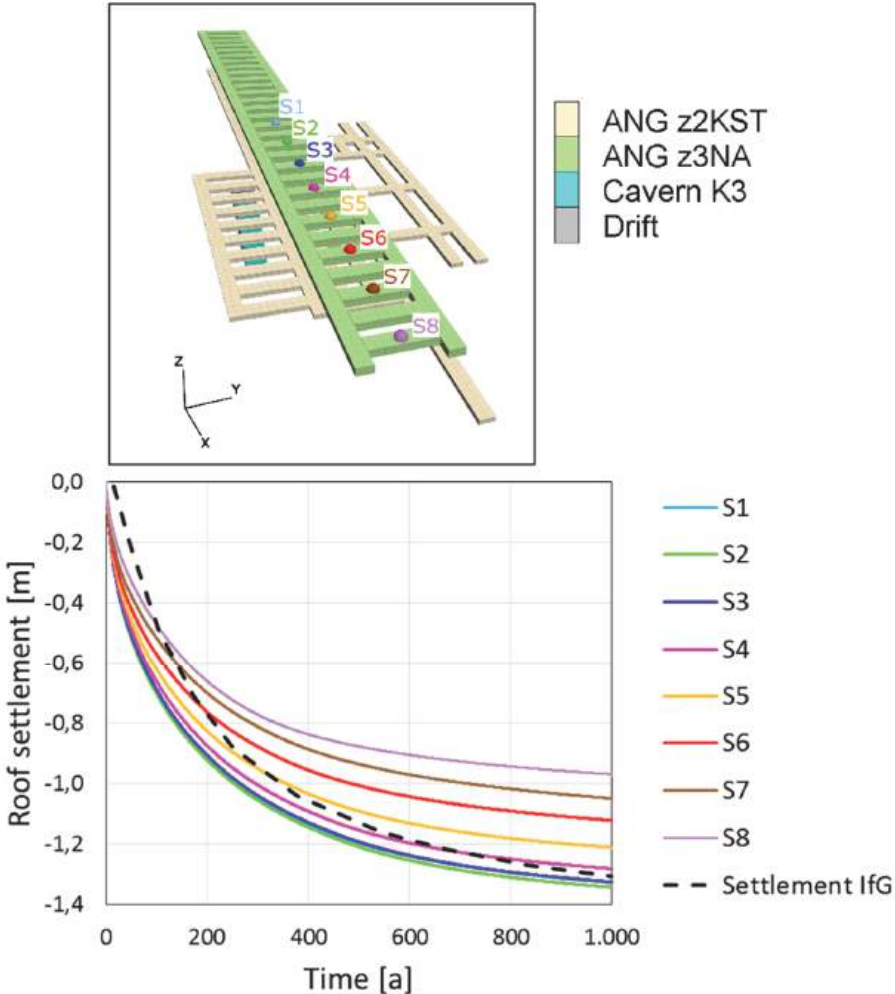


Fig. 3.4: Simulated roof settlement in rock salt chambers in ANG.

Fig. 3.5 show the modelled minimum principal stress (σ_3 , compressive stresses negative) distribution in cross view around the excavations in ANG. The results are in good coincidence with the simulations from IfG (not visualized). Stress decreases close to the chambers (0 - 5 MPa) and increases inside the pillars (12.5 - 22.5 MPa).

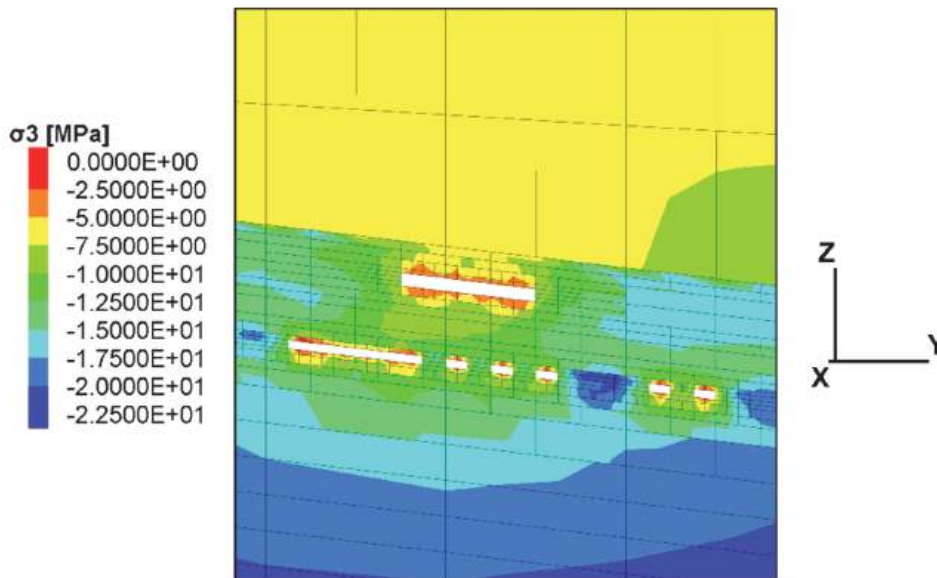


Fig. 3.5: Smallest principle stress (σ_3) around the excavations in ANG.

For a central part of the mining field TEU the geomechanical behaviour is verified based on stress measurements in the pillars and lateral pillar deformation measurements. The maximum principal stress is shown as cross-view (Fig. 3.6, top). The stress decreases at the roof and floor of the chamber and it increases inside the pillars up to 23 - 24 MPa. In the past K-UTEC measured stresses in pillars and estimated them with about 25 MPa. The numerical results confirm such values in a suitable manner. From deformation measurements a lateral pillar strain rate of about 3 mm/a is estimated for the pillars in TEU. This would result in about 30 cm after 100 years. Horizontal displacements (Fig. 3.6, bottom) of the pillar contours in lateral direction reach about 29 cm after 100 Years. Numerical and measured values are in good agreement compared to each other.

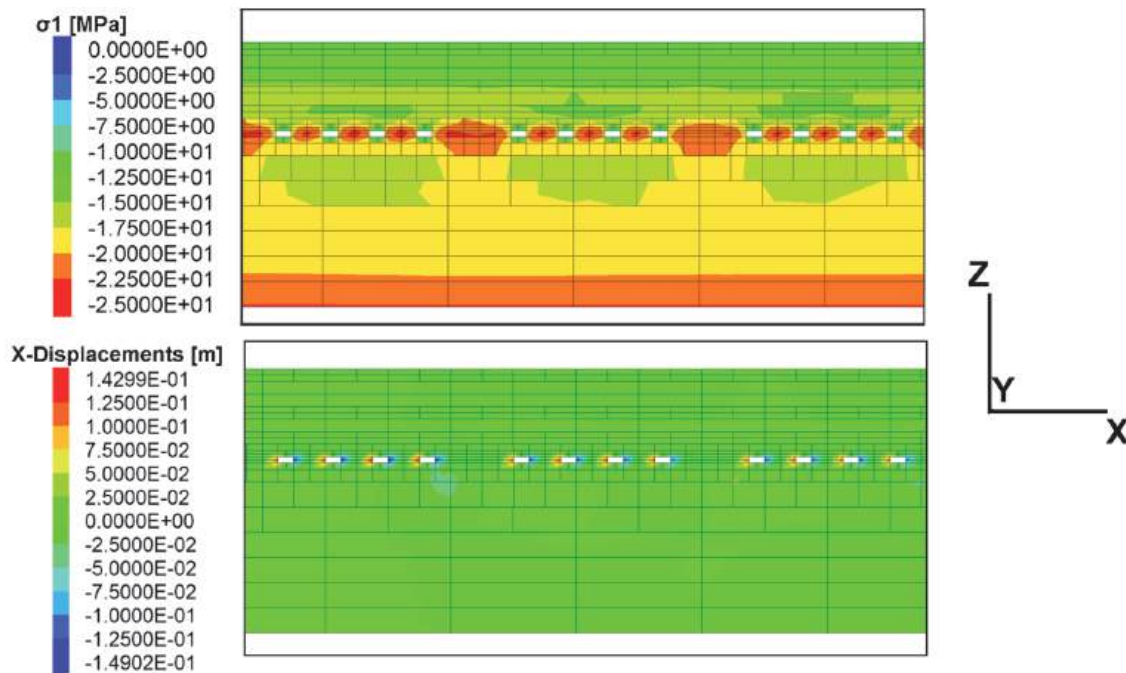


Fig. 3.6: Minimum principal stress (top) and horizontal displacements (bottom) for calibration simulations of TEU.

4 Expected results

The numerical long-term prediction for the underground mine Teutschenthal will be used to evaluate two specific topics. On the one side the results will give some insights into the fluid pressure evolution within the backfilled excavations. On the other side results will be used to evaluate the integrity of the barrier represented by the Leinsteinsalz.

The time depending saturation and pore pressure distribution inside the mine will be a major outcomes of the simulations. These values are extracted for the whole mine and can be visualized by contour plots for any specific point in time. Additionally, history points are distributed over the modelled excavations. These points offer the opportunity to obtain a time series of fluid pressure evolution over the complete calculation time for several particular points.

The integrity of the barrier has to be proven since the fluid can pass through the carnallite up to the lower boundary of Leinsteinsalz where a fluid pressure can build up. In order to evaluate the integrity of the barrier the fluid pressure on the lower boundary of the Leinsteinsalz is observed. Considering a minimum principal stress criteria which supposes fracturing if the fluid pressure at the lower boundary of the Leinsteinsalz exceeds the acting minimum principal stress allows an evaluation of the integrity of the barrier. This conservative criteria assumes zero tensile strength for the Leinsteinsalz. The integrity of the barrier can be guaranteed if the fluid pressure is smaller than the acting minimum principal stress. A ratio ($R_{P-\sigma_3}$) between fluid pressure and minimum principal stress can be calculated and visualized as a contour plot along the dipping boundary between the Hauptanhydrit and Leinsteinsalz. Some kind of a 'risk map' can be obtained which may show areas with high or low fluid pressure acting on the lower boundary of the barrier. The distribution of fluid

pressure history points along the boundary are used to estimate appropriate times for evaluating $R_{P-\sigma 3}$.

First simulations have shown, that the integrity of the barrier is not violated and a significant factor of safety exist. The proposed model can also be used to optimize the planned underground flow barriers and sealing constructions.

The developed modelling strategy is worldwide unique and offers excellent opportunities to predict the hydro-mechanical coupled long-term behaviour of complex underground structures and is a valuable tool for design and optimization of sealing and flow barrier constructions underground.

5 References

- Biot, M. A., 1941. *General Theory of Three-Dimensional Consolidation*. Journal of Applied Physics, 155 - 164.
- ITASCA, 2013. *FLAC3D manual*, Itasca Consulting Group Inc., Minneapolis, Minnesota, USA.
- Norton (1929): Norton, F. H., *Creep of Steel at High Temperatures*. New York: McGraw-Hill Book Company, 1929.

Simulation of Gas migration in Canadian Potential Host Rocks for Radioactive Waste Disposal

Simulation von Gasmigration in potentiellen kanadischen Wirtsgesteinen für die Endlagerung radioaktiver Abfälle

M. Fall, Z. Li, G. Guo, X. Wei

Department of Civil Engineering, University of Ottawa, Canada
161 Louis Pasteur, K1N 6N5, Ottawa, Canada; email: mfall@uottawa.ca

Abstract

One of the most important factors that can have negative consequences on the safety of deep geological repositories (DGRs) for radioactive wastes is the gas generated within the repository. Therefore, the assessment of the long term safety of repositories for nuclear wastes in deep geological rock formations requires a good understanding of the mechanisms as well as the prediction of gas and contaminant migration from DGRs. A multi-year research program has been conducted at the University of Ottawa (Canada) to understand and predict gas and contaminant migration in potential Canadian DGRs as well as to assess the potential impacts on the integrity of the host rocks and engineered barriers. Some results of this research program are presented in the present paper. The results of the numerical investigations of gas migration in potential sedimentary host rocks for nuclear repositories, located in Ontario, Canada, are discussed. The results have shown that the limestone and shale formations act as an effective natural barrier with regards to gas migration. It is also found that, up to 400 000 years after the closure of the proposed repositories for nuclear wastes in Ontario and irrespective of the scenario considered, the gas migration will still remain in the host sedimentary rock barrier. However, at 1 000 000 years and regardless of the scenario selected, the simulation results indicate that some gas can flow (upward) through the shaft and then reach the shallow bedrock groundwater zone. Thus, an adequate engineered design of the shaft is critical for the safety of the DGR.

Zusammenfassung

Eine der wichtigsten Faktoren in Bezug auf negative Konsequenzen für die Sicherheit tiefer geologischer Endlager (DGRs) für radioaktiven Abfall ist die Gasfreisetzung im Endlager. Deshalb verlangt die Bewertung der Langzeitsicherheit von radioaktiven Endlagern in tiefen geologischen Formationen ein gutes Verständnis der Mechanismen der Gasmigration incl. der Verunreinigungen ausgehend von DGRs. Ein mehrjähriges Forschungsprogramm wurde an der Universität von Ottawa (Kanada) durchgeführt, um die Gasmigration in potentiellen kanadischen DGRs zu verstehen und zu prognostizieren und die potentiellen Auswirkungen auf die Integrität des Wirtsgesteins und der Ingenieur-Barrieren abzuschätzen. Einige Ergebnisse aus diesem Forschungsprogramm werden in diesem Artikel präsentiert. Ergebnisse von numerischen Untersuchungen der

Gasmigration in potentiellen sedimentären Wirtsgesteinen für nukleare Endlager, gelegen in Ontario, Kanada, werden diskutiert. Die Ergebnisse haben gezeigt, dass Kalkstein- und Schieferformationen als effektive Barriere in Bezug auf Gasmigration fungieren können. Es wurde gefunden, dass bis zu 400 000 Jahre nach Ende der Einlagerung des radioaktiven Abfalls und unabhängig vom betrachteten Szenario die Gasmigration innerhalb des sedimentären Wirtsgesteins verbleibt. Nach 1 000 000 Jahren allerdings und unabhängig vom betrachteten Szenario zeigen die Simulationsergebnisse an, dass gewisse aufwärtsgerichtete Gasbewegungen durch die Schächte erfolgen und die oberflächennahe Grundwasserzone erreichen. Deshalb ist ein entsprechendes Design der Schachtverschlüsse entscheidend für die Sicherheit eines DGR.

1 Introduction

Radioactive wastes are generated by numerous civil and military activities, such as nuclear power generation, decommissioning of nuclear service facilities, medical and research uses of radioactive materials, and diverse industrial activities. For example, Canada produces about one-third of the global supply of medical radioisotopes. The nuclear power reactors in Ontario, Quebec and New Brunswick have generated about 17 percent of the electricity in Canada (NWMO, 2010; Noorden, 2013; Shehata et al. 2015). In all cases, radioactive wastes require to be managed responsibly to guarantee public safety and protection of the environment at present and in the future (Osidele et al. 2008). The development of strategies and technologies for sustainable and safe management of radioactive wastes has been one of the major technical challenges in waste management worldwide (Fall et al. 2014).

A broadly accepted approach for management of radioactive wastes is to deposit the wastes into a deep geological repository (DGR) with a multi-barrier system to prevent hazardous radionuclides from leaking into the biosphere (e.g., Figure 1). Achieving this multi-barrier concept is fundamental to all DGR programs in the world and the long-term containment of radioactive wastes. The multi-barrier system consists of an engineering barrier system (EBS) and natural barrier system or host rock (e.g., sedimentary rocks, magmatic rocks) (Guo and Fall, 2018). Many countries including Canada are currently pursuing deep geological disposal as the most preferred option for the long-term management of radioactive wastes.

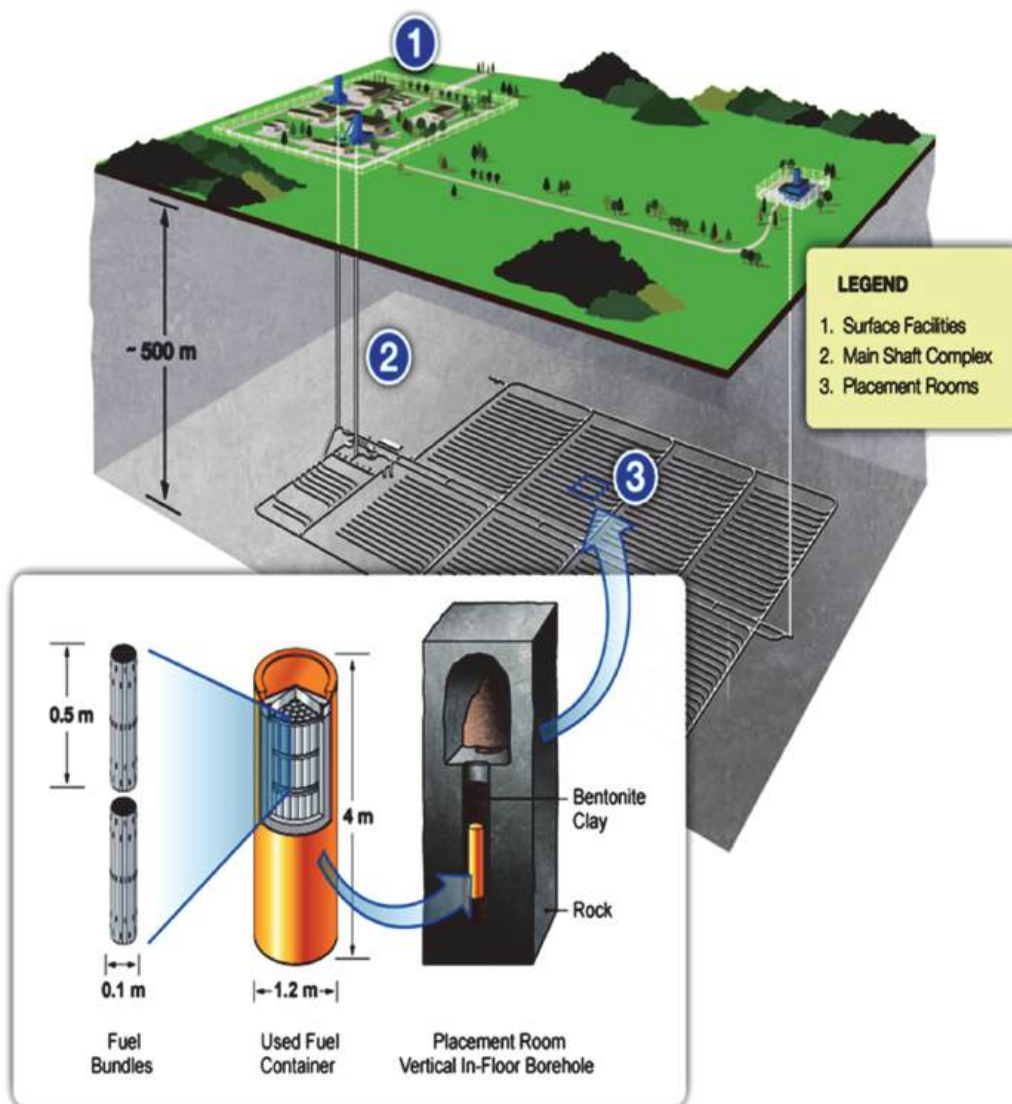


Fig. 1 Deep geological repository design in crystalline rock (Villagran, 2012).

In Canada, a repository for low and intermediate levels of radioactive wastes is being proposed in Ontario's sedimentary rock formations. A key aspect of the DGR safety is the integrity and long-term stability of the sedimentary host rock (natural barrier) to isolate nuclear waste (radioactive contaminants) at timeframes of up to 1 Ma. Hence, any anticipated factor that could jeopardize the protective functions of this natural barrier must be thoroughly evaluated and understood (Shehata et al. 2015).

One of the most important factors that can have negative consequences on the performance of the natural barrier systems is the gas generated within the repository. Significant quantities of gas can be generated in a DGR for radioactive wastes from several processes as discussed below. These gases could migrate not only through the engineered, but also through the natural geological barrier systems. The pressure of the generated gas would build up, and could induce the formation of either microcracks or

macrocracks, which would affect the integrity of the natural barrier and geosphere as a long-term contaminant barrier (Fall et al. 2014). Furthermore, these gases could enable the easy transport of radioactive contaminants and thus significantly impact the biosphere and groundwater (Figure 2). Thus, the assessment of the long term safety of a repository for nuclear wastes in Ontario's sedimentary rock formations requires a good understanding and assessment of the mechanisms as well as the prediction of gas migration in these rock formations.

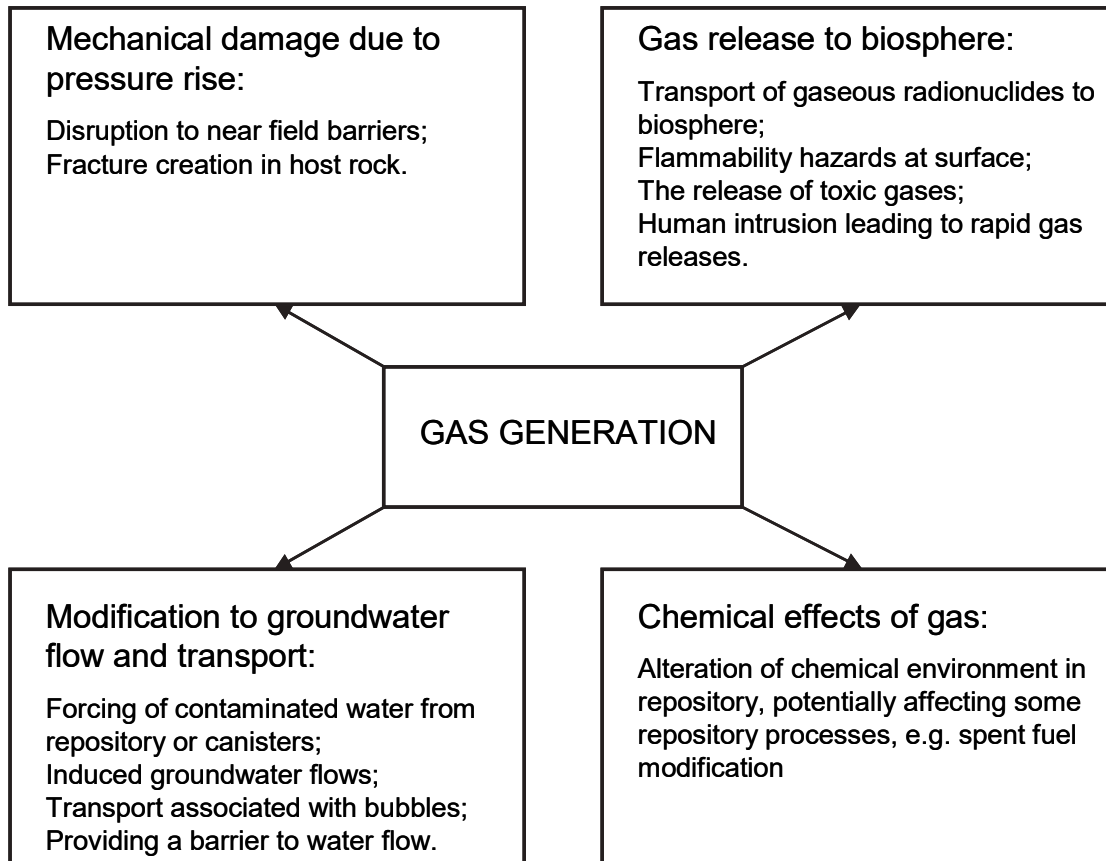


Fig. 2 Schematic of the range of effects that may follow from gas generation in a repository (Rodwell et al. 2003)

The gas transport in host sedimentary rock is a complex phenomenon, and is governed by several Multiphysics or coupled processes including, mechanical, hydraulic, geochemical and thermal processes. The understanding and assessment as well as the prediction of gas migration through the host rock and its impact on the integrity of the natural barrier require the consideration of the aforementioned Multiphysics processes. A large and multi-year research program has been conducted at the University of Ottawa (Canada) to assess and predict gas migration from the proposed DGR in Ontario by considering the aforementioned Multiphysics processes. In the present paper, developed simulation tools as well as a part of the modeling and simulations results related to the gas migration in the Ontario's potential DGR mentioned above are presented and discussed.

2 Sources of Gas in DGR

In deep repositories, several mechanisms have been identified which could contribute to gas generation in different degrees. The main gas generation mechanisms include:

- The corrosion of metals in waste and packaging (production of hydrogen). It is widely accepted that the largest source of gas generation will be the anaerobic corrosion of iron. Indeed, after closure of an underground nuclear waste repository, anaerobic conditions will be reached rapidly in the repository (within a few hundred years).
- The radiolysis of water and certain organic materials in packaging (mainly production of hydrogen; also oxygen, carbon dioxide, methane, etc., which can be produced in lower quantities). Internal and external radiolyses have been recognized as the two mechanisms that can lead to the decomposition of chemical compounds by radiation (Mueller 2000). Internal radiolysis means processes that take place in the waste product and its packaging. External radiolysis occurs in the backfill material that surrounds the waste and possibly in the host rock.
- The microbial degradation of organic waste components (production of methane and carbon dioxide). Organic matter includes a variety of materials, such as cellulose waste materials, ion-exchange resins, bitumen, plastics, rubbers, and oils. Some organic wastes are easily degradable, such as cellulose, while others, such as plastics, resins and bitumen, may resist complete degradation. Carbon dioxide and methane (CH₄) are the main gases produced by microbial degradation of organic matter.
- Other mechanisms; there are other possible mechanisms that could contribute to gas generation. However, the amount of gases produced would be generally less significant as compared to the previous mechanisms. These mechanisms are: (i) gas release from the host rock. But, the production of radioactive gas is insignificant relative to non-radioactive gases in term of volume; and (ii) radioactive decay or chemical reactions other than corrosion. The volume of gases that is produced may be significant compared to that for non-radioactive gases.

The gas generating materials will be mainly the wastes and their containers. However, in some repository concepts, there may also be significant quantities of “construction” steel, including for example, rock bolts, abandoned machinery, and concrete reinforcement (Rodwell et al. 2003). The gas generation rates are likely to be significantly higher for repositories with Intermediate Level Waste (ILW) and Low Level Waste (LLW) than for those for High Level Waste (HLW) or spent fuel. The reason is that there are larger volumes of metals and organic materials in the former compared to the two latter (Rodwell 1999) types of repositories. The aforementioned gas generation mechanisms are described below.

3 Location and Characteristics of the studied DGR

The DGR area is located south of Ontario, east of Lake Huron at the Bruce Nuclear site (Figure 3). Ontario Power Generation’s (OPG) proposed DGR will be located at a depth

of 680 m below the surface (Figure 4). A multi-year site investigation program has been conducted at the site of the proposed DGR, consisting of seismic surveys, and a series of deep vertical and inclined boreholes, and hydraulic, petrographic, geochemical and mechanical testing performed in-situ and in the laboratory (e.g., Gartner Lee Limited, 2008; Jensen et al. 2009; NWMO, 2011d; NWMO, 2011e). The results of the site characterization program have provided a comprehensive description of the geological, geotechnical and hydrogeological characteristics of the DGR site. The results reveal that the geological profile of the DGR site displays approximately 20 m of Cambrian sandstone, 5 m of Ordovician siltstone and sandstone, 180 m of Middle Ordovician argillaceous limestone, 212 m of Upper Ordovician shale, 324 m of Silurian dolostone, argillaceous dolostone, shale and evaporite and 104 m of Devonian dolostone (Figure 4-5). The DGR underground facilities will be located within the low permeability Middle Ordovician argillaceous limestone of the Cobourg Formation that is overlain by more than 212 m of low permeability shale. The thicknesses of the Middle and Upper Ordovician formations are particularly constant with variation less than 5% across the Bruce nuclear site, and beyond (NWMO, 2011d). Furthermore, the lithofacies within the key DGR units are laterally homogenous. The DGR site is structurally simple and undeformed, and is located in a stable tectonic regime with low seismicity and no evidence of neotectonic faulting (NWMO, 2011d). The deep groundwater system that exists in these Ordovician formations is very old and highly saline (approximately 300 g/L). The intermediate system covers all of the Silurian formations. This zone has mixed permeability formations (e.g., high permeability Guelph Formation and low permeability shale/anhydrite beds in the Salina Formation) with groundwater salinity ranging from saline to slightly salty. The Devonian and Quaternary formations represent the shallow groundwater system for the successive formations and layers over the proposed DGR (Hobbs et al. 2008). The hydraulic, geochemical and mechanical properties for each formation are given in NWMO (2011a, d) and Fall et al. (2012). Figure 6 shows the mineralogical composition of the rock formations in the DGR site.

Transport of non-wetting fluids in a low-permeability formation, such as the aforementioned Cobourg limestone and Queenston shale, is largely controlled by the microstructure of the rock. Hence, an assessment of gas transport processes in those formations requires careful consideration of both structure and texture. Figure 7 shows samples of the upper Ordovician Queenston Shale and Upper Ordovician Cobourg (Lindsay) Limestone (Vilks and Miller, 2007).

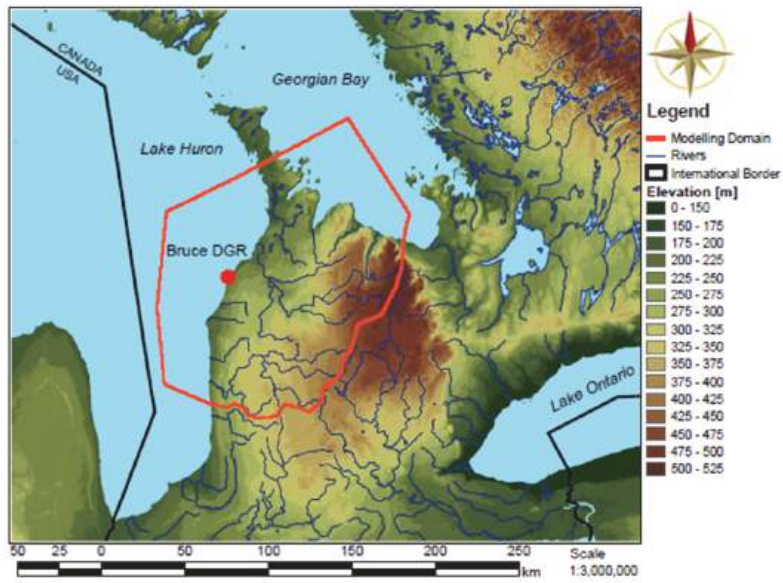


Fig. 3 Map that shows the location of the OPG proposed deep geological repository for low and intermediate level waste (NWMO, 2011c)

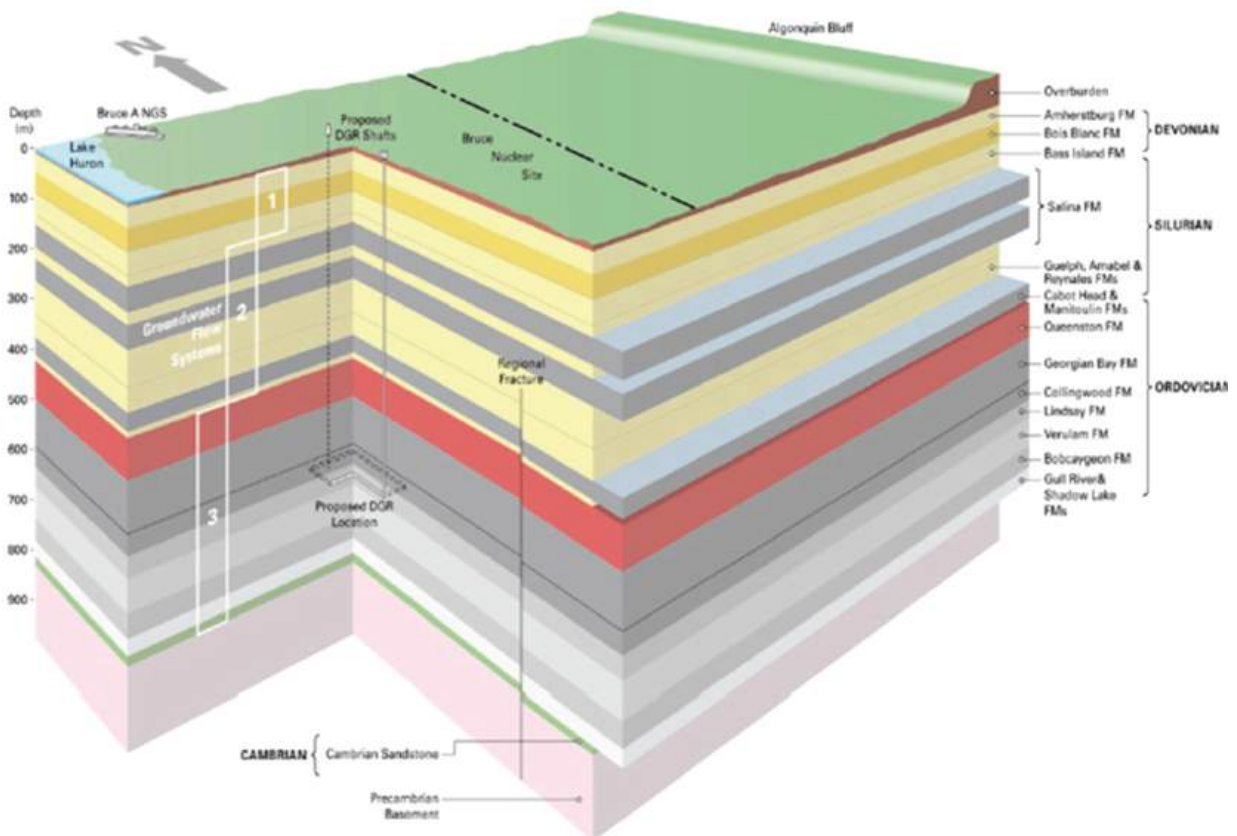
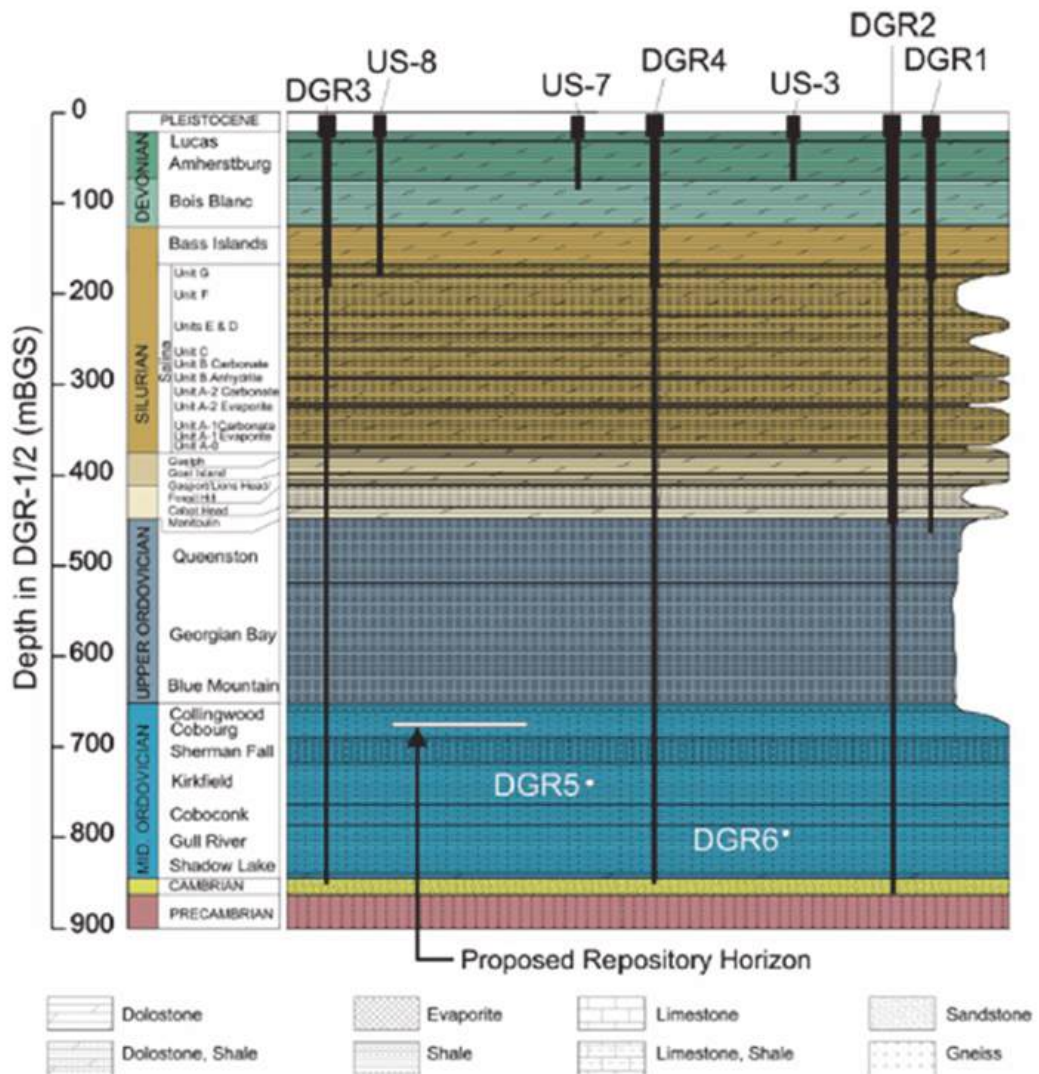


Fig. 4 Conceptual geosphere model of the proposed DGR (Gartner Lee Limited, 2008)



Notes: Vertical borehole penetration depths are indicated by vertical black lines. White dots indicate approximate depth of penetration for angled boreholes DGR-5 and DGR-6. Figure was developed based on information from INTERA (2011).

Fig.5 Subsurface stratigraphy in the study area (NWMO, 2011b)

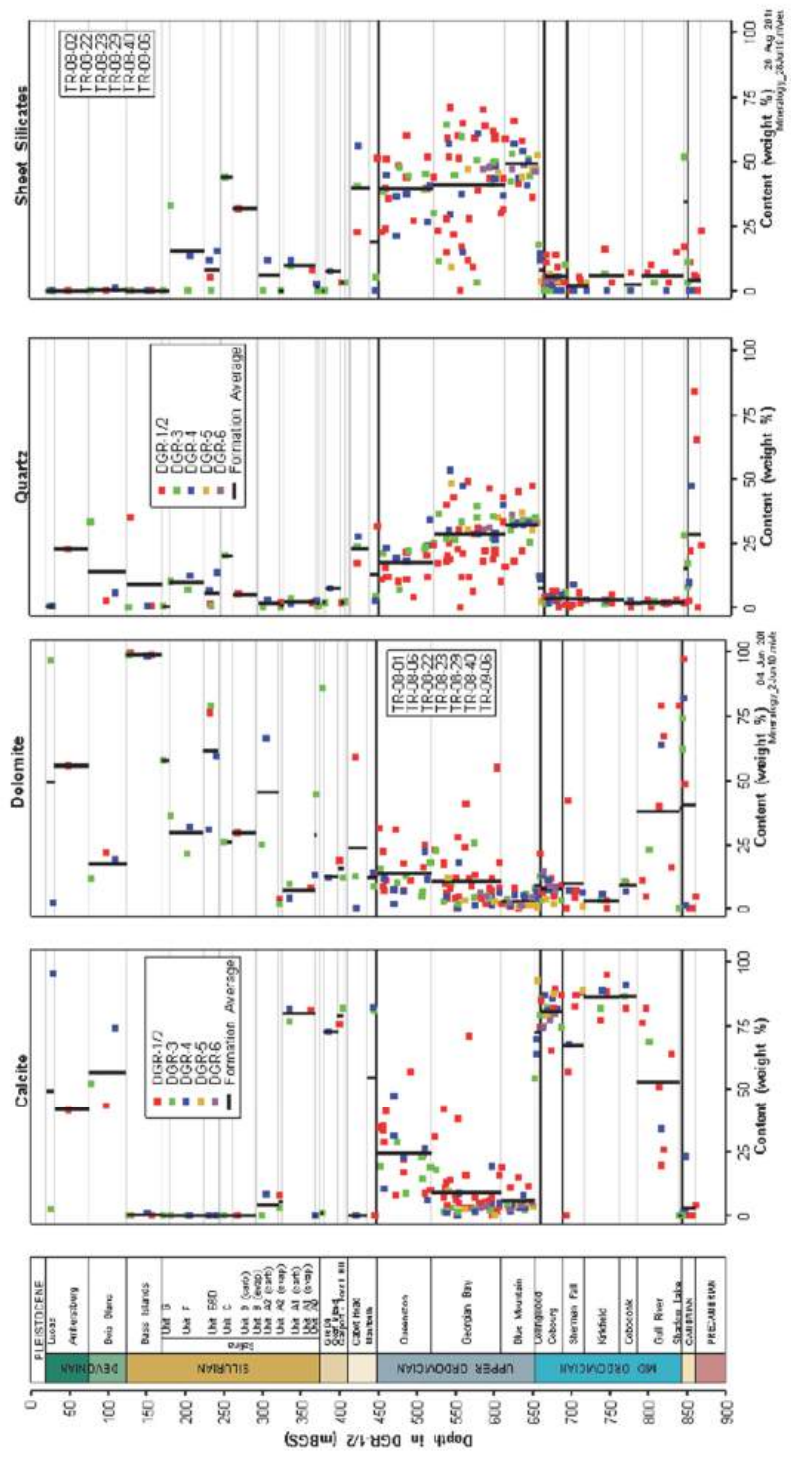


Fig 6 Rock formation mineralogy (NWMO, 2011b)



Fig. 7 Drilled core samples from Queenstone Shale and Cobourg Formations (Vilks and Miller, 2007)

4 Development of Simulation Tools

Two types of numerical simulators for predicting gas migration in host sedimentary rocks have been developed in the modeling part of the aforementioned research program. The simulators include a hydro-mechanical simulator (HM-Simulator) and thermo-hydro-mechanical-chemical simulator (THMC-Simulator). Relevant hydro-mechanical processes have been considered in the HM-Simulator, whereas THMC processes relevant for gas migration were implemented in the THMC-Simulator. The capabilities of the developed simulators to simulate gas migration in host rock were then successfully tested against well controlled laboratory experiments and fieldgas injection tests (e.g., in situ gas injection test in the underground Mont Terri Rock Laboratory in Switzerland) on potential host rock for nuclear repositories. The validation results have shown good agreement between the predicted and experimental results. This validation provides confidence in validity and reliability of the developed simulators for predicting and simulating gas migration in host sedimentary rocks under multiphysics loading conditions. The simulators are briefly described below, whereas detailed descriptions of the simulators are published elsewhere (e.g., Fall et al. 2014; Li and Fall 2013; Guo and Fall, 2018).

4.1 HM-Simulator

A coupled hydro-mechanical (HM) model for predicting and analyzing gas migration in sedimentary rock was developed. The coupled HM model was implemented in the FEM code COMSOL Multiphysics. The latter can perform diverse categories of analysis including: stationary and time-dependent, linear and nonlinear, eigen-frequency and modal analysis by using finite element method (FEM) in concert with adaptive meshing and error control which employ a variety of numerical solvers (COMSOL, 2009).

In the HM-model, the host sedimentary rock is considered as a continuum porous medium made of three constituents: a solid and two fluids (water, gas), which in the context of the theory of mixtures are regarded as three independent overlapping continua. Water is wetting, whereas gas is not. The pores of the solid skeleton are partially filled with liquid water, and partially with gas. The solid matrix is chemically inert with regard to the water and gas contained in its pores. The three constituents are distributed in solid, liquid and gas phase. The gas phase is regarded as a perfect mixture of dry air (gas generated by the repository is assumed to have the same properties as air and would be indistinguishable from it, and water vapour. The liquid phase can contain dissolved gas (Fall et al. 2014).

In addition to standard hydraulic and mechanical coupled processes, the HM model considers the elastic degradation due to microcracks or damage, mechanical damage-controlled gas flow as well as coupling of fluid flow and mechanical stresses, coupling between diffusion coefficient and induced damage, coupling between tortuosity and rock deformation and damage, influence of rock deformation on permeability, capillary pressure and diffusion coefficient, as well as variation of porosity with deformation and induced damage. Moreover, the model also considers the modification of capillary pressure due to the variation of the pore structure of the sedimentary rock. This variation can result from rock deformation and/or mechanical damage. Tensile and compressive damage in the host rock are accounted for too. The model parameters are easy to be obtained (Fall et al. 2014). Some examples of simulation results of gas migration in the studied DGR using the HM-simulator are shown and discussed below.

4.2 THMC-Simulator

The key thermo-hydro-mechanical-chemical (THMC) processes and their coupling considered in the simulator developed are shown in Figure 8. Two well-established numerical codes, FLAC3D (adopted for mechanical (M) analysis) and TOUGHREACT (THC code), have been modified, and then coupled to act as a robust THMC coupled simulator for assessment purposes to investigate gas migration in the study area.

Although, the sequential coupling of two codes is less efficient than using a single code, its biggest advantage is that both codes, i.e. TOUGHREACT and FLAC3D, have been well verified and widely used in their relevant fields. The TOUGHREACT code is a class of FORTRAN subroutines, which address the time dependent transport of multiphase/unsaturated flow and reactive transportation of chemical species in porous media. Three factors, which are the temperature, hydraulic and chemical fields, have been successively accounted for in TOUGHREACT. Permeability variation due to

porosity change and mineral dissolution/precipitation can also be considered in these codes. Executable files for specific modules have been provided for TOUGHREACT. FLAC3D is a robust finite-difference program for geomechanical analysis, and especially professional and convenient in light of its capability to simulate the behavior of various geomaterials that undergo plastic flow when deviatoric stress yielding has been reached (Itasca, 2009). Specific numerical algorithms, e.g. the Lagrangian calculation scheme and the mixed-discretization zoning technique, are used to ensure the accurate modeling of plastic flow.

We first developed an elasto-plastic damage (EPD) model and incorporated this model into Flac3D (Flac3D^{DM}). A series of programs were scripted by using C++ and FISH languages to transfer the primary variables, e.g. pore pressure, temperature and porosity, between Flac3D^{DM} and TOUGHREACT. Figure 9 shows a schematic diagram of this coupling process. As variables are applied onto grids in Flac3D^{DM} instead of elements in TOUGHREACT, data interpolation was exemplified when introducing these data from the simulation results of TOUGHREACT. On the other hand, the results from Flac3D^{DM} can be directly outputted into the elemental centers, and as a result, no interpolation is necessary to import results into TOUGHREACT.

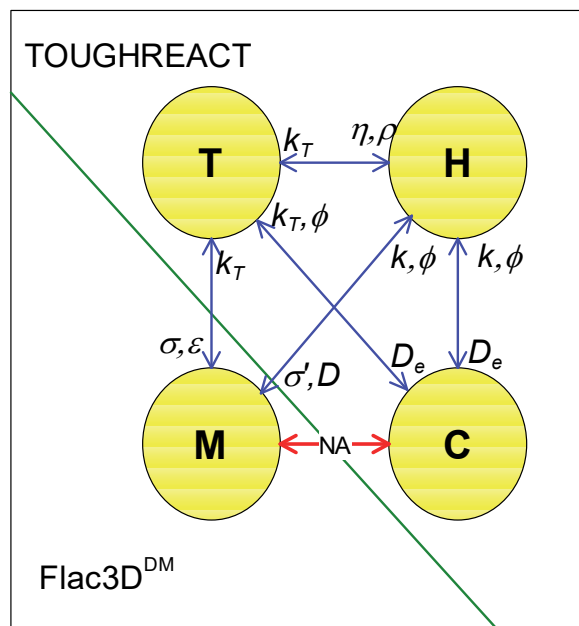


Fig. 8 Conceptual diagram of THMDC coupling and interaction of relevant parameters (D , damage factor; D_e , effective diffusion coefficient; k , permeability; k_T , thermal conductivity; P , pore pressure; q , liquid flux; T , temperature; ϕ , porosity; σ , stress; ϵ , strain; ρ , dry density; and η , viscosity)

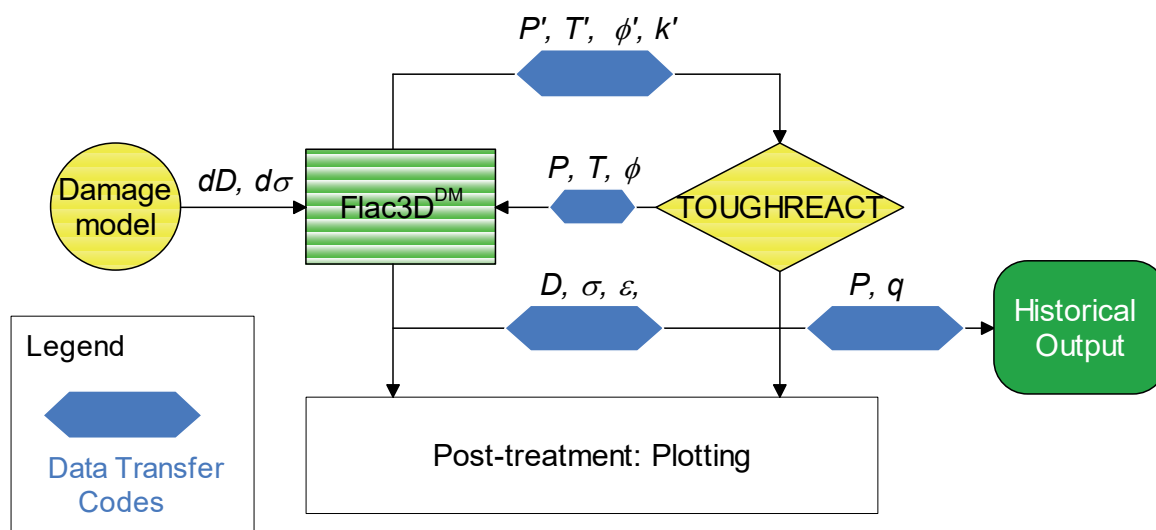


Fig. 9 Schematic diagram for major modules and data interchange between Flac3DDM and TOUGHREACT (D , damage factor; k , permeability; P , pore pressure; q , liquid flux; T , temperature; ϕ , porosity; σ , stress; ε , strain; and subscript DM: damage mechanics)

The capabilities of the developed simulator (TOUGHREACT-FLAC3D^{DM}) to simulate gas migration in host rock were then successfully tested against well controlled laboratory and field experiments and. After the successful validation of the simulator, it was applied to simulate gas migration in the host rock of the studied DGR. Various factors were studied or considered in the simulation. These factors include, pore pressure, saturation index, concentration of chemical species, rock mineral composition evolution, damage factor, phase velocity vector, rock porosity evolution, pH, gas velocity, and rock permeability. Some examples of the simulation results obtained are presented and discussed below.

5 Simulations of Gas Migration from a DGR in Ontario's Sedimentary Rocks

The conceptual model of the study area is depicted in Figure 10. An equivalent shaft area with a radius of 13m including the Excavation Damaged Zone (EDZ) is adopted to model the two shafts proposed in the OPG's design. Axi-symmetric conditions are assumed with the axis of symmetry centred along the equivalent shaft. Furthermore, it is anticipated that the gas generated will also accumulate in the access tunnel and will reach its maximum pressure in the tunnel. From the perspective of gas modelling, this is conservative as the large space or void of the tunnel would diminish the gas pressure originated from the chambers. Thus, the gained results will be on the safe side from an engineering point of view. The initial and boundary conditions adopted as well as the mechanical, hydraulic, thermal and geochemical properties used as input data are given in various publications (e.g., NWMO 2011; Fall et al. 2012, 2014; Li and Fall, 2013). Two case scenarios were studied with regards to the properties of the shaft: (i) a normal case scenario (material properties obtained from lab tests) and (ii) a failed shaft case (worst

case scenario) where the properties of the bentonite-based material (e.g., permeability, porosity) are significantly deteriorated. Moreover, two cases were considered with respect to the gas pressure applied in the tunnel. In the first case, the peak repository gas pressure is in the range of 7 to 8 MPa. In the second case, a peak repository gas pressure of 15 MPa (worst case scenario) is considered. The consideration of these various scenarios helps to take into account the uncertainties related to the maximum gas pressure to be expected in the DGR as well as to the time-dependent evolution of the properties of the bentonite-sand barrier material in a DGR.

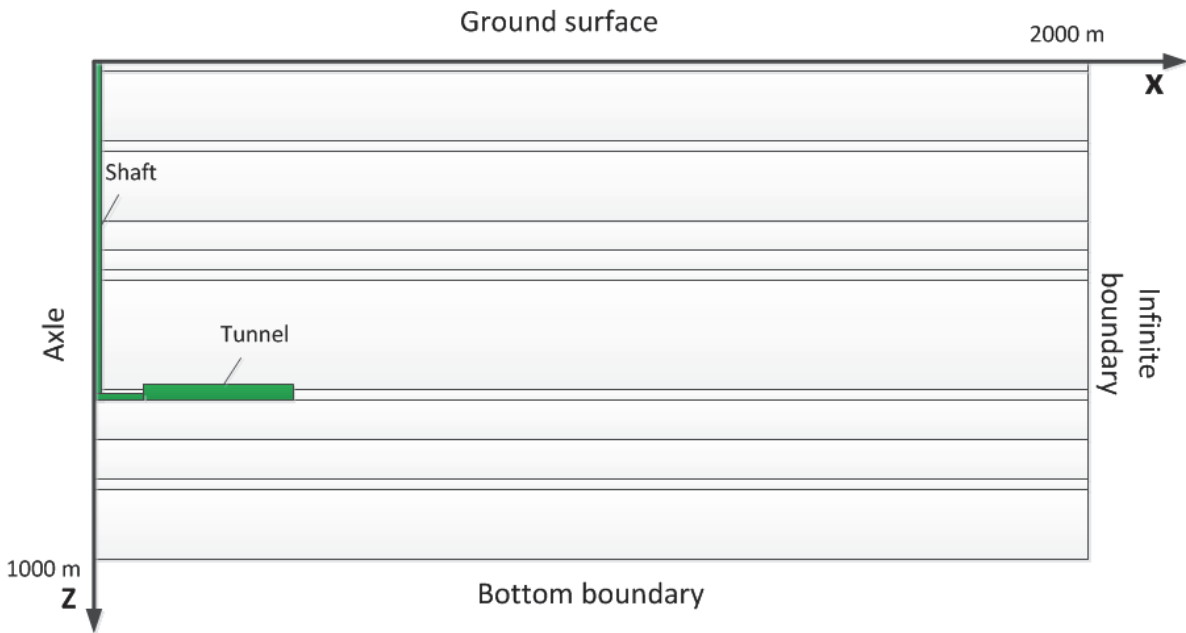


Fig.10 Conceptual numerical model of the DGR

Several numerical simulation results have been obtained. Some samples of results are presented and discussed below. Figure 11 illustrates two patterns of gas flow in the DGR host rock for the normal case scenario: (i) one vertical pattern (upward or downward) in the rock formations with lower permeability; (ii) another horizontal pattern in the rock formations with higher permeability (e.g., Salina formation). The gas flow is vertical in the shaft. This figure indicates that, up to 600 000 years after the closure of the repository, the high gas pressure and gas migration is still contained in the natural shale barrier layer. This indicates that the limestone and shale formations act as an effective barrier with regards to gas migration after the closure of the repository. Moreover, the maximum gas pressure in the surrounding near-field is below the lithostatic pressure, suggesting that no tensile fractures would develop in the natural barrier. This is positive with regards to the safety of the DGR. However, at 1 000 000 years, it can be seen that some gas can reach the shallow bedrock (e.g., Salina formation) groundwater zone; the gas escaped through the shaft. The two simulators, HM- and THMC-simulators, produced similar results.

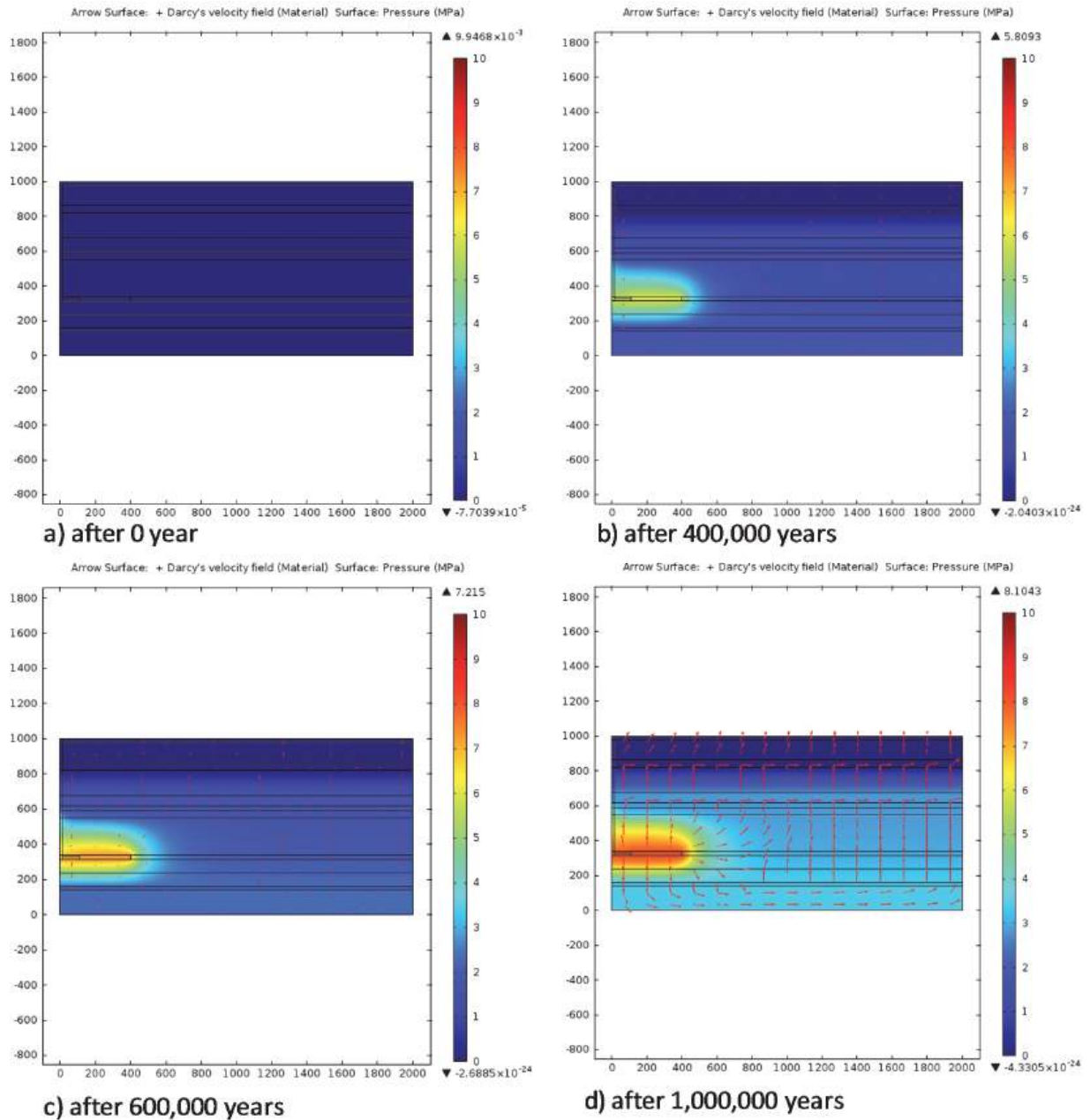


Fig. 11 Evolution of the gas flow velocity and gas pressure (normal case scenario)

Figure 12 shows the spatial distribution and temporal evolution of the gas saturation degree in the DGR repository and host rock for the worst case scenario. It can be seen that at 500 000 years, gas can escape through the failed shaft to reach the shallow bedrock groundwater zones. The simulation results have shown that gas mainly migrates towards upward direction. The migration primarily takes the route of vertical failed shaft. The velocity vector indicated good coincidence with the gas saturation index. Consequently, the effects of gas reaching the shallow rock formations when the shaft fails should be considered in the DGR safety assessment. The results have also

shown that the porosity of the rock layer at 150 m depth significantly increases due to the gas migration. This change could be due to the dissolution of carbonate minerals. Moreover, it is also observed that because of the initial mineral components of the geological repository site, which consist of mainly carbonate, the initial solution pH is at alkaline side, in the range of 7.3 - 8.8. With the increase of post-closure period, the majority of the solution pHs in groundwater reduce to some extent, in the range of 7.1 - 7.9 after 500 000 years. It is also noteworthy that the pH at repository tunnel turns out to be more alkaline than the surrounding geological stratification in the same depth or even deeper with the consistent increase of period of time. This might be related to the mineral compositions, e.g. bentonite, that is used to fill the tunnel and the shaft. Since bentonite is originally saturated with sodium and thus exhibits strong alkalinity, which also makes it more resistant to chemical neutralization effect.

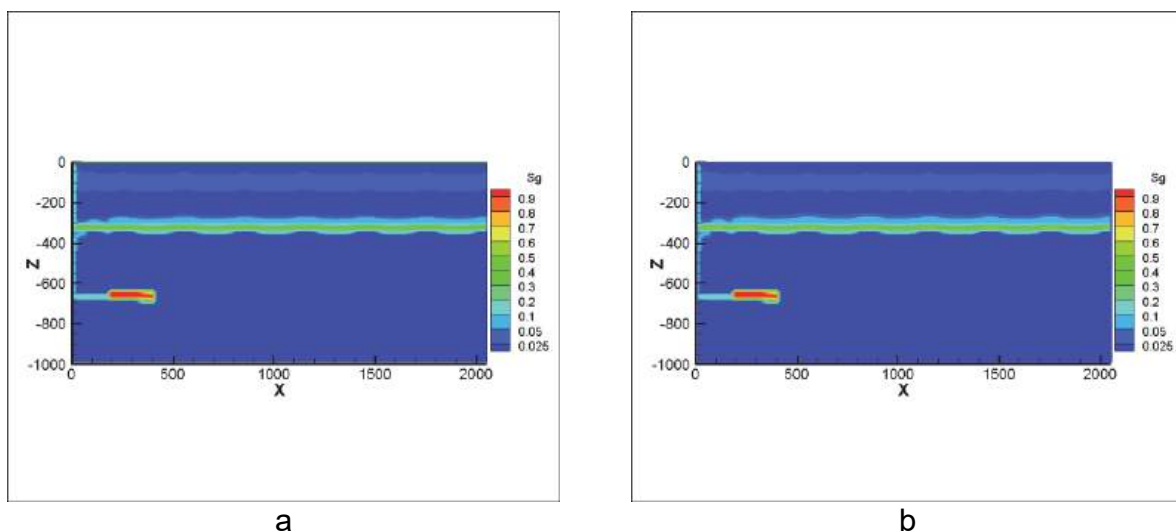


Fig. 12 Contour map of gas saturation (S_g) at different post-closure time: (a) 500,000 years; (b) 1,000,000 years (worst scenario)

6 Summary and Conclusions

HM and THMC simulators for simulation of gas migration in DGR have been developed. The simulators are applied to simulate and predict the gas migration in Ontario's host sedimentary rocks of DGR for radioactive wastes. Valuable results are obtained. The numerical results provided a better understanding of the mechanism of gas migration within the Ontario's host sedimentary rocks and its effect on the rocks. The obtained results have shown that the natural rock barrier DGR in Ontario (Canada) can effectively retain the gas generated by various processes in the DGR when normal scenario is considered. However, it is noted that, at 1 000 000 years after the closure of the proposed DGR and regardless of the scenario considered (normal, worst case), gas flows (upward) through the shaft and thus reach the shallow bedrock groundwater zone. The quantity of gas reaching the shallow bedrock should be estimated for use in long term safety assessments.

7 References

- COMSOL, (2009). *Comsol Multiphysics 3.5a*. <http://www.comsol.com>
- Fall M, Nasir O., Nguyen T.S. (2012). *Coupled hydromechanical modeling of Gas Migration in Ontario's Sedimentary Rocks, Potential Host Rocks for Nuclear Waste Repositories*. Canadian Geotechnical Conference – Geomanitoba 2012.
- Fall, M., Nasir, O., Nguyen, S. (2014). *A coupled hydro-mechanical model for simulation of gas migration in host sedimentary rocks for nuclear waste repositories*. Engineering Geology, 176, 24 - 44.
- Gartner Lee Limited. (2008). *Phase I Regional Geology, Southern Ontario. Supporting Technical Report for OPG's Deep Geological Repository for Low and Intermediate Level Wastes*. Prepared for Ontario Power Generation. OPG 00216-REP-01300-00007-R00.
- Guo, G., Fall, M (2018). *Modelling of dilatancy-controlled gas flow in bentonite based materials with double porosity and double effective stress concepts*. Engineering Geology, 243(4), 253 - 271.
- Hobbs, M.Y., Frape, S.K., Shouakar-Stash, O., Kennell L.R., (2008). *Phase I Regional Hydrogeochemistry, Southern Ontario*. Supporting Technical Report, OPG 00216-REP-01300-00006-R00.
- Itasca (2009). *Flac3D: Fast Lagrangian Analysis of Continua in 3 Dimensions*. Itasca Consulting Group Inc., Minnesota, USA.
- Jensen, M., Lam, T., Luhowy, D., McLay, J., Semec, B and Frizzel, R., (2009). *Ontario Power generation's Proposed L&ILW Deep Geologic Repository: An Overview of Geoscientific Studies*. Canadian Geotechnical Conference, GeiHalifax2009.
- Li. Z., Fall M. (2013). *A modeling tool for assessment of potential groundwater contamination in response to CO2 leakage from geological disposal of CO2*. 3rd Climate Change Technology Conference, CCTC 2013, Montreal Canada. Paper Number 1569728941
- Mueller W. (2000). *Gas generation*. In Proceedings of the Workshop: GGM in RWD, 67-72
- Noorden, R. V. (2013). *The medical testing crisis*. Macmillan Publishers Limited 2014 - Nature- Vol -504- 12 December news feature©.
- NWMO (2010). *Moving Forward Together: Process for Selecting a Site for Canada's Deep Geological Repository for Used Nuclear Fuel*. Nuclear Waste Management Organization, May.
- NWMO, (2011a). *Geosynthesis*. NWMO DGR-TR-2011-11.
- NWMO, (2011c). *Hydrogeological modelling report*. NWMO DGR-TR-2011-16, 261p
- NWMO, (2011d). *Geosynthesis*. NWMO DGR-TR-2011-11, 418p.
- NWMO, (2011e). *Geosphere Site Model report*. NWMO DGR-TR-2011-24, 426p

- Osidele O., Pensado o., Mcurry J., Mohanty S.v (2008). *Decision-analysis framework to support risk. assessment for geologic radioactive waste. disposal systems*. The integrated assessment journal, bridging sciences & policy, vol. 8, iss. 2 (2008), 127 - 136.
- Rodwell (1999). *Gas migration and two-phase flow through engineered and geological barriers for a deep repository for radioactive waste*. A Joint EC/NEA Status Report, EUR 19112 EN, Brussels.
- Rodwell W., Norris S., Cool W., Cunado M., Johnson L., Maentynen M., Sellin P., Snellman M., Talandier J., Vieno T., Vines S. (2003). *A Thematic Network on gas issues in safety assessment of deep repositories for radioactive waste (GASNET)*. Final report, EURATOM, 45 p.
- Shehata A., Fall M, Detellier C (2015). *Swelling characteristics of bentonite based barriers for deep geological repository for nuclear wastes: impact of underground water chemistry and temperature*. Geoquebec 2015 – the 68th Canadian Geotechnical Conference (CGC) and 7th Canadian Permafrost Conference, Sep. 20-23 2015, Quebec, Canada CD Rom.
- Vilks P. and MillerN.H. (2007). *Evaluation of Experimental Protocols for Characterizing Diffusion in Sedimentary Rocks*. NWMO TR-2007-11.
- Villagran, J.E. (2012) *Development of a Monitoring Program for a Deep Geological Repository for Used Nuclear Fuel NWMO*. NWMO TR-2012-18.

Geology, geometry and kinematics of an active deep-seated rock slide (Ötztal valley, Austria)

Geologie, Geometrie und Kinematik einer aktiven, tiefgründigen Massenbewegung (Ötztal, Österreich)

Christina Rechberger, Christian Zangerl, Christine Fey

Institute of Applied Geology, Department of Civil Engineering and Natural Hazards
University of Natural Resources and Life Sciences Vienna
Peter-Jordan-Strasse 82, 1190 Vienna, Austria

Abstract

Regarding failure processes and deformation behaviour of deep-seated rock slides in a glacier-retreat environment, the geology, the geometry and the kinematics of the highly active deep-seated "Marzell" compound rock slide in the Ötztal valley (Tyrol, Austria) was examined. Geomorphological-geological mapping, geodetic survey campaigns and historic and remote sensing data analysis was applied.

The rock slide is located at the SE-facing slope above the Marzell valley glacier (Marzellferner) and extends over a width of 600 m in NE-SW direction and over a height of 400 m from 2450 m a. s. l. (slope toe) to 2850 m a. s. l. (main scarp at 2850 m a. s. l.). Geologically, the rockslide is situated within the fractured, foliated poly-metamorphic rocks of the Ötztal Crystalline (i. e. paragneisses, mica schists and banded amphibolites). Based on historic maps and remote sensing data, the valley glacier has retreated approx. 2 km and more than 150 m in thickness from 1893 onwards. Results from geodetic surveys, starting in 2012, show an actual annual slope velocity ranging from 0.2 m to 0.3 m per year. Distinctive geomorphological features, i. e. primary and secondary scarps, downhill- and uphill-facing scarps, horst and graben structures, as well as trenches and tension fractures indicate the failure and deformation processes of the rock slide. These gravitational morpho-structures preferably evolved along pre-existing tectonic lineaments. The structural features and the measured displacement rates depict the evolution of two different rock slide systems. In addition, deformation monitoring (geodetic surveys, remote sensing data) highlights the evolution of six individual rock slide slabs and their partly response to the Marzellferner glacier retreat.

Zusammenfassung

Im Hinblick auf die Entstehungsprozesse und Deformationseigenschaften von tiefgründigen Massenbewegungen in hochalpinen, ehemals vergletscherten Gebieten, wurde die Geologie, Geometrie und Kinematik der tiefgründigen „Marzell“ Massenbewegung im hintersten Ötztal (Tirol, Österreich) näher untersucht. Die Ergebnisse basieren auf einer geomorphologischen-geologischen Kartierung, geodätischen Vermessungen und der Auswertung von historischen Karten und Fernerkundungsdaten. Die „Marzell“ Massenbewegung befindet sich am südöstlichen Hang des sogenannten Marzellkamms, oberhalb des Marzellferner Gletschers, und erstreckt sich

mit ca. 600 m in NE-SW Richtung und mit ca. 400 m von 2450 m bis 2850 m ü. A. Geologisch betrachtet, liegt die Massenbewegung in den geschieferten, poly-metamorphen Gesteinen des Ötztal Kristallins (d. h. Paragneise, Glimmerschliefer und Amphibolitbänder). Auf Basis von historischen Karten und Fernerkundungsdaten ist der Marzellferner Gletscher seit 1893 um ca. 2 km an Länge und ca. 150 m an Eismächtigkeit zurückgewichen. Die seit 2012 regelmäßig durchgeführten geodätischen Vermessungen zeigen eine aktuelle Bewegung der Massenbewegung von ca. 0,2 m bis 0,3 m/Jahr. Markante geomorphologische Strukturen, wie z. B. Haupt- und Nebenabbrisskanten, Horst- und Grabenstrukturen, Nackentäler und Zugspalten sind vorwiegend entlang ehemaliger tektonischer Lineamente und Klüften entstanden und verdeutlichen die Deformations- und Entstehungsprozesse innerhalb der Massenbewegung. Anhand der geomorphologischen Strukturen und der gemessenen Bewegungsraten, setzt sich die „Marzell“ Massenbewegung aus zwei unterschiedlichen Systemen zusammen. Zudem zeigen Deformationsmessungen eine Untergliederung der Massenbewegung in insgesamt sechs Teilschollen, deren Bewegungsraten z. T. in einem zeitlichen Zusammenhang mit dem Gletscherrückzug stehen.

1 Introduction

Deep-seated rock slides are common phenomena in high mountainous regions, especially in deeply incised Alpine valleys, where many are encountered in foliated metamorphic rock masses, e. g. phyllites, mica-schists, paragneisses (ZANGERL et al, 2010; AGLIARDI et al., 2001). An increased occurrence and/or activity of rock slides is observed in recently de-glaciated regions, most likely related to the debuttressing effect of long term glacial unloading (e. g. MCCOLL, 2012; BALLANTYNE, 2002; etc.). For hazard assessment, prevention and mitigation measures as well as for reliable prediction, the behaviour of rock slides (i. e. kinematics, deformation and failure processes) need to be profoundly understood.

Deep-seated rock slides are usually characterized by a downslope movement of a mass of rock along one or several rupture surfaces or within a relatively narrow zone of intense shear strain (CRUDEN & VARNES, 1996). Considering compound rock slide systems, the rupture surface is usually of an uneven curvature or consists of several planes so that internal distortion of the rock mass is required for sliding (HUNGR et al., 2014). The geometry of the basal rupture surface is commonly characterized by a bilinear or curved plane that daylight as a steep main scarp at the crown and mostly follows horizontal, gently inclined planes of weakness (e. g. foliation planes) that daylight at the slope toe (HUNGR et al., 2014; HUTCHINSON, 1988). The phenomenon is often accompanied by certain morpho-structural features, such as doubled ridges, ridge top depressions, scarps and counterscarps, trenches, horst and graben structures and open tension cracks (AGLIARDI et al., 2001; HUNGR et al., 2014).

In general, deep-seated rock slide slopes can display different deformation modes: (i) first-time failures with catastrophic rapid movements (ii) continuous, slowly movements often with acceleration phases and (iii) more rarely long periods of slow movement followed by sudden failure (PETLEY & ALLISON, 1997). However, in foliated, metamorphic rocks the deformation pattern is often characterized by slow movement and no sudden failure or high velocities. The continuous slope movement leads to progressive rock mass disintegration and internal deformation that in turn influences the rock mass strength and successively favours secondary rock failures, e. g. rock slide/topple at the toe area (MOSER, 2002). Nevertheless, the danger of rapid failure

and subsequently far-reaching, devastating run-out rock avalanches cannot be excluded. Furthermore, rock avalanches could also result in valley blocking and subsequent creek damming that by failure might lead to hazardous landslide break-outs.

The temporal and spatial evolution of these slope instabilities is controlled by predisposing factors. Crucial controlling factors are e. g. topography, lithology, geological structures, in-situ-stresses, groundwater flow, glacier and permafrost degradation, and temperature fluctuations (CROSTA et al., 2013). Furthermore, stress redistribution processes, such as glacier retreat and interactions with valley infillings (erosion at the toe of the rock slide) display a fundamental role on slope stability. Towards a better understanding regarding the controlling factors, the progressive failure mechanisms and slope deformation behaviours, several deep-seated rock slides have been investigated in the last decades, e. g. La Saxe (France) (CROSTA et al., 2013), Valfurva (Italy) (AGLIARDI et al., 2001; CROSTA & AGLIARDI, 2002), Campo Vallemaggia (Italy) (BONZANIGO et al., 2007; PREISIG et al., 2016), Mitchell Creek Landslide MCL (Canada) (CLAYTON et al., 2017), Niedergallmigg (Austria) (ZANGERL et al., 2015), Hochmais-Atemkopf (Austria) (ZANGERL et al., 2010), etc. However, the deformation behaviour of deep-seated rock slides, especially those in foliated metamorphic rocks, needs to be further investigated. And the geo-mechanical behaviour of deep-seated rock slides and the processes that cause fracturing, fragmentation and internal deformation of rock masses is still not comprehensively understood and plays an important role on the stress-strain regime and failure processes (ZANGERL et al., 2010).

The presented study focuses on the investigation of (i) rock slide kinematics, (ii) rock slide deformation and failure processes, and (iii) the debuttrressing effect on slope stability. Therefore, the highly active, deep-seated Marzell rock slide in a high Alpine, glacier-retreat environment in the Ötztal valley in Northern Tyrol, Austria (Vent: 46°47'37.16" N, 10°52'54.96" E) is examined. The investigated Marzell rock slide is a compound, deep-seated rock slide located in fractured, foliated metamorphic rocks and exhibits an actual average velocity of 0.2 m to 0.3 m per year. The slide is located at the SE-facing slope of the NE-SW trending Marzell ridge above the Marzellerferner glacier and close to the Martin-Busch hut (2501 m a. s. l.) (Fig. 1). Due to increased slope deformations and frequent rock fall events, a passing hiking trail of the Austrian Alpine Association (ÖAV) had to be relocated. Since 2012, investigations regarding the rock slide evolution and the glacier retreat, based on historic maps and remote sensing data, have been carried out by FEY et al. (2017). The performed data analyses show a temporal relationship between glacier retreat and rock slide activity. Hence, deglaciation of the Marzell valley glacier is seen as a contributing key factor on the slope instability.

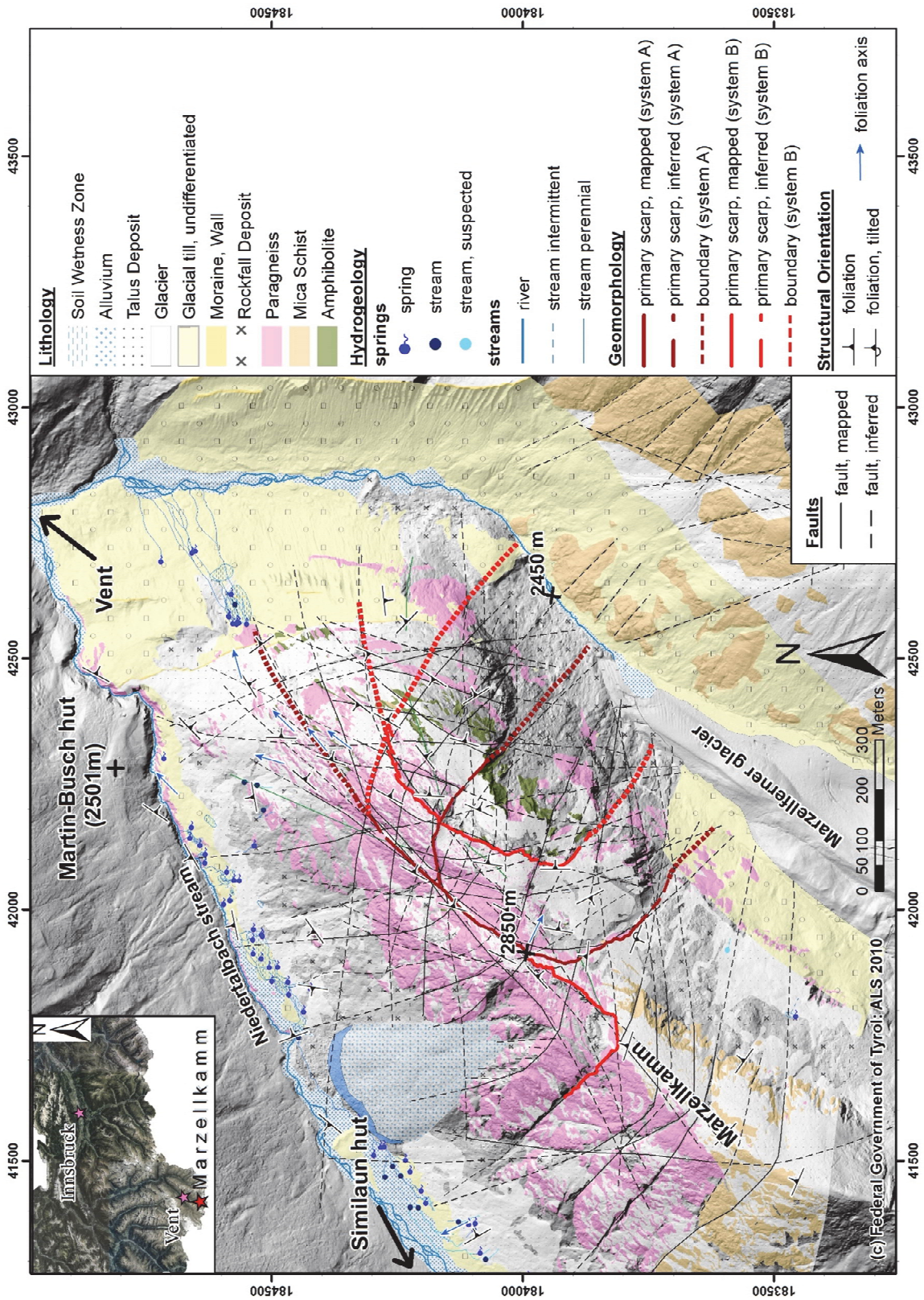


Fig. 1: Geological and tectonic setting of the Marzell ridge (Marzellkamm) and its immediate vicinity.

2 Methods & Data

In order to reconstruct the initial failure processes and subsequent deformation characteristics of the deep-seated Marzell rock slide, a multi-disciplinary approach is applied. The compound rock slide is examined by field mapping (i. e. geology, geomorphology), geodetic field surveys, historic maps and remote sensing techniques (i. e. LiDAR and photogrammetry). Due to the remote, partly inaccessible and dangerous terrain of the study site, the in-situ investigation of the Marzell rock slide is limited and expensive, e. g. seismic surveys and drillings for borehole data, inclinometers and piezometers aren't feasible.

2.1 Geological and geomorphological mapping

To understand the influence of geological, structural and geomorphological structures on slope stability, a geological-geomorphological mapping campaign was carried out. The mapping was performed by using ortho-images and topographic maps on a scale of 1:1000. Additionally, existing geological map sheets of the study site on a scale of 1:50.000 and 1:75.000 (KREUSS, 2016, SCHMIDEGG, 1932) were used. Furthermore, shaded relief maps of different illumination angles as well as a slope gradient map of 1 m resolution, derived from the 2010 Digital Elevation Model (DEM), were applied. Due to hard-accessible terrain, especially at the toe of the rock slide, the mapping was partially limited.

The geological mapping consisted of the lithological recording of bedrock and unconsolidated rock outcrops at the study site as well as of the determination of their structural feature. Since rock discontinuities predominantly characterize rock mechanic behaviour (ZANGERL et al., 2008), extensive measurements of structural features across the project site were performed. The general emphasis was set on the determination of the discontinuity type (foliation, joint sets, faults) and its orientation (dip, dip direction). For each discontinuity type, several measurements of the dip and dip direction were performed to achieve a representative averaged orientation value. For graphical and statistical analysis, the recorded orientation data was illustrated in a contoured pole density plot using a stereographic hemispherical projection of equal area and equatorial plane. Furthermore, observed secondary folds (S-, Z-, and M-folds) were used to map out the local fold structure.

A fundamental basis for understanding rock slide evolution is given by geomorphological mapping (AGLIARDI et al., 2001) and consisted of the identification of geomorphological structures. Focus was set on the mapping of such structures, such as head scarps, secondary scarps, downhill- and uphill-facing scarps, horst and graben structures, trenches and open tension cracks. Measurements of total displacements along scarps and of the opening width of cracks display deformation processes within the rock slide system. Mapped lichen coverage, tensioned roots and cracks in soil cover give further information about the actual slope activity. Glacial morphological structures, i. e. lateral moraines, moraine walls and glacially polished bedrocks were identified. Additionally, the hydrogeological setting of the project site was investigated regarding springs, streams and wet zones.

2.2 Deformation and glacier monitoring

In order to assess and reconstruct the Marzell glacier retreat and the rock slide evolution, historical maps and remote sensing data were analysed. Digital elevation

models (DEM) created from the historical maps 1893 and 1949 (KLEBESBERG, 1949), from glacier inventories from 1969 and 1997 (PATZELT, 2013; GROß, 1987; LAMBRECHT & KUHN, 2007; KUHN et al., 2013; ABERMANN et al., 2009; FISCHER et al., 2015), from photogrammetrically processed aerial images (2003), from airborne laser scan (ALS) flights (2006 and 2010), and from a terrestrial laser scan campaign in 2014 were used to quantify the temporal evolution of glacial retreat by reconstructing the glacier surface and thickness (FEY et al., 2017).

The rock slide behaviour is reconstructed from 1953 onwards by means of already available data from national and federal state aerial imaging campaigns (1953, 1971, 1997, 2003, 2009) and airborne laser scans (2006, 2010). From 2012 onwards, the rock slide was monitored by campaigns of geodetic surveying by tachymetry and GNSS (2012, 2013, 2014, 2017) (see geodetic network in Fig. 3), TLS (2014) and an aerial imaging campaign by UAV (2012) (FEY et al. 2017). The remote sensing data from the different data sources were compiled and studied with the aim to analyse the rock slide deformation evolution by extracting information about the displacement direction, dip angle, velocity and partial failure of rockslide slabs since 1951. For a detailed description of the data processing and analyses methods see FEY et al. 2017.

3 Results

3.1 Glacier retreat reconstruction

Based on the historic and remote sensing data, the Marzell glacier retreat has been reconstructed focussing on spatial extent and volume change (Fig. 2). From 1893 onwards, the valley glacier has retreated approx. 2 km in length (Fig. 2, bottom right) and has shrunk more than 150 m in thickness (Fig. 2, top left). In the last decades, an acceleration of the Marzell glacier retreat has been observed, e. g. between 1893 and 1949 (56 years) the glacier has shrunk approx. by 25 m and lost approx. 500 m in length, whereas between 1949 and 2006 (57 years) the glacier retreated approx. 80 m in thickness and 1.5 km in length. Notably, in 1893 almost half of the SE-facing rock slide slope was covered by glacial ice and till, whereas these days all glacial ice coverage has gone. For further calculations of changes in glacier volume, ice load and ice surface extent between 1893 and 2014 adjacent to the project site, see FEY et al., 2017.

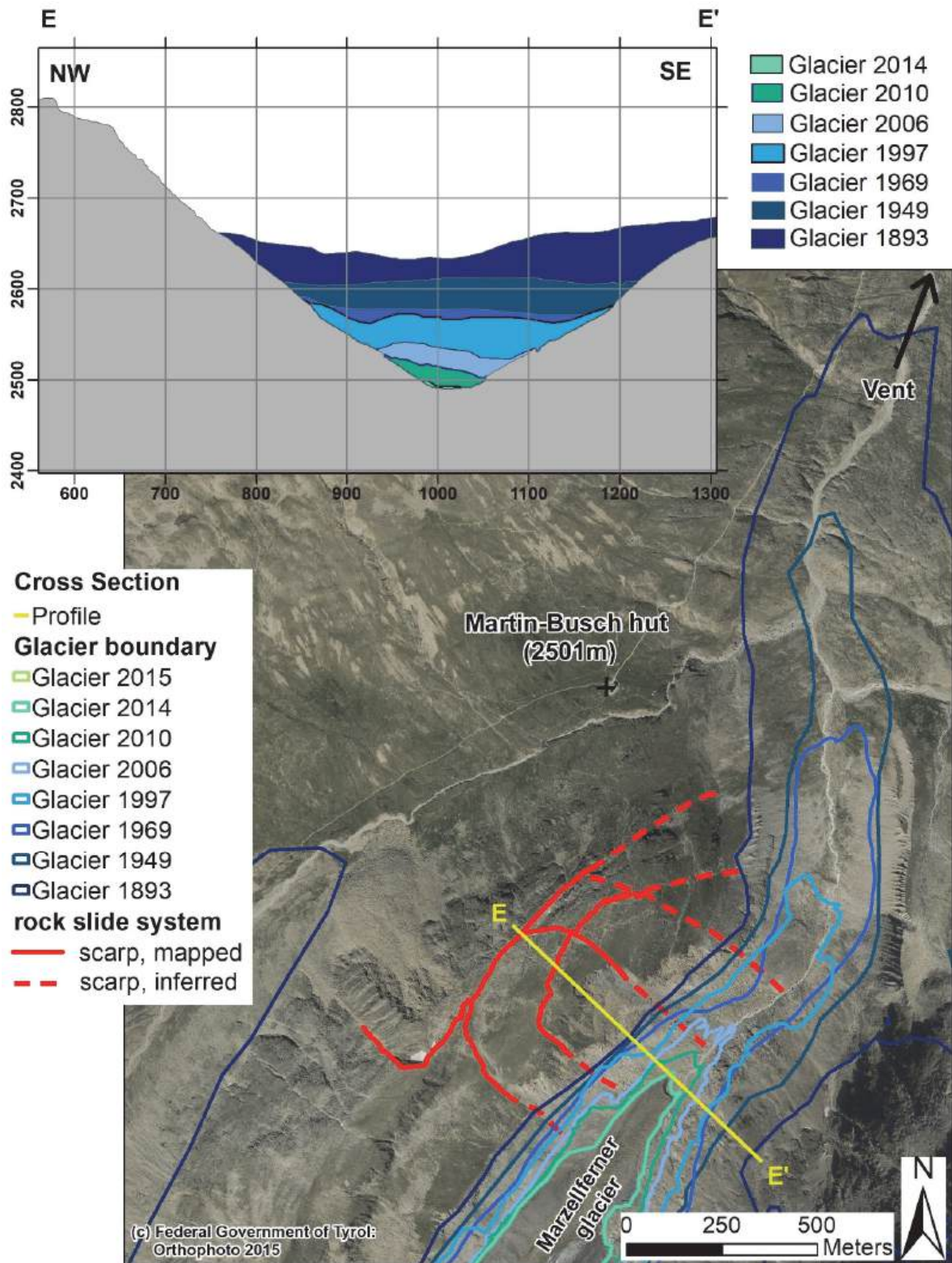


Fig. 2: Illustration of the Marzellferner glacier evolution between 1893 and 2015. Bottom right: spatial glacier extent; and top left: the glacier ice thickness along the cross section E-E' (modified after FEY et al., 2017).

3.2 Geology and Geomorphology

The Marzell rock slide extends approx. 600 m in NE-SW direction and approx. 400 m from the slope toe at 2450 m a. s. l. to the main scarp at 2850 m a. s. l. A morphological characteristic of the rock slide is the evolution of two interlocking main scarps (Fig. 1, Fig. 4). Offsets on the main scarps indicate a total displacement of the rock mass of 20 m to 30 m (Fig. 6 a). Gravitational morpho-structures, such as secondary scarps (Fig. 6 b, Fig. 7 c), opened cracks (Fig. 5 b, Fig. 7 b) and trenches (Fig. 6 b, Fig. 7 d) as well as horst and graben structures (Fig. 6 b) are observed. Considering these morphological features and different stages of lichen coverage at the scarp planes, a differentiation of the Marzell rock slide into two rock slides of a different formation age can be made: system A (main scarp at 2850 m a. s. l.), system B (main scarp at 2750 m a. s. l.). In contrast to system A, morphological structures, such as the main scarp of system B (Fig. 6 a), are almost free of lichen coverage and indicate a more recent formation. A further characteristic of system B is that it consists of an area outside and inside the older system A. The area outside of system A is characterized by a stepped secondary scarp, approx. 50 – 100 m below the main scarp, and shows an offset of about 8 m (Fig. 7 c). Below that secondary scarp, several distinctive NE-SW orientated trenches transect the rock slide system B (Fig. 7 d), whereas horst- and graben structures mark the area above. In 2017, newly formed soil cracks, tensioned roots, frequent rock falls (Fig. 3) and rock avalanches (Fig. 7 a) were observed at the slope toe of system B. According to the determined geomorphological structures (i. e. newly opened tension cracks, newly formed secondary scarps, trenches, etc.), an obvious higher activity of system B is given.

Geologically, the rock slide is situated within the poly-metamorphic units of the Ötztal Crystalline of the Upper Austroalpine Nappe System (SCHMID et al., 2004). It is mainly composed of three metamorphic rock types, i. e. paragneiss, mica schist and banded amphibolite. Locally, the rock units are characterized by steeply inclined fold axes, known as the so-called “Schlingensbau” that originated during the Caledonian orogeny (SCHMIDEGG, 1936). In the northern part of the study area, the foliation is striking NE-SW with a steep fold axis to the NE. In the southern part, the foliation strikes E-W with a moderate dipping fold axis to the E (Fig. 1). The primary foliation of the rock mass is moderately to steeply dipping towards SE, in slope direction, respectively (Fig. 8 a).

Steeply inclined NE-SW and E-W striking brittle fault zones separate the rock mass into large slabs (Fig. 1, Fig. 8 b). The fault zones at the Marzell ridge are generally characterized by internal deformation features, i. e. fault gouges, fracturing and fragmentation. Visible mylonites within the fault zones suppose an initial ductile overprint of the rock mass. The intensive faulting of the rock mass influences the rock mass strength and leads to a loosening of the rock mass (Fig. 5 c). On several scarp planes of system A and system B, slickenside features with flat, almost horizontal striations indicate tectonic movements. Thus, the main rock slide structures, e. g. scarps and trenches generally evolved along pre-existing fault zones and planes (Fig. 1). It is assumed that distinctive foliation and transecting fault zones influence the hydrogeological setting, particularly rock hydraulics. At the SE-facing slope of the Marzell ridge springs or wetness zones are completely missing, whereas multiple springs have been observed in the lower slopes along the Niederbachtal valley (Fig. 1).

Glacial morphological characteristics, i. e. U-shaped valleys, lateral moraines and rock glaciers (Fig. 1), as well as striated and smoothed bedrock reflect the glacial history of the Marzell ridge and its immediate surrounding. Thus, the SE-facing slope of the Marzell ridge was shaped by the Marzell glacier. For instance, lateral moraine walls, belonging to the last glacial maximum in 1850 (LIA), are observed approx. 300 - 350 m below the main scarp of the rock slide system (Fig. 2, Fig. 4). Striated and smoothed bedrock are found on top and within the sliding rock mass (e. g. crest, horst and graben structure).

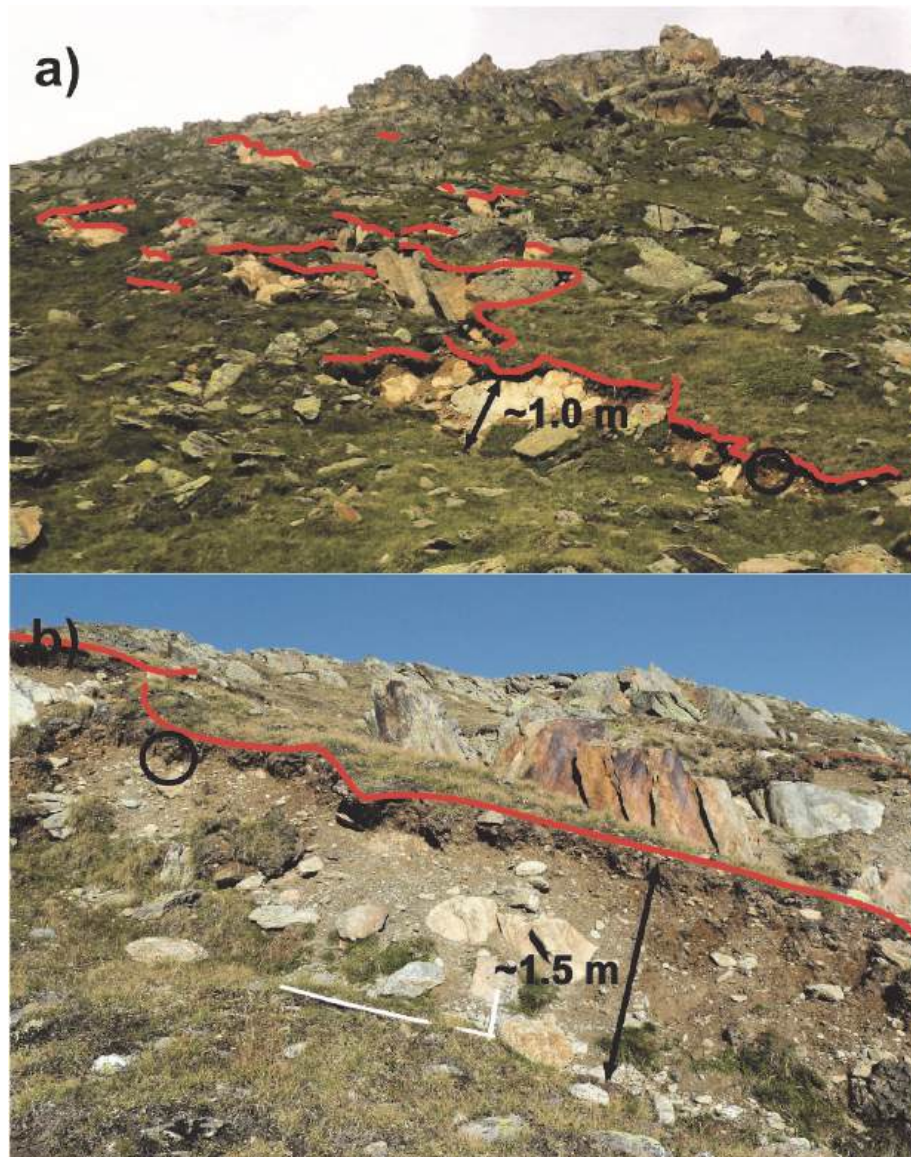


Fig. 3: Fresh cracks in soil (red lines) and tensioned grassroots (black circle) within the rock slide slab VI (system B) indicating recent displacement. a) Several fresh soil cracks (without lichen coverage) within the transit zone of an active rock fall area. b) A fresh soil crack showing a total displacement of approx. 1.5 m. The location of slabs is shown in Fig. 9.

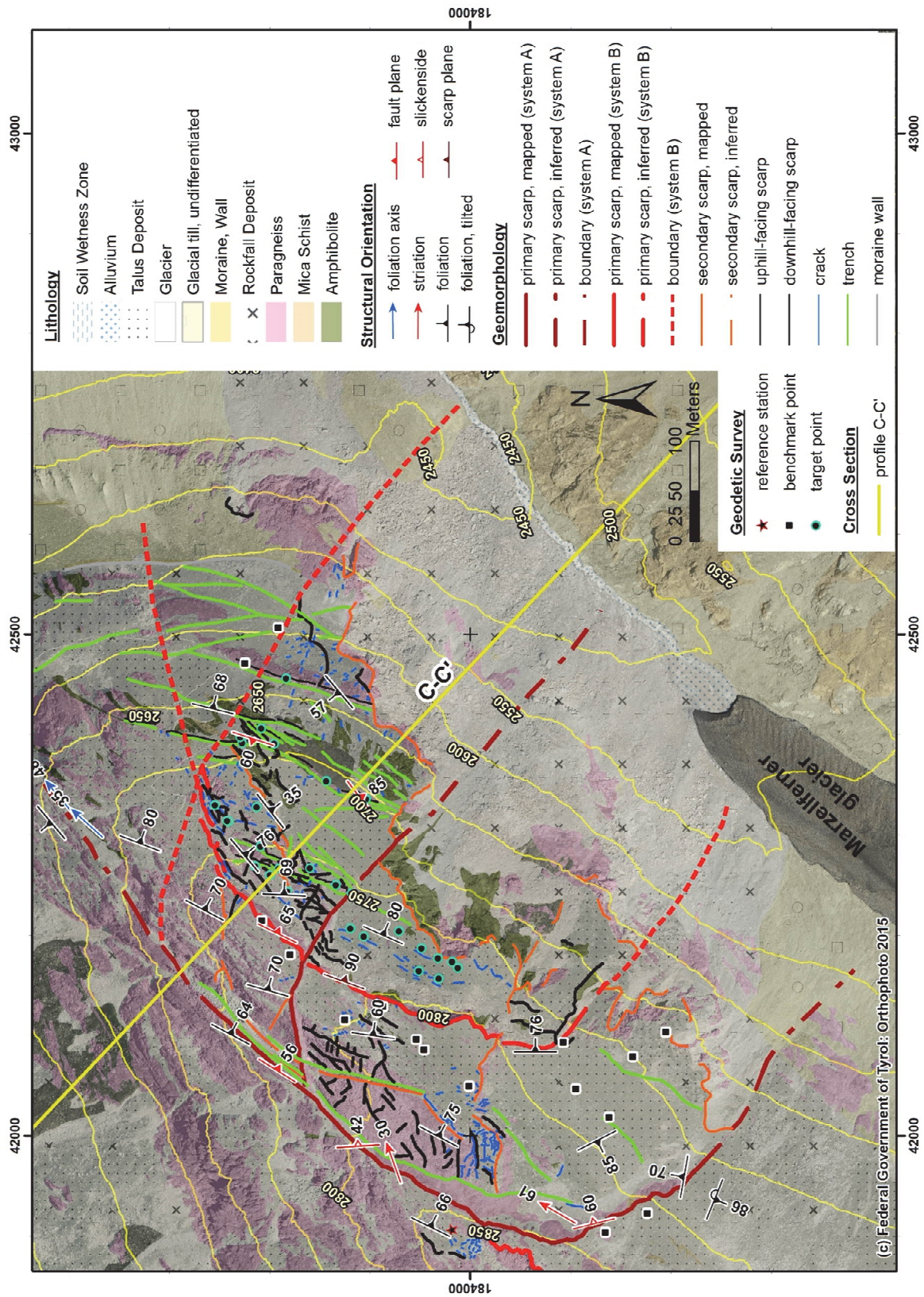


Fig. 4: Geological map showing rock type, structural and geomorphological features of the Marzell rock slide.

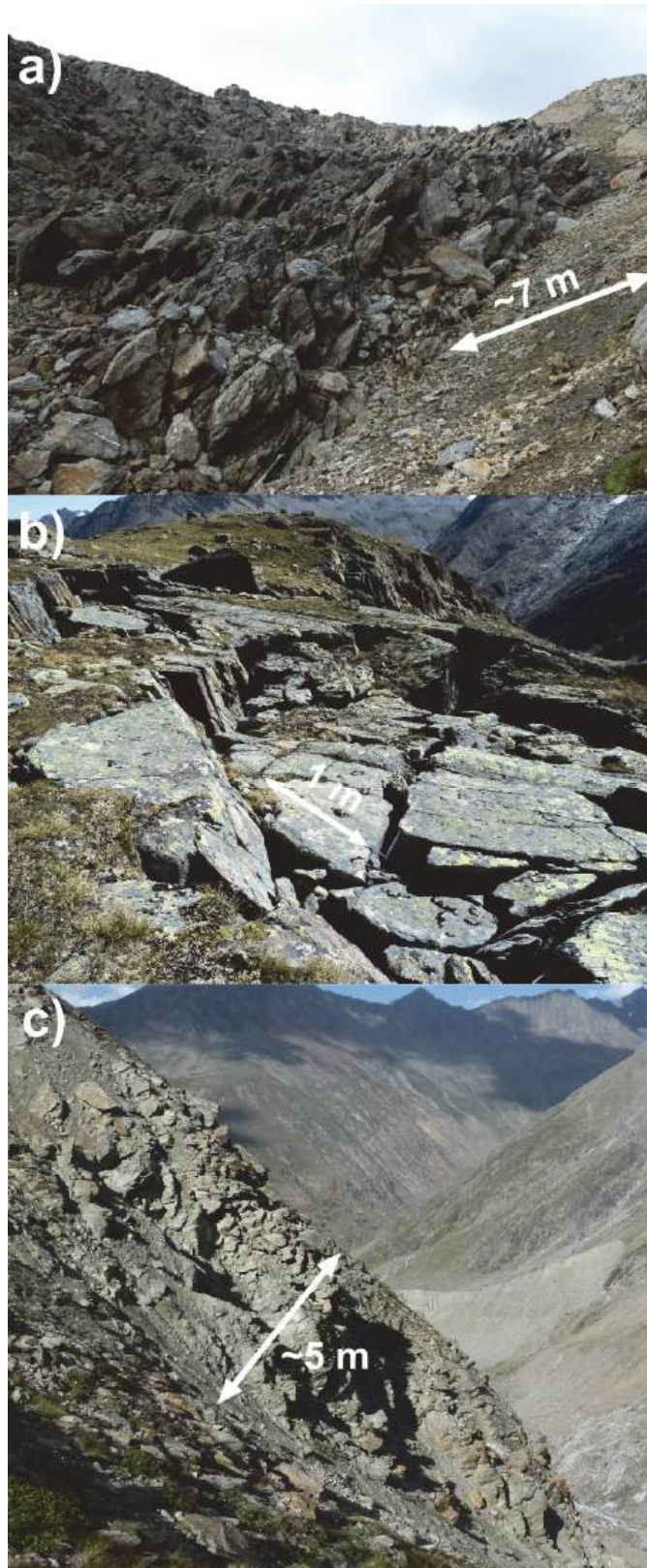


Fig. 5: Geomorphological features within the rock slide system A. a) Detached mass of slab II beneath main scarp; b) tension cracks subparallel to secondary scarps within slab II; c) dislocated and disintegrated rock slide mass within slab I. The location of slabs is shown in Fig. 9.

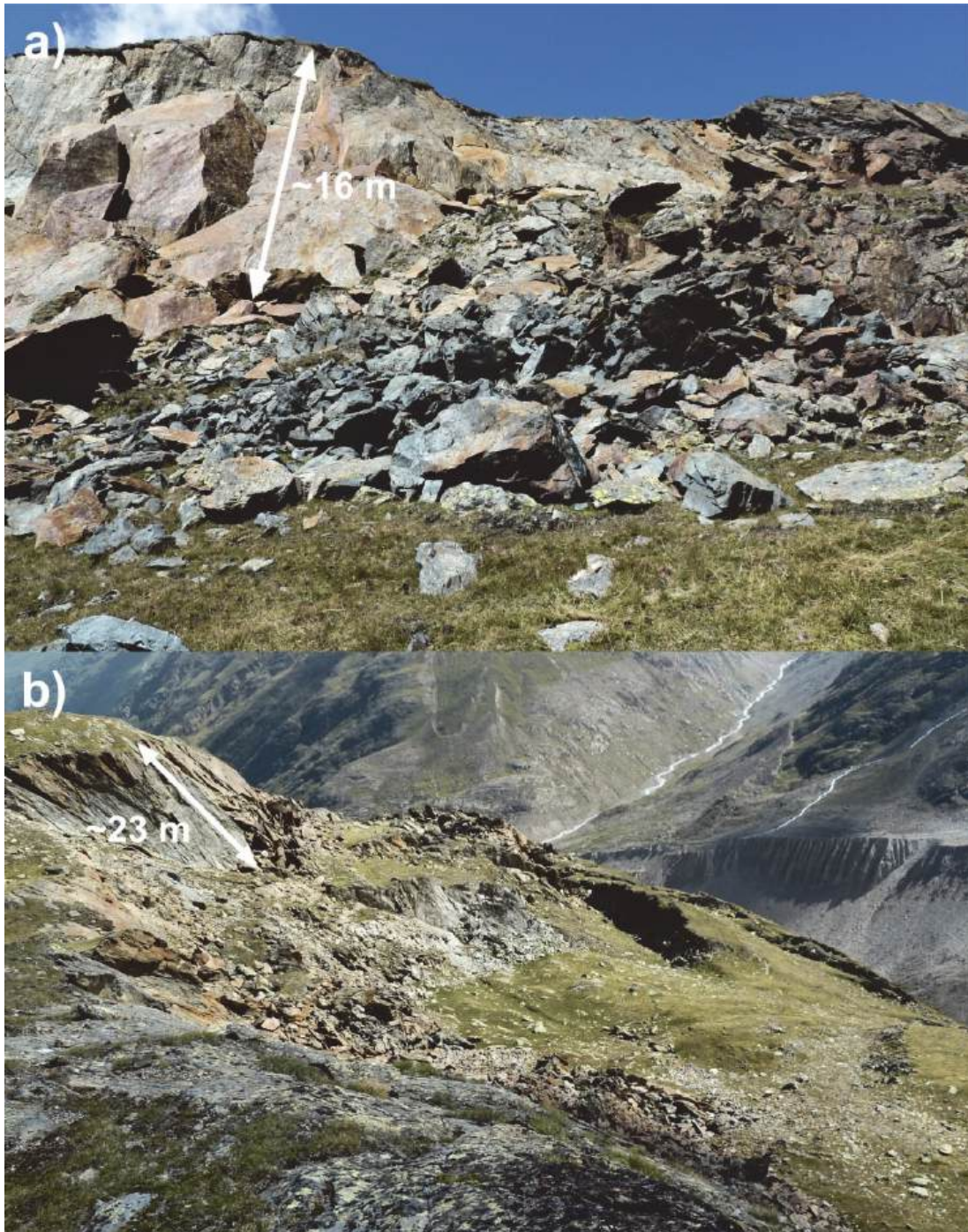


Fig. 6: Geomorphological features within the rock slide system B. a) Main scarp without lichen coverage; b) slab III (in front), slab V and VI (behind), which are characterized by horst and graben structures, several secondary scarps and trenches. The location of slabs is shown in Fig. 9.

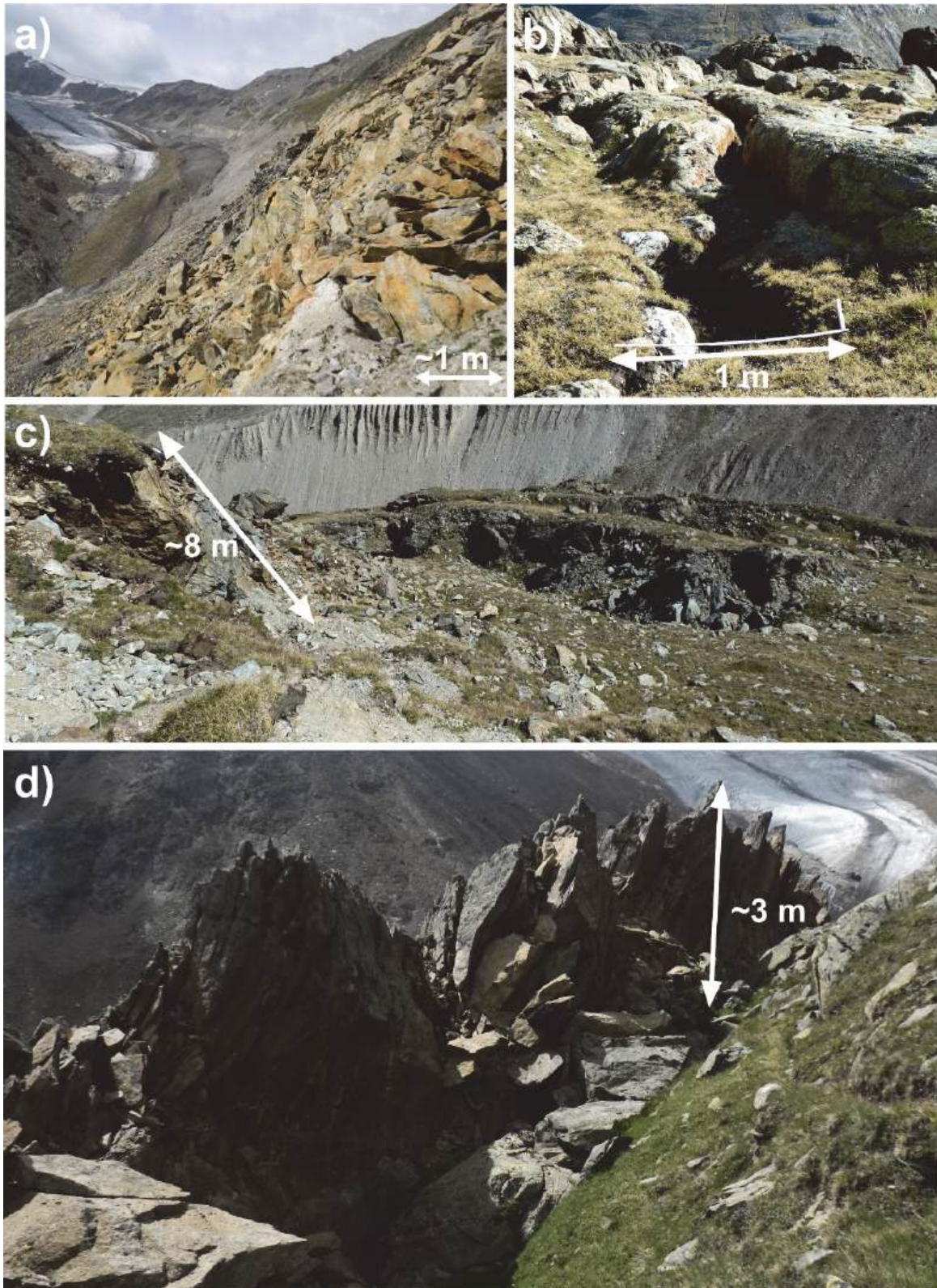


Fig. 7: Geomorphological features within the rock slide system B. a) Failed rock slide mass beneath secondary scarp of slab III; b) tension cracks within the graben structure of slab V; c) secondary scarps within slab VI; d) formation of trenches within slab VI, which are characterized by uphill-facing scarps. The location of slabs is shown in Fig. 9.

3.3 Structural analysis

In order to ensure an area-wide analysis of the structural setting of the study site, numerous orientation measurements of the encountered bedrock outcrops were recorded and statistically analysed in DIPS v7.0 (Rocscience). The analysis is illustrated in a contoured pole density plot, showing foliation (Fig. 8 a), faults (Fig. 8 b) and joint sets (Fig. 8 c). The metamorphic rock mass shows a primary foliation (f1) dipping moderately towards SE (097/69) (Fig. 8 a). Additionally, a minor foliation (f2) dipping moderately to steeply towards N (097/69) is observed. The measured foliation planes are distributed along a great circle (π -circle, Fig. 8 a), whose pole corresponds to the fold axis (fx). The fold axis is also indicated by the intersection of the mean great circles f1 and f2. Hence, the primary foliation axis is dipping moderately towards NE (055/60).

The contoured density plot of fault planes (Fig. 8b) indicates a moderately (fs1) to steeply (fs2) inclined NNE-SSW striking fault system (fs1: 117/45; fs2: 108/83). A third major fault system is dipping steeply towards S (196/79). Joint set analysis shows that the joint planes are distributed along a great circle. The major joint sets are dipping steeply to moderately towards NE to E direction (Fig. 8 c).

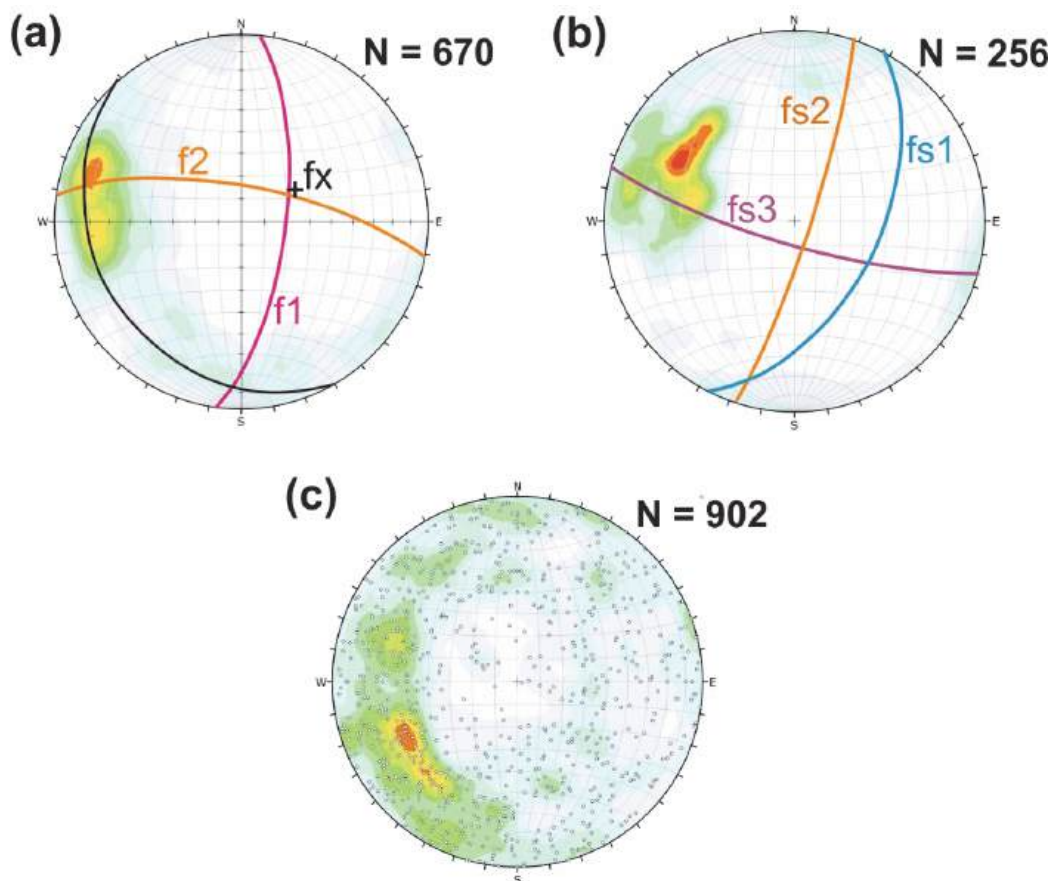


Fig. 8: Hemispherical projection (lower hemisphere, equal angle) of the measured structural field data within the rock slide system and its immediate vicinity: Contoured pole density plots of (a) foliation planes and its distribution along the π -circle (black); (b) fault planes; and (c) joints sets.

3.4 Slope displacement from 2012 to 2017

Analysis of the geodetic measurements, starting in 2012 (i. e. reference survey), show a general movement of the Marzell rock slide towards SE (Fig. 9). The total displacements (Δ_{xyz}) increase from the main scarp to the slope toe and from the lateral boundaries towards the central rock slide zone. Based on the structurally, geological features and the measured displacements, six slabs I-VI were distinguished (Fig. 9). For each rock slide, the average total displacement vectors between the years 2012 and 2017 are shown in Tab. 1. The total displacements for the individual rock slide slabs are displayed in Fig. 10. Displacements up to 1.0 m to 1.5 m for slab III and slab VI and up to 0.4 m for slab I and V are observed. The displacements of slab II and V vary between < 0.04 m (below surveying precision) and 0.25 m. The movement rates of slab III, V, and VI indicate a high activity of the newly formed rock slide system B. Generally, the rock slide is characterized by an acceleration phase in 2013, which is now followed by continuously ongoing deceleration phase.

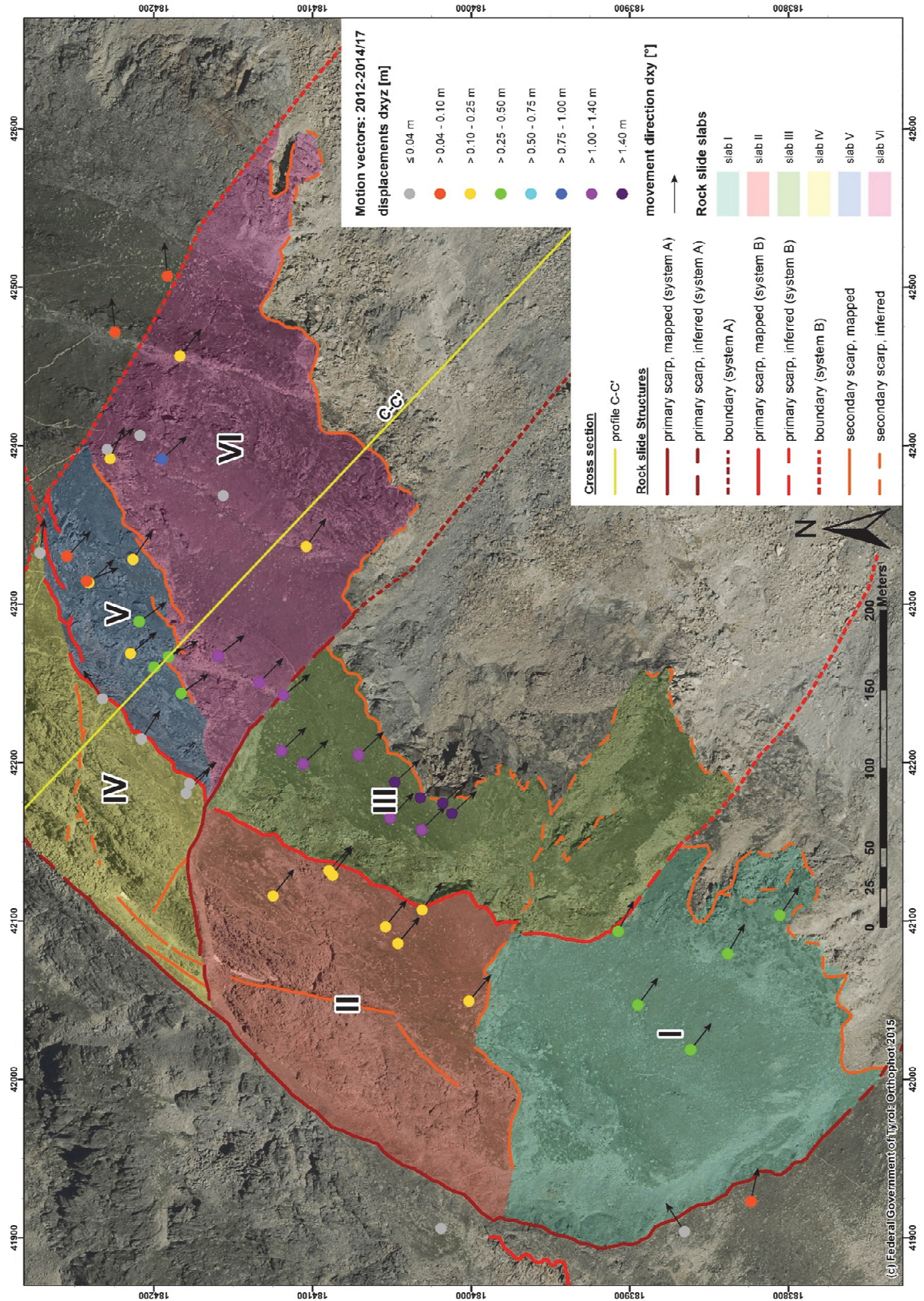


Fig. 9: Displacement vectors illustrating the movement directions (black arrows) and displacements (colour dots) of the individual slabs of the geodetic survey points between 2012 and 2017.

Tab. 1: The total displacement vectors (3D) between 2012 and 2017 of the individual rock slide slabs. *system A

	total displacement (Δxyz) [m]	Azimuth [°]	dip angle (of vector) [°]
slab I*	0.25 – 0.50	117 – 128	25 - 38
slab II*	0.10 – 0.25	126 – 132	42 - 60
slab III	1.00 – 1.40 > 1.40 (near scarp)	133 – 138	48 - 54
slab IV*	< 0.04	123 – 135	33 - 44
slab V	0.10 – 0.25 0.25 – 0.50 (near scarp)	125 – 152	36 - 58
slab VI	0.10 – 0.75 1.00 – 1.40 (near slab III)	137 – 142	39 - 54

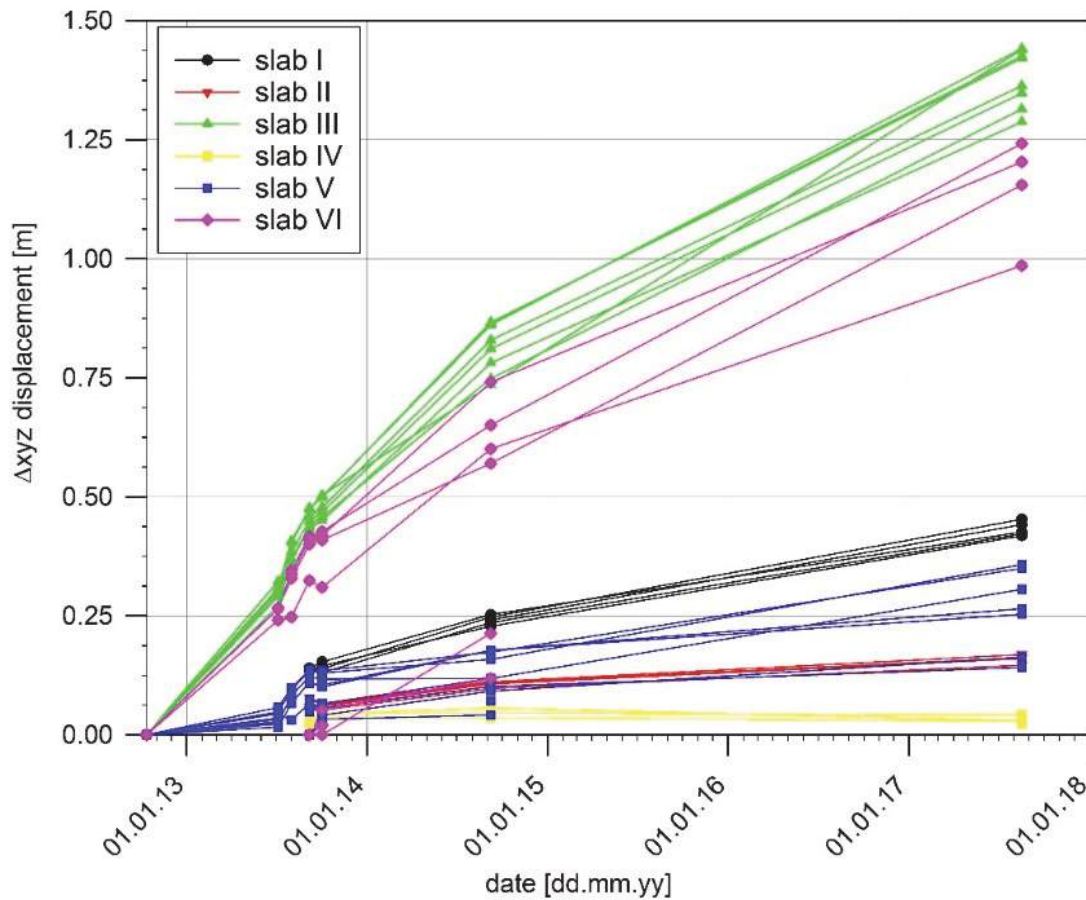


Fig. 10: 3D-displacements [m] of slab I, II, III, IV, V and slab VI from 10/2012 to 08/2017.

3.5 Rock slide evolution and its interaction with glacier retreat

Based on the topographic maps and ortho-images, the spatio-temporal deformation pattern of the rock slide was reconstructed from various displacement features observed within the rock slide mass. Hence, a temporal relationship between glacier retreat (Fig. 2) and rock slide activity could be observed (see FEY et al., 2017). In the period between 1971 and 1997, the average loss of ice thickness was about 0.1 m/year, whereas the average rock slide displacement rate was about 0.05 m/year. In the 2000s, the displacement rates accelerated up to 1.5 m/year and the average ice thickness loss was about 5 m/year. However, a deceleration of the rock slide activity is observed since 2010. Additionally, reconstructions of the Marzell glacier volume change correlate with the rock slide displacement rates. For further details on the reconstruction of the rock slide evolution and its interaction with the glacier retreat see FEY et al. (2017).

3.6 Geometrical-geomechanical and kinematical model

A preliminary geometrical, geological and geo-mechanical model, showing the kinematics and deformation processes, is derived along a NW-SE orientated cross section (Fig. 11). The cross section transects the eastern part of the Marzell rock slide system, i. e. slabs IV, V and VI (see Fig. 4, Fig. 9) which are characterized by SE directed displacements. These rock slide slabs are basically separated by shear zones with distinct displacements. Along these scarp planes, sub-horizontal slickenside (fault breccia and gouge) features indicate that these shear zones partly or totally evolved along pre-existing fault systems.

At the crown of the rock slide (about 2780 m a. s. l.), the basal shear zone outcrops as a steep main scarp (approx. 65°) with an offset of 23 m and separates system B (slab V, slab VI) from the older system A (slab IV). Geological field data and surface deformation monitoring suggest a persistent basal shear zone flattening towards the slope toe that presumably daylight above the valley floor at about 2480 m a. s. l. However, this could not be proven because no seismic and borehole data are available. Along the basal shear zone, deformation is characterized by a maximum displacement near the top (i. e. offset at the head scarp) which continuously declines towards the bottom.

A distinct secondary scarp, dipping approx. 51° towards SE, evolved about 50 m below the main scarp, separating slab VI with an offset of 8 m from slab V. The wedge-like slab V is generally characterized by horst and graben structures (Fig. 6 b) indicating an extensional regime near the top of the rock slide. On top of slab V, the more active slab VI continuously slides downwards SE. Between 2010 and 2017, successive rock mass failures at the slope toe of slab VI, resulting in rock fall deposits covering large areas of the valley floor, were observed (Fig. 7 a). Furthermore, slab V and slab VI are characterized by NE-SW orientated trenches (uphill-facing scarps) that were formed along pre-existing fault zones (Fig. 7 d).

Considering the presented NW-SE orientated cross section (Fig. 11), the total Marzell rock slide comprises a maximum slab thickness of approx. 70 m.

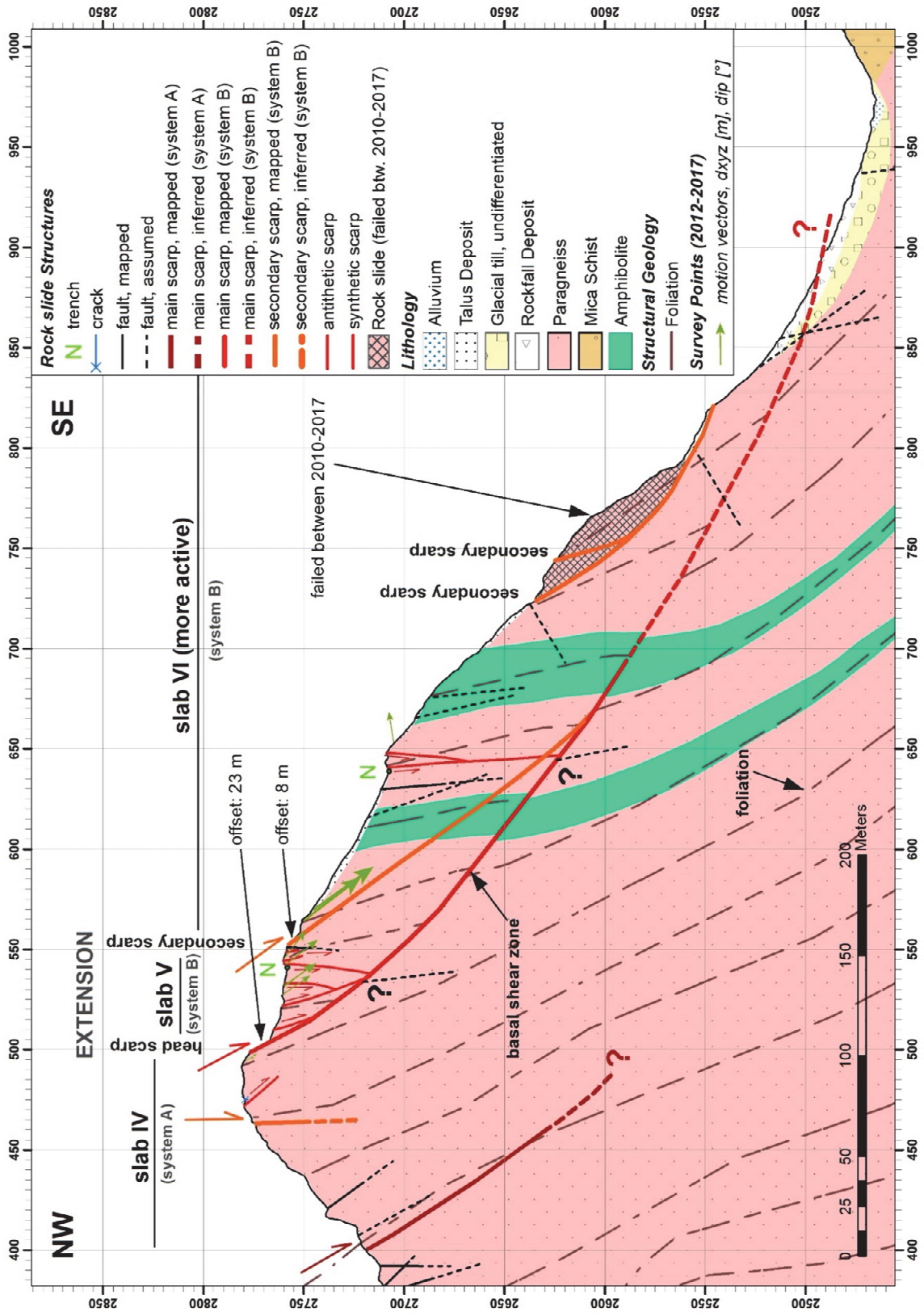


Fig. 11: Preliminary NW-SE cross section along C-C' (see Fig. 4) showing the rock slide geometry, geological setting and dip of total displacement vectors of geodetic survey points.

4 Discussion & Conclusion

At the Marzell rock slide, geological and geomorphological structures and different stages of lichen coverage highlight the evolution of two rock slide systems of different formation age: system A (main scarp at 2850 m a. s. l.), system B (main scarp at 2750 m a. s. l.). In contrast to system A, the scarp of system B is almost free of lichen and indicates a more recent formation. Additionally, surface deformation monitoring (geodetic surveys, remote sensing data) enables a differentiation of the Marzell rock slide into six individual slabs of different failure and deformation processes.

The evolution of the individual rock slide slabs is characterized by zones of intense shear along which displacement occurs. Tectonic-related slickenside features show that the basal and secondary shearing zones generated along pre-existing fault zones, hence rock mass weakness zones. Distinctive morphological structures, such as secondary downhill- and uphill-facing scarps, trenches and open tension fractures are typical features across the Marzell rock slide.

Generally, ongoing slope movement towards SE lead to extensional features near the head scarp (horst and graben, trenches, tensioned fractures) and to bulging and slope steepening at the lower part of the rockslide. According to surface deformation measurements (see motion vectors in Fig. 11), it is assumed that in the early stage of rock slide failure, extensional features (i. e. horst and graben structure) developed, which are currently moving downwards the basal shear zone.

Furthermore, surface deformation monitoring displays a high activity of system B of an annual average velocity of 0.2 m to 0.3 m per year, whereas system A shows hardly any movement. The higher velocity pattern of system B agrees with the missing lichen coverage and the mapped geomorphological structures (i. e. newly opened tension cracks, etc.). Since 2013, decelerating movement rates of system B are observed. Generally, the Marzell compound rock slide is characterized by continuous movement rates of several centimetres per year.

The case study further shows a temporal relationship between rock slide evolution and loss in glacier volume (FEY et al., 2017). Hence, long-term glacial unloading is assumed to hydro-geomechanically impact the rock mass stability causing temporal changes on progressive failure processes and different deformation behaviour.

In conclusion, the Marzell rock slide demonstrates that geological structures and geomorphological mapping campaigns, surface deformation monitoring and historic and remote sensing data analyses enable to generate a preliminary conceptual geological, geometrical and kinematical rock slide model. Based on this conceptual rock slide model, numerical modelling regarding the impact of glacier retreat on stress distribution, rock mass strength and slope stability will be performed.

Acknowledgment

The authors wish to acknowledge and thank the Austrian Society for Geomechanics (ÖGG) for supporting this study. We further thank the Federal Government of Tyrol for the provision of ortho-images and Digital Elevation Models and Erwin Heine, the Institute of Surveying, Remote Sensing and Land Information (IVFL) of the University of Natural Resources and Life Sciences Vienna, for assisting the geodetic measurement campaigns in 2017.

References

- ABERMANN, J., LAMBRECHT, A., FISCHER, A., KUHN, M., (2009): *Quantifying changes and trends in glacier area and volume in the Austrian Ötztal Alps (1969-1997-2006)*. Cryosphere 3, 205 - 215.
- AGLIARDI, F., CROSTA, G., ZANCHI, A. (2001): *Structural constraints on deep-seated slope deformation kinematics*. Engineering Geology, 59, 83 - 102.
- BALLANTYNE, C. K. (2002): *Paraglacial geomorphology*. Quaternary Science Reviews, 1, 1935 - 2017
- BONZANIGO, L., EBERHARDT, E., LOEW, S. (2007): *Long-term investigation of a deep-seated creeping landslide in crystalline rock. Part I. Geological and hydromechanical factors controlling the Campo Vallemaggia landslide*. Canadian Geotechnical Journal 44, 1157 - 1180.
- CLAYTON, A., STEAD, D., KINAKIN, D., WOLTER, A. (2017): *Engineering geomorphological interpretation of the Mitchell Creek Landslide, British Columbia, Canada*. Landslides, 14, 1655 - 1675.
- CROSTA, G. B., AGLIARDI, F. (2002): *How to obtain alert velocity thresholds for large rockslides*. Physics and Chemistry of the Earth, Parts A/B/C, 27, 1557 - 1565.
- CROSTA, G. B., PRATTINI, P., AGLIARDI, F. (2013): *Deep seated gravitational slope deformations in the European Alps*. Tectonophysics, 605, 13 - 23.
- CRUDEN, D. M., VARNES, D. J. (1996): *Landslide Types and Processes*. In: TUNER, A. K., SCHUSTER, R. L. (eds.) (2006): *Landslides Investigation and Mitigation*. – 36-75, Transportation Research Board Special Report 247.
- FISCHER, L., SEISER, B., STOCKER WALDHUBER, M., MITTERER, C., ABERMANN, J. (2015): *Tracing glacier changes in Austria from the Little Ice Age to the present using a lidar-based high-resolution glacier inventory in Austria*. Cryosphere, 9, 753 - 766.
- FEY, C., WICHMANN, V., ZANGERL, C. (2017): *Reconstructing the evolution of a deep seated rockslide (Marzell) and its response to glacial retreat based on historic and remote sensing data*. Geomorphology, 298, 72 - 85.
- GROß, G. (1987): *Der Flächenverlust der Gletscher in Österreich 1850-1920-1969*. Zeit. Gletscherk. Glazialgeol., 131 - 141.
- HUNGR, O., LEROUÉIL, S., PICARELLI, L. (2014): *The Varnes Classification of landslide types, an update*. Landslides, 11, 167 - 194.
- HUTCHINSON, J. N. (1988): *GENERAL REPORT: Morphological and geotechnical parameters of landslides in relation to geology and hydrogeology*. Proceedings, Fifth International Symposium on Landslides (Ed: Bonnard, C.), 1, 3 - 35.
- KLEBESBERG, R. (1949): *Von den Gletschern auf Blatt Gurgl und den Gletschermessungen des Alpenvereins*. Österreichischer Alpenverein (ÖAV). Jahrbuch 1949 – Alpenvereinszeitschrift, Wagner, Innsbruck, 30 - 36.
- KREUSS, O. (2016): *Geofast 1:50 000, Blatt 173 Sölden*. Geologische Bundesanstalt.

- KUHN, M., LAMBRECHT, A., ABERMANN, J. (2013): *Austrian Glacier Inventory 1998 (G II)*.
- LAMBRECHT, A., KUHN, M. (2007): *Glacier changes in the Austrian Alps during the last three decades, derived from the new Austrian glacier inventory*. Ann. Glaciol., 46, 177 - 184.
- MCCOLL, S. T. (2012): *Paraglacial rock-slope stability*. Geomorphology 153-154, 1 - 16.
- MOSER, M. (2002): *The effect of deep-seated mass movements on the Alpine environment*. International Congress INTERPRAEVENT 2002 in the Pacific Rim (Masumoto/Japan), 2, 641 - 653.
- PATZELT, G. (2013): *Austrian glacier inventory 1969 (G I)*.
- PETLEY, D. N., ALLISON, R. J. (1997): *The mechanics of deep-seated landslides*. Earth Surface Processes and Landforms, 22, 747 - 758.
- PREISIG, G., EBERHARDT, E., SMITHYMAN, M., PREH, A., BONZANIGO, L. (2016). *Hydro-mechanical Rock Mass Fatigue in Deep-Seated Landslides Accompanying Seasonal Variations in Pore Pressures*. Rock Mechanics and Rock Engineering, 49, 2333 - 2351.
- SCHMID, S. M., FÜGENSCHUH, B., KISSLING, E., SCHUSTER, R. (2004): *Tectonic map and overall architecture of the Alpine orogen*. Eclogae Geologicae Helvetiae 97 (2004), 93 - 117.
- SCHMIDEGG, O. (1932): *Geologische Spezialkarte der Republik Österreich 1:75 000, Blatt 5246 Sölden und St. Leonhard*. Geologische Bundesanstalt.
- SCHMIDEGG, O. (1936): *Steilachsige Tektonik und Schlingenbau auf der Südseite der Tiroler Zentralalpen*. Jahrbuch der Geologischen Bundesanstalt, 86, 89 - 114.
- ZANGERL, C., PRAGER, C., BRANDNER, R., BRÜCKL, E., EDER, S., WOLFGANG, F., TENTSCHERT, E., POSCHER, G., SCHÖNLAUB, H. (2008): *Methodischer Leitfaden zur prozessorientierten Bearbeitung von Massenbewegungen*. Geo.Alp, 5, 1 - 51.
- ZANGERL, C., EBERHARDT, E., PERZLMAIER, S. (2010): *Kinematic behaviour and velocity characteristics of a complex deep-seated crystalline rockslide system in relation to its interaction with a dam reservoir*. Engineering Geology 112, 53 - 67.
- ZANGERL C., HOLZMANN M., PERZLMAIER S., ENGL D., STRAUHAL T., PRAGER C., STEINACHER R., MOLTERER S. (2015): *Characterisation and Kinematics of Deep-Seated Rockslides in Foliated Metamorphic Rock Masses*. In: LOLLINO, G., GIORDAN, D., CROSTA, G. B., COROMINAS, J., AZZAM, R., WASOWSKI, J., SCIARRA, N. (Eds.), Engineering Geology for Society and Territory – 2, Springer International Publishing Switzerland 2014, 571 - 575.

TRIPLE C - the host rock adaptable container concept for disposal of high radioactive waste

TRIPLE C - Das Wirtsgestein adaptive Behälterkonzept zur Endlagerung von hochradioaktivem Abfall

Albert Kerber¹, Jürgen Knorr², Heinz Konietzky³, Ya-Nan Zhao³

¹ SiCeram GmbH

Am Nasstal 10, 07751 Jena, Germany

² GWT-TUD GmbH, Nuclear Power Engineering,
Freiberger Str. 33, 01067 Dresden, Germany

³ TU Bergakademie Freiberg
Institut für Geotechnik

Gustav-Zeuner-Str. 1, 09599 Freiberg, Germany

Abstract

It is acknowledged worldwide that high radioactive, heat generating nuclear waste (HHGW) must be safely isolated from the biosphere for a time period of 1 Mio years. The disposal concepts foresee deep geological disposal with a combination of geological and engineered retention barriers also denominated as defense-in-depth-concept. Since the lifetime of all types of metallic canisters, weather its copper, stainless steel or spheroidal graphite iron, is admittedly much less than the storage time due to corrosion, the main retention function has been attributed to the geological barriers in the past. Generations of scientists and engineers have been looking for suitable host rock types and sites - but with limited success: because rarely a host rock will be found which fulfils the main safety function satisfactorily. It is difficult to find acceptable compromises for host rock formations in countries confronted with the disposal on its own territory of HHGW from its nuclear activities. So the time has come to reconsider the contribution of the engineered barriers for the long-term safety. New developments in ceramics provide a sound scientific-technical basis for the industrial production of ceramic waste containers even with the legitimate claim and goal for the transition of the main safety function from the geological barriers to the engineered barriers. In this sense the TRIPLE C concept is a promising alternative to metallic waste containers – a ceramic multi-barrier container concept with the main retention barrier made of sintered silicon carbide (SSiC) [1].

After a short introduction in the TRIPLE C concept the presented paper focuses on three aspects:

- the state-of-the-art in manufacturing the SiC containers for all types of existing HHGW waste forms
- the degree of the host rock adaptability of a TRIPLE C waste package in principle; the specific adaption of the final design of the waste package and its deposition due to the given geo-mechanical data of the site
- first results of the load behaviour of test SiC containers.

Due to the differentiation of functionalities of its three different layers, the TRIPLE C concept is applicable for all kind of host rocks such as salt, clay or granite. Thus, the

necessary completion of the technology and its application on the existing national inventory of spent nuclear fuel should, in no case, be postponed until the German repository site has finally been determined in the year 2031.

Zusammenfassung

Es besteht weltweites Einvernehmen darüber, dass hochradioaktive, Wärme erzeugende Nuklearabfälle (HHGW) über einen Zeitraum von 1 Mio. Jahren sicher von der Biosphäre isoliert werden müssen. Die Endlagerkonzepte sehen geologische Tiefenlager mit einer Kombination von geologischen und technischen Rückhaltebarrieren vor, was auch als Konzept der „Verteidigung–in–der–Tiefe“ bezeichnet wird. Da die Lebensdauer aller metallischen Behälter, ob aus Kupfer, Edelstahl oder Sphäroguss in Relation zur Lagerzeit aufgrund von Korrosion zugegebenermaßen klein ist, wurde in der Vergangenheit die Hauptrückhaltefunktion dem Wirtsgestein zugeschrieben. Generationen von Wissenschaftlern und Ingenieuren waren mit mäßigem Erfolg auf der Suche nach Wirtsgesteinen und Standorten, weil es schwierig ist, ein Wirtsgestein zu finden, das die Hauptsicherheitsanforderung zufriedenstellend erfüllt. Es ist schwierig, akzeptable Kompromisslösungen in Ländern zu finden, die mit der Endlagerung von HHGW aufgrund ihrer nuklearen Aktivitäten konfrontiert sind. Damit ist die Zeit gekommen, den Beitrag der technischen Barrieren zur Langzeit-Sicherheit zu überdenken. Neue Entwicklungen in der Keramik liefern eine profunde wissenschaftlich-technologische Basis für die industrielle Produktion von keramischen Abfallbehältern mit dem berechtigten Anspruch und Ziel, die Hauptsicherheitsfunktion von der geologischen auf die technischen Barrieren zu verlagern. In diesem Sinne stellt das TRIPLE C Konzept eine Erfolg versprechende Alternative zu metallischen Containern dar - ein keramisches Multi-Barrieren System mit der Hauptrückhaltebarriere aus gesintertem Siliziumkarbid (SSiC) [1].

Nach einer kurzen Einführung in das TRIPLE C Konzept liegt der Fokus dieser Veröffentlichung auf drei Aspekten:

- Stand der Technik bei der Herstellung der SiC Container für alle existierenden Typen von HHGW-Abfall,
- Grad der Adaptierbarkeit des TRIPLE C Abfallgebindes auf das Wirtsgestein im Allgemeinen; die spezifische Anpassung der endgültigen Auslegung des Abfallgebindes und seiner Endlagerung aufgrund vorgegebener geomechanischer Daten des Endlagerstandortes,
- erste Ergebnisse zum Verhalten der Container unter Lastbedingungen.

Aufgrund der differenzierten Funktionalitäten seiner drei Schichten ist das TRIPLE C Konzept für alle Arten von Wirtsgestein einsetzbar, ob Salz, Ton oder Granit. Aus diesem Grund sollten die notwendige Komplettierung der Technologie und deren Anwendung auf existierende Lagerbestände auf gar keinen Fall so lange hinausgezögert werden, bis ein Endlagerstandort im Jahr 2031 bestimmt wurde.

1 Introduction

There is a worldwide agreement amongst countries operating nuclear power plants that HHGW must be safely separated from biosphere for at least 1 Mio. years. Furthermore, the defense-in-depth concept is generally recognized, either as deep geological or deep borehole deposition. Fig. 1 shows the existing and proposed solutions to provide the long-term safety of a repository. The ultimate goal is to prevent radioactive material from entering the biosphere ($M = 0$).

hazardous material M, arriving in biosphere:		$M \sim QP$	ideal enclosure: $M(t) = 0$ with $Q = 0 ; P = 0$
			total enclosure: $M(t) = 0$ with $Q = 0 ; P > 0$
			safe enclosure: $0 < M(t) < M_{krit}$ $Q > 0 ; P > 0$ for all time t
waste package	engineered barrier	geological barrier	biosphere
metallic container	$Q(t) > 0$	MAIN RETENTION BARRIER $0 < P \ll 1 ?$	$0 < M(t) \stackrel{?}{<} M_{krit}$
ceramic container TRIPLE C	MAIN RETENTION BARRIER $Q(t) = 0$	$0 < P$ $0 < P \ll 1$	$M(t) = 0$

Fig. 1: Zero release from TRIPLE C waste package, claim and goal ($Q(t) = 0$)

First approaches to achieve this goal assumed that the right choice of host rock and site could lead to the wanted success. But the characteristics of geological sites, such as changes over long time periods and unforeseeable events as the water ingress into the ASSE mine in Germany, have contributed to a different assessment and found their reflection in the German “Endlagergesetz”, where an engineered barrier as additional retention capability is mentioned.

It is planned in many countries to use metal containers as engineered barriers together with a surrounding layer of bentonite. Sweden and Finland want to apply copper canisters, Germany spheroidal graphite iron and the United States stainless steel for example. The Swedish concept of SKB has very often been cited as reference project, but came under harsh criticism by the decision of the Swedish Environmental Court at the beginning of 2018 [2]. It is generally known that all metals exhibit a relatively poor corrosion resistance under disposal conditions, especially if time periods as requested are considered [3], [4], [5]. In literature it is mentioned that earth-laid pipes of spheroidal cast iron must obtain an external and internal corrosion protection. Taking into account the above said, it seems to be appropriate to search for an alternative container solution.

Ceramic materials are well known for exhibiting better corrosion resistance than metals and especially silicon carbide (SiC) outperforms due to its resistance in various chemical environments [6] and its radiation resistance. The commonly mentioned drawback of ceramics is their brittleness as compared to metals.

2 SSiC – it's potential as main safety barrier

The choice of SiC as container material is based on different criteria which are listed in the following, but an important suggestion came as well from the former activities in Germany concerning the HTR-reactor and the encapsulation of the fuel, so-called TRISO particles, in a very thin shell of SiC [7]:

- high corrosion resistance in acidic, neutral and basic environment,
- radiation resistance,
- high temperature stability at variable atmospheres,
- high thermal conductivity and shock resistance,
- diamond-like hardness,
- high mechanical, especially compressive strength,
- gas tightness (no open pores).

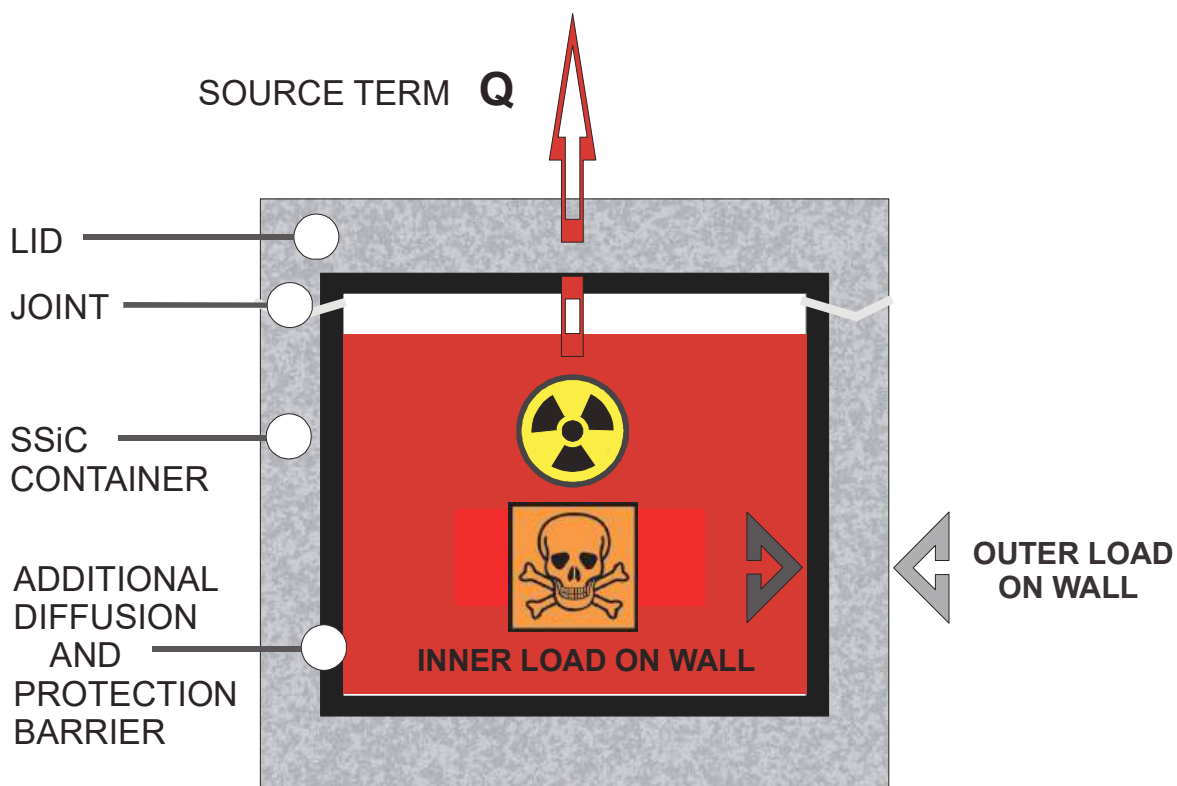


Fig. 2: High-tech ceramic silicon carbide (SSiC) container as main retention barrier suitable for all kinds of host rocks

The basic design elements of such a container are demonstrated in Fig. 2. From the work of Nabelek and Verfondern [7] it is known that the diffusion coefficient of strontium (Sr) in SiC is much higher than that of the other fission products. But even for Sr the calculated break-through-time through a 10 mm SiC wall is in the range of 100 Mio. years. In other words, a wall thickness in the range from 1 to 5 cm provides a complete retention of the radioactive material inside as well as the basic mechanical stability of the SiC container.

Furthermore, it is known, that at very high temperatures - about 1000 K higher than typical temperatures in a repository - silver (Ag) and palladium (Pd) cause a definite corrosive attack on SiC. The corrosion of the inner container surface can be eliminat-

ed by a coating of glassy carbon. The very thin glassy carbon layer acts simultaneously as corrosion protection and additional migration barrier (ion trap).

3 SSiC – container for all types of spent fuel elements

SiC and especially pressure-less sintered silicon carbide (SSiC) fulfils all the criteria mentioned above. The technological base for manufacturing SiC-containers for all types of spent fuel elements and vitrified waste is available today or will become industrial practice very soon. Examples of containers for HTR pebbles and CANDU spent fuel are shown in Fig. 3.

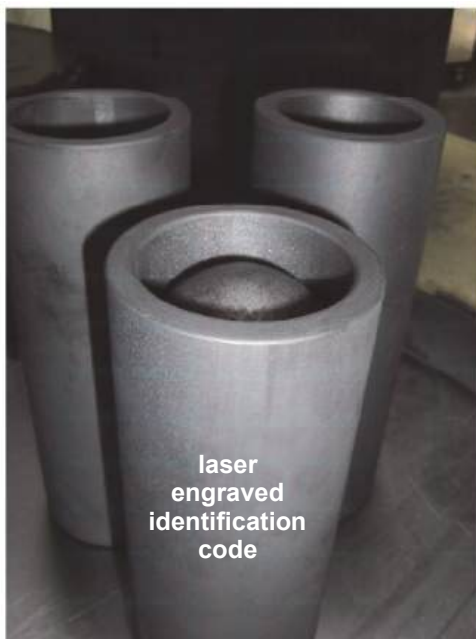


foto SiCeram GmbH



(V)HTR

CANDU

Fig. 3: SSiC container for all types of spent fuel elements and vitrified waste; here: (V)HTR pebbles and CANDU spent fuel

The hermetic closing of the container as well as the bonding of segments for forming very large containments was considered for a long time as the fundamental drawback, but with the native bonding technology [8] “Rapid Sinter Bonding” (RSB) a quick and reliable process for a strong and gas tight seam has been developed. Thus, the key technologies for encapsulation of high radioactive nuclear waste in SSiC-containments are available.

4 TRIPLE C concept - multi-layer waste package

The main generally expressed concern against the application of all kinds of ceramics is still their brittleness and the risk of failure under mechanical load in general and impact in special. In order to improve and proof the performance of the SSiC canister system, two measures have been undertaken: differentiation of the barrier functions

and numerical simulation of the mechanical loads under deposit conditions based on measured material properties.

Since it's obvious that no host rock nor canister material can fulfil all requirements for a safe storage of high radioactive waste, the functions of the barriers have to be differentiated and optimized according to their specific needs and characteristics. The retention of the fission products is the dominant function of the whole system, which leads to the corrosion resistant and long-term stable material silicon carbide. The inherent deficiencies must be compensated by the counter measures described in the following as TRIPLE C concept (Fig. 4).

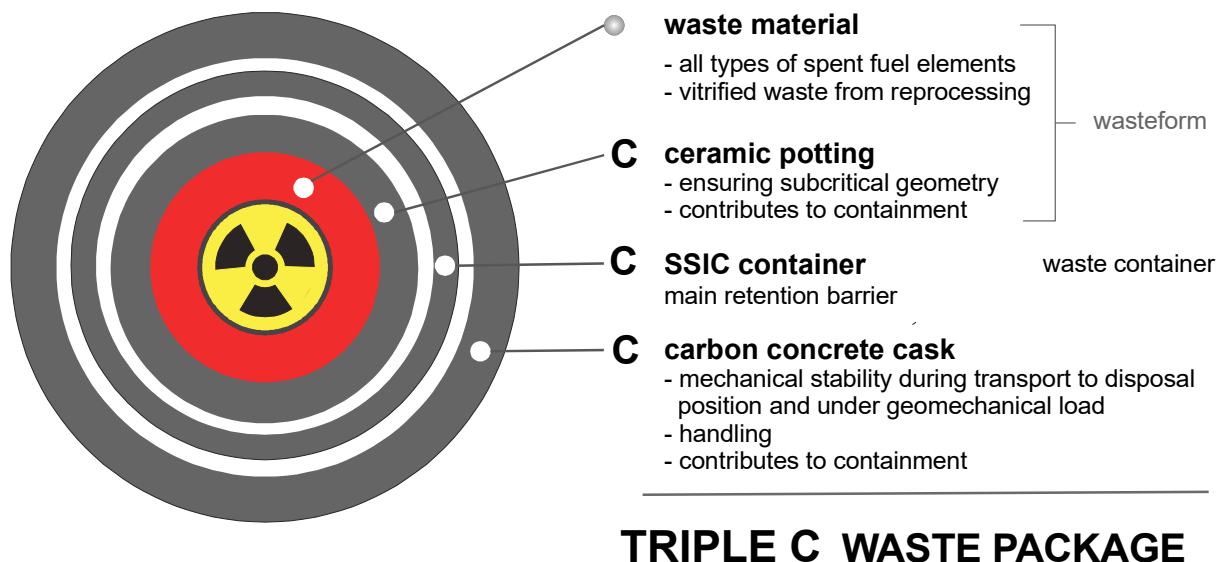


Fig. 4: TRIPLE C concept – threefold ceramic encapsulation

The cladding tubes of the spent fuel elements with a wall thickness of 0.8 mm are pre-damaged by 5 years of reactor operation and by the following storage in the cooling pool. A failure of the tubes after 50 years of life time is very likely and expected. For named reason the dismantling of spent fuel elements is not intended although it would allow to store 3 times more tubes in one canister, but for risk minimization the fuel element shall be disposed as a whole. Nevertheless, a failure of the cladding tubes can lead to a pile formation of the nuclear fuel at the bottom of the storage container and thus to the formation of a critical mass. As a solution of this problem the numerous voids between the single fuel rods are filled with a so-called potting compound with different functions (Fig. 5).

The material composition of silicon and carbon in the atomic ratio 1:1 leads to the formation of SiC under the neutron radiation of the spent fuel. The newly generated SiC is solid, but very porous and thus provides additional absorption surface for the fission products after the expected breakage of the cladding tubes.

The solidified potting compound keeps the shape of the cladding tubes even after their failure, thus avoiding the pile formation at the bottom of the canister. As an additional safety measure, the potting compound contains boron carbide as a neutron absorber in order to guarantee sub-criticality.

fuel rod
with metallic cladding

SSiC container



a) **POTTING**

b) foto SiCeram GmbH

Fig. 5: Potting compound containing boron; a) principle arrangement b) bundle of 7 rods surrounded by potting in SSiC container

Carbon Concrete

The brittleness of the SiC-canister will be compensated by an over-pack of a newly developed material, called carbon concrete. The armour of this concrete consists of woven carbon fibre structures instead of steel, making the whole composite much stronger, lighter and less susceptible to corrosion. The closed SiC-canister with its content of nuclear waste is placed into the carbon concrete container for the further handling from the filling station to the final storage position. The complete arrangement consisting of the ceramic potting compound, the ceramic SSiC-container and the carbon concrete surrounding is denominated as TRIPLE C concept.

5 Contribution of geo-mechanics for design of the TRIPLE C waste package

A schematic representation of the TRIPLE C waste package in its final repository environment is illustrated in Fig. 6. The inner retention barriers, consisting of the ceramic potting compound and the solid wall of SSiC, are invariant for all kinds of host rocks, since their predominant function is to keep the source term for spreading of fission products at zero. This can only be guaranteed, if the container wall is not corroded during the whole storage period of 1 Mio. years. The interspace between the container and the carbon concrete cover may be filled with shock absorbers of hollow spheres of a suitable material. The thickness of the carbon concrete over-pack must be designed according to the needs for handling and transport protection. The required thickness of the embedding bentonite is dependent on the surrounding host rock and the respective load parameters are contributed by geo-mechanics. As their main function the embedding bentonite and the carbon concrete over-pack have to protect the inner retention barrier from mechanical damage by the host rock.

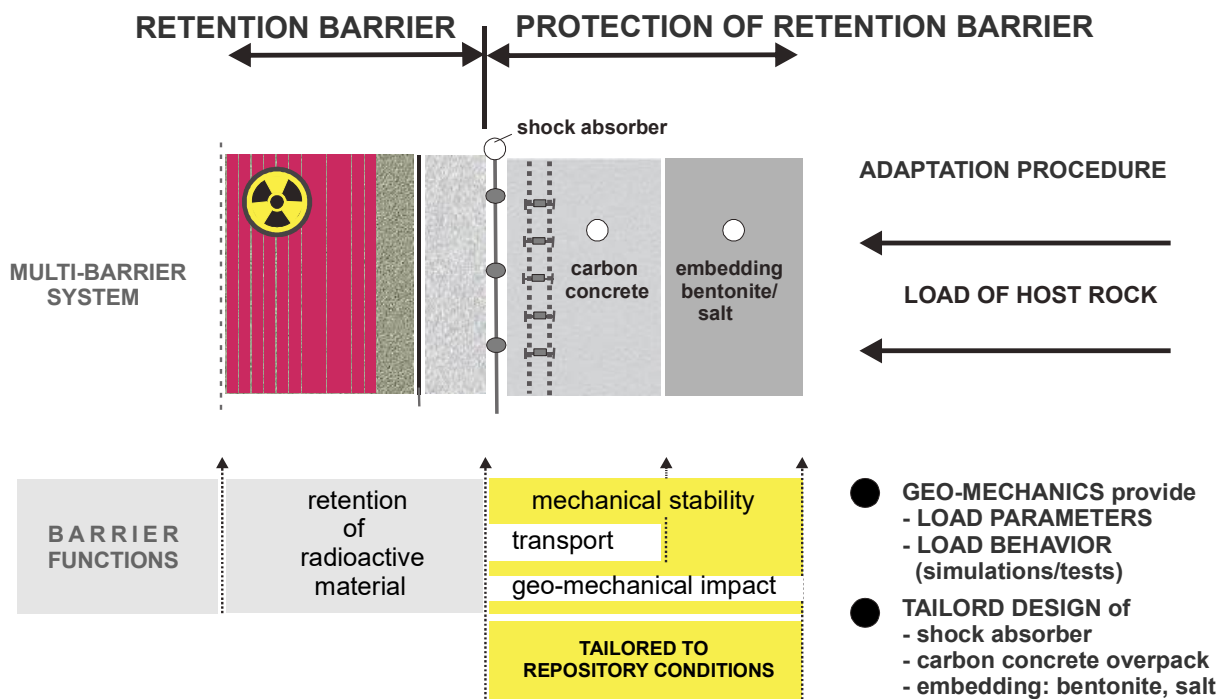


Fig. 6: TRIPLE C – combination of split and shared functions; geo-mechanics provides the load parameters for adaption to repository conditions

6 First results of mechanical behaviour of SiC container

The mechanical behaviour of the bare SSiC-canister has been numerically simulated by the Geotechnical Institute of TU Bergakademie Freiberg and are presented in detail in [9]. In mentioned work, a hollow cylinder shaped canister made of SSiC has been studied preliminary to investigate adaptability of bare canister to potential dangerous loading scenarios. The line loading test, illustrated in Fig. 7, has indirectly measured the minimum tensile strength of SSiC sample of about 150 MPa (Fig. 8).

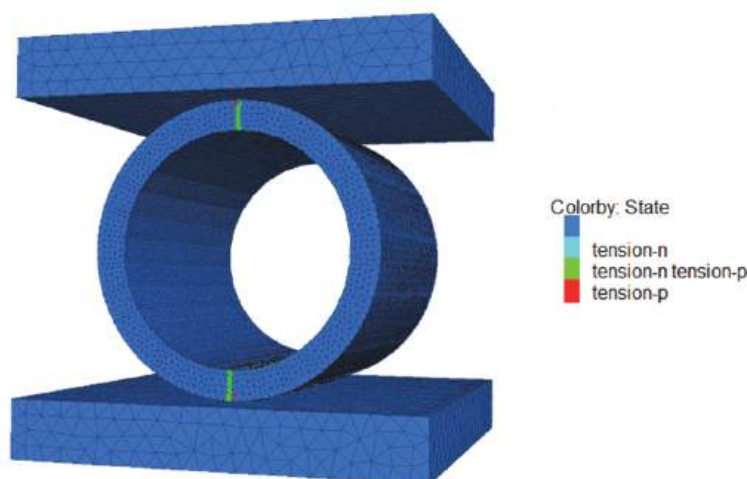


Fig. 7: Test arrangement for line loading test

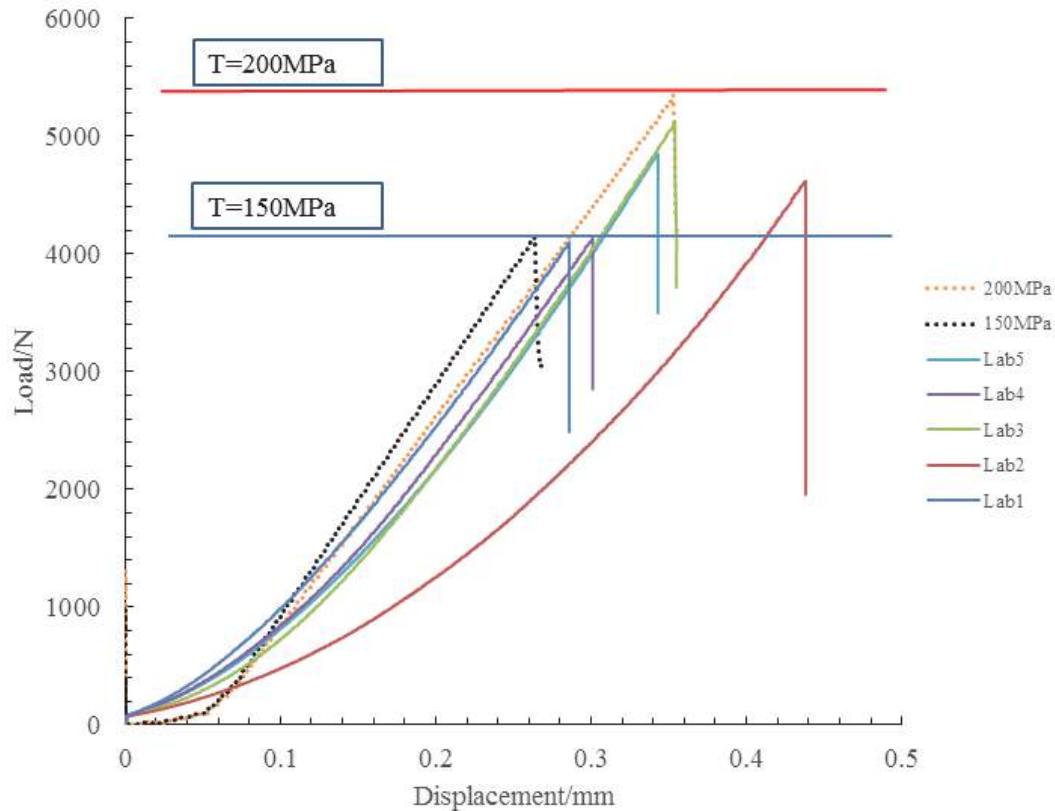


Fig. 8: Lab results of line loading test (acc. to Fig. 7) on hollow SSiC cylinders

Both, analytical and numerical results of line loading test have been obtained for comparison. A review of published data helps to rule out the possibility of shear failure of SiC. The only potential critical failure mode of SSiC is tensile failure. Therefore, all subsequent documented investigations consider loading cases inducing tensile stresses.

First, canister freefall simulation from height of 2.0 m has been performed. Results show that the canister alone cannot bear impact from freefall loading. Subsequently, the canister is wrapped with a soft coating layer and the maximum tensile stress generated has been reduced to about half of that in bare canister (83 MPa). Consequently, a coating layer of carbon concrete e. g. is needed for safety concern and can guarantee safe conditions.

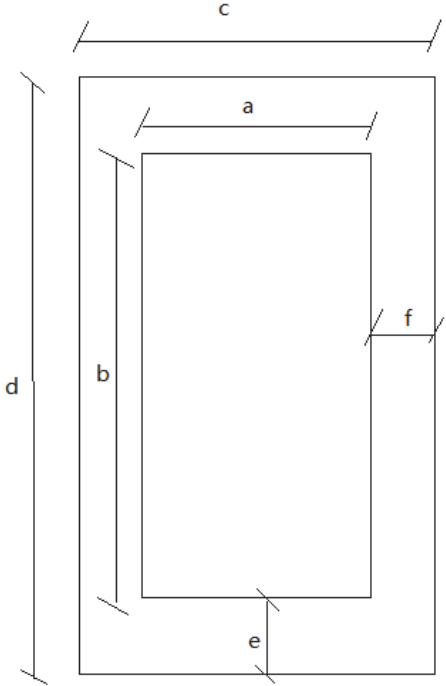
Second, the impact from falling rock (falling height 2.0 m) has been studied. A 6 kg rock is considered. Pure elastic calculation results in a maximum principle stress of 324 MPa, much bigger than the tensile strength. Considering that this result is not realistic, a DEM model that divides the rock into tens of thousands of jointed blocks has been performed for comparison, so that also rock disintegration during impact is included. Such a DEM model gives a maximum principle stress of 112 MPa, much lower than the pure elastic solution. Point-line contact impact from a tetrahedron shaped rock block (DEM model) produces maximum principle stress of no more than 40 MPa.

Third, stress concentration effect has been explored. A small stone subdivided into several hundred blocks (DEM model) is inserted between canister and foundation and corresponding maximum principle stress exceed tensile strength of SSiC.

Fourth, it is assumed that the SSiC canister is protected by a layer of compacted bentonite (8 cm thick, swelling pressure assigned 30 MPa) and embedded in the rock mass which is characterized by a vertical stress component of 10 MPa and a horizon-

tal principal stress of 30 MPa. Results show a maximum tensile stress in the canister of 92 MPa. The canister can withstand very high anisotropic in-situ stress ratio (3:1) if fully covered by bentonite.

Consequently, based on these preliminary simulations it can be stated that a coating layer is needed for safety concern and can guarantee safe conditions. After these preliminary studies real-size containers (see Fig. 9) are under investigation for different load cases.



(a) Cross-section of cylinder canister



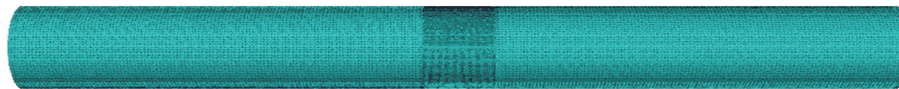
(b) HTR canister (a = 62 mm, b = 305 mm, c = 92 mm, d = 335 mm, e = 15 mm, f = 15 mm)



(c) CANDU canister (a = 102 mm, b = 510 mm, c = 142 mm, d = 550 mm, e = 20 mm, f = 20 mm)



(d) Vitriified Waste canister (a = 450 mm, b = 1350 mm, c = 500 mm, d = 1400 mm, e = 25 mm, f = 25 mm)



(e) PWR/BWR canister (a = 400 mm, b = 4930 mm, c = 470 mm, d = 5000 mm, e = 35 mm, f = 35 mm)

Fig. 9: Cross sections of SSiC containers for different waste forms and corresponding meshed numerical models

7 Ecological and Economical Aspects

Silicon Carbide as a chemical compound was detected in stellar matter, meaning that it's extremely stable, but it rarely exists on earth as a natural mineral. SiC can be synthesized in any required quantity from the abundantly available raw materials sand and coke by applying electrical energy.

If copper is used as canister material, a very valuable metal is discharged from the material flow in principle for ever. Since the material density of SiC is roughly 3 times lower than of copper and the wall thickness of the copper container must be 2 times larger for corrosion reasons, the mass per copper-canister is 6 times that of silicon carbide. From this it follows that the price per kg of material may be 6 times higher for SSiC in order to obtain the same canister price as for copper.

8 Conclusions

All aspects investigated in this paper clearly indicate that the TRIPLE C concept with its main barrier of pressure-less sintered silicon carbide represents the best of all possible solutions for the safe encapsulation of high radioactive nuclear waste. The brittleness of SSiC is overcome by differentiated functionalities, but the focus lays on the retention of fission products as its predominant task. The generally expressed opinion that the development of a canister for final waste disposal could only be started after the decision for the host rock and the site has been concluded is wrong for two main reasons. The main function of retention of fission products is fulfilled by the two inner barriers, the potting compound and the SSiC-canister wall whereas the influence of the host rock on the container must be minimized by the dimensioning of the over-pack and the embedding into the outmost engineered barrier, the bentonite. If embedded in sand or salt with plastic behaviour, even the bare SSiC-canisters would perform very well.

A further argument to immediately start the industrial development of the containers is the limited life time of the cladding tubes of the fuel rods. Should some of the rods be destroyed already, the necessary reloading from the intermediate to the final storage container becomes impossible. The consequence would be to declare the intermediate to the final storage container with potentially disastrous scenarios for further generations. Despite the wide-spread social scepticism towards nuclear activities in general, we do expect a broad public acceptance of the new strategy for nuclear waste disposal, because the utmost possible long-term safety will be guaranteed by the innovative TRIPLE C concept.

References

- [1] Knorr, J., Kerber, A.: *Triple C – the paradigm changing concept for disposal of high radioactive waste*. Manuscript submitted to atw
- [2] *Decision of the Swedish Environmental Court, 23.01.2018, Summary of the Court's statement, 180123 >>* (in Swedish)
- [3] Deutsches Kupferinstitut, *Werkstoffdatenblätter Cu-ETP, Cu-HCP und Cu OFE, Korrosionsbeständigkeit*
- [4] Deutsche Edelstahlwerke, *Acidur 4301, Werkstoffdatenblatt X5CrNi18-10, 1.4301*
- [5] Bundesverband der Deutschen Gießerei-Industrie (BDG), *Gusseisen mit Kugelgraphit, Herstellung-Eigenschaften-Anwendung, konstruieren + gießen 32* (2007) Nr. 2, 69 - 70
- [6] Lay, L. A.: *Corrosion Resistance of Technical Ceramics*. National Physical Laboratory, Teddington, Middlesex. Pub H.M.S.O., ISBN 0114800510, 1983
- [7] Nabielek, H., Verfondern, K.: *Integrity of TRISO Particle Coating during Long-Term Storage under Corrosion*. EU co-funded RAPHAEL program D-BF2.1, Jülich, March 2010
- [8] Deutsche Patentanmeldung 10 2018 114 463.6 „*Verfahren zum Verbinden von Bauteilen aus SSiC*“
- [9] Zhao, Y.-N., Konietzky, H., Knorr, J., Kerber, A.: *Preliminary study on geo-mechanical aspects of SiC canisters*. Adv. Geosci., 45, 63 - 72, 2018

Neubau Albulatunnel II, Herausforderungen beim Bau des zweithöchsten Alpendurchstichs der Schweiz

Construction of New Albula Tunnel II, Challenges during the construction of the second highest tunnel in Switzerland

Uwe Holstein
AF Toscano AG
Rätusstrasse 12
CH-7000 Chur

Abstract

The Albula Line is the most important rail link to the Upper Engadine region and to St. Moritz. The Albula Tunnel, opened in 1903, is the heart of the section. Due to its poor structural conditions and with the aim of improving safety, Rhaetian Railway (RhB) decided to build a new tunnel. Preparatory operations started in 2014 and the tunnel excavations began in summer 2015. The single-track 5'860 m long Albula Tunnel will be built parallel to the existing tunnel in a distance of 30 m. Both tunnels will be connected by 12 interconnections. The old Albula Tunnel I will be reconstructed after the new tunnel is put into operation and will be used as a safety tunnel. The train stations will be disabled-adapted with corresponding platforms and a passenger tunnel in Preda.

Until autumn 2017 the most complicated tunnel sections are overcome. In October 2018 the tunnel punch is expected. 2021 the new Albula Tunnel II will be put into operation.

Zusammenfassung

Die Albulalinie ist die wichtigste Bahnverbindung in das Oberengadin und nach St. Moritz. Der 1903 eröffnete Albulatunnel ist das Herzstück der Strecke. Aufgrund seines schlechten baulichen Zustands und zur Erhöhung der Sicherheit beschloss die Rhätische Bahn (RhB), den neuen Albulatunnel II zu bauen. Die vorbereitenden Arbeiten begannen 2014 und im Sommer 2015 starteten die Tunnelvortriebe. Der eingleisige, 5'860 m lange Albulatunnel II wird im Abstand von 30 m neben dem bestehenden Tunnel erstellt. Die beiden Tunnelröhren werden durch zwölf Querverbindungen miteinander verbunden. Der alte Albulatunnel I wird nach der Inbetriebnahme des Albulatunnel II instandgesetzt, umgebaut und als Sicherheitstunnel genutzt. Die Bahnhöfe werden behindertengerecht ausgebaut und mit entsprechenden Bahnsteigen sowie einem Personentunnel in Preda ergänzt.

Bis zum Herbst 2017 wurde der Vortrieb in den tunnelbautechnisch anspruchsvollsten Tunnelabschnitten bewältigt. Der Durchschlag der neuen Tunnelröhre wird im Oktober 2018 erwartet. Ab 2021 soll der neue Albulatunnel II betrieben werden.

1 Einleitung

Die im Jahre 1903 eröffnete Bahnlinie von Thusis bis nach St. Moritz ist eine Meisterleistung der Ingenieurkunst. Die gesamte Strecke ist 62 km lang und überwindet insgesamt über 1'000 Höhenmeter. Sie führt über 144 Brücken und durch 42 Tunnel. Der auf über 1'800 m Höhe gelegene Albulatunnel ist mit 5'864 m der längste Tunnel auf der Strecke und zugleich der zweithöchste Alpendurchstich der Schweiz. Die Bauzeit der gesamten Strecke betrug nur 5 Jahre. 2008 wurde die Strecke in das UNESCO Weltkulturerbe aufgenommen.

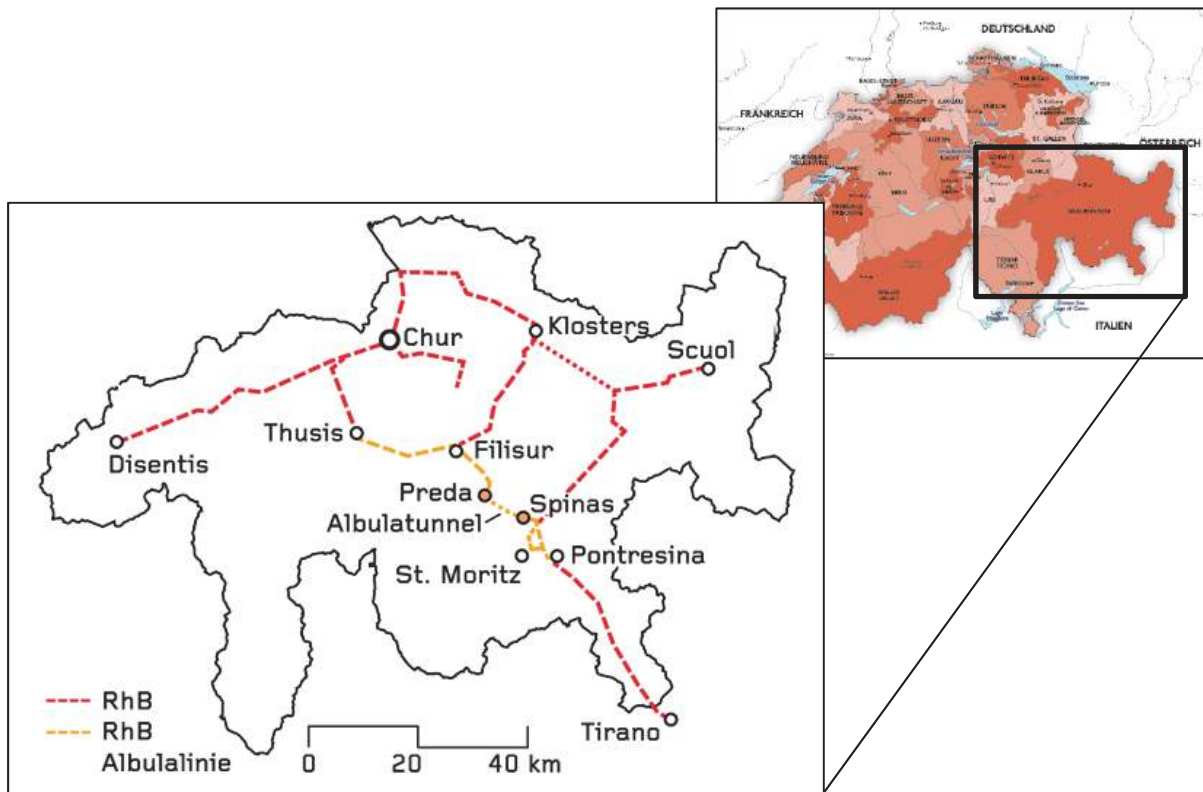


Fig. 1: RhB-Streckennetz mit Albulalinie

Der alte Tunnel weist nach über 110 Jahren trotz regelmäßiger Instandhaltung einen sehr schlechten baulichen Zustand auf. Das Natursteinmauerwerk, die Entwässerungsanlage, die Tunnelsohle und auch die nachträglich ergänzten Spritzbetonschalen weisen erhebliche Schäden auf.



Fig. 2: Der bestehende Albulatunnel

Deshalb beschloss die RhB das Projekt der integralen Erneuerung des Albulatunnels. Ziel ist ein Bauwerk, das hinsichtlich Sicherheitstechnik, Betrieb und Umwelt den heutigen Ansprüchen gerecht wird. 30 m neben dem alten Bahntunnel wird der neue Albulatunnel II gebaut und über 12 Querverbindungen mit dem Albulatunnel I verbunden. Danach wird der bestehende Tunnel instandgesetzt und als Sicherheitstunnel genutzt. Die Bahnhöfe in Preda und Spinass werden behindertengerecht ausgebaut und die Bahnsteige entsprechend ergänzt. In Preda werden eine Personenunterführung und ein neues Gleis für den Schlittenbahnbetrieb gebaut.

2 Vorarbeiten

Bevor mit dem eigentlichen Tunnelbau begonnen werden konnte, mussten von 2012 bis 2015 Erkundungs- und Vorbereitungsarbeiten ausgeführt werden. Vom Albulatunnel I aus wurde über eine Querverbindung eine in der Achse des neuen Tunnels liegende Kaverne aufgefahren. Aus dieser Kaverne heraus konnte die Störzone Raibler Rauwacke mit zwei 160 m langen, preventergeschützten Kernbohrungen erkundet werden.

2014 und 2015 wurden zwei an den Portalen gelegene Bauplätze erschlossen, Wasserversorgungsanlagen und Entwässerungsanlagen gebaut, Baustromstationen errichtet und Zufahrtstraßen ausgebaut. In Spinass wurde eine neue Bahnunterführung errichtet. In Preda mussten zwei denkmalgeschützte Gebäude verschoben sowie Materialverladeanlagen und Baubahnhöfe errichtet werden. Für die Ablagerung des nicht verwertbaren Ausbruchmaterials wurde auf der Seite Preda die Deponie Las Piazzettas erschlossen. Die Verkleidung des alten Albulatunnels wurde in den Portalbereichen und auf Höhe der zwölf neuen Querverbindungen mit bewehrten Spritzbetonschalen verstärkt und die Einmündungsbereiche der Querverbindungen wurden ausgebrochen. Zur Wasserversorgung der Baustellen wurde im bestehenden Tunnel eine Brauch- und Löschwasserleitung verlegt.



Fig. 3: Vorarbeiten im Albulatunnel I – zukünftige Querverbindung zum neuen Albulatunnel II

3 Albulatunnel II

3.1 Projekt und Geologie

Der neue Albulatunnel II wird 5'860 m lang und verläuft mit einem Achsabstand von 30 m parallel zum bestehenden Albulatunnel I. Der Tunnel steigt von Preda aus mit 1 % bis zum Hochpunkt in der Tunnelmitte an und weist ab dort in Richtung Spinas ein Gefälle von 0.2 % auf. Zwölf neue Querverbindungen werden im Abstand von ca. 450 m angeordnet. Jede dritte Querverbindung wird für Rettungsfahrzeuge befahrbar sein.



Fig. 4: Gesamtübersicht Albulatunnel I und II

Von Preda aus durchquert der Tunnel zunächst auf etwa 1'100 m den Allgäuschiefer. Anschließend folgt auf einer Länge von 110 m der bautechnisch schwierigste Tunnelabschnitt in der Raibler Rauwacke, einem mit karstartigen Hohlräumen durchsetzten Gestein aus Zellendolomit. Es folgt eine ca. 50 m lange Strecke im Mylonit, einem relativ kompakten, harten Gestein aus rekristallisierten Sedimenten. Nach dem Mylonit durchquert der Tunnel auf einer Strecke von ca. 4'300 m den Albulagranit, der lediglich zweimal durch Mylonite gestört wird. In Portalbereich Spinas liegt der Tunnel auf einer

Länge von 250 m im Lockergestein, das zu ca. 50 % aus einer konsolidierten, relativ standfesten Grundmoräne und zu ca. 50 % aus Bach- und Gehängeschutt besteht.

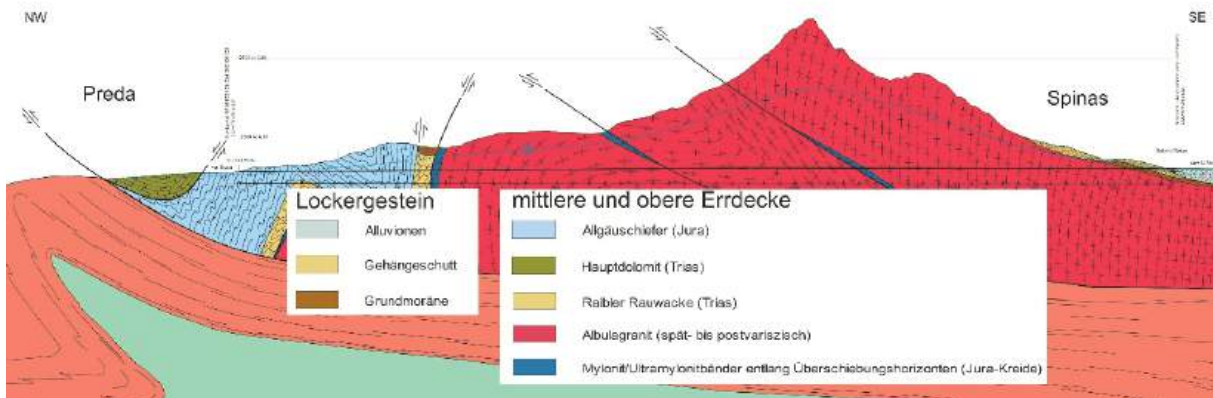


Fig. 5: Geologisches Längensprofil

3.2 Baustellenlogistik und Baustelleneinrichtungen

Die Baustelle ist das ganze Jahr per Schiene erreichbar, aber nur von Mitte März bis Mitte Dezember über die Straße. Von Mitte Dezember bis Anfang März wird die Passstraße zwischen Preda und Bergün gesperrt und als Schlittenbahn touristisch genutzt. Gleichzeitig wird die Logistik der Baustelle durch die dann im Hochgebirge vorherrschenden klimatischen Bedingungen erheblich erschwert. Deshalb werden die Bauarbeiten im Winter eingestellt. Von März bis Mitte Dezember wird im Tunnel an 7 Tagen in der Woche im Durchlaufbetrieb gebaut.

Im April 2015 begann der Aufbau der Baustelleneinrichtungen. In Preda und Spinas wurden je eine Werkstatt, eine Wasseraufbereitungsanlage, eine Betonanlage sowie Förderband- und Verladeanlagen für den Materialtransport errichtet. Die Unterkünfte für die Mannschaften, die Büros der Bauleitung und ein Kieswerk zur Aufbereitung des Tunnelausbruchmaterials wurden auf dem Installationsplatz in Preda errichtet. Für den Materialtransport von Preda zur Deponie Las Piazzettas mussten insgesamt ca. 1'600 m Förderbandanlagen erstellt werden.



Fig. 6: Installationsplatz Preda mit Kieswerk, Förderbandanlagen, Personenunterkünften

3.3 Vortrieb Preda

Als Voraussetzung für den Tunnelvortrieb und als Baugrube für das neue Tunnelportal wurde gleichzeitig mit dem Aufbau der Installationen ein Voreinschnitt erstellt. Weil das neue Portal unmittelbar neben dem bestehenden Tunnelportal liegt, musste die Baugrube auf beiden Seiten mit Bohrpfehlen gesichert werden.



Fig. 7: Voreinschnitt Preda

Am 17. August 2015 startete der Vortrieb des Albulatunnels II. Wegen der geringen Überdeckung wurden die ersten 37 m im Schutze von vier Rohrschirmetappen aufgeföhren, die Sicherung bestand dabei aus HEB-Bögen und mindestens 20 cm bewehrtem Spritzbeton.

Ab Tunnelmeter (Tm) 37 begann der Regelvortrieb im Allgäuschiefer. Der Ausbruchquerschnitt betrug ca. 40 - 45 m². Entsprechend der Prognose war auf etwa 20 % dieses Abschnitts mit ungünstigen geologisch - bautechnischen Eigenschaften zu rechnen. Bei solchen Verhältnissen sollte ein Ausbruchprofil mit ausgerundeter Sohle ausgebrochen werden, die Abschlagslänge sollte 1 m bis 2 m betragen. Auf der restlichen Tunnelstrecke im Allgäuschiefer waren weniger schlechte Gebirgseigenschaften prognostiziert und es sollte ein Profil mit flacher Sohle ausgebrochen werden. Die Abschlagslänge sollte dann zwischen 3 m und 4 m liegen.

Das schon beim Bau des ersten Albulatunnels beobachtete nachbrüchige Verhalten des Gebirges zeigte sich auch beim Vortrieb des neuen Tunnels. Die Auswirkungen waren beim Vollausbuch stärker als erwartet und die Verhältnisse änderten sich zum Teil innerhalb weniger Meter. Insgesamt überwogen die ungünstigen bautechnischen Eigenschaften des Allgäuschiefers. Deshalb konnten die Ausbruchklassen mit flacher Sohle nicht eingesetzt werden. Die Abschlagslänge betrug beim Baggervortrieb im verwitterten Allgäuschiefer maximal einen Meter. Im weniger stark verwitterten Allgäuschiefer kam Sprengvortrieb zum Einsatz, die Abschlagslänge betrug dabei aber ma-

ximal zwei Meter. Die im Allgäuschiefer vorgesehene Bauzeit wurde wegen der ungünstigen geologisch - bautechnischen Gebirgseigenschaften letztendlich um 9.5 Monate überschritten.



Fig. 8: Rohrschirmvortrieb Preda



Fig. 9: Ortsbrust beim Vortrieb im Allgäuschiefer

3.3.1 Raibler Rauwacke

Bei Tm 1'100 erreichte der Vortrieb die Raibler Rauwacke. Bautechnisch ist das der Bereich mit den schlechtesten Verhältnissen im gesamten Tunnel. Deshalb wurde die Rauwacke in der Planungsphase mit langen Kernbohrungen intensiv erkundet.

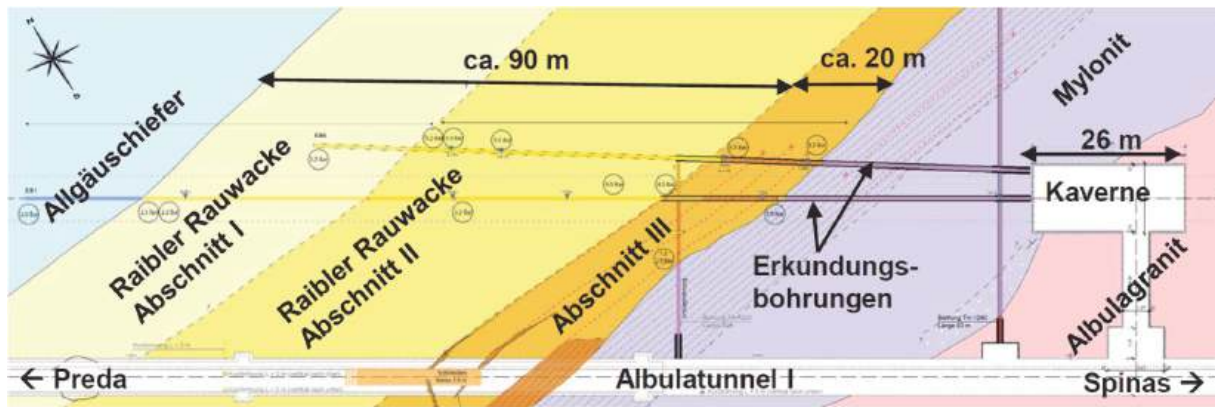


Fig. 10: Raibler Rauwacke – Erkundung in der Achse Albulatunnel II (Grundriss)

Aufgrund der Erkundungsergebnisse konnte die Raibler Rauwacke in drei Abschnitte unterteilt werden, die sich durch ihre geologisch- bautechnischen Eigenschaften wesentlich unterscheiden. Die beiden nördlichen Abschnitte I + II bestehen aus festem Zellendolomit mit kleineren karstartigen Hohlräumen. Im Abschnitt III sind die Hohlräume mit feinkörnigem, zerbrochenem Material gefüllt, welches als Feinsand unter Wasserdruck von bis zu 0.5 MPa zum Teil als schwimmendes Gebirge ansteht. Genau hier kam es beim Bau des ersten Albulatunnels am 29. Juli 1900 zum Einbruch von Schlamm. Bevor es gelang den Vortrieb fortzusetzen, verging damals ein ganzes Jahr.

Der Albulatunnel II wird in der Raibler Rauwacke mit Ringschluss in der Sohle gesichert und zweischalig ausgebaut. Damit die statisch notwendige 60 cm dicke Felssicherung und die 60 cm dicke Innenverkleidung eingebaut werden können, muss der Ausbruchquerschnitt 65 m² betragen. Zwischen der Ausbruchsicherung und der Innenschale wird eine druckhaltende Abdichtung eingebaut. Sowohl die Sicherung als auch die Innenschale sind stark bewehrt.

Das Konzept des Bauherrn sah vor, dass der Abschnitt III der Rauwacke von der Erkundungskaverne aus mittels Baugrundvereisung vorausgehend gesichert wird. Dazu sollte dieser Teil der Störzone zuerst von der Kaverne aus vollständig gefroren werden. Anschließend sollte der Ausbruch im Gefrierkörper durch den von Preda kommenden Vortrieb ausgeführt werden.

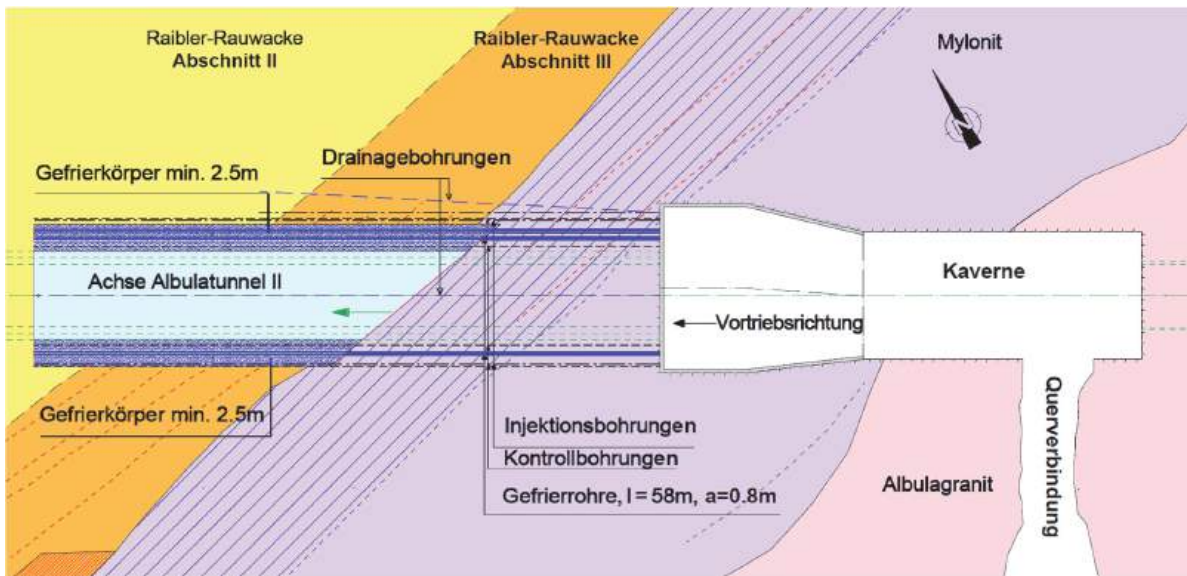


Fig. 11: Konzept Gefrierkörper und Gegenvortrieb im Abschnitt III der Rauwacke – Grundriss

Statische Berechnungen hatten ergeben, dass der Gefrierkörper außerhalb des Ausbruchquerschnitts mindestens 2.50 m dick sein musste. Deshalb wurden rund um den Tunnelquerschnitt Gefrierbohrungen von 60 m Länge erstellt. Weil gefrorener Boden ein spannungs-, temperatur- und zeitabhängiges Kriechverhalten aufweist, war es trotz der Baugrundvereisung erforderlich, dass unmittelbar nach jedem Abschlag eine massiv bewehrte 65 cm dicke Spritzbetonsicherung eingebaut wurde.

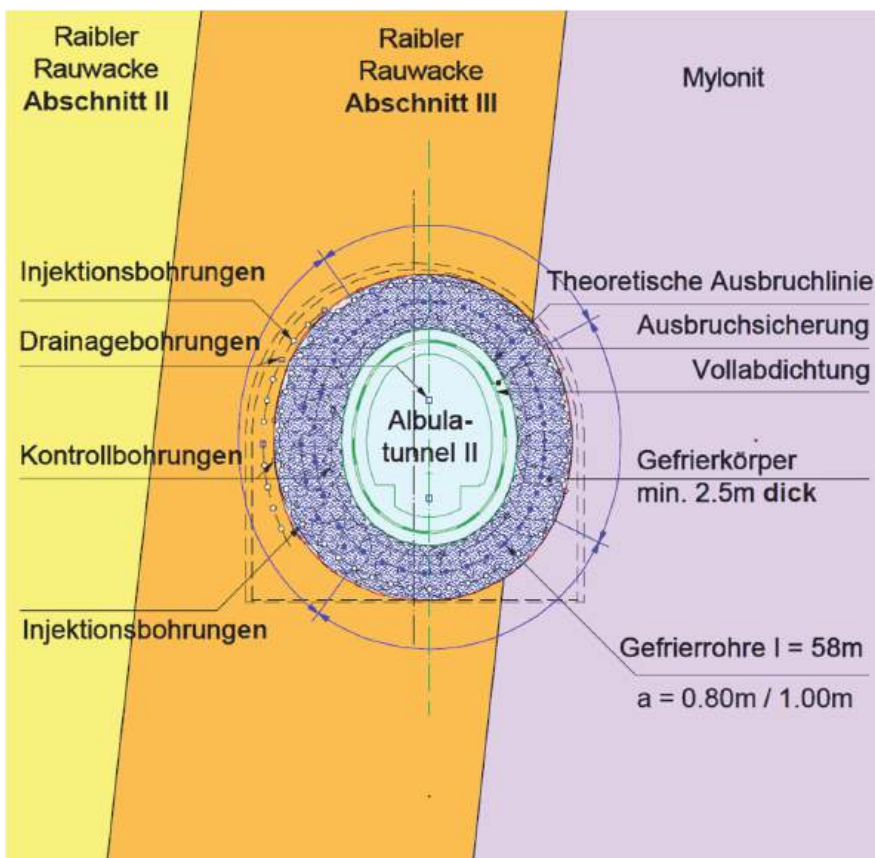


Fig. 12: Konzept Gefrierkörper und Gegenvortrieb im Abschnitt III der Rauwacke - Querschnitt

Die Bohrarbeiten für die Vereisung begannen am 1. September 2015. Am 1. März 2016 begann die Gefrierphase und bereits im Juli 2016 war der Gefrierkörper vollständig aufgefroren. Die Eigenschaften des unter hohen Wasserdrucks stehenden Feinsandes konnten im Gefrierkörper so verbessert werden, dass der Vortrieb im Abschnitt III der Raibler Rauwacke sicher und erfolgreich möglich war.

Zur Kompensation des im Allgäuschiefer eingetretenen zeitlichen Rückstands beschloss der Bauherr, den Bauablauf umzustellen. Eine im Werkvertrag enthaltene Option wurde ausgelöst und der Abschnitt III von der Erkundungskaverne aus aufgefahren, gesichert und verkleidet. Dieser Gegenvortrieb begann am 7. Oktober 2016. Der gefrorene Zellendolomit wurde mit einem 42-t-Bagger mit Abbauhammer in bis zu 0,5 m³ großen Blöcken im Vollausbuch ausgebrochen. Die durchschnittlich erzielte Leistung für Ausbruch und Sicherung betrug 0.7 m je Tag. Ausbruch und Sicherung wurden am 2. Februar 2017 abgeschlossen.

Für den Einbau der stark bewehrten Innenschale aus Spritzbeton benötigte der Unternehmer weitere zwei Monate. Am 12. April 2017 war der neue Tunnel im Abschnitt III der Rauwacke fertig verkleidet.



Fig. 13: Vortrieb in der Rauwacke durch den Gefrierkörper im Abschnitt III

Nach Fertigstellung der Innenverkleidung konnte das Gefrieren eingestellt werden. Vom fertiggestellten Abschnitt III aus konnten die Abschnitte I + II der Rauwacke über lange Bohrungen mit Zement injiziert werden. Dadurch wurde der Zellendolomit bereits vor Eintreffen des Hauptvortriebs verfestigt und teilweise abgedichtet. Nachdem sämtliche für das Gefrieren, Injizieren und Ausbrechen des Tunnels erforderliche Baustelleneinrichtungen aus der Kaverne entfernt waren, konnte die Kaverne an den Hauptunternehmer übergeben werden.

Für den Ausbruch in der Rauwacke Abschnitte I und II wurde das Gebirge vom Hauptvortrieb Preda aus nochmals vorauseilend injiziert. Der Vortrieb erfolgte im Vollausbuch, das Gebirge wurde mit dem Tunnelbagger gelöst und abgebaut. Die Abschlagslänge betrug 90 Zentimeter. Die Sicherung bestand in den Abschnitten I + II aus einer 55 cm dicken Spritzbetonschale, die mit zwei Lagen Armierungsnetzen K335 bewehrt wurde. Auf den Einbau von Gitterträgern oder Stahlbögen wurde verzichtet.



Fig 14: Ortsbrust beim Vortrieb in der Rauwacke - Abschnitt II

Die Raibler Rauwacke konnte mit den beschriebenen bautechnischen Maßnahmen sicher bewältigt werden. Mit dem Durchschlag vom Abschnitt II zum Abschnitt III am 17. Oktober 2017 war die Schlüsselstelle beim Neubau des Albulatunnel II bezwungen.

3.3.2 *Albulagranit*

Bevor der Vortrieb im Albulagranit Richtung Spinas wieder starten konnte, musste das Tunnelförderband bis zur Kaverne nachgezogen werden. Der Unternehmer installierte den Brecher in der Kaverne. Für die Schutterung von der Ortsbrust bis zur Kaverne wurden zweiachsige Tunneldumper eingesetzt. Auf den weiteren Einbau des Förderbandes im Vortrieb Preda verzichtete der Unternehmer.

Am 7. November 2017 startete der Vortrieb Preda im Albulagranit. Der Ausbruchquerschnitt beträgt 35 m² und die Sicherung besteht aus 15 cm Stahlfaserspritzbeton mit Reibrohrankern. Wenn die Prognose eintrifft und die geplanten Leistungen erreicht werden, dann wird der Durchschlag zum Vortrieb Spinas im Oktober 2018 erfolgen.

3.4 Vortrieb Spinas

3.4.1 *Lockergestein*

Das neue bergmännische Portal in Spinas ist nur geringfügig gegenüber dem Portal des Albulatunnel II zurückversetzt und liegt näher am Betriebsgleis als das Portal in Preda. Allerdings ist das alte Portalmauerwerk in Spinas so massiv ausgebildet, dass

auf Bohrpfähle verzichtet werden konnte, die Portalwand wurde nur mit Ankern gesichert.



Fig. 15: Spinas – Situation Albatunnel I und Albatunnel II im Bauzustand

Der Vortrieb Spinas startete am 7. September 2015. Der Ausbruch im Lockergestein erfolgte im Schutze von 25 Rohrschirmetappen zu je 10 m Länge. Die Abschlaglänge betrug einen Meter, die Sicherung bestand aus HEB-Trägern im Gewölbe und in der Sohle sowie 30 cm bewehrtem Spritzbeton. Schwierigkeiten bereiteten vor allem die im Bachschutt zahlreich angetroffenen bis zu 1 m³ großen Felsblöcke. Die Ortsbrustsicherung aus Spritzbeton musste deshalb zum Teil mit Netzen ergänzt werden. Bei Bedarf wurde ein Brustkeil angeordnet, damit sich die Felsblöcke nicht selbständig aus der Brust lösten. Im Schnitt konnte eine Rohrschirmetappe im Bachschutt in 10 Arbeitstagen erstellt werden, in der Grundmoräne in 8.5 Arbeitstagen.

3.4.2 Albulagranit

Ab Tm 200 wurde in der Sohle der Albulagranit angetroffen und nach 254 m Vortrieb stand die Ortsbrust am 3. Oktober 2016 vollständig im Albulagranit. Das Ausbruchprofil betrug wie in Preda 35 m². Die Felssicherung bestand aus 15 cm Stahlfaserspritzbeton mit Reibrohrankern.



Fig. 16: Sprengvortrieb Spinas

Die Vortriebslogistik basierte auf dem Einsatz eines Tunnelförderbandes, so wie beim Vortrieb Preda im Allgäuschiefer. In Spinas konnten Vortriebsleistungen von durchschnittlich ca. 6.2 m je Tag erreicht werden. Die wie prognostiziert angetroffene Störung durch den Mylonit bereitete im Vortrieb keine Probleme. Das Vortriebsende soll entsprechend der Prognose im Oktober 2018 mit dem Durchschlag der beiden Tunnelröhren erreicht werden.

3.5 Innenverkleidung

Die portalnahen, im weniger standfesten Gebirge gelegenen Tunnelabschnitte in Preda und Spinas werden zweischalig verkleidet. Sie erhalten ein 30 cm dickes unbewehrtes Innengewölbe mit einer hinter der Ortbetonverkleidung angeordneten Regenschirmabdichtung. Auf der Seite Preda wird der gesamte ca. 1'100 m lange Tunnelabschnitt im Allgäuschiefer bis zur Rauwacke zweischalig ausgebaut, auf der Seite Spinas die ersten 300 m ab dem Tunnelportal. Die in der Sohle und im Gewölbe umlaufende Innenschale in der Raibler Rauwacke wird aufgrund der hohen Gebirgsspannungen und Wasserdrücke mit einer Vollabdichtung versehen, 60 cm dick und massiv bewehrt ausgeführt. Im Albulagranit wird der Tunnel einschalig mit 20 cm Spritzbeton verkleidet.

4 Materialbewirtschaftung

Die Baustellenlogistik stellte eine besondere Herausforderung dar, weil spezielle Randbedingungen zu berücksichtigen waren. Die Baustelle befindet sich in einem vom Tourismus geprägten, sensiblen Umfeld. Die Deponiekapazitäten in Preda sind beschränkt, in Spinas gibt es keine Möglichkeit zur Deponierung von Ausbruchmaterial. Massentransporte auf der Straße waren zu vermeiden und per Bahn standen nur begrenzte Transportkapazitäten zur Verfügung. Deshalb sollte das Tunnelausbruchmaterial durch Aufbereitung vor Ort grösstmöglich wiederverwertet werden.

Der gesamte Materialfluss auf der Baustelle musste über Förderbänder und mit der Bahn abgewickelt werden. In Preda wurde das Ausbruchmaterial mit den Förderbändern direkt aus dem Tunnel bis auf das Zwischenlager nach Las Piazzettas abgeführt. Das Ausbruchmaterial aus dem Vortrieb Spinass wurde mit Förderbändern aus dem Tunnel bis auf den Bauplatz transportiert und dort auf Bahnwagen der RhB verladen.

Mit dem von der RhB bereitgestellten Materialtransportzug „Albulasprinter“ wurden vier- oder achtmal je Wochentag 100 m³ Ausbruchmaterial von Spinass nach Preda transportiert. Dort wurden die Wagen entleert und mit dem Förderband auf das Zwischenlager neben der Deponie Las Piazzettas transportiert. Im Zwischenlager wurde das Ausbruchmaterial getrennt nach Materialklassen gelagert. Das nicht wiederverwertbare Material wurde vom Betreiber der Deponie Las Piazzettas abtransportiert und eingebaut.



Fig. 17: Deponie Las Piazzettas

Das verwertbare Material wurde in Las Piazzettas bis zur Aufbereitung im Kieswerk Preda gelagert und nach Bedarf im Kieswerk zu Bahnschotter für die RhB oder zu Betonzuschlagstoffen für den Tunnelbau aufbereitet. Der aufbereitete Bahnschotter wurde vom Kieswerk auf Bahnwagen verladen, von der RhB abtransportiert und zum Teil direkt auf anderen Bahnbaustellen eingebaut.

Die im Kieswerk produzierten Betonzuschlagstoffe gelangten entweder mit Förderbändern zur Betonanlage in Preda oder mit dem Albulasprinter per Bahn zur Betonanlage nach Spinass.



Fig. 18: Schotterverladung im Baubahnhof Preda

5 Ausblick

Der Durchschlag der beiden Vortriebe erfolgt im Oktober 2018. Anschließend werden die Förderbandeinrichtungen zurückgebaut und in den einschalig verkleideten Tunnelabschnitten wird die Sicherung komplettiert. Danach wird im gesamten Tunnel die Sohle aus Ortbeton eingebaut, auf der später eine feste Fahrbahn aufgebaut wird. In den zweischalig zu verkleidenden Abschnitten wird nach dem Einbau der Sohle die Gewölbeabdichtung eingebaut und das Innengewölbe betoniert. Danach können die Bankette mit vorfabrizierten Kabelrohrblöcken eingebaut werden. Die Fertigstellung des Tunnelrohbaus und die Übergabe an die Bauherrschaft zum Einbau der Bahntechnik sind 2020 geplant.

Nach Abschluss der bahntechnischen Ausrüstung des Tunnels, dem Rückbau der Installationsplätze und nach dem Umbau der Bahnhöfe soll der neue Albulatunnel 2021 in Betrieb genommen werden. Zum Abschluss der integralen Erneuerung wird im Jahr 2022 der alte Albulatunnel saniert und zum Sicherheitstunnel umgebaut.

6 Erfahrungen und Schlussfolgerungen

Aufgrund des an gleicher Stelle errichteten Albulatunnel I konnte auf eine detaillierte Dokumentation der Geologie und des damaligen Bauablaufs zurückgegriffen werden. Somit waren die Schlüsselstellen des Projekts bekannt. Das daraufhin erstellte Konzept zur Bewältigung der Störzone Rauwacke war erfolgreich. Die Kenntnisse vom Bau des ersten Albulatunnels wurden in dieser Hinsicht bestmöglich genutzt.

Zu optimistisch war die Prognose der zu erwartenden Ausbruchklassenverteilung im Allgäuschiefer. Wegen der für die Festlegung der Sicherungsklassen relevanten Nachbrüchigkeit des Schiefers konnten nur Abschlagslängen von ein bis zwei Meter realisiert werden und es überwogen die schlechten Sicherungsklassen.

Die ursprünglich nur für die Erkundung der Rauwacke vorgesehene Kaverne wurde sowohl vom Bauherrn als auch vom Unternehmer genutzt, um den Bauablauf zu optimieren. Die Entscheidung des Bauherrn zur Umstellung des Bauablaufs und Durchführung eines kurzen Gegenvortriebs im bautechnisch schwierigsten Abschnitt der Rauwacke hat sich als richtig erwiesen. Die Verzögerungen, die beim Vortrieb im Allgäuschiefer in Kauf genommen werden mussten, wurden durch diese Umstellung des Bauablaufs teilweise wieder kompensiert. Auch der Unternehmer nutzte die vorab erstellte Erkundungskaverne und optimierte ab dort die Logistik für den Vortrieb im Albulagranit.

Festzustellen ist, dass wir trotz unserer modernen Technologie und trotz der wissenschaftlich fundierten Erkenntnisse aus den Geowissenschaften und der Geotechnik heute nicht schneller bauen als vor über 100 Jahren. Und so werden zukünftig am zweithöchsten Alpendurchstich der Schweiz zwei Bauwerke zeigen, zu welchen Leistungen die Tunnelbauer in der Vergangenheit in der Lage waren und welche Leistungen in der Gegenwart möglich sind.

Blasting experiences from different tunnel excavations

Erfahrungen von Sprengungen verschiedener Tunnelvortriebe

Alfred Zettler

zConsult ZT GmbH

Kühbergstrasse 30, 5324 Faistenau, Österreich

Abstract

The estimation of the amount of explosive and necessary number of boreholes in the design and calculation phases in tunneling is often based on examples in the literature and on experiences made by tunnels in comparable geologic formations and comparable tunnel cross sections.

Examples in the literature are often based on medium blastable rock. In this paper examples of hard blastable rock conditions are compared with the medium blastable rock and with hard blastable rock.

Zusammenfassung

Die Festlegung der Sprengstoffmenge und der Anzahl der notwendigen Bohrlöcher in der Planungs- und Kalkulationsphase von Tunneln wird oft auf Basis von Beispielen in der Literatur oder von eigenen Erfahrungen bei Tunnelbauten mit vergleichbarer geologischer Formation und vergleichbarem Tunnelquerschnitt getroffen.

Beispiele in der Literatur werden sehr oft auf Basis von mittelschwer zu sprengendem Gebirge dargelegt. In diesem Beitrag werden Beispiele mit schwer zu sprengendem Gebirge mit mittelschwer zu sprengendem Gebirge und mit schwer zu sprengendem Gebirge gegenübergestellt.

1 Examples from literature

1.1 Loading explosives

In different publications the suggested amount of explosive is based on medium blastable rock conditions. An example is given by Johansen et al [1] for different borehole diameters, with a parallel cut and medium blastable rock the suggested amount of explosive is a variable of the tunnel cross section (see figure 1.1). In the publication the exact geological name of the medium blastable rock is not given.

The diagram in figure 1.1 shows, that the cross section of the tunnel influences the suggested amount of specific explosive consumption. The larger the tunnel cross section the lower the specific amount of explosive consumption per cubic meter of medium blastable rock.

The diagram in figure 1.1 also shows that the diameter of the drilled borehole has an influence, the larger the borehole diameter the lower the specific amount of explosive consumption per cubic meter of medium blastable rock.

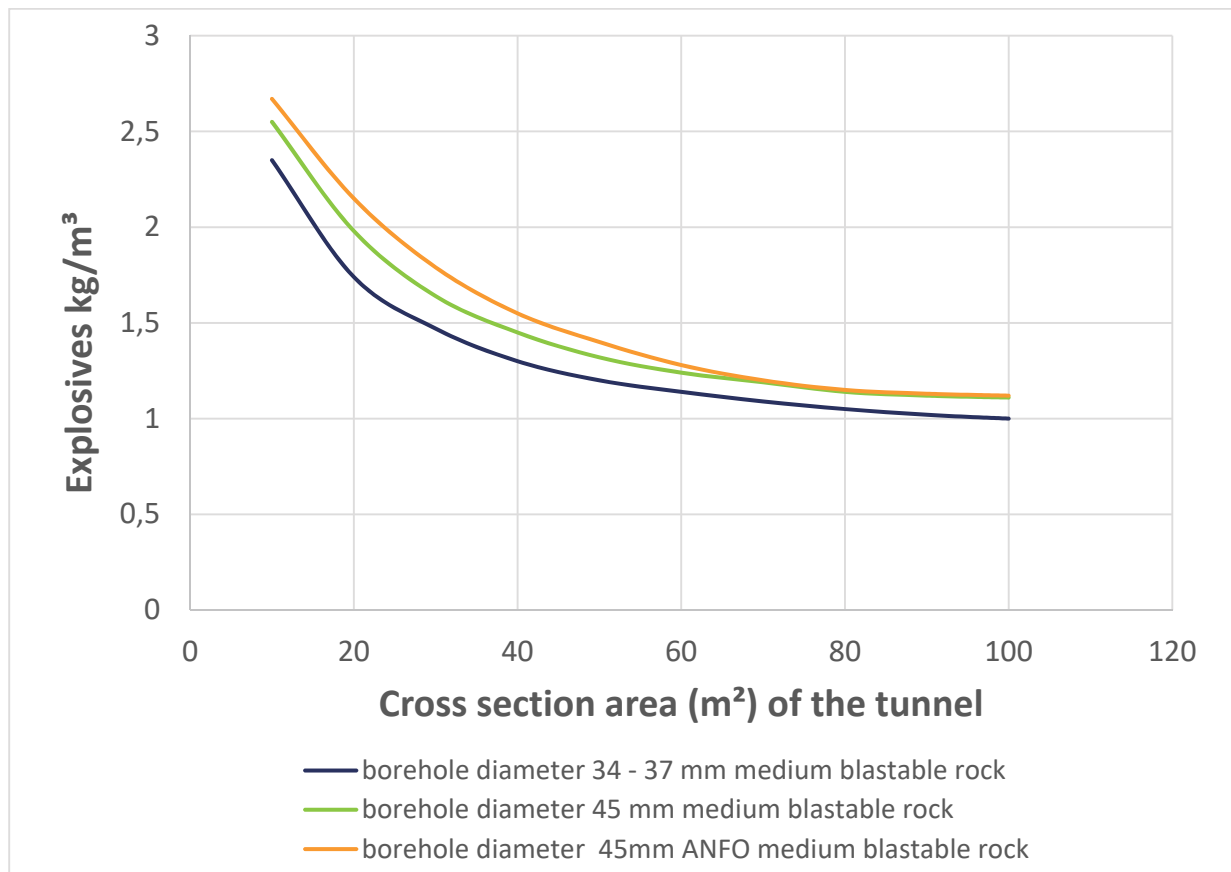


Fig. 1.1: Suggested loading different borehole diameter, parallel cut, medium blastable rock (Source: after J. Johansen et al [1], figure 5,1, 5.2 and 5.3)

1.2 Number of boreholes

The suggested number of boreholes given in different publications is also often based on medium blastable rock conditions. An example is given by Johansen et al [1] for different borehole diameters, with a parallel cut and medium blastable rock. The suggested number of boreholes is also function of the tunnel cross section (see figure 1.2). In the publication the exact geological name of the medium blastable rock is not given.

The diagram in figure 1.2 shows, that the cross section of the tunnel influences the suggested number of boreholes. The larger the tunnel cross section the higher the number of required boreholes. The diagram in figure 1.2 also shows, that the diameter of the drilled borehole has an influence, the larger the diameter of the borehole the lower the number of required boreholes.

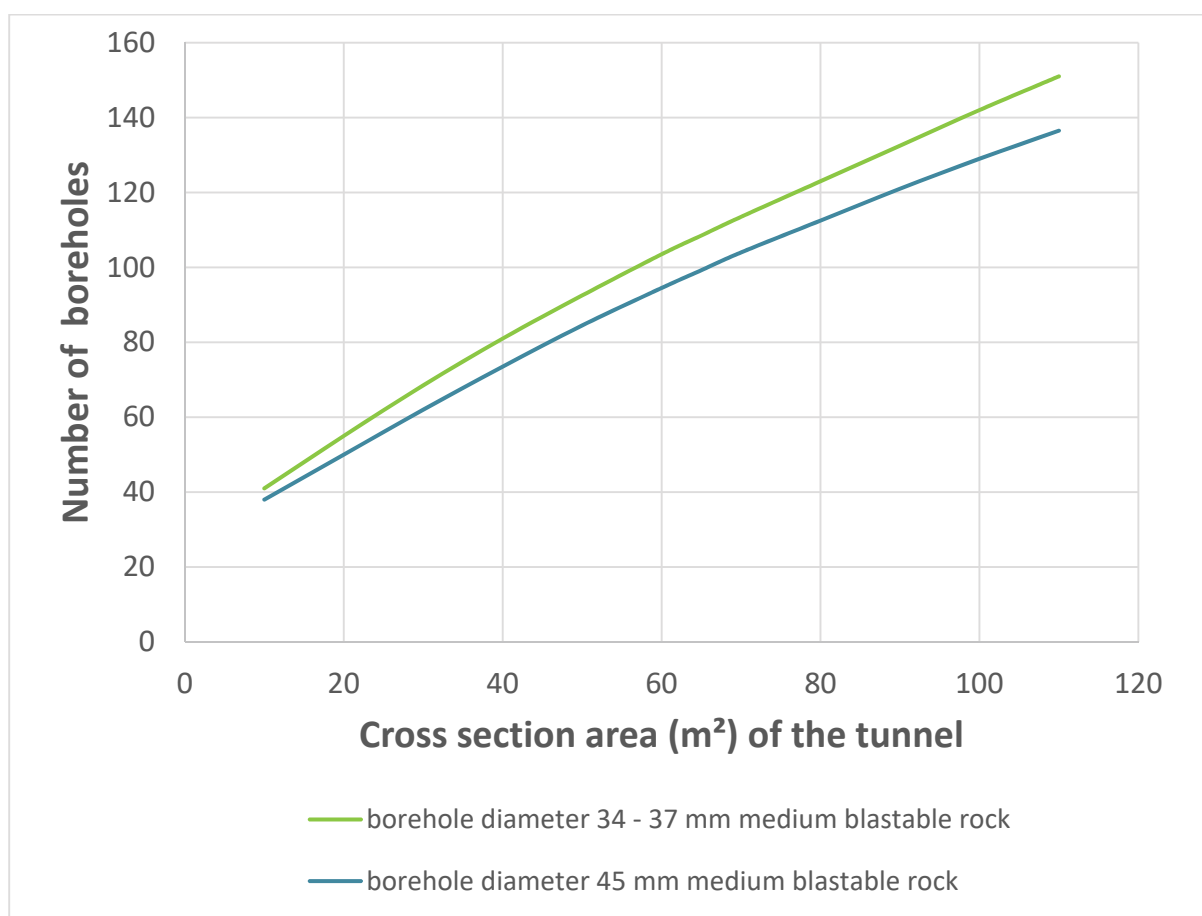


Fig. 1.2: Suggested number of boreholes for different borehole diameter, parallel cut, medium blastable rock (Source: after J. Johansen et al [1], figure 4.13)

2 Comparison between field investigations and literature

2.1 Loading explosives

In figure 2.1 the comparison of suggested loading explosives based on different borehole diameters for parallel cut with medium blastable rock and hard blastable rock is given. In all investigated examples the hard blastable rock was a granite or a granodiorite.

For hard blastable rock the required loading is higher than for medium blastable rock with approximately the same borehole diameter. For a tunnel cross section area of 20 m² approximately 23 % and for a 100 m² cross section area approximately 41 % more specific explosives in kg/m³ are required than for hard rock conditions.

The comparison with a publication by Schillinger [4] leads to higher results than investigated in the field. For this comparison the average values in table 5.21 from Schillinger [4] for 10 m² and 40 m² for hard rock (granite, gneis, basalt) was taken into account. The rest of the graph was found using a potential extrapolation (see figure 2.1 dotted line).

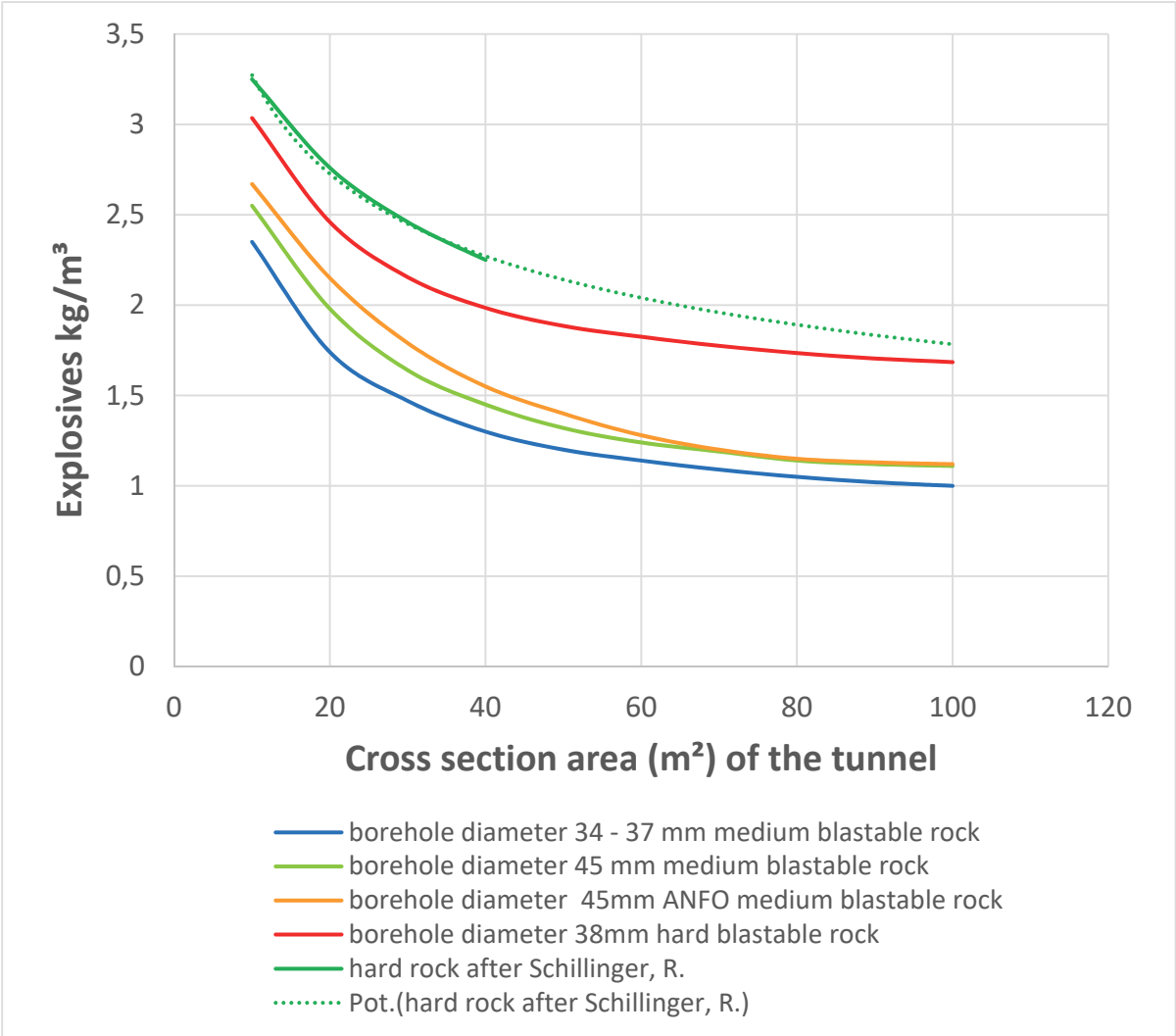


Fig. 2.1: Comparison of suggested loading explosive of different borehole diameter, parallel cut, medium blastable rock and hard blastable rock (Source: A. Zettler and after J. Johansen et al [1], figure 5,1, 5.2 and 5.3 and after Schillinger [4], table 5.21 for 10 m² and 40 m² the average in the table was taken and the rest was extrapolated by a potential law)

2.2 Number of boreholes

In figure 2.2 the comparison of suggested number of boreholes based on different borehole diameters for parallel cut with medium blastable rock and hard blastable rock is given. For hard blastable rock the required number of boreholes are higher than for medium blastable rock with approximately the same borehole diameter. For a tunnel cross section area of 20 m² approximately 28 % and for a 100 m² cross section area approximately 17,5 % more boreholes are required for hard rock conditions.

The comparison with the Blasters' Handbook by ISEE [2] shows that for poor blastability rock (in this publication poor blastable rock is used for hard to blast rock) with the suggestion for the required number of boreholes is much lower, approximately 60 %, than based on the field investigations for hard blastable rock.

The comparison with a publication by Maidl [3] for hard blastable rock leads to similar results investigated in the field.

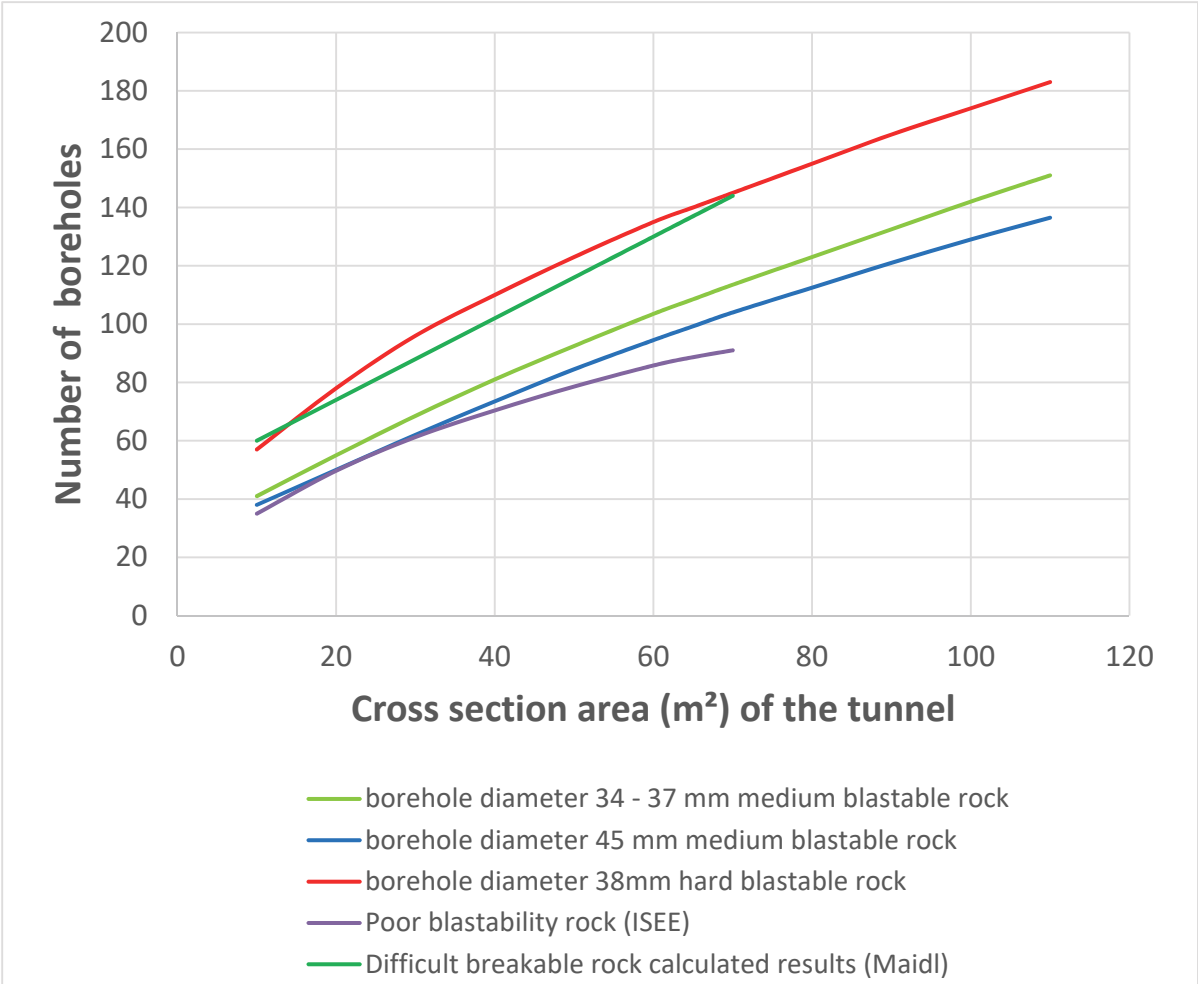


Fig. 2.2: Suggested number of boreholes for different borehole diameter, parallel cut, medium blastable rock and hard blastable rock (Source: A. Zettler and after J. Johansen et al [1], figure 4.13 and after International Society of Explosives Engineers [2], figure 35.20 and after Maidl [3])

3 Conclusion

Examples show that for comparable borehole diameter for hard blastable rock the required loading explosives and the number of boreholes are higher than for medium blastable rock. For a small tunnel cross section approximately 23 % and for a large cross section area approximately 41 % more specific explosives (kg/m^3) are required in hard rock conditions than in medium blastable rock. The required number of boreholes are also higher. For a small tunnel cross section area approximately 28 % and for a large cross section area approximately 17,5 % more boreholes are required in hard rock conditions than in medium blastable rock.

Comparable results for specific explosive consumptions and required number of boreholes are received if results the same geological conditions are used to describe the rock mass. The nomenclature of medium blastable rock or poor blastable rock is not very useful and leads to misunderstanding of the real conditions.

4 References

- [1] Johansen, J.; Mathiesen, C. F.: *Modern Trends in Tunnelling and Blast Design*. Taylor and Francis, 2000
- [2] International Society of Explosives Engineers: *Blasters' Handbook* 18th Edition Third Printing, 2016
- [3] Maidl, B.: *Bohrlochanzahl n in Abhängigkeit von der Querschnittsfläche F*. Schweizerische Bauzeitung, Band 90, 1972
- [4] Schillinger, R.: *Sprengtechnik und Umwelt in der Praxis*. Carl Hanser Verlag, 2009

The Koralm tunnel underground emergency stop – geotechnical design and construction

**Die Nothaltestelle des Koralmtunnels –
Geotechnische Planung und Bauausführung**

Thomas Pilgerstorfer, Harald Hölzl
Geoconsult ZT GmbH
Hölzlstraße 5, 5071 Wals/Salzburg, Austria

Bernd Moritz
ÖBB-Infrastruktur AG
Griesgasse 11/1, 8020 Graz, Austria

Abstract

The Koralm Tunnel, a twin-tube single-track railway tunnel with an overall length of almost 33 km and a maximum overburden of about 1.200 m, closes the most significant gap of the future high-capacity railway line from Graz to Klagenfurt, Austria. Located close to the tunnel center, an emergency stop will provide the facilities for future travelers to be evacuated to safety in case of an emergency. The following paper discusses the challenges of the design and incorporates the current state of the ongoing construction works of the emergency stop. In addition, the structure and content of the geotechnical safety management plan, as well as the applied monitoring program are presented in detail, emphasizing the analysis of the observed system behavior in connection with the encountered geological conditions.

Zusammenfassung

Der Koralmtunnel, ein zweiröhriger, eingleisiger Eisenbahntunnel mit einer Gesamtlänge von knapp 33 km und einer maximalen Überlagerung von rund 1.200 m schließt die Lücke der zukünftigen Hochleistungsstrecke zwischen Graz und Klagenfurt. In Tunnelmitte befindet sich eine Nothaltestelle, welche für die zukünftigen Passagiere eine Einrichtung zur sicheren Rettung bei Eintreten eines Störfalls bietet. Der vorliegende Artikel beleuchtet die Herausforderungen in der Planungsphase und umfasst den derzeitigen Stand der laufenden Arbeiten in der Nothaltestelle. Die Struktur und der Inhalt des Geotechnischen Sicherheitsmanagementplans sowie das eingesetzte Monitoringprogramm werden im Detail vorgestellt, wobei die Analyse des beobachteten Systemverhaltens in Kombination mit den angetroffenen geologischen Verhältnissen hervorgehoben wird.

1 Introduction

The 32.9 km long Koralm Tunnel connects the cities Graz and Klagenfurt and is the main part of the new Baltic-Adriatic axis, the high capacity railway corridor between Gdansk and Bologna. At the main construction lot KAT2, 2 x 17 km (of total approx. 40 km) excavation is done by two double shield TBMs (Figure 1.1). The centerpiece of the lot is an approx. 1 km long underground emergency stop with a maximum overburden of 1.200 m, which is excavated conventionally (NATM) between and parallel to the two main tunnel drives [1]. It is evident, that for such a complex underground structure special logistical facilities are required to ensure an effective construction process.

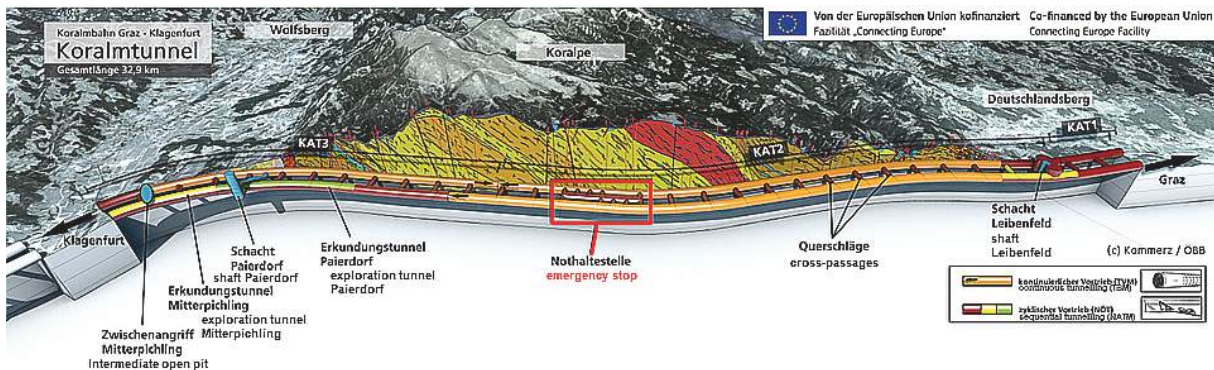


Fig.1: Layout of the Koralm Tunnel.

2 Geological Conditions

The area of the Koralm Tunnel project is mainly located in the Koralm crystalline complex (Figure 2.1), with a tectonic boundary to the neogene sediments of the Lavanttal Basin in the west and plunges under the likewise neogene deposits of the Western Styrian Basin in the east. The rockunits mentioned are covered over wide areas by quaternary sediments. These younger deposits are underlain by thick sequences of Miocene fine- and coarse-grained sediments of the Lavanttal Basin [2].

The unit of the Koralm crystalline complex in the central part of the Koralm is assigned to the crystalline basement of the Koralm, which is mainly composed of middle-east Alpine and polymetamorphic paragneisses. Amphibolites, eclogites and marbles are embedded in mainly mica- and quartz-rich gneisses and schists. Pegmatites are found subordinately as concordant and discordant to the foliation-oriented deposits. Ground water inflows with occasional high water pressures are usually related to areas with intense fracturing, damage zones or faults [4].

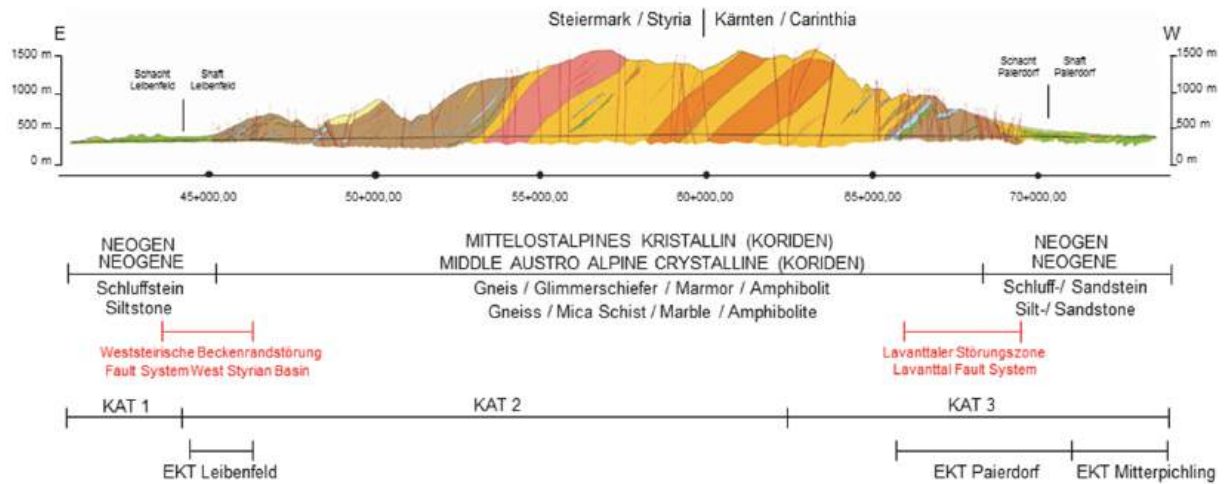


Fig. 2.1: Simplified geological longitudinal section along the Koralm Tunnel, depicting the main lots KAT1, KAT2 and KAT3 and sections with exploration structures of Leibenfeld, Paierdorf and Mitterpichling (taken from [2]).

The emergency stop is situated in the Koralm crystalline complex. The overburden is between 1.090 m and 1.200 m. The rock mass section of the emergency stop is mainly composed of a sequence of fine-grained gneisses. In addition, subordinately quartzites, mica slates, shale gneisses, marbles and amphibolites occur. The rock mass is mainly massive, has high strength and is unweathered. The foliation planes mainly strike in acute to obtuse angles to the tunnel axis and dip flatly against direction of excavation. Steeply dipping joints and slickensides strike parallel to perpendicular to the tunnel axis. The eastern part is characterized by an intensive local folding of the foliation and a frequent change of above mentioned rocks. The geological documentation performed in the northern and southern tube, which were excavated prior to the construction of the emergency stop, shows ground types having a high (> 100 to 150 MPa) to extraordinary high (> 150 MPa) rock strength and moderate to slight fracturing of the rock mass (20 – 60 cm to 60 – 200 cm). The geotechnical design was carried out based on the rock mass parameters of the ground types which were dominantly encountered at the examined calculation cross-sections (Table 1).

Tab. 1: Rock mass parameters of the ground types K2 and K3 used in the geotechnical design.

ground type K2		
rock mass parameter	median	value range (from – to)
rock mass strength σ_D [MPa]	36	21 – 66
Young's modulus rock mass E_m [MPa]	30.000	25.000 – 45.000
friction angle (drained) ϕ' [°]	35	30 – 40
cohesion (drained) c' [MPa]	10	6 – 16
specific weight (drained) γ' [MN/m ³]	0,026	-
Poisson's ratio ν [-]	0,3	-
rock mass permeability k [m/s]	1xE-9	-
dilatancy angle i [°]	0,0	-

ground type K3		
rock mass parameter	median	value range (from – to)
rock mass strength σ_D [MPa]	17	10 – 29
Young's modulus rock mass E_m [MPa]	19.000	12.000 – 30.000
friction angle (drained) φ' [°]	33	28 – 38
cohesion (drained) c' [MPa]	4	2,5 – 7
specific weight (drained) γ' [MN/m ³]	0,026	-
Poisson's ratio ν [-]	0,3	-
rock mass permeability k [m/s]	1xE-9	-
dilatancy angle i [°]	0,0	-

3 Tunnel Design and Layout

The emergency stop with a total length of 981 m is situated in the middle between the two tunnel bores, which have an offset of approx. 50 m. Main elements of the facility are 5 cross- and 16 escape passages. These structures have an overall offset of 50 m of centre distance. Due to the logistical concept during construction, two additional adits (access tunnels) and a logistic cavern have been added to the basic design of the emergency stop. The logistic cavern has a cross section of 125 m² and a length of approx. 100 m (Figure 3.1, Figure 3.2 and Figure 3.3).



Fig. 3.1: Emergency stop – logistic cavern (courtesy of OeBB).

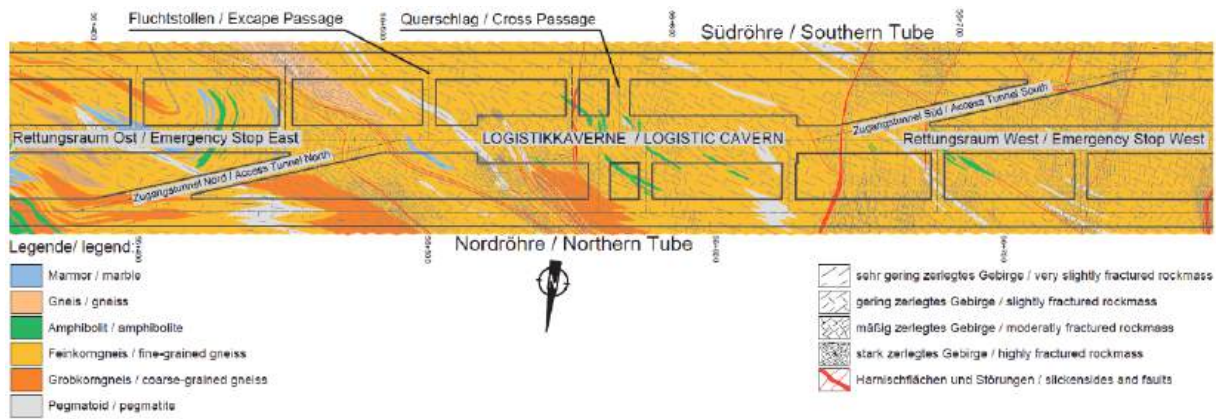


Fig. 3.2: Layout of the emergency stop in the vicinity of the logistic cavern, underlaid with geological horizontal section.

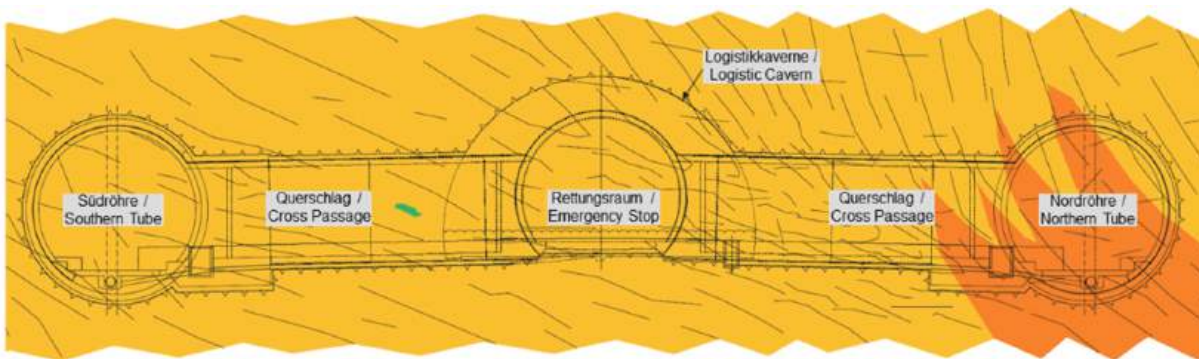


Fig. 3.3: Cross section of main tubes, cross passage QS 33 and logistic cavern/emergency stop with documented geological conditions.

The challenge of the design was the interaction of the whole tunnel system due to the resulting narrow rock pillars and the glancing intersections of the adits with the TBM drives and the emergency stop in between (Figure 3.4 and Figure 3.5). The minimum rock pillar between the TBM drives and the logistic cavern resulted a distance of only 12 m.



Fig. 3.4: Intersection of logistic cavern and access tunnel north (courtesy of OeBB).



Fig. 3.5: Intersection of northern tube (TBM) and access tunnel north (courtesy of Geoconsult ZT GmbH).

In order to accomplish and ensure a safe design, the system behaviour and ground utilization by evaluation of the ratio between the strength of the ground and the spatial stress situation in the vicinity of the underground openings was derived by numerical methods. Special consideration was given to the unfavourable situation of remaining rock pillars in the design phase. In order to ensure an accurate, realistic assessment of the superposing secondary stress states due to the individual tunnel advances, influencing the pillar stability, a 3D numerical analysis was carried out. In the numerical calculation, the construction process was simulated according to the intended excavation concept to fully capture all relevant constructional influencing factors. The performed numerical study allowed a proper estimation of the spatial distribution of overstressed rock mass in the pillars and provided a sound basis for an appropriate selection of support measures. After evaluating the system behaviour in the excavation area a determination of construction measures were decided in detail (Figure 3.6). This led to a framework plan with criteria for excavation and support and the layout of the support measures on site.

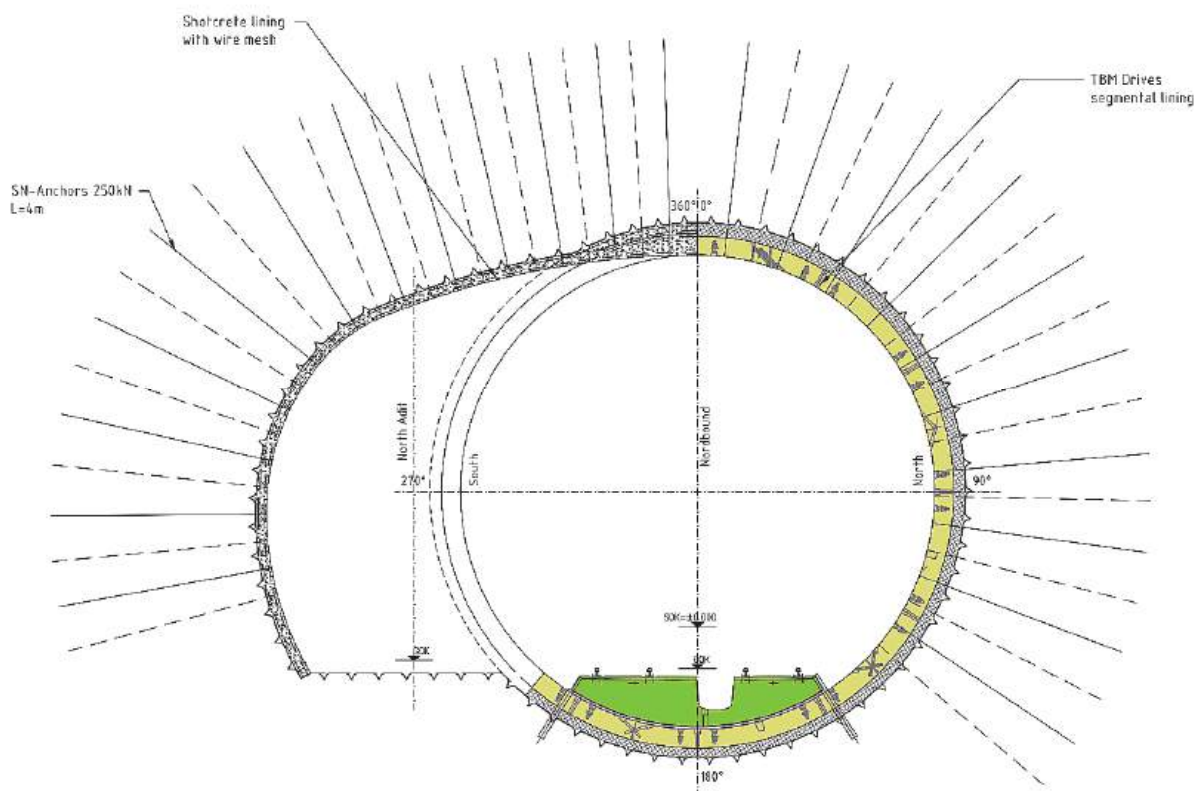


Fig. 3.6: Excavation and support at the intersection of access tunnel with main tube (TBM-tunnel).

4 Geotechnical safety management plan

Despite a complex investigation program, extensive laboratory testing and ground characterization uncertainties in the geological conditions will remain. Thus the reaction of the ground due to the tunnel excavation might not be fully captured and cannot be estimated precisely enough in advance, yielding residual risks during the construction phase. These boundary conditions require the use of the observational method in combination with the principles of Eurocode EC 7. In order to ensure safe and economical tunnelling it is of vital importance that a qualified geotechnical safety management program is implemented during the construction phase [3].

Due to the complexity of the emergency stop a separate section was developed and integrated in the existing geotechnical safety management plan of the lot KAT2.

Based on the observed system behaviour during the tunnel advance of the two main tubes, it was possible to predict the expected system behaviour in the emergency stop with utmost prediction accuracy. The anticipated amount of displacement magnitudes of the shotcrete shell was determined through numerical analyses, in which the input parameters were calibrated on the observed displacement behaviour in the main tubes. The intervention matrix, which forms the core element of a geotechnical safety management plan, summarizes the defined preliminary warning, warning and alarm criteria, together with required mitigation measures and all-clear criteria. The matrix is twofold: The part "general", valid for the entire excavation works of the

emergency stop, includes the safety-relevant parameters face stability, water inflow, gas influx, displacement behaviour during construction states, stability of the tunnel structure after construction of the invert, swelling pressure and utilization of the shotcrete shell. The intervention matrix is further grouped in the particular advance-sections:

- advance of escape galleries and cross passages (with full face excavation and sequential excavation - top heading/bench/invert),
- advance of rescue zone/logistic cavern (with sequential excavation top heading/bench/invert).

For the individual advance sections further safety-relevant parameters like admissible displacement magnitudes, utilization of the shotcrete shell, rock block stability (both for open round and the supported areas), and system behaviour “rock burst” were defined. Taking into account the complex spatial conditions, safety-relevant parameters were specified for the influence of the excavation of the emergency stop on the main tubes:

- additional displacements in the main tubes, caused by the emergency stop advance,
- displacement behaviour of the opened pre-cast concrete segment rings (opening due to intersection with escape galleries, cross passages, etc.),
- utilization of the precast concrete segment shell,
- admissible vibration velocities in the main tubes (due to the drill and blast excavation in the emergency stop).

5 Monitoring program

An extensive program for monitoring, observation and interpretation was developed to capture the range of expected system behaviours. One of the main purposes of the program is to examine if the observed system behaviour lies within expected limits, and to validate the appropriateness of the excavation and support measures.

5.1 3D-Displacement monitoring

During excavation of the emergency stop a detailed 3D-displacement monitoring was carried out on a dense grid of monitoring cross sections. Monitoring cross sections were usually installed in a distance of 10 meters. Additionally, parallel 3D-displacement monitoring was performed in the main tubes, in the vicinity of the current tunnel faces of the emergency stop (excavation-influenced region in the main tubes, approx. +/- 50 – 100 m). In order to ensure a convincing monitoring data interpretation, the monitoring cross section distance was densified in the main tubes in the vicinity of the emergency stop.

5.2 Measurement pre-cast concrete rings

In order to obtain an enhanced understanding of the system behaviour, especially with regard to the capacity reserves of the support and general load conditions, measurement pre-cast concrete rings are used at the construction lot KAT2 of the Koralm Tunnel. These are equipped with a strain gauge in each reinforcement layer, thus allowing direct measurement of the strains in every pre-cast concrete segment.

Based on this information, the stress distribution in the respective segment cross-section can be calculated, allowing section forces determination by integrating them [5]. Measurement pre-cast concrete rings, which are usually installed in more challenging ground conditions such as tectonical faults, were installed in a dense sequence in the area of the emergency stop. In both tubes five measurement pre-cast concrete rings were installed, focusing on the more sensitive tunnel stretches like coincidence of cross passages, escape galleries and the main tube, forming relatively slender remaining pillars, or intersections in acute angles of emergency stop structures with the main tubes.

5.3 Measurement of blasting-induced vibrations

One of the main issues was to gain knowledge about the impact of the excavation works of the emergency stop on the pre-cast concrete segment support of the main tubes. Especially the amount of blasting-induced vibrations on the support should be determined. Basically, the amplitudes of the vibrations, which are caused by blasting, depend on several, partly geometrical, factors, like severity of the event, location of the event and distance to the event. Since all these influencing factors are known, it is possible to determine the blasting-induced vibrations for each loading quantity per ignition stage by measurements on the pre-cast concrete segments.

Calibrated monitoring systems were used (VIBRAS® System, Walesch Electronic GmbH), which measure the vibration impact on a structure in terms of vibration velocity [6]. In order to determine the blasting seismic vibrations at the pre-cast concrete segments, three monitoring units are mounted on the emergency stop facing side of the tunnel sidewall in both main tubes (Figure 5.1). The asymmetrical allocation of monitoring units was deliberately chosen, allowing a sound determination of the dependence of the amplitude of vibrations on the distance and hence a potential geometrically anisotropic propagation of vibrations.

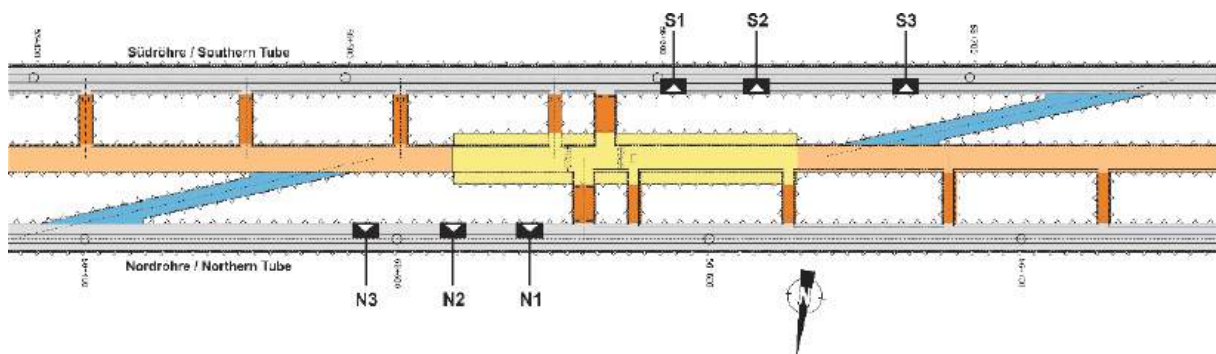


Fig. 5.1: Geometric allocation of monitoring units for the measuring system Vibras (taken from [6]); N ... northern tube, S... southern tube.

The system consists of several monitoring stations and a monitoring unit, which processes and stores the data. The monitoring stations and the unit are mounted on a pre-cast concrete segment (Figure 5.2). The data transmission out of the tunnel tubes is carried out by GSM-network.

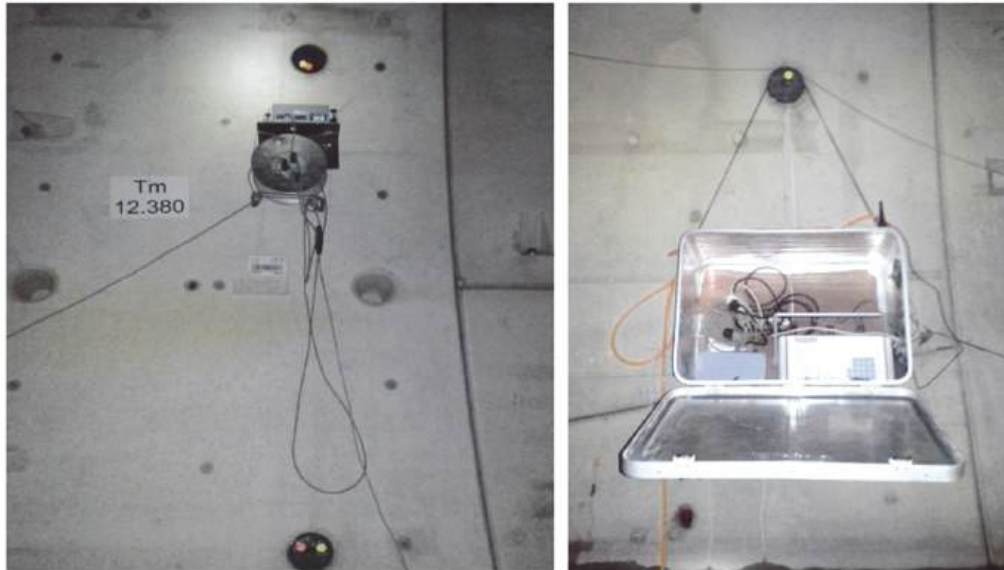


Fig. 5.2: Installed monitoring station (left) and monitoring unit (right) in the main tunnel (taken from [6]).

The vibrations are detected in terms of vibration velocities in three directions. Through data evaluation the maximum vibration velocities and thus the load, acting on the pre-cast concrete segments, can be determined. The vibration measurements allow an optimization of the loading quantity per ignition stage when threshold values for allowable vibration velocities at the pre-cast concrete segments are specified. According to Austrian standard ÖNORM S9020 and based on own experience, ≤ 50 mm/s of vibration velocity were defined as nominal behaviour. A tolerance range between > 50 mm/s and ≤ 90 mm/s was set as tolerable for single events. The threshold value was fixed at > 90 mm/s of vibration velocity. If vibration velocities systematically exceed 50 mm/s the geotechnical safety management plan provides that proactive measures have to be undertaken to contain the vibration velocities (e. g. change of blasting pattern, reduction of round length, etc.).

6 Observed system behaviour

During the excavation works a systematic documentation of geological and geotechnical conditions and observation of system behaviour was carried out. The advance of the emergency stop showed mainly favourable system behaviour with mostly stable conditions. Subordinately, gravitational, local detachment of rock blocks from the tunnel face and the excavation perimeter due to kinematically unfavourable orientation of discontinuities was observed. In massive sections the system behaviour was characterized by brittle failure of the rock mass in the vicinity of the tunnel, which led to plate-like breakouts from the tunnel face and the excavation perimeter. Regarding the displacement behaviour, mostly low displacement magnitudes were monitored (max. vertical displacement in the crown < 25 mm), with rapid stabilization and low utilization of the support. The predicted displacement magnitudes, which were in the amount of approximately 20 mm for the logistic cavern, were in good accordance with the in-situ measured displacements. The determination of the utilization of the shotcrete lining, based on the monitored displacement magnitudes by applying the hybrid method implemented in the evaluation software, showed mainly utilization rates < 50 %. However, rock mass sections with steeply dipping foliation planes,

striking perpendicular to the tunnel axis led to an increased shear movement along foliation planes. In such geological conditions total displacements of max. 70 mm were observed in a few exceptional cases (Figure 6.1). Thus yielding a higher utilization of the shotcrete shell which was successfully mastered by specific additional rock bolting.

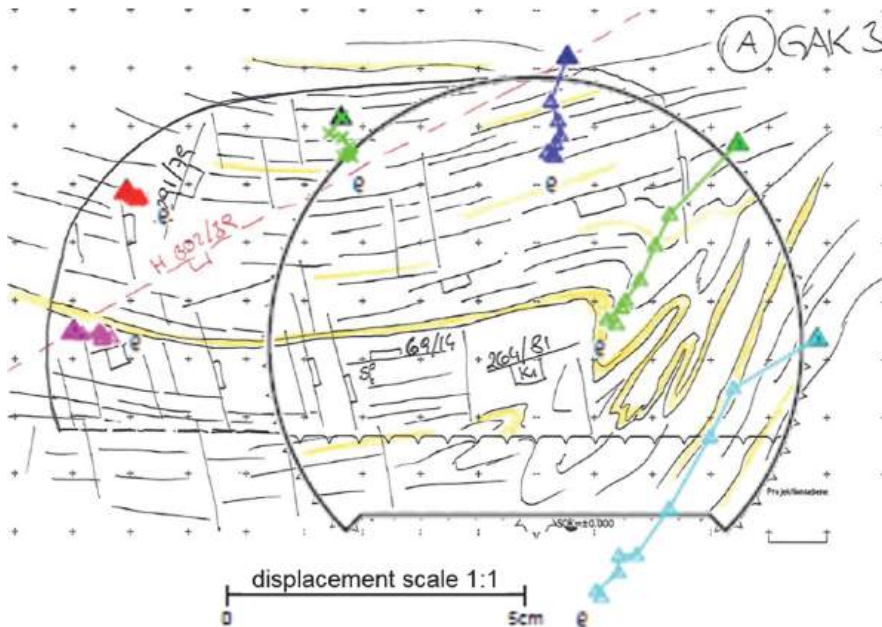


Fig. 6.1: Monitoring cross section plot at chainage 369 (\pm km 58+506.5) with geological tunnel face documentation at the intersection of logistic cavern – access tunnel north; shearing along foliation at right side wall.

Intensified rock bolting was also performed in the slender rock pillars at the intersections between main tube and access tunnel or logistic cavern and access tunnel, respectively.

The blasting induced vibrations showed to have minor influence on the pre-cast concrete segments in the main tubes. Mostly vibration velocities far below the defined threshold of 50 mm/s between nominal behaviour and tolerance range were observed (Figure 6.2).

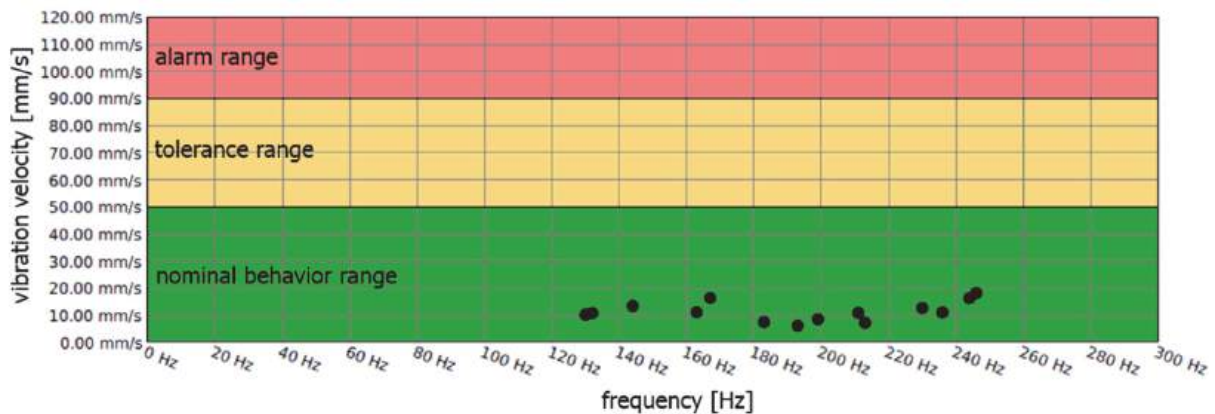


Fig. 6.2: Exemplary depiction of measured vibration velocity versus frequency (courtesy of arge:geo:kat2).

The results of the installed measurement pre-cast concrete rings in the main tubes for the determination of the load acting on the support further confirmed the observed favourable system behaviour during the construction of the emergency stop. In general only a slight increase of normal forces or bending moments in the pre-cast concrete rings due to the excavation works of the emergency stop could be determined. Higher increases of normal forces were registered in a measurement pre-cast concrete ring which is situated at the intersection of the access tunnel south and the southern tube. A normal force increase in the lower meganewton-range was evident, but still a generally low utilization of the whole pre-cast concrete ring (Figure 6.3). Hence, this indicates that large-scale stress redistribution processes in the rock mass did not occur, which could have caused adverse effects on the pre-cast concrete support of the main tunnels.

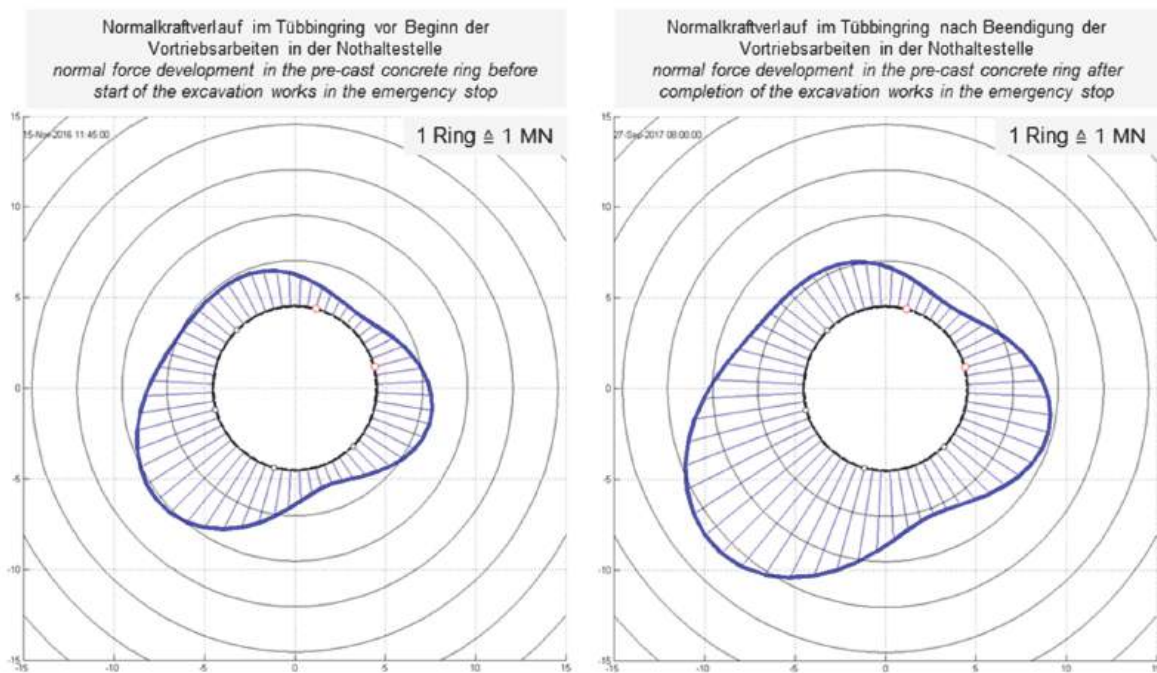


Fig. 6.3: Comparison of normal force development in measurement pre-cast ring (ring no. 5.592 south, intersection of access tunnel south and southern tube) before start (left) and after completion (right) of the excavation works in the emergency stop.

7 Conclusion

The entire tunnel advance, support requirements and observational approach concept presented above have been verified and justified by the advance of the emergency stop. All the tunnelling activities were performed parallel to the running TBM advance in the northern and southern tube. The introduced logistical facilities (i. e. logistic cavern and additional access tunnels) were established into the final tunnel design and will serve for the logistical accomplishment and concrete supply of the inner lining installation of the running tunnels. The advance of the tunnel system has shown that the key to success are a sound design which is constantly improved by the designers and the site team as the level of experience rises and a custom-tailored geotechnical safety management.

Literature

- [1] Neumann, C., Diernhofer, F., Sommerlechner, C., Burghart, M.: *Tunnel Safety Concept Koralm Tunnel*. Geomechanics and Tunnelling 1 (2008), No. 4, 264 - 270.
- [2] Moritz, B., Handke, D., Wagner, H., Harer, G., Mussger, K.: *Criteria for the selection of tunnelling method through the example of the Koralm Tunnel*. Geomechanics and Tunnelling 4 (2011), No. 4, 305 - 316.
- [3] Moritz, B., Koinig, J., Vavrovsky, G.-M.: *Geotechnical safety management in tunnelling – an efficient way to prevent failure*. Geomechanics and Tunnelling 4 (2011), No. 5, 472 - 488.
- [4] Moritz, B., Pilgerstorfer, T., Pointner, P.: *Experience of conventional excavation in crystalline rock mass on Koralm Tunnel contract KAT3*. Geomechanics and Tunnelling 8 (2015), No. 6, 489 - 502.
- [5] Radoncic, N., Kern, M., Weissnar, M., Moritz, B.: *Strain gauges in precast concrete segments: working principle, evaluation and interpretation*. Geomechanics and Tunnelling 8 (2015), No. 3, 265 - 272.
- [6] arge:geo:kat2.: *Construction of the emergency stop at lot KAT2 – measurement concept*. Internal report 2015, unpublished.

Solutions for Geotechnical Challenges in the Design of the Boezbergtunnel

Umsetzung der geotechnischen Herausforderungen in der Planung zum Projekt Bözbergtunnel

Karl Grossauer¹, Thomas Zieger², Werner Schmid³

¹ Amberg Engineering AG, Regensdorf-Watt, Switzerland

² Swiss Federal Railway Authorities, Lucerne, Switzerland

³ Implenia Schweiz AG, Wallisellen, Switzerland

Abstract

The new Boezberg tunnel is the largest and most important project of a large railway upgrade program of the Swiss railway authorities in order to further increase the transfer of transalpine traffic through Switzerland from rail to road. The tunnel was designed and built in an environmentally sensitive area with complex geological and hydrogeological conditions. One of the main challenges is swelling and complex ground conditions due to the presence of Opalinus clay, Anhydrite and Gypsum. In the first 180 m of tunnel, extensive exploratory drillings from the surface were performed parallel to the tunnel excavation in order to precisely determine the best place for starting the TBM excavation. By means of the systematic underground exploratory drillings a zone of swelling ground was identified below the tunnel with a limited extent. For this area the final lining was designed as a monolithic tube over a length of 37.5 m with continuous reinforcement in longitudinal direction in order to distribute and transfer any swelling pressure into zones with no swelling. The critical zone below the tunnel is permanently monitored by means of deformation meters.

Zusammenfassung

Der Neubau des Bözbergtunnel ist das grösste und wichtigste Projekt der SBB im Zuge eines groß angelegten Programms zur Verlagerung der alpenquerenden Gütertransporte von der Straße auf die Bahn. Der Tunnel liegt in einem umwelttechnisch sensiblen Gebiet mit komplexen geologischen und geotechnischen Verhältnissen. Eine der Herausforderungen ist quellendes Gebirge aufgrund von Opalinuston, Anhydrit und Gips. Auf den ersten 180 m des Tunnels wurden umfangreiche Erkundungsbohrungen von der Oberfläche parallel zu den laufenden Vortriebsarbeiten abgeteuft, um den passenden Ort für den Start der Tunnelbohrmaschine zu bestimmen. Unterhalb des Tunnels wurde eine quellfähige Linse mit systematischen Erkundungsbohrungen von untertage erkundet. Für diesen Bereich wurde die Innenschale über eine Länge von 37.5 m monolithisch mit einer durchgehenden Bewehrung verbunden, um den erwarteten Quelldruck auf einen längeren Bereich zu verteilen. Die kritische Zone unterhalb des Tunnels wird permanent messtechnisch überwacht.

1 Introduction

The freight traffic corridor Rhine-Apls is part of the Trans European Network and runs from the ports around Rotterdam and Antwerp through Germany to Genoa in Italy. The new railway link through the Alps with the Loetschberg and Gotthard Base tunnel is a key element for the important European rail freight corridor.

With the new “4-meter-corridor” a continuous rail line with low inclination is created over the Alps running from Basel in the north western part of Switzerland and Chiasso next to the border to Italy (see Fig. 1.1). This corridor allows for transportation of truck semi-trailers with a height of 4 m via rail and hence substantially contributes reducing road traffic across the Alps which is a main goal of the Swiss traffic strategy. The corridor will go into full operation by end of 2020. One of the last projects to be completed to reach this goal is the New Boezberg tunnel.

The clearance profile of the existing Boezberg tunnel which was built in 1875 and accommodating two tracks does not fulfil the requirements for the "4-meter-corridor". In preliminary project phases the Swiss Federal Railway Authorities assessed different options in order to integrate the existing tunnel into the corridor. The primary goal was to enlarge and refurbish the existing tunnel during operation. This option was discarded due to the long duration of the construction phase. Finally, a new twin-track tunnel parallel to the existing one was considered as best option including also an modification of the existing tunnel to a rescue tunnel which is also to be used for operational purposes of the new tunnel.



Fig. 1.1: Overview “4-meter-corridor” in Switzerland (red line, with main stations indicated with red dots).

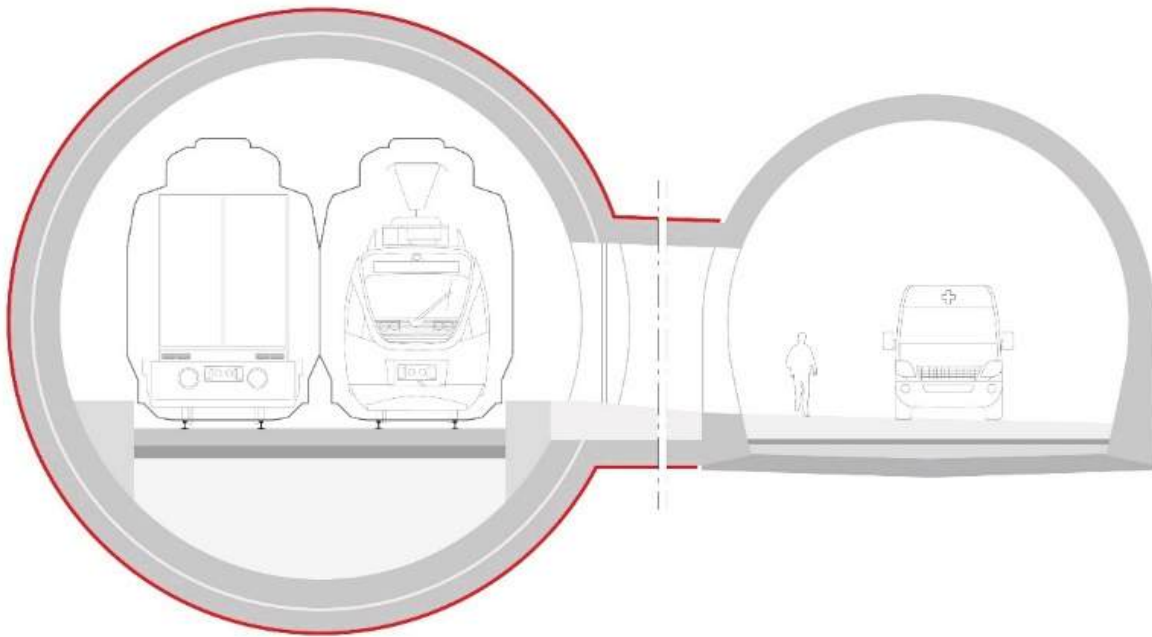


Fig. 1.2: Layout of new tunnel and rescue and maintenance gallery (existing tunnel to be refurbished).

1.1 Improvement of tunnel safety

The new tunnel with a total length of 2'693 m runs parallel to the existing tunnel with an average distance of approximately 50 m - see Fig. 1.2. Both tunnels are connected by 5 cross passages with a maximum spacing of 500 m which allows in case of any incident additional escape and intervention possibilities. The railway and safety equipment is also placed in the cross passages. This allows operating the new tunnel already after completion of the construction before the existing tunnel is refurbished and converted to a rescue and maintenance tunnel and also will simplify and lower costs for maintenance. For a further reduction of maintenance costs a slab track system is installed as a low vibration track system over the entire length of the tunnel excluding the portal areas.

1.2 New contract model for construction works and equipment

The SBB awarded the construction works of the tunnel within a new contractual framework. The contractor is responsible for all construction works for the tunnel and structural works and the installation of the track system, safety systems and tunnel equipment. Additionally, the contractor must undertake the detailed design and the site supervision. The project was awarded to the contractor Implenia Schweiz AG end of 2015 which subcontracted the design works to the joint venture IG Bözberg-Plus consisting of Amberg Engineering, Basler & Hofmann, Preisig AG, and Heierli. The main excavation works started in September 2016 and the tunnel excavation completed by end of 2017. The commissioning of the new tunnel is scheduled for December 2020. The existing tunnel will subsequently be converted to a service and rescue tunnel and starts operation by end of 2022.

2 Geological conditions with swelling rock mass

2.1 General geological conditions

The tunnel passes through complex and challenging conditions of the Swiss Jura which extends all over the north-western part of Switzerland. The Jura is subdivided in two tectonic units - the Faltenjura and the Tafeljura including a main thrust fault of the Faltenjura on the Tafeljura [1]. The northern part consists of sandstone, clay stone, marl, and limestone corresponding to the Tafeljura which slightly dips to the south. The southern part of the tunnel crosses mainly limestone, dolomite, anhydrite, and Opalinus clay corresponding to the Faltenjura. Both tectonic units are separated by a main thrust fault area called back folded zone. In this area the orientation of the strata changes from sub-horizontal to sub-vertical. In the first 175 m from the south portal quaternary deposits and strongly weathered rock masses are encountered. The overburden varies from a few meters in the portal areas up to maximum 290 m in the central part of the tunnel.

Tunnelling through zones of rock mass susceptible to swelling – clay swelling in the Opalinus clay, clay and sulphate swelling in the Gypsum Keuper and the Anhydrite group – poses a particular geotechnical challenge. A number of tunnels in such rock mass conditions in the Swiss Jura formation have been exposed to and suffered from long-term effects from swelling phenomena [2]. Despite the geological documentation of the construction of the adjacent railway tunnel and also a close road tunnel, surface mapping and exploration by means of bore holes with core recovery, the Faltenjura is still subject to considerable uncertainty. Hence further exploration and continuous update of the geological model during construction was done in order to reduce the risk of unexpected conditions which might cause serious negative impact on the construction works and schedule.

For about 400 m from the south portal the tunnel crosses the strata of the Hauptmuschelkalk (limestone) which belongs to the catchment of a close thermal spa. For this "spa protection zone" particular protection are required in order to prevent drainage and any negative influence on the hydrothermal groundwater conditions as well as any long-term damage of concrete structures due to highly mineralised ground water.

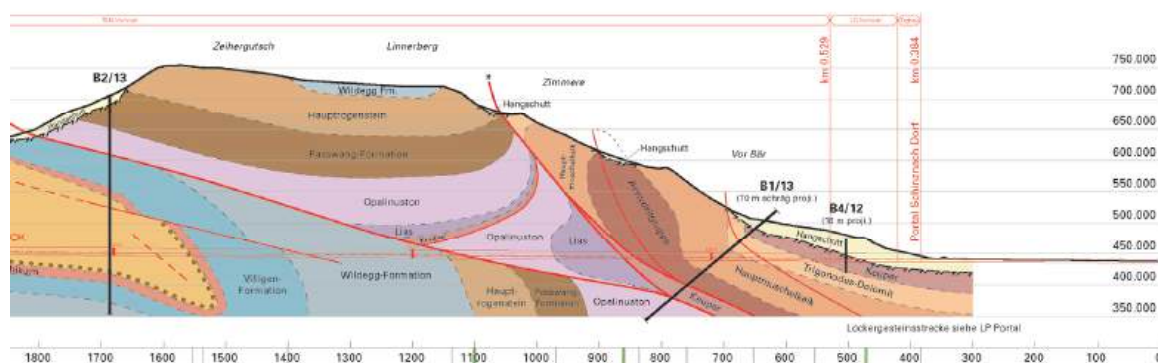


Fig. 2.1: Geological longitudinal section of the Folded Jura section, south portal area.

2.2 Determination of swelling pressure

The swelling process in rock mass containing anhydrite is complex. Long-term swelling processes are expected and the tunnel lining shall be designed providing sufficient resistance and serviceability over the entire service life.

It is quite challenging interpreting and transferring swelling pressure determined by means of lab testing to in-situ conditions. Also the extent of swelling is highly dependant on the mineralogy (type and quantity of the clay minerals as well as the various sulphate mineral anhydrite and gypsum), the distribution of sulphate in the rock mass and the chemistry of introduced water. It needs to be acknowledged that the current knowledge of the detailed mechanism and the possibility of evaluating swelling potential in-situ are often insufficient for reliable decision making and structural design. Hence rather conservative assumptions for the design are therefore often made.

The design of the Boezberg tunnel is based on maximum swelling pressures derived from back calculations of the load bearing capacity (considering valid structural codes) of a number of existing tunnels built in gypsum Keuper in Switzerland and southern part of Germany and which do not show any structural damage [3]. It could be confirmed that an effective in-situ swelling pressure is considerably lower than what could be expected from lab test. The maximum swelling pressure considered is 4 MPa resulting in a double shell lining with a permanent segment lining (30 cm) and a reinforced concrete inner lining with a thickness of 53 cm.

3 General tunnel design concept

The major part of tunnel is located in competent rock mass although several zone prone to swelling (mainly clay swelling) and fault zones are encountered. This part is excavated with a single-shield hard rock TBM with a diameter of 12.36 m and a segmental lining with a thickness of 30 cm. The remaining approximately 180 m is done with conventional excavation. A double-shell lining is installed throughout tunnel. The types of cross sections are shown in Fig. 3.1. For the ground water protection zone at the south portal the tunnel is sealed against water ingress. The remaining sections are drained with a single layer of waterproofing membrane.

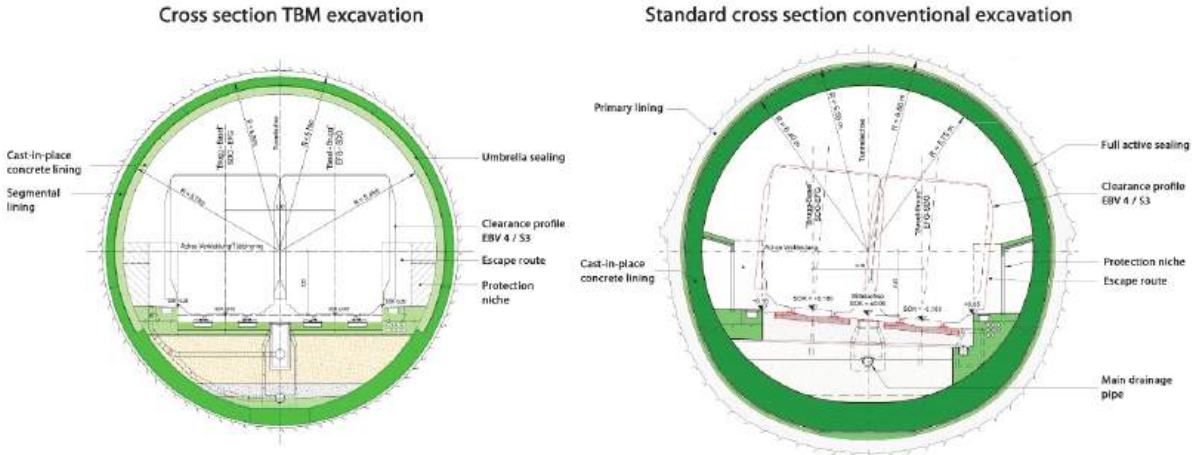


Fig. 3.1: Cross section of TBM tunnel (left) and conventional tunnel (right)

3.1 Conventional excavation in the Anhydrite section

Starting from the south portal the transition from soft ground to competent rock mass occurs continuous. This transition is characterised with differently weathered Keuper resulting in a variation of soft ground up to competent rock. The depth of weathering

was mainly encountered at the height of the bench which ascended with increasing overburden. The top heading was mainly in soft ground and mixed face conditions – see Fig. 3.2.

The excavation is done conventionally with excavator and a total excavation area of 150 up to 180 m² until competent ground conditions are reached allowing commencing the TBM excavation. The advance is done in top heading excavation with a temporary top heading invert under the protection of a pipe roof umbrella, bench and invert excavation. Main support measures are shotcrete with mesh reinforcement (up to 45 cm), lattice girders, systematic face bolting and pipe roof umbrella (length 16 m, overlap 4 m, pipe dia. 159 mm).



Fig. 3.2: Top heading face showing mixed face conditions with competent rock alternating with soft ground.

3.2 TBM excavation and support design

The rock section following the conventionally excavated part is excavated with the single-shield hard rock TBM. The primary support consists of segmental lining with 2 m ring length and without any sealing. Each ring consists of five segments with a keystone in the invert. The segments have a constant thickness of 30 cm in the crown and the side walls. The invert segment thickness varies between 30 cm and 60 cm. This is due to two different water proofing systems – drained and un-drained - with a continuous 30 cm ring for the un-drained tunnel section and a 60 cm invert segment where the water proofing membrane is installed at the upper part of the tunnel. This allows for omitting the installation of the inner concrete lining in the invert and hence reduced construction time.

The annular gap of the segmental lining is filled with grout in the invert and pea gravel in the crown. To prevent water circulation in the water protection zone the pea gravel is subsequently grouted. A final cast in place concrete lining is installed over the whole tunnel length. From the south portal on for about 400 m the tunnel is completely sealed in order to prevent water drainage in the spa protection zone. The remaining tunnel is drained with a standard plastic membrane and a dewatering system in the tunnel invert.

4 Experience made during conventional tunnel excavation

4.1 Surface and underground settlements

The development of the displacements both underground and on the surface have been intensely monitored by means of spatial displacement monitoring, reverse head extensometer and inclinometer. Surface settlements occurred up to approximately 9 cm and corresponded well up to an overburden of approximately 2 tunnel diameter with the vertical displacement monitored underground. Fig. 4.1 shows the development of surface settlement versus horizontal distance to the tunnel face for a number of observed points above the tunnel axis. The surface settlements continuously increase with growing overburden. Quite pronounced is the consolidation effect (increase in settlements without any tunnel progress) after the excavation was stopped for a certain period.

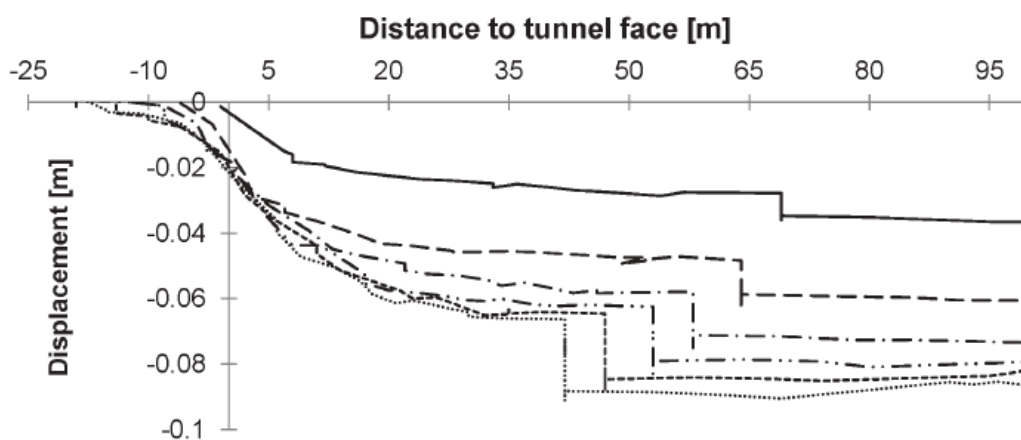


Fig. 4.1: Development of surface settlement vs distance to the face position.

4.2 Extensive exploration during tunnel construction

During the conventional excavation an extensive exploration program was performed in addition to the investigation program before starting the excavation with the objective to (a) identify any ground conditions prone to swelling in the tunnel and / or below the tunnel and (b) to determine a suitable starting position for the TBM. The TBM was already assembled in front of the south portal parallel to the conventional excavation and the TBM shall be moved to the starting position after proper conditions are encountered allowing for a save start.

Such proper conditions in this context mean (a) stable face conditions as the TBM used is a hard rock type machine without any face support and (b) sufficient rock cover and overburden in order to omit any heaving of the tunnel due to swelling pressure in or below the tunnel invert.

As of the geological prediction and the experience made during excavation of the fist approximately 50 m the transition from soft to competent rock was quite complex and heterogeneous. Typical for the geological conditions in the Folded Jura this section showed frequently changing conditions within even one excavation step with soft ground and strong rock due intense weathering of rock mass reaching deeply below the surface and due to faulting in both transverse and longitudinal direction.

4.3 3D geological model and determination of TBM starting position

A spatial geological model was developed and continuously updated which contains all relevant information from tunnel face mapping, past exploration drillings as well as the drillings conducted during excavation, resulting in a continuously update of the geological prediction. Fig. 4.2 and Fig. 4.3 show the spatial geological model developed including the position and orientation of the exploratory drillings. The model was combined with a 3D model of the tunnel structure containing both the temporary tunnel support structures as well as the final support. The frequently update and interpretation of the model allowed for accurately determine the required continuation of the conventional excavation and the determination of the optimum starting position for the TBM with (a) competent rock cover of 4 m above the crown and (b) the tunnel invert being outside of the swelling prone Keuper formation in order to omit any swelling pressure onto the tunnel. Finally, the effectively encountered ground conditions differed only in a few meters from the predicted ones.

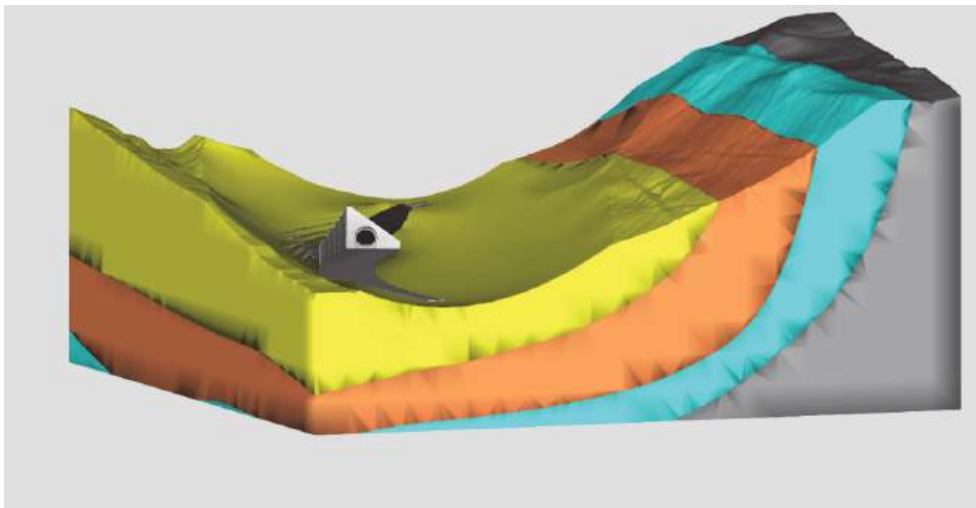


Fig. 4.2: General 3D geological model of south portal area (covering quaternary layer not shown).

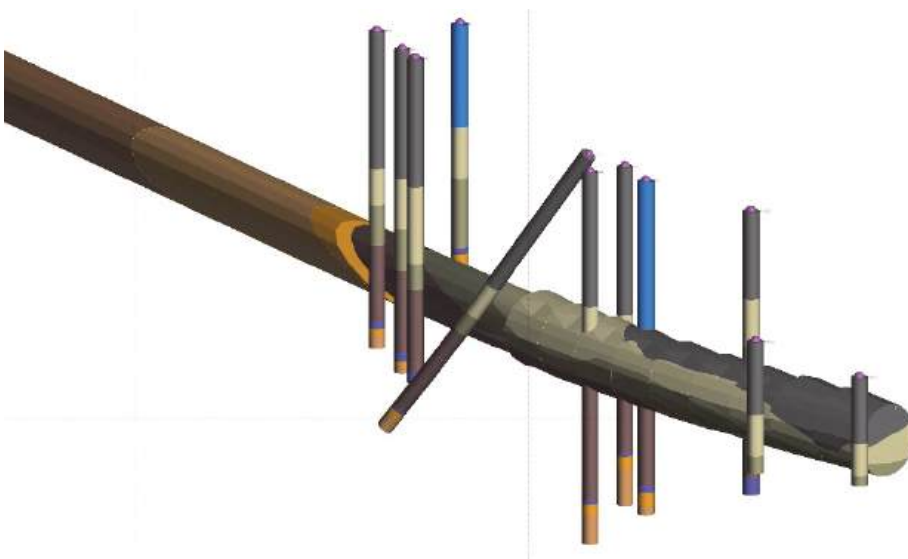


Fig. 4.3: Detailed geological 3D model of the tunnel showing exploration drillings from surface.

4.4. Measure for limiting tunnel heaving due to swelling (swelling at low overburden)

The extent and exact location of anhydrite within the Keuper formation was not detected in detail prior to the tunnel excavation. The exploration drillings during early design stages showed only gypsum and claystone. As a measure for reducing the risk of negative impact onto the final tunnel structure due to long term swelling above mentioned exploration drillings were performed parallel to the excavation of the soft ground section in order to identify anhydrite lenses below the tunnel. In total 20 vertical drillings with a length from 15 m up to 60 m were performed from the top heading invert as well as from the surface.

An anhydrite lens with limited extent was detected approximately 85 m from the south portal and 6 m below the final tunnel invert. Considering the construction schedule the swelling potential of the lens was determined based on the analysis of the mineralogical composition of samples taken as well as test from previous investigation and evaluation of experience with comparable conditions. Finally, the swelling pressure to be considered for the final design of the permanent tunnel inner was determined with 800 kPa.

The ground cover above the tunnel section with the anhydrite lens is not enough to provide sufficient and reliable resistance against the main hazard of lifting the whole tunnel due to the swelling pressure. Such a lifting of the tunnel would result in differential displacements between the blocks of the permanent lining and subsequently to differential displacements of the rail tracks with serious impact on the operation of the railway infrastructure. In order to prevent such a hazard the permanent concrete lining is monolithically connected over 3 blocks, each with a length of 12.5 m resulting in a total length of 37.5 m – the so called monobloc (see Fig 4.4). With this measure a larger weight of the ground above the tunnel can be mobilised allowing for sufficient resistance against the swelling pressure and the swelling stresses acting on a local area of the inner-lining are distributed over a longer section. A non-linear structural analysis of this monobloc was done utilising a 3D shell model and 2D FE-models (see below Fig. 4.4). Based to the analysis done the final vertical lifting of the entire tunnel section for the full swelling pressure is limited to less than 4 cm which is in accordance with the maximum value for the serviceability of the tracks.

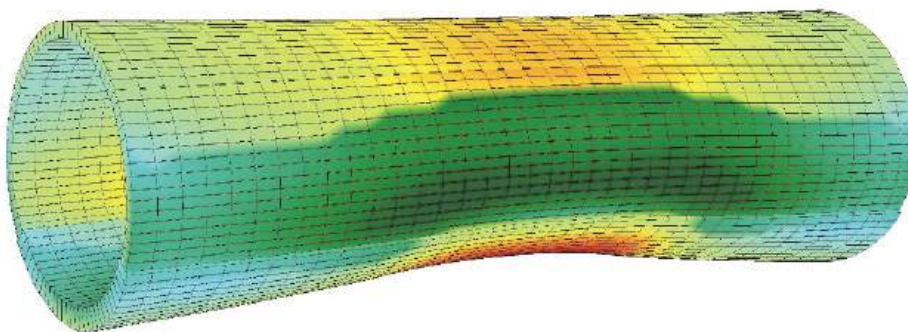


Fig. 4.4: Deformed shell model of the monobloc showing the stresses in the tunnel due to swelling pressure.

4.5 Permanent monitoring

The behaviour of the anhydrite zone identified below the tunnel is permanently monitored. Boreholes with a length up to 41 m lowered from the tunnel level are equipped

with high precision vibrating wire deformation meters and the cables are routed to the portal area. The monitoring results are evaluated frequently during tunnel construction and later on during tunnel operation in order to provide early indication of any heaving of this zone. So far no substantial expansion of the zone has been identified.

5 References

- [1] Von Moos AG. 2014. *Geological Report*. Tender documents new Bözberg double track tunnel.
- [2] Anagnostou, G., Pimentel, E., Serafeimidis, K. 2010. *Swelling of sulphatic claystones – some fundamental questions and their practical relevance*. *Geomechanics and Tunnelling*, No. 5 (2010), 567 - 572.
- [3] Kovari, K. & Vogelhuber, M. 2014. *Empirical Basis for the Design of Tunnel Linings in Swelling Rock containing Anhydrite*. Proc. World Tunnel Congress 2014. Iguassu Falls.

Stress Measurements using Hydraulic Fracturing for the Assessment of the State of Stress and the Softening Conditions in Potash and Salt Mining

Spannungsmessungen mittels Hydraulic Fracturing als bewährtes Messverfahren zur Bewertung des Spannungs- und Entfestigungszustandes im Kali- und Salzbergbau.

Axel Stäubert, Alexander Lechner

K-UTECH AG Salt Technologies Sondershausen
Am Petersenschacht 7, D-99706 Sondershausen

Abstract

Stress measurements using *Hydraulic Fracturing* have been evolving to be a reliable and essential method in the geotechnical assessment of in-situ stress conditions in potash and salt mining since the 1980s. The measurement of the in-situ stress conditions in mining pillars, in unworked areas and at the edge of mining fields is the basis for a deduction of scientifically justified assessment criteria for mining, mine closure and the use of open voids in salt mines as well as for rock mechanical model calculations. This also applies to the exploration and operation of radioactive waste repositories in salt deposits.

K-UTECH AG Salt Technologies Sondershausen, the former *Kaliforschungsinstitut*, carried out more than 30,600 hydro frac measurements in over 1,800 underground drill holes between 1979 and August 2018 (carnallite, hartsalz, rock salt, anhydrite, salt clay).

One focus of the measurements is the verification of softening in the load bearing source rock to be able to provide an up-to-date sequence for essential backfilling tasks in a couple of closed down potash mines in northern Thuringia and Saxony-Anhalt based on the actual pillar softening (time and material dependent) and the underground deformation.

Further systematic measurements are carried out during backfilling activities using non-mining wastes as well as during rock salt mining and the development of new mining techniques.

Measurement procedures and assessment criteria are explained using recent results.

Zusammenfassung

Spannungsmessungen mittels *Hydraulic Fracturing* wurden seit den 1980er Jahren zu einem zuverlässigen und unverzichtbaren Verfahren bei der geotechnischen Bewertung des In-situ-Spannungszustandes im Kali- und Salzbergbau entwickelt. Die messtechnische Bestimmung des In-situ-Spannungszustandes in Abbaupfeilern, an den Baufeldrändern und im Unverritzten sowie in Restflächen ist eine Grundlage für die Ableitung von wissenschaftlich begründeten Bewertungskriterien für den Abbau, die Verwahrung oder Hohlraumverwertung von Grubenbauen im Salinargebirge so-

wie für gebirgsmechanische Modellrechnungen. Dies gilt gleichermaßen für den Betrieb und die Erkundung von Endlagern radioaktiver Abfälle im Salzgebirge. Durch die *K-UTEC AG Salt Technologies Sondershausen*, vormals *Kaliforschungsinstitut*, wurden von 1979 bis August 2018 mehr als 30.600 Hydrofracmessungen in über 1800 Untertagebohrungen vorgenommen (Carnallit, Hartsalz, Steinsalz, Anhydrit, Salzton).

Einen Schwerpunkt der Messungen bildet der Nachweis und die Quantifizierung von Entfestigungsprozessen in den Tragelementen, um in einer Reihe von stillgelegten Kalibergwerken in Nordthüringen und Sachsen-Anhalt eine jeweils aktualisierte Rang- und Reihenfolge für erforderliche Versatarbeiten nach dem jeweiligen Stand von zeit- und materialabhängiger Pfeilerentfestigung und untertägigem Deformationsgeschehen vorgeben zu können.

Weitere systematische Messungen erfolgen in Begleitung von Versatarbeiten mit bergbaufremden Abfällen bzw. bei der Steinsalzgewinnung und der Entwicklung neuer Abbaufahren.

Es werden Messverfahren und Bewertungskriterien anhand aktueller Beispiele erläutert.

1 Introduction

K-UTEC AG Salt Technologies Sondershausen, the former Kaliforschungsinstitut / K-UTEC GmbH Sondershausen, carried out 30,691 hydro frac measurements in 1,811 underground drill holes between 1979 and the end of July 2018 (Figure 1):

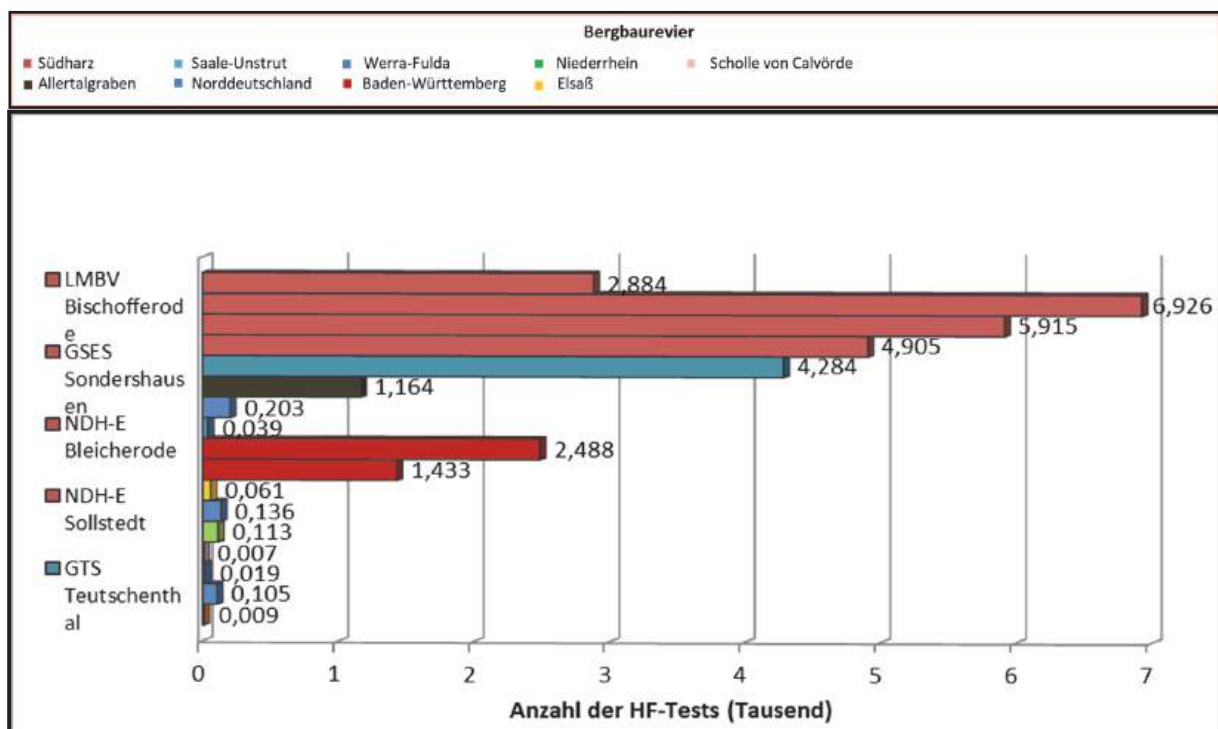


Fig. 1: Number of stress measurements using *Hydraulic Fracturing* carried out by K-UTEC.

Stress measurement using *Hydraulic Fracturing* has been evolving to be a reliable and essential method in the geotechnical assessment of in-situ stress conditions in potash and salt mining since the 1980s.

Stress determination using *Hydraulic Fracturing* has been evolving to be a reliable and essential method in the geotechnical assessment of in-situ stress conditions in central German salt mines since 1986/87 and has been used subsequently in other salt mining districts (see Figure 1). With this measuring technique the value of the smallest principle normal stress in a particular area of investigation can be determined efficiently. In the context of complex metrological monitoring, stress measurements using *Hydraulic Fracturing* produce specific location parameters for:

- preservation of evidence and monitoring during operation of a mine,
- panel dimensioning, mining layout and optimisation, stope design,
- mine abandonment concepts and planning of dams and barriers,
- safety analysis for the post-operational phase of mines,
- deduction of scientifically justified assessment criteria for mining, reclamation, mine closure or use of open voids in salt mines as well as for tasks concerning the mine safety,
- proof of safe mining operation or safe operation of repositories and underground disposal sites including backfilling of non-mining wastes as well as
- validation of rock mechanical models and model calculations.

The research and development of machinery and the interpretation of hydro frac measurement results carried out by K-UTEC AG Salt Technologies Sondershausen, the former Kaliforschungsinstitut, from the mid 80 s to the mid 90 s are the base for the realisation of such monitoring routines.

2 Classification of Stress measurements using *Hydraulic Fracturing* within the concept of complex geomechanical monitoring of potash and salt mining

To ensure the long term safety of mining districts of abandoned potash mines in central Germany it was necessary to carry out extensive close-down works after the end of production to protect the surface. Important issues are the prevention of deformation and tremors that might affect overlying or close-by towns, the stabilisation and improvement of the hydrogeological conditions of several surface streams, the protection of railway lines, motorways and other traffic infrastructure from unacceptable ground motion. Some of these operations still continue today.

The basic premises for geomechanical monitoring of abandoned salt mining areas that have to be secured (preservation of evidence) are summarised in Figure 2 [2], [3].

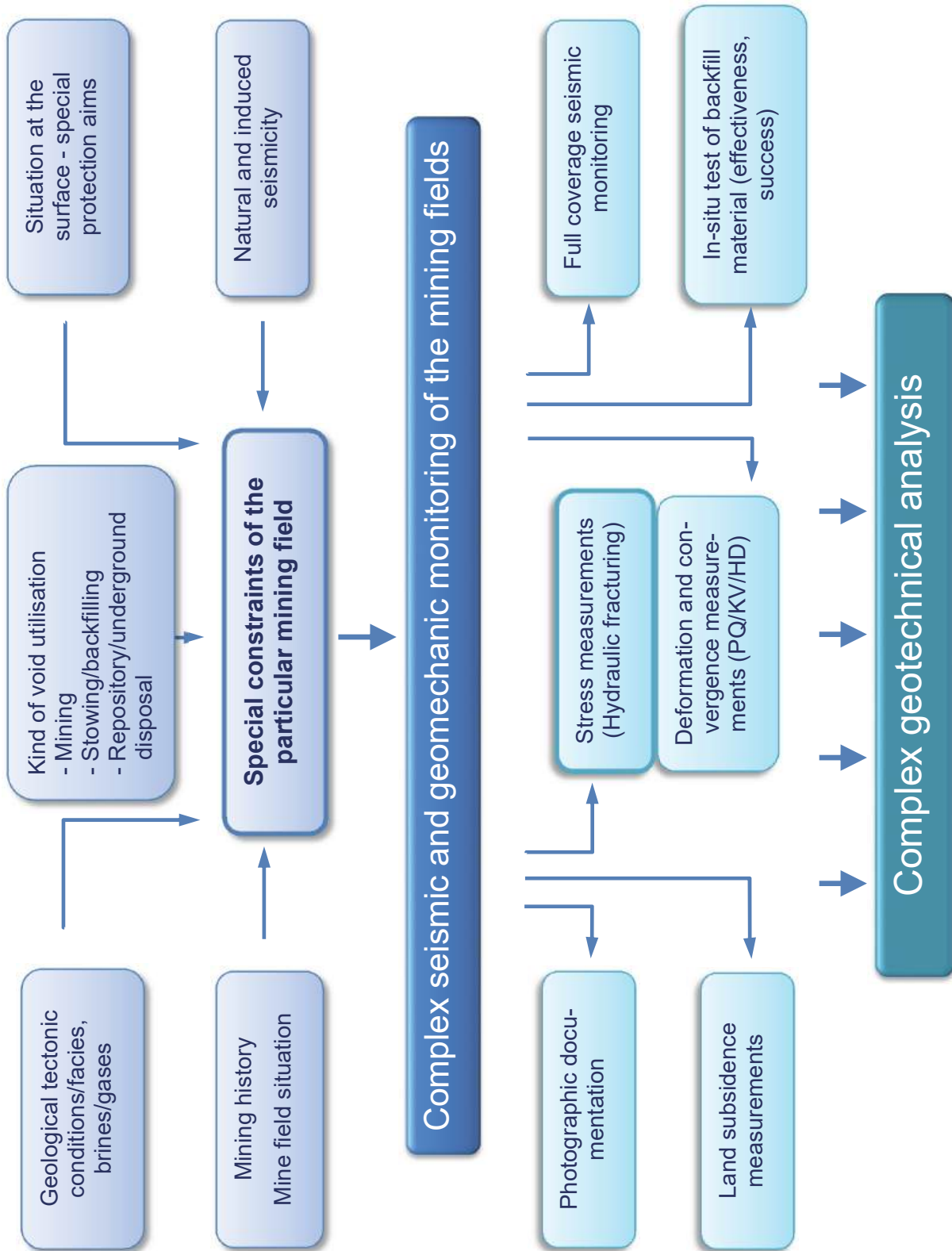


Fig. 2: Complex monitoring of (salt-) mining areas.

Complex geomechanical monitoring of salt mine fields, which was developed end of the 1980s, includes the combination of several in-situ measurement techniques:

- registration of in-situ stress and deformation conditions through systematic hydro frac measurements and underground deformation measurement facilities;
- registration of the pillars' softening and load bearing behaviour in particular mining fields through stress logging using *hydraulic fracturing*;
- underground deformation monitoring covering the whole mining field;
- recording of surface subsidence by mine surveyors;
- seismic monitoring using underground and surface sensors covering the whole mining field; locating, investigation and geotechnical analysis of registered large-scale seismic events;
- documentation of rock-mechanical conditions in particular mining areas and of their time dependence (preservation of evidence);
- in-situ testing to proof the effectiveness of the backfill and the success of the closing-down procedures, long-term geomechanical monitoring of selected mining areas using remote surveillance [2], [3].

3 Selected stress logging investigations using *hydraulic fracturing* of the last 30 years

In the 1980s frac measurements were concentrating on the potash mining fields south of the Harz mountains. After 1994 frac measurements spread to other salt mining districts due to the reunification of Germany. Until 1990 the work load was divided between Kaliforschungsinstitut (later K-UTEK) and IfG (Institut für Bergbausicherheit) in Leipzig. Later the latter took over the Werra potash district.

Stress logging using hydraulic fracturing concentrated on the following topics in the stated salt mining districts:

- Southern Harz potash district (Northern Thuringia), especially Glückauf Sondershausen GSES mbH, NDH Entsorgungsbetreibergesellschaft NDH-E mbH, the mines of Bleicherode und Sollstedt as well as Bischofferode - all under administration of GVV mbH:
 - preservation of evidence during active mining, documentation of the July 2nd, 1983 rock burst; mine closure, underground backfilling using non-mining wastes (including underground disposal site Sondershausen) (project period: (1979-) 1983 to this day).
- Saale potash district (Saxony-Anhalt), mine of Teutschenthal Sanierungsgesellschaft mbH & Co. KG:
 - preservation of evidence / mine closure, underground backfilling of non-mining wastes, control measurements after the rock burst of September 11th, 1996 (project period: 1981 to this day).
- Werra potash district (south west Thuringia), mine of Merkers:
 - control measurements after the severe rock burst of March 13th, 1989 (project period: 1989)

- Werra potash district (Hesse), Kali und Salz GmbH, Werra factory, mine of Hattorf:
 - assessment of the shaft safety pillar Hattorf, 1st mining level (project period: 1999).
- Solvay Salz GmbH, formerly planned underground disposal Niederrhein / rock salt mine Borth (North Rhine-Westphalia):
 - planning approval investigations for the underground disposal site (project period: 1994).
- Northern Harz potash district / Allertalgraben (Saxony-Anhalt), repository for radioactive waste Morsleben (DBE mbH):
 - geotechnical in-situ investigation program (project period: 1994 to 1996 and 2003 to 2004).
- Northern Germany (Lower Saxony), Erkundungsbergwerk Gorleben (DBE mbH):
 - underground exploration of the salt diapir in Gorleben (project period: 1998 - 1999).
- Western Swabian Alb (salt deposit in shelly limestone), Wacker-Chemie AG, salt mine of Stetten (Baden-Württemberg):
 - preservation of evidence during active mining and underground backfilling of non-mining wastes (project period: 2000 to this day).
- Südwestdeutsche Salzwerke AG, Heilbronn (salt deposit in shelly limestone; Baden-Württemberg):
 - preservation of evidence during active mining, underground disposal site and underground backfilling of non-mining wastes (project period: 2008 to this day).
- Mines de Potasse d'Alsace (MDPA) / StocaMine, Wittelsheim):
 - preservation of evidence during retrieval of the wastes disposed of in the underground mine (project period: 2015).

The main business for more than 30 years has been the collection of geomechanical data through *Hydraulic Fracturing* as well as the underground deformation measurements to carry out complex geomechanical monitoring and assessment of salt mines. K-UTEC AG Salt Technologies Sondershausen installed 1,497 underground deformation measurement sites (vertical convergence, pillar lateral extension, roof deformation) with 3,937 single measurement planes in central Germany in the last 35 years – two thirds of them are in operation at the moment. Another 479 measurement sites with 678 measurement planes are actively working in the salt mines of Baden-Württemberg.

Through this monitoring activity carried out over decades it was possible to obtain an extremely high understanding of in-situ stress and deformation conditions.

Nearly all salt mines in Germany have seismic monitoring covering the complete mining field.

4 Examples of recent cases

During work-over operations of old mining areas as preparation for the placement of backfill, the control of the stress and softening situation using hydraulic fracturing as well as the placement of pillar lateral extension and convergence measurement sites is carried out.

Figure 3 shows a mine map section of a hartsalz mine field with a time span of 40 - 45 years that the mining voids stayed open. This field was worked-over in spring 2018.

The results of the hydro frac measurements carried out in May 2018 are brought together in Figure 4; the findings of selected measurement locations are corresponding to the different mining situations:

- The measurement locations show a complete loss of strength up to 3 m into the sidewall, which is quite moderate considering the time span of 40 – 45 years that the mining voids stayed open.
- Bore hole F362 represents the stagnant high pressure zone at the edge of the mining field. It doesn't show any critical overload, though.
- Bore holes F363 and F364 show “normal“ load situations being situated in the forefront and a crotch of the mining field.
- With bore hole F365 a residual pillar covering an area of around 800 m² between two intensively mined areas was monitored. Showing an average pressure at rest of 11 MPa, it was possible to detect a noticeable stress relief caused by softening over a time period of years that had a far-reaching effect. After scaling the loss of strength still reached 3 m into the sidewall.

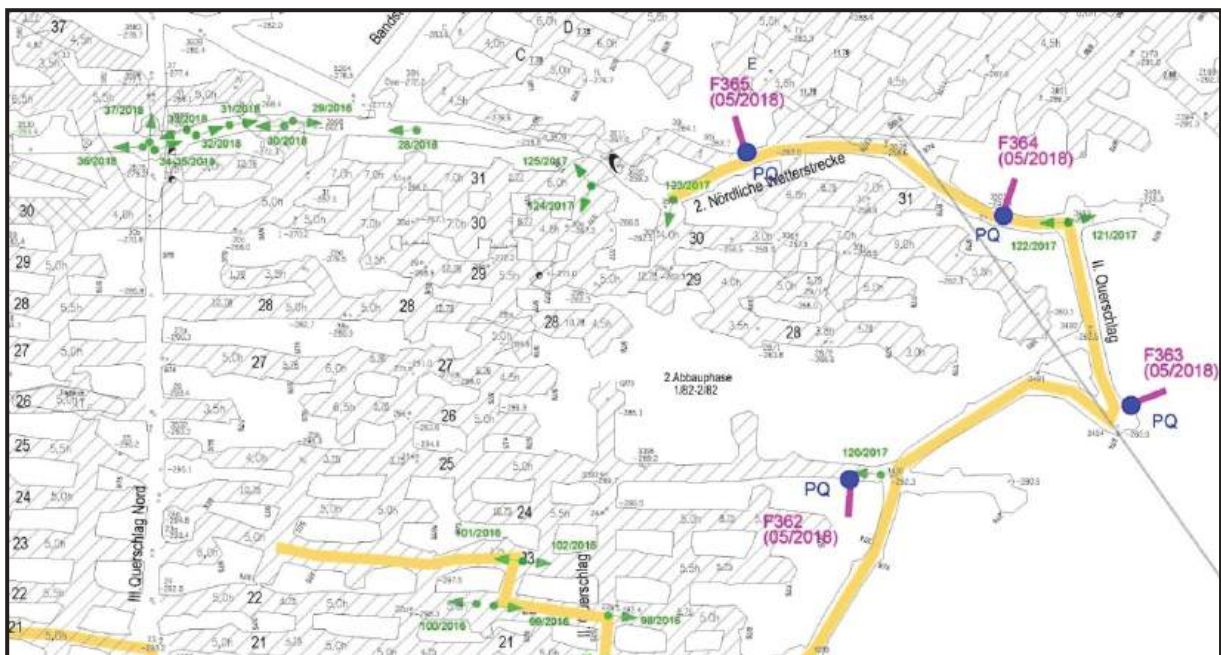


Fig. 3: Example: work-over of an old hartsalz mining field to be used for backfilling.

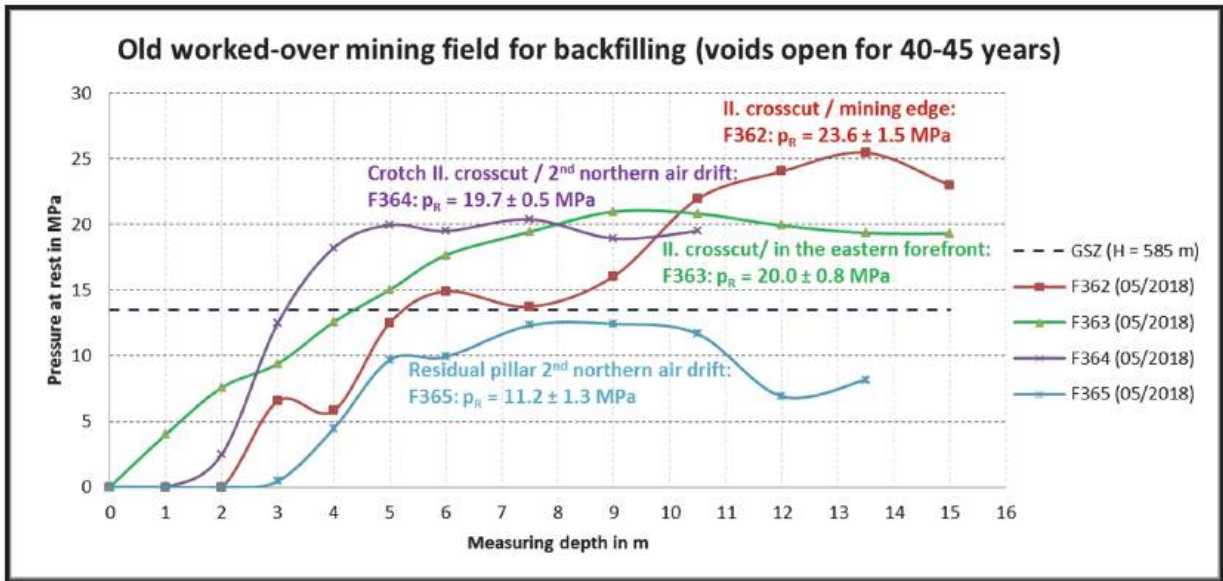


Fig. 4: Example: Investigation through *hydraulic fracturing* of an old hartsalz mining field before the application of backfill.

Another example is shown in Figure 5. In this figure the systematic measurements in an approximately 50 years old carnallite field are shown:

- After contour adjustment with a roadheader all the measurement locations show a moderate depth with complete loss of strength of 2 m into the sidewalls.
- The carnallite pillars with a width of 30 - 45 m show a pressure at rest of 13 - 15 MPa in their cores, which can be considered “normal” (F199 und F202); this is equivalent to about 20 ... 23 MPa actual pillar stress.
- Pillar F200, which was chosen particularly because of its low width of 24 m, shows a lower stress; it has partly eluded the load.
- Contrarily the stress accumulated in a residual pillar with an area of 7,650 m². Pillar F201 showed an average pressure at rest of 23.3 MPa, with a maximum in a small “high pressure zone” (HPZ) of 24.6 MPa. Calculated with a simple approach this equals 35 - 37 MPa actual pillar stress, which is close to the formerly maximum permissible pillar load of ≤ 40 MPa in laminated carnallite.

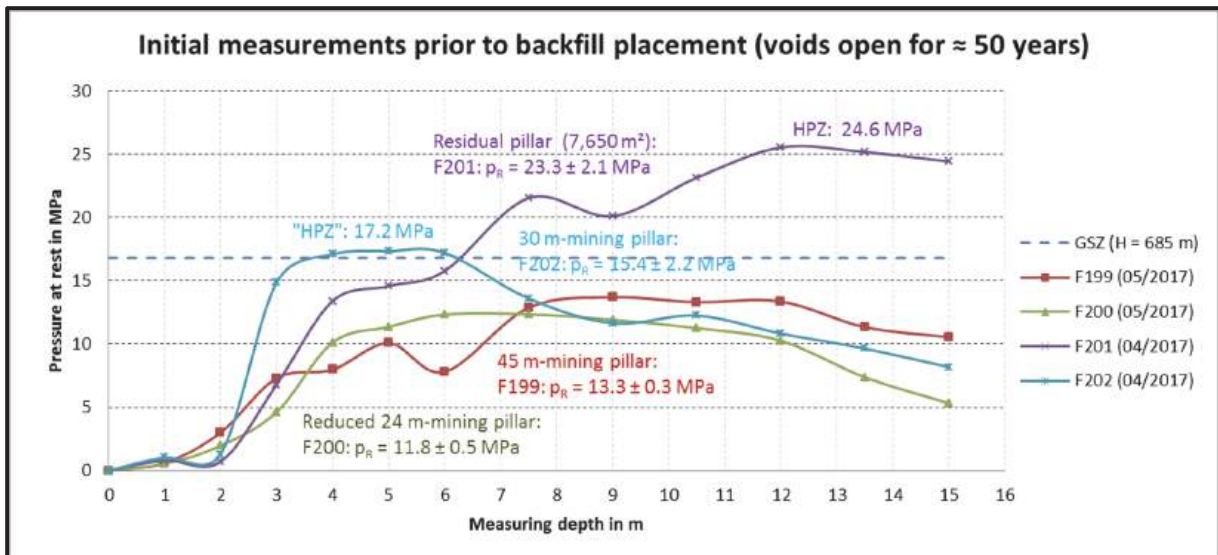


Fig. 5: Example: work-over of an old carnallite field in preparation for backfilling.

Periodic hydro frac measurements in combination with underground deformation measurements and station based seismic monitoring can recognise critical loss of strength early enough to plan and control the order and sequence of necessary back-fill works.

In the extended forefront of the rock burst field in Bleicherode mine from July 2nd, 1983 (area of 90,000 m²) a residual pillar with an area of about 2,200 m² had systematically been controlled since 1994 using hydraulic fracturing tests and it then showed a high load. Figure 6 shows how this originally stabilising element has been losing its strength intensively in the last 15 years and would – if no backfill was applied – lose the rest of its strength in the medium term.

Compared to the years 1994 to 2002 the average core pressure at rest was reduced from 25 - 27 MPa to 16.3 MPa in 2017. The complete loss of strength of the contour reached “only” 1 m into the sidewall, owing to the presence of anhydritic barren rock in the residual pillar.

It is well known that the intensity of time-dependent softening is especially high with carnallite. Figure 7 gives the measurement results of a normally loaded pillar in Staßfurt rock salt immediately after advance (F260, 2006) as well as 11 years later (F395) and how contour softening develops with time.

Until 2017 the average pressure at rest in the pillar’s core only decreased marginally. In the future the core pressure at rest will continue to decrease until at around ≤ 10 MPa it will be necessary to apply backfill in the medium term.

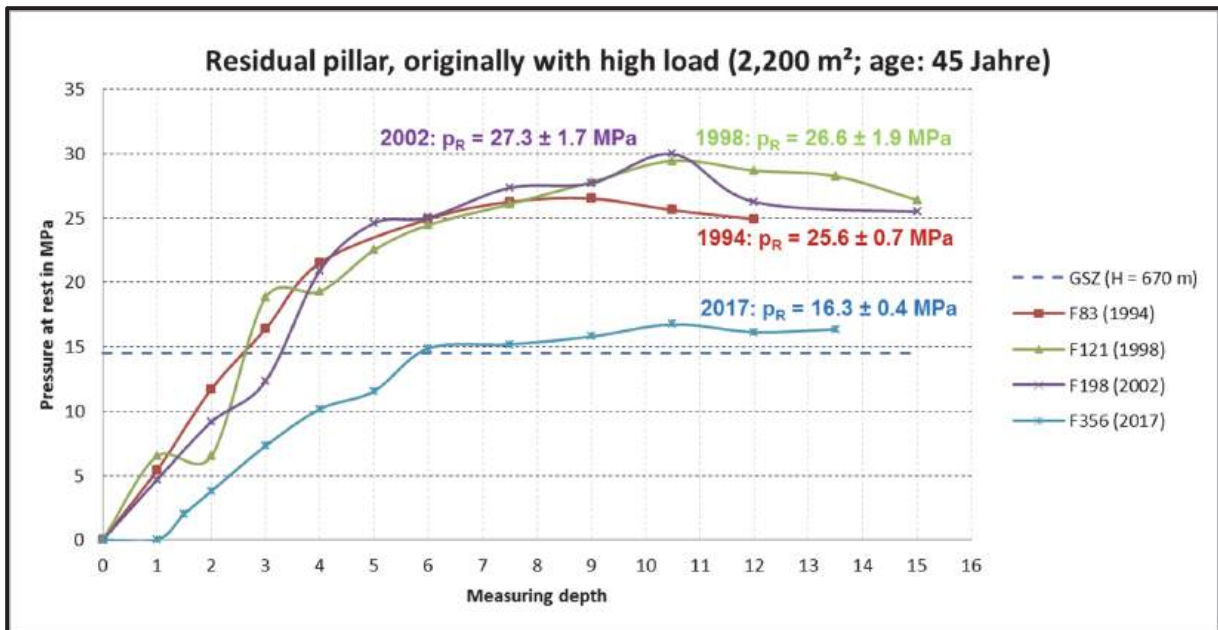


Fig. 6: Example: change of load in residual pillars caused by stress relief.

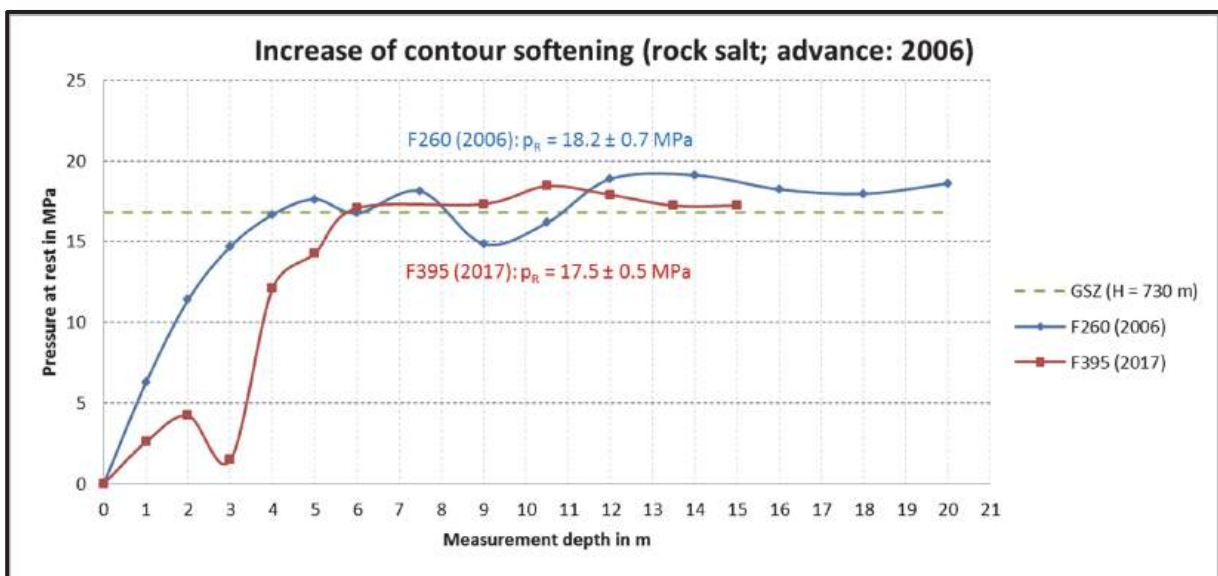


Fig. 7: Proof of increasing contour softening in a rock salt pillar (Staßfurt rock salt).

The last example is dealing with multiple strata mining in potash and salt. In certain cases stress accumulations can be expected at the edges of the mining field. The top mining layer acts like a safety layer and stress release in the seam mined last can be observed. Systematic research using hydro frac investigations were carried out already in the 1980s to see the influence of an existing mining layer on a second layer to be mined later [1].

On the one hand multi-layer mining was tested successfully in the southern Harz potash mining district within a carnallite accumulation leaving 20 m thick roofs. On the other hand it could be proven by *hydraulic fracturing* in the Werra potash district that a vertical interaction of up to 60 m exists between the Thüringen seam and the Hessen seam.

In the mine of Sondershausen the extraction of rock salt below the former potash mine has been monitored since 2008 (Figure 8):

- Stations F346 and F358 showed a moderate increase of stress: one being situated in the rock salt field 30 m below the abandoned potash mine, the other one below a residual area in the Staßfurt potash seam close to a geological fault.
- In a residual area (F398) within the Staßfurt potash seam that was not rich enough for mining, an average pressure at rest of 26.6 MPa (maximum of 28.3 MPa) – corresponding to an actual load of 36 - 42 MPa – effects caused by the field edge of the mine and a residual area effect can be shown very clearly. In rock salt this load is not critical, though.
- F357 is an example for a mined seam that works as a protective layer, which has a load reducing effect; below the mined Staßfurt potash seam the actual load on the pillar is around 19 MPa, which is only 55 % of the calculated load.

The investigation of multi-seam and multi-layer mining concerning the interaction between the seams resulted in practical applications for the access of new mining areas and with voids that will have a long life span.

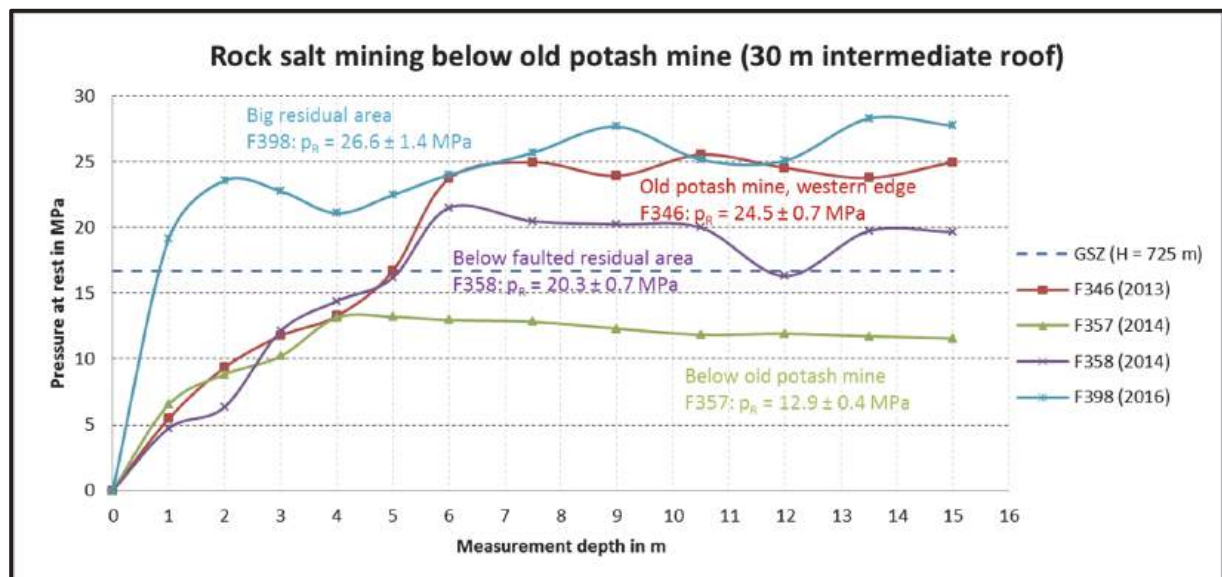


Fig. 8: Multilayer mining of potash and rock salt - different mining situations.




Based on the assessments of these five current examples it can be shown that hydro frac measurements in combination with underground deformation measurements and station based monitoring can give an early warning of critical softening processes. Details of measurement methodologies and other constraints when using hydraulic fracturing methods to determine stress and softening conditions in salt mines can be found in the literature given at the end of this article.

5 Complex assessment of potash and salt mining fields

Data gained through hydraulic fracturing is perfectly suited for an assessment complex together with geologic-tectonic deposit conditions and other monitoring

measures to determine the volume, the sequence and the ranking of backfilling works (see Table 1).

Tab. 1: General requirements for the complex validation of mining panels for safeguarding and stabilisation measures (hazard increases from top to bottom).

Deformation capability (under-ground)	Time-dependent softening	Seismic Activity	Hazard	Type of salt/ facies	Geotectonics	Bedding conditions
± Static / Low (20 - 40 mm/a)	Low (± intact)	Inconspicuous	Low    High	rock salt; Mixed salt (< 30% carnallite)	Inconspicuous	± Horizontal Intact
“Normal” (40 - <100 mm/a)	Average	Occasional		Mixed salt (> 30% carnallite)	Typical salt tectonics	Shallowly dipping
Increased (100 - 150 mm/a)	High or long lasting standing times	Micro seismicity (low energy)		Fragmental carnallite Bedded carnallite	Intensive fault and fold tectonics	Rippled, irregular, high variations
Deformation active (> 150 - 250 mm/a)	Extreme, post failure	Seismic active macro seismicity (high energy)		Carnallite, tachyhydritic	Seismic-tectonical activities	Steep or folded

6 Literature

- [1] STÄUBERT, A.: *Spannungssondierungen mittels Hydraulic Fracturing zur geomechanischen Überwachung des Kalibergbaus im Südharz-Kaligebiet der DDR*. Neue Bergbautechnik, Leipzig 20 (1990) 9, S. 335 - 339
- [2] STÄUBERT, A., LEHMANN, W.: *Markscheiderische und gebirgsmechanische Überwachung von Verwahrungsarbeiten in stillgelegten Südharz-Kaliwerken. - Geoforschung, Geotechnik und Geoinformatik aus markscheiderisch-geodätischer Sicht*. Vorträge zum 49. Berg- und Hüttenmännischen Tag 1998 in Freiberg. Freiberg: TU Bergakademie, 1998; Freiburger Forschungshefte, A 847, S. 100 - 124
- [3] STÄUBERT, A.: *Spannungsmessungen mittels Hydraulic Fracturing zum Nachweis zeitabhängiger Entfestigungsprozesse im Salzbergbau*. Glückauf-Forschungshefte, Essen 59 (1998) Nr. 4, S. 116 - 122

Additional Paper

Experimental study on Mode I and Mode II fracture of granite after thermal shock treatments

Experimentelle Studie zu Mode I und Mode II Rissausbreitung in Graniten nach Thermoschockbehandlungen

Xiang Li¹, Wei Chen², Zhuoyao Zhang¹

¹ School of Resources and Safety Engineering, Central South University

² School of Civil Engineering, Central South University
No.932 Lushan South Road, 410083 Changsha, China

Abstract

In this study, the effect of thermal shock (TS) on the mechanical properties of granite is investigated. Two schemes are performed to provide different cooling rates in the TS processes. Decreasing trend of dry density and P-wave velocity with ascending TS temperatures are observed. The porosity has an increasing trend with ascending TS temperatures. Brazilian tests are performed on the cracked straight through Brazilian disc (CSTBD) of granite. Mode I and Mode II fracture toughness values are obtained. Scanning electron microscope (SEM) is adopted to observe the fracture surfaces of the TS-treated specimens after the tests.

Zusammenfassung

In dieser Studie wurde der Einfluss von Thermoschocks (TS) auf die mechanischen Eigenschaften von Granit untersucht. Zwei Versuchsarten wurden durchgeführt, um unterschiedliche Abkühlraten in den TS-Prozessen zu realisieren. Es wurde abnehmende Trockendichte und P-Wellengeschwindigkeit mit steigenden TS-Temperaturen beobachtet. Die Porosität nimmt mit steigenden TS-Temperaturen zu. Brasilianische Tests im CSTBD-Modus wurden mit Granitproben durchgeführt. Die Bruchzähigkeitswerte für Mode I und II wurden ermittelt. Ein Rasterelektronenmikroskop (REM) wurde verwendet, um die Bruchflächen der TS-behandelten Proben nach den Tests zu untersuchen.

1 Introduction

In underground engineering projects such as deep mining, oil drilling, geothermal energy engineering and deep nuclear waste storage where rock serves as the main load bearing material, the rock's exposure to high temperature can happen. Thus, analyzing the mechanical properties of rock under high temperature treatment is essential for the structural stability for such underground works. In fact, the influence of temperature on the physical and mechanical behavior of rocks has long been a focus of research in the field of rock mechanics, geological engineering, geomorphology, etc. (Hall and André, 2001; Smart and Wakabayashi, 2009; Zhang et al., 2016; Mardoukhi et al., 2017). Under certain conditions, in-situ rocks can undergo sharp change of temperature within a short period of time, for example, in the process of extinguishing fire in mines and buildings (sudden temperature drop) (Sirdesai et al. 2017), or lightning strike (sudden temperature rise) (Hall and Thorn 2014). Sharp variations in temperature can also be encountered in enhanced geothermal systems and underground gasification process (Sirdesai et al. 2017). Such sudden (large) change in temperature is capable of generating thermal stress and producing fracture, and consequently results in a decrease of rock strength, which is known as thermal shock (TS) (Yatsu 1988; Mirkin et al. 2006; Zhang et al. 2010; Hall and Thorn 2014). So far, various temperature changing rates ($\Delta T/\Delta t$) have been proposed as the threshold for inducing TS, ranging from 2 °C/min to 44 °C/min (Richter and Simmons 1974; Ghaffarian 2001; Ferrero and Marini 2001; Peng et al. 2008).

Although various TS-related studies were reported, researches involving single thermal shock with comparatively high changing rate of temperature are quite scarce (Brotons et al. 2013; Chen et al. 2012; Liu and Xu 2015; Zhang et al. 2016; Nasserri et al. 2007). Besides, in the current researches involving TS, the temperature changing rate is usually very low (e.g. usually below 10 °C/min, many at 1~2 °C/min). Investigations about the effect of single TS on the fracture properties and fracturing characteristics of rock are also very rare, although it is widely accepted that TS involves fractures induced by thermal stress which are responsible for the deterioration of the mechanical properties of rocks (Hall and Thorn 2014; Ghobadi and Babazadeh 2015). Therefore, current knowledge about single TS in rock is insufficient. In this study, TS treatments are applied to granite with temperature ranging up to 800°C. Two cooling methods are adopted to provide different temperature changing rates. Physical and mechanical properties of the granite samples before and after TS treatment are obtained. The fracturing characteristics under different TS temperatures are also compared. The findings of this study can be used as a reference in the evaluation of the fracturing conditions in rocks under sudden and severe temperature change.

2 Fracture toughness determination with CSTBD

The laboratory tests adopt the cracked straight through Brazilian disc (CSTBD) to obtain Mode-I and Mode-II fracture toughness (Awaji and Sato 1978; Atkinson et al. 1982; Liu et al. 2007). The geometry of the specimen is shown in Fig. 2.1.

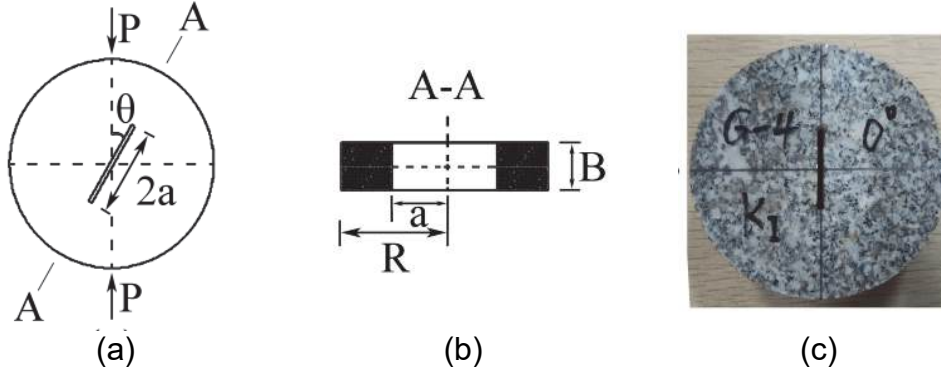


Fig. 2.1: Geometry of the CSTBD: (a) side view of the specimen; (b) cross-section of the specimen along the crack plane; (c) example of granite specimen

The explicit solution of stress intensity factor for CSTBD is expressed as (Atkinson et al. 1982)

$$K_I = \frac{P\sqrt{a}}{\sqrt{\pi}RB} N_I \quad (1)$$

$$K_{II} = \frac{P\sqrt{a}}{\sqrt{\pi}RB} N_{II} \quad (2)$$

where a denotes half-crack length, R denotes the radius of the disc, B denotes the thickness of the disc, P denotes external load, N_I and N_{II} are non-dimensional coefficients determined by the crack orientation and dimensions of the crack and the specimen. The expressions for N_I and N_{II} are given as (Wang et al. 2004)

$$N_I = f_{11} + 2 \sum_{i=1}^n (i \cos(2i\theta) - i \cos(2(i-1)\theta)) f_{1i} \alpha^{2(i-1)} \quad (3)$$

$$N_{II} = 2 \sum_{i=1}^n (i \sin(2i\theta) - (i-1) \sin(2(i-1)\theta)) f_{2i} \alpha^{2(i-1)} \quad (4)$$

with the angle between crack plane and loading direction θ . The coefficients f_{ji} ($j = 1, 2; i = 1, 2, \dots, n$) are given as

$$f_{ji} = \frac{|(2i-3)|!}{(2i-2)!} \left[1 + \frac{c_{j1}}{2i} + \frac{3c_{j2}}{4i(i+1)} \right]$$

where $n!!$ denotes the double factorial of n and c_{j1} and c_{j2} ($j = 1, 2$) are expressed as

$$c_{11} = \frac{8 - 4\alpha + 3.8612\alpha^2 - 15.9344\alpha^3 + 24.6076\alpha^4 - 13.234\alpha^5}{\sqrt{1-\alpha}} - 8 \quad (5)$$

$$c_{12} = \frac{-8 + 4\alpha - 0.6488\alpha^2 + 14.1232\alpha^3 - 24.2696\alpha^4 + 12.596\alpha^5}{\sqrt{1-\alpha}} + 8 \quad (6)$$

$$c_{21} = \frac{5 - 2.5\alpha + 1.4882\alpha^2 - 2.376\alpha^3 + 1.1028\alpha^4}{\sqrt{1-\alpha}} - 5 \quad (7)$$

$$c_{22} = \frac{-4 + 2\alpha + 0.4888\alpha^2 + 0.81112\alpha^3 - 0.7177\alpha^4}{\sqrt{1-\alpha}} + 4 \quad (8)$$

According to Eqs. (3) and (4), the non-dimensional coefficients N_I and N_{II} are determined by α and θ . The geometry of the specimens used in this study renders that $\alpha = a/R = 0.33$, where the average values of a and R is approximately 12.5 mm and 37.5 mm, respectively (Fig. 2.1). Under this conditions, the value of N_I and N_{II} at various θ are obtained at the 30-term approximations ($i = 30$), as shown in Fig. 2.2. Specifically, the pure Mode I condition occurs when $N_I = 1.1647$ and $N_{II} = 0$, where $\theta = 0^\circ$. The pure Mode II condition occurs when $N_I \approx 0$ and $N_{II} \approx 1.8967$, where $\theta \approx 26.7^\circ$.

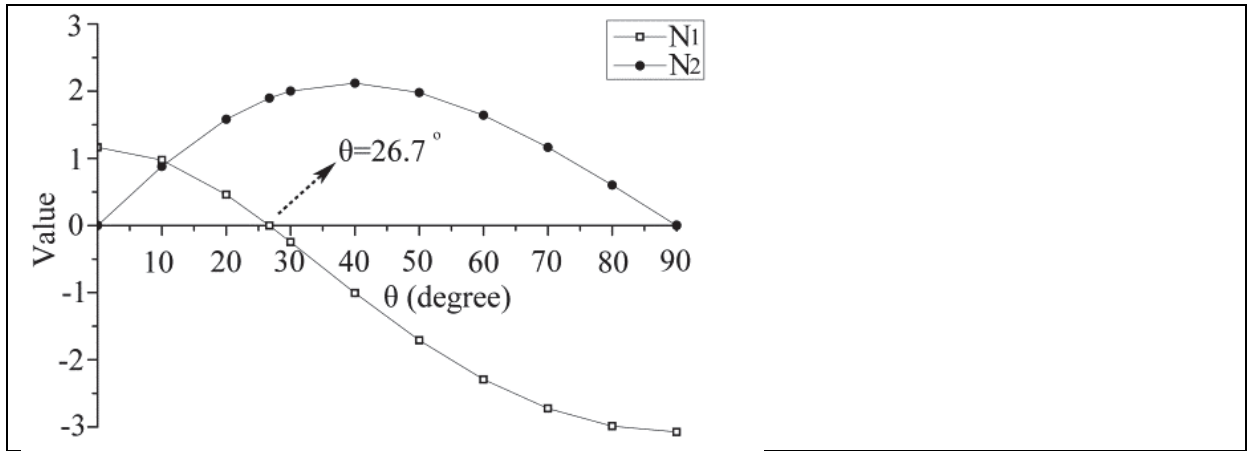


Fig. 2.2: Non-dimensional coefficients of N_I and N_{II} under the condition $\alpha = 0.33$

3 Laboratory tests

3.1 Specimen characterization and preparation

The granite tested in this work is quarried from the Miluo district, Hunan Province, China. The thin-section analysis indicates that this medium-grained granite is composed of quartz (40 %), Microcline (25 %), Orthoclase (20 %), Plagioclase (8 %), Biotite (5 %), Muscovite (2 %) and minute trace of Magnetite. The diameter of the specimen is 75 mm and the thickness is 25 mm. A slot is cut along the diameter of the disc with the length of 25 mm and width of 1 mm (Fig. 2.1 (c)). Buoyancy techniques are adopted to obtain the density ρ and the porosity n of the specimens (Wang et al., 2016). The P-wave velocity (v_P) of the granite specimen is detected by a portable non-destructive ultrasonic detector (model SET-CWA-01 produced by Hunan sine electronic technology Co., Ltd.). The average P-wave velocity value is included in Table 1, among other basic properties of the acquired granite.

Table 1. Physical and mechanical properties of the granite

Density ρ	2648 kg/m ³
Porosity n	0.736 %
P-wave velocity v_P	4554 m/s
Young's modulus E	48.1 GPa
Poisson's ratio μ	0.26
Internal friction angle φ	49 °
Uniaxial compressive strength σ_c	139 MPa
Tensile strength σ_t	7 MPa

3.2 Testing procedures

The granite specimens are placed in a box-type electrical furnace and heated to respective high temperatures with the increment of 100 °C. The temperature is kept constant for 2 hours once the designated temperature is reached. Then the specimens are immediately cooled at ambient temperature (air cooled), or immersed into water at ambient temperature (water cooled), where the ambient temperature is approximately 30 °C. In the heating process, the temperature is read from the monitor of the oven every 60 s. In the cooling process, the temperature is read from the infrared thermometer (Type PM6530D produced by Shenzhen Huayi Peakmeter Technology Co., Ltd.). The temperature is recorded every 60 s in the air cooling process, and every 20 s in the water cooling process. The heating rate is calculated by dividing the difference between the high temperature and ambient temperature by the time span. According to the temperature profiles (Fig. 3.1), the average heating rate is about 14.9 °C/min, and the cooling rate for the air-cooled and water-cooled specimens are about 5.6 °C/min and 46.2 °C/min respectively.

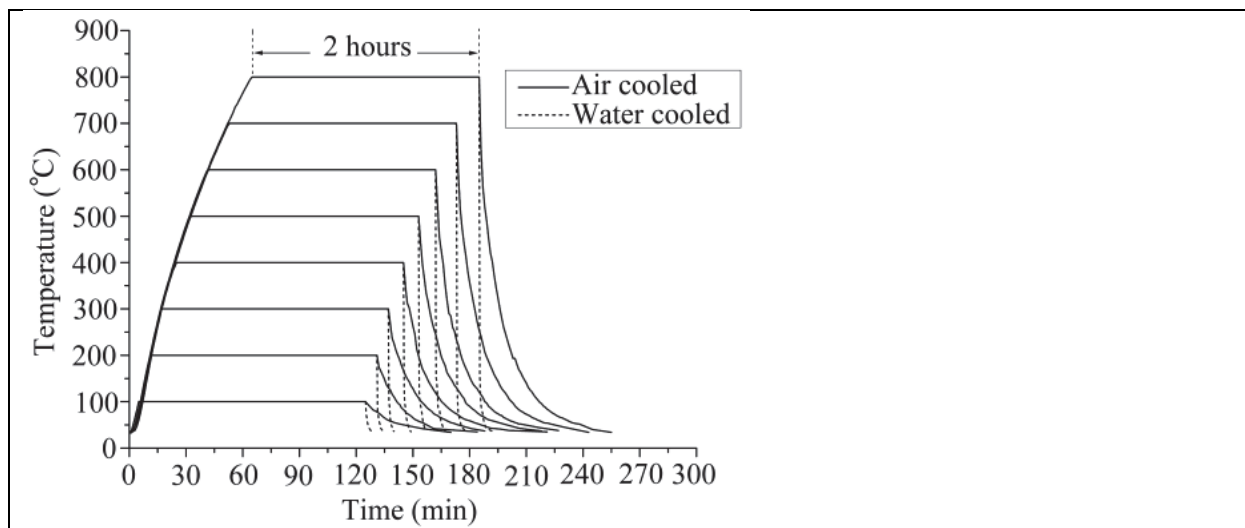


Fig. 3.1: Temperature profiles of TS treatments

4 Test results and discussion

4.1 Physical and mechanical properties of CSTBD after TS

For each cooling method under one level of temperature in TS treatment, at least three specimens are tested. The corresponding dry density (ρ_{TS}), porosity (n_{TS}) and

P-wave velocity (v_{P-TS}) normalized to the values obtained from untreated specimens (ambient temperature) are illustrated in Fig. 4.1 with respect to TS temperatures.

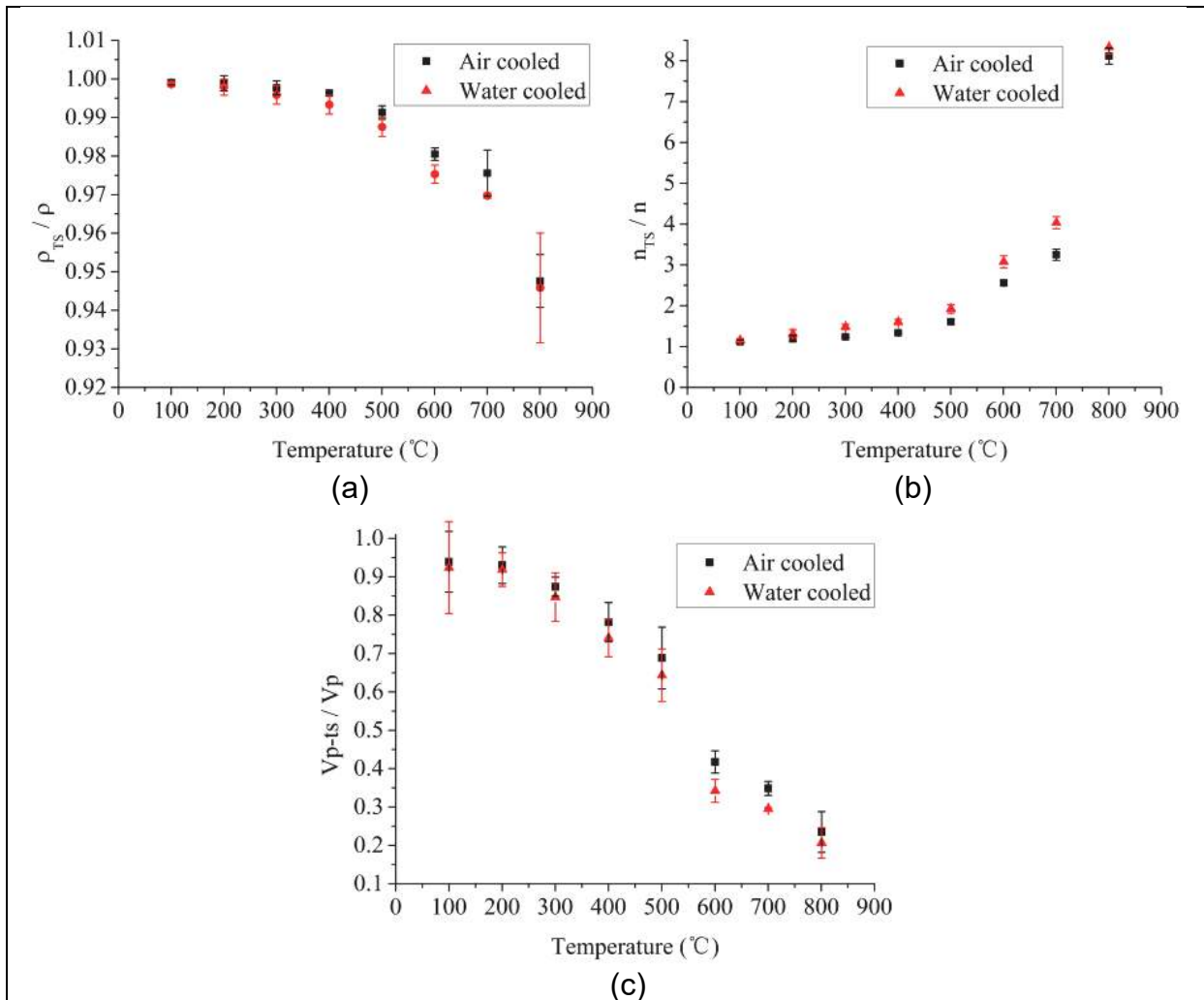


Fig. 4.1: Variation of (a) dry density, (b) porosity and (c) P-wave velocity with TS temperatures (error bar represents standard deviation)

Fig. 4.1 illustrates that the density and P-wave velocity of the specimens present a declining trend with increasing TS temperatures, while the porosity shows an ascending trend. The decrease of P-wave velocity is more significant when TS temperature exceeds 200 °C, where the strong bound water and constitution water start to escape, causing evident damage of mineral crystalline structure and increase of microcracking (Zhang et al. 2016). Abrupt drop of dry density and P-wave velocity, and abrupt increase of porosity are also observed between a TS temperature of 500°C and 600°C. Such trend is in accordance with former test data on P-wave velocity (Nasseri et al. 2007).

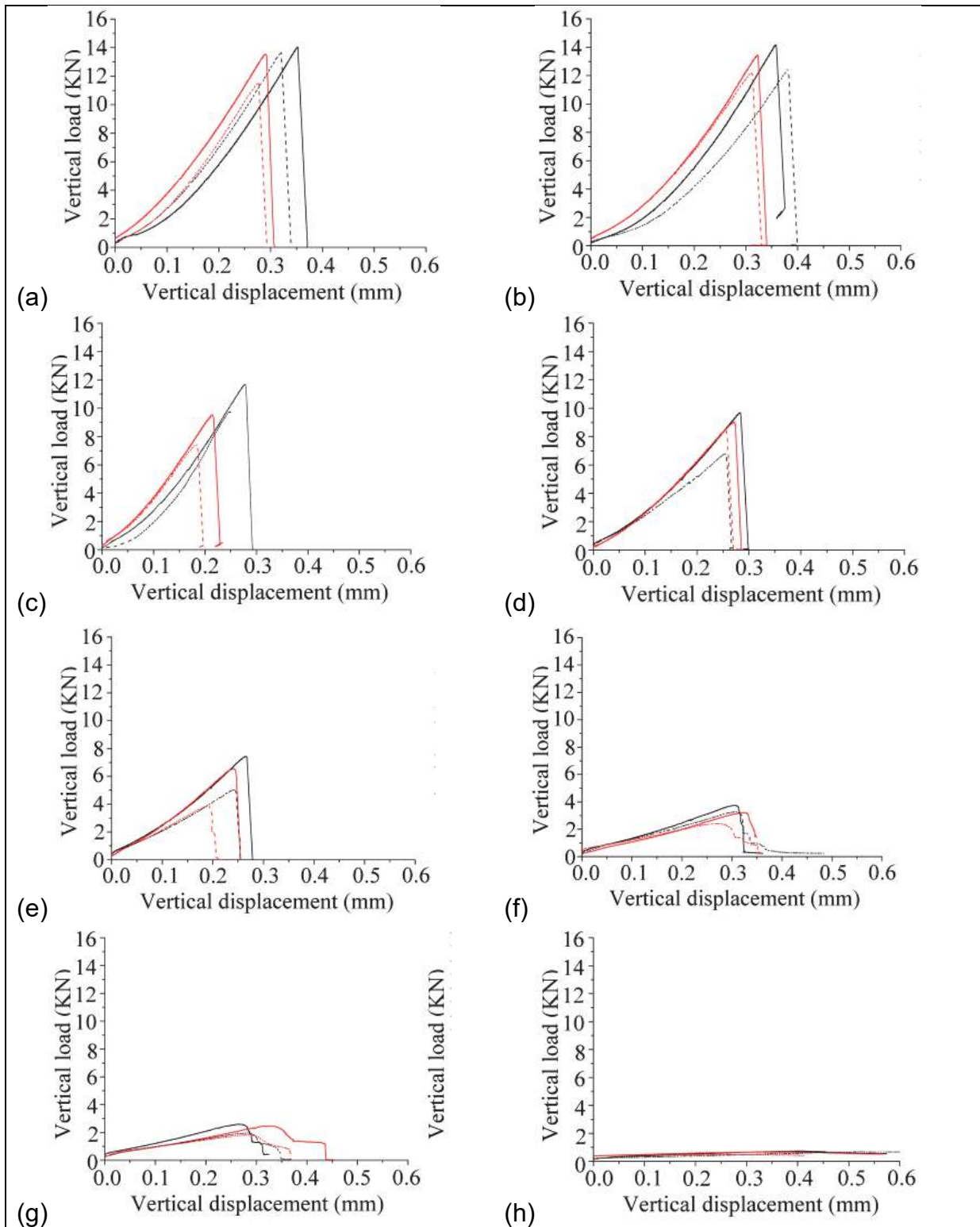


Fig. 4.2: Vertical load-displacement curves for CSTBD of granite under TS of (a) 100 °C, (b) 200 °C, (c) 300 °C, (d) 400 °C, (e) 500 °C, (f) 600 °C, (g) 700 °C, and (h) 800 °C (Black line: Mode I loading; red line: Mode II loading; solid line: air cooled; dash line: water cooled)

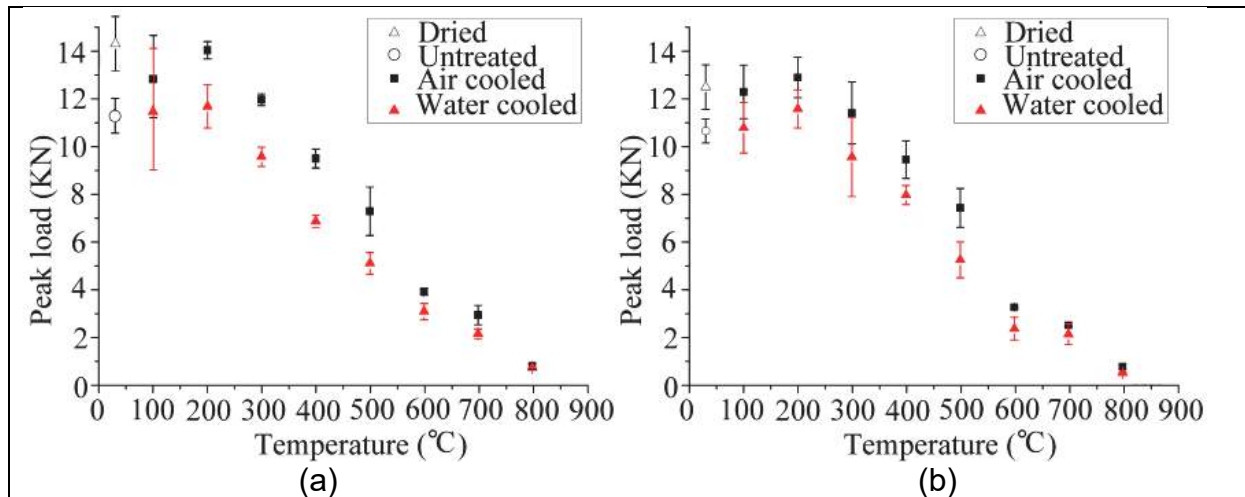


Fig. 4.3: Peak load values at different TS temperatures under (a) Mode I loading, and (b) Mode II loading (error bar represents standard deviation)

The Brazilian tests are carried out on the heat treated granite specimens with the servo-controlled rock mechanical test system MTS 322 at a loading rate of 0.2 mm/min. The mechanical responses of the specimens are illustrated in Fig. 4.2. For comparatively low TS temperatures such as 100 °C ~ 400 °C (Fig. 4.2 (a), (b), (c) and (d)), a slow increase of the load is observed at the initial testing stages forming a concave curve. The curve starts to develop almost linearly at later stages of the loading until failure occurs, where a sudden drop of the curve is resulted. Such feature is not observed for higher TS temperatures (Fig. 4.2 (f), (g) and (h)), where overall low slope of the curves is obtained, and non-linear development of the curves occurs before the failure of the specimens. Besides, at these high TS temperatures (Fig. 4.2 (f), (g) and (h)), larger strain is observed after the peak load is reached, indicating more obvious damage caused by TS.

The peak load values of the specimens after the TS treatments are illustrated in Fig. 4.3. Accordingly to Zhang et al. (2016), at lower TS temperatures (e.g. 100 °C and 200 °C), the attached water evaporates sharply as temperature grows. The loss of water in micro pores alleviates stress corrosion, which results in the increase of fracture toughness (Kataoka et al., 2015). At the same time, the structures of the mineral grains are less affected by the low TS temperature (Fig. 4.5). Therefore, it is assumed that the increasing trend of fracture toughness below 200 °C is dominated by the decrease of pore water. This argument can be supported by the peak load values of the specimens which are not treated by TS, but are dried at 105 °C before the test. Fig. 4.3 indicates that, the peak values of these specimens are at the same level as those at TS temperature of 100 °C and 200 °C. It is observed that a significant drop of strength occurs from TS temperature of 500 °C to 600 °C, which is more clearly identified for the Mode II loading case (Fig. 4.3 (b)). For each TS temperature, the strength for the water-cooled specimens is lower than for the air-cooled specimens. As seen in Fig. 4.3, the strength difference is more prominent at lower TS temperatures (e.g. 100 °C ~ 400 °C), and diminishes as TS temperature further ascends. The observation indicates, that temperature as high as 800 °C can already cause substantial damage to the specimen, thus making the effect of TS not evidently manifested.

4.2 Mode I and Mode II fracture toughness

According to the averaged peak load values of the CSTBD of granite, Mode I and Mode II fracture toughness are obtained according to Eqs. (1) and (2). The variation of fracture toughness with varying TS temperature can be seen in Fig. 4.4.

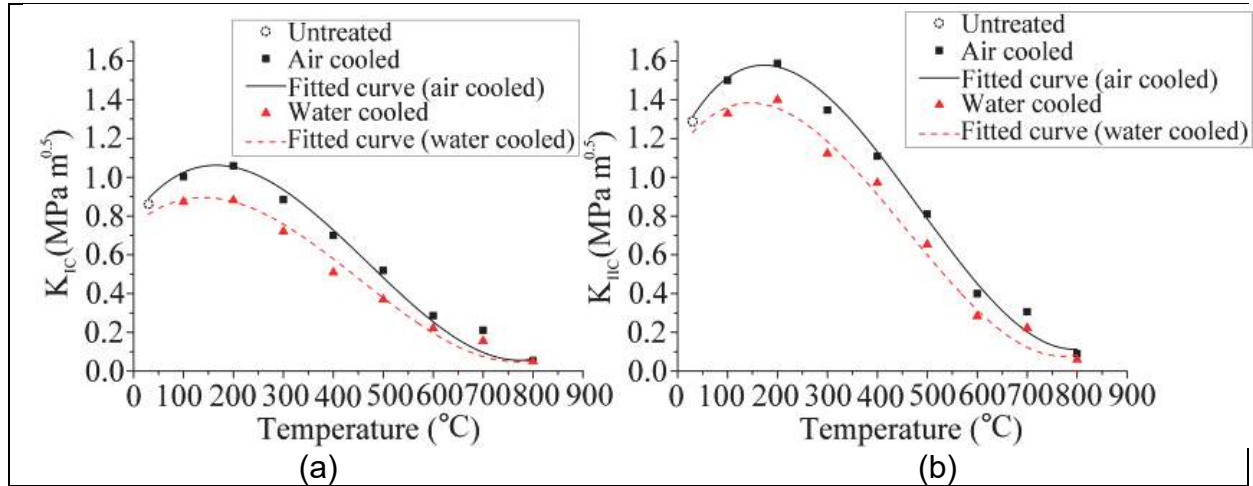


Fig. 4.4: Fracture toughness values with different TS temperature: (a) Mode I fracture toughness; (b) Mode II fracture toughness

At ambient temperature, the Mode I and Mode II fracture toughness is respectively $0.863 \text{ MPa}\cdot\text{m}^{1/2}$ and $1.290 \text{ MPa}\cdot\text{m}^{1/2}$. The variation of fracture toughness has a similar trend to the corresponding peak load values shown in Fig. 4.3. At a TS temperature of $800 \text{ }^\circ\text{C}$, the Mode I fracture toughness values are $0.054 \text{ MPa}\cdot\text{m}^{1/2}$ (air cooled) and $0.050 \text{ MPa}\cdot\text{m}^{1/2}$ (water cooled) respectively, accounting for only 6.29 % and 5.81 % of corresponding fracture toughness at ambient temperature. The Mode II fracture toughness values are $0.090 \text{ MPa}\cdot\text{m}^{1/2}$ (air cooled) and $0.059 \text{ MPa}\cdot\text{m}^{1/2}$ (water cooled) respectively, accounting for only 6.98 % and 4.60 % of corresponding fracture toughness at ambient temperature.

4.3 Microscopic characteristics of fracture surface after TS

The effect of TS on rock involves multifactorial processes due to the anisotropic expansion within minerals and heterogeneous contents of rock materials. Thermal stress can be induced by mismatches of different mineral grains and cement (Hall and Thorn 2014; Ghobadi and Babazadeh 2015). To elucidate physical and mechanical data obtained lab tests, scanning electron microscope (SEM) is utilized to identify the microscopic features of the fracture surface of tested specimens.

The microscopic observations under low TS temperatures are featured by the smooth fracture surfaces (Fig. 4.5 (a)-(d)), as compared with the rough and grainy fracture surfaces under high TS temperatures (Fig. 4.5 (e)-(i)). The smooth fracture surface under low TS temperatures reflects trans-granular fractures (fractures penetrating more than one mineral) and intra-granular fractures (fractures inside one mineral). The rough and grainy fracture surface under high TS temperatures indicate inter-granular fractures (fractures between minerals) (Hall and Thorn, 2014). The brittle intra- or trans-granular fracture largely observed in low TS temperatures leads to the linear development of vertical load before peak strength, and the sudden drop of load bearing capacity upon failure (Figs. 4.2 (a), (b) and (c)). In contrast, at high TS tem-

peratures, inter-granular fractures indicate that interlocking of mineral grains and bonding of cementation are largely lost, which results in the non-linear vertical load-displacement curves and lower strength values (Figs. 4.2 (f), (g) and (h)).

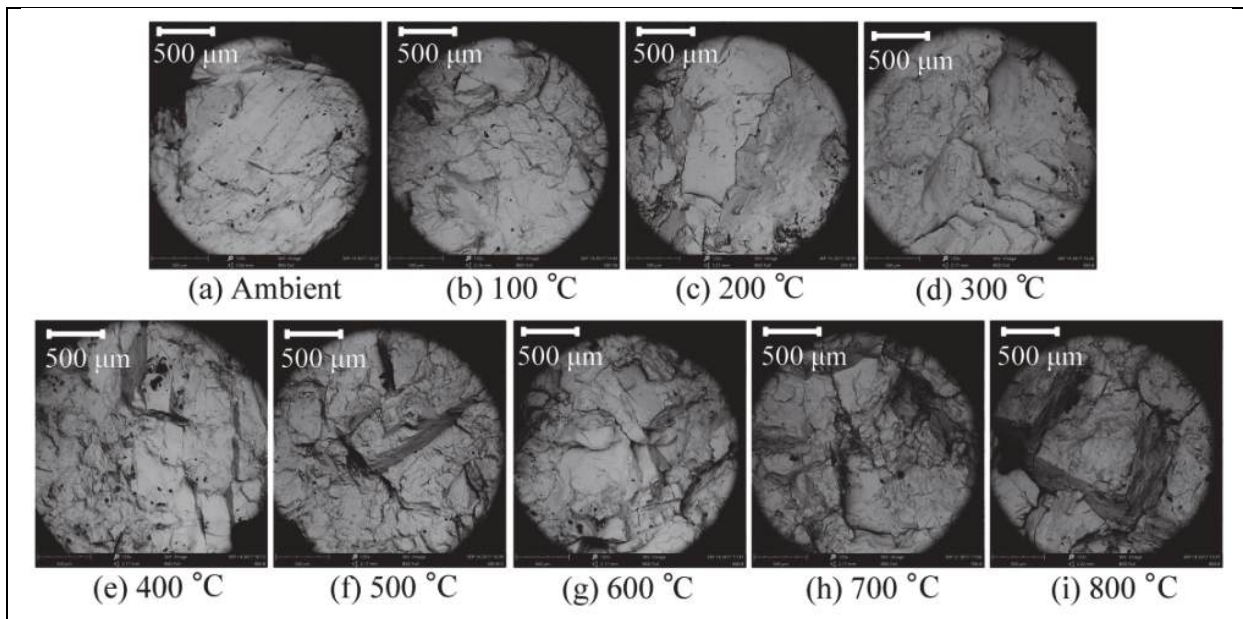


Fig. 4.5: SEM images of fracture surfaces under Mode II loading after TS treatments with water-cooling process (Magnified 125 times)

5 Conclusions

Physical properties and mechanical responses are obtained from granite after TS treatments. SEM observations of fracture surface are performed to interpret the pattern of mechanical behaviors under the influence of TS. The following conclusions can be drawn.

1. The dry density and P-wave velocity decrease with ascending TS temperature. Whereas porosity increases with ascending TS temperature. It should be noted that the difference diminishes as TS temperature ascends.
2. At lower TS temperatures (e.g. 100 °C ~ 400 °C), the vertical load-displacement curves of the Brazilian test develop linearly approaching peak load. At higher TS temperatures, obvious deviation from linearity is observed before peak load. For both Mode I and Mode II loading conditions, the peak load value increases with ascending TS temperature up to 200 °C, and start to decrease since then.
3. Under lower TS temperatures (ambient ~ 300 °C), trans-granular fractures and intra-granular fractures are often observed through SEM. Under higher TS temperatures (400 °C ~ 800 °C), the fracture surface features inter-granular fractures. The observations serve to elucidate the pattern of the lab data.

The test data provides informative hints for projects where high temperature and sudden change of temperature are expected.

References

- Atkinson, C., Smelser, R.E., Sanchez, J. (1982). *Combined mode fracture via the cracked Brazilian disk test*. Int. J. Fracture., 18(4), 279 - 291.
- Awaji, H.S.S. (1978). *Combined mode fracture toughness measurement by the disk test*. Journal of Engineering Materials and Technology, 100, 175 - 182.
- Brotóns, V., Tomás, R., Ivorra, S., Alarcón, J.C. (2013). *Temperature influence on the physical and mechanical properties of a porous rock: San Julian's calcarenite*. Eng. Geol., 167, 117 - 127.
- Chen, Y., Ni, J., Shao, W., Azzam, R. (2012). *Experimental study on the influence of temperature on the mechanical properties of granite under uni-axial compression and fatigue loading*. Int. J. Rock Mech. Min., 56, 62 - 66.
- Ferrero, A.M., Marini, P. (2001). *Experimental Studies on the Mechanical Behaviour of two Thermal Cracked Marbles*. Rock Mechanics & Rock Engineering, 34(1), 57 - 66.
- Franklin, J.A., Vogler, U.W., Szlavin, J., Edmond, J.M., Bieniawski, Z.T. (1979). *Suggested Methods for Determining Water Content, Porosity, Density, Absorption and Related Properties and Swelling and Slake-Durability Index Properties*. Int. J. Rock Mech. Min. Sci. and Geomech., 16, 141 - 156.
- Ghaffarian, R. (2001). *Thermal cycling/shock behavior of CSP assemblies*. NASA Electronics Parts and Packaging Program, 7(2), (5 pp).
- Ghobadi, M.H., Babazadeh, R. (2015). *Experimental Studies on the Effects of Cyclic Freezing–Thawing, Salt Crystallization, and Thermal Shock on the Physical and Mechanical Characteristics of Selected Sandstones*. Rock Mech. Rock Eng., 48(3), 1001 - 1016.
- Hall, K., André, M.O. (2001). *New insights into rock weathering from high-frequency rock temperature data: an Antarctic study of weathering by thermal stress*. Geomorphology, 41(1), 23 - 35.
- Hall, K., Thorn, C.E. (2014). *Thermal fatigue and thermal shock in bedrock: An attempt to unravel the geomorphic processes and products*. Geomorphology, 206, 1-13.
- Heuze, F.E. (1983). *High-temperature mechanical, physical and Thermal properties of granitic rocks – A review*. International Journal of Rock Mechanics & Mining Sciences & Geomechanics Abstracts, 20(1), 3 - 10.
- Kataoka, M., Obara, Y., Kuruppu, M. (2015). *Estimation of Fracture Toughness of Anisotropic Rocks by Semi-Circular Bend (SCB) Tests Under Water Vapor Pressure*. Rock Mechanics & Rock Engineering, 48(4), 1353 - 1367.
- Liu, H.Y., Kou, S.Q., Lindqvist, P.A., Tang, C.A. (2007). *Numerical Modelling of the Heterogeneous Rock Fracture Process Using Various Test Techniques*. Rock Mechanics & Rock Engineering, 40(2), 107 - 144.
- Liu, S., Xu, J. (2015). *An experimental study on the physico-mechanical properties of two post-high-temperature rocks*. Eng. Geol., 185, 63 - 70.
- Mardoukhi, A., Mardoukhi, Y., Hokka, M., Kuokkala, V. (2017). *Effects of Heat Shock on the Dynamic Tensile Behavior of Granitic Rocks*. Rock Mech. Rock Eng., 50(5), 1171 - 1182.

- Mirkin, L.I., Shesterikov, S.A., Yumashev, M.V., Yumasheva, M.A. (2006). *Instability of thermal fracture under the conditions of constrained deformation*. Mater. Sci., 42(6), 778 - 785.
- Nasseri, M.H.B., Schubnel, A., Young, R.P. (2007). *Coupled evolutions of fracture toughness and elastic wave velocities at high crack density in thermally treated Westerly granite*. Int. J. Rock Mech. Min., 44(4), 601 - 616.
- Peng, G.F., et al. (2008). *Effect of thermal shock due to rapid cooling on residual mechanical properties of fiber concrete exposed to high temperatures*. Construction & Building Materials, 22(5), 948 - 955.
- Richter, D., Simmons, G. (1974). *Thermal expansion behavior of igneous rocks*. International Journal of Rock Mechanics & Mining Sciences & Geomechanics Abstracts, 11(10), 403 - 411.
- Sirdesai, N.N., Singh, T.N., Ranjith, P.G., Singh, R. (2017). *Effect of Varied Durations of Thermal Treatment on the Tensile Strength of Red Sandstone*. Rock Mechanics & Rock Engineering, 50, 1 - 9.
- Smart, C.M., Wakabayashi, J. (2009). *Hot and deep: Rock record of subduction initiation and exhumation of high-temperature, high-pressure metamorphic rocks, Feather River ultramafic belt, California*. Lithos, 113(1-2), 292 - 305.
- Wang, P., Xu, J., Liu, S., Wang, H. (2016). *Dynamic mechanical properties and deterioration of red-sandstone subjected to repeated thermal shocks*. Eng. Geol., 212, 44 - 52.
- Wang, Y., Xia, Y., Dong, S. (2004). *Stress intensity factors for central cracked circular disk subjected to compression*. Eng. Fract. Mech., 71(7), 1135 - 1148.
- Yatsu, E. (1988). *The nature of weathering: an introduction*. Sozosha, Tokyo.
- Zhang, W., Sun, Q., Hao, S., Geng, J., Lv, C. (2016). *Experimental study on the variation of physical and mechanical properties of rock after high temperature treatment*. Appl. Therm. Eng., 98, 1297 - 1304.
- Zhang, Z., Shao, Y., Song, F. (2010). *Characteristics of crack patterns controlling the retained strength of ceramics after thermal shock*. Frontiers of Materials Science in China, 4(3), 251 - 254.